Heinrich-Heine-Universität Düsseldorf

Investigation of ion acceleration from underdense targets using a high intensity short pulse laser

Inaugural-Dissertation

zur Erlangung des Doktorgrades der
Mathematisch-Naturwissenschaftlichen Fakultät der
Heinrich-Heine-Universität Düsseldorf

Vorgelegt von

Anna-Marie Schroer
geb. in Wuppertal

Düsseldorf
Januar 2018

aus dem Institut für Laser- und Plasmaphysik
der Heinrich-Heine-Universität Düsseldorf

Gedruckt mit der Genehmigung der
Mathematisch-Naturwissenschaftlichen Fakultät der
Heinrich-Heine-Universität Düsseldorf

Berichterstatter:
1. Prof. Dr. Oswald Willi,
2. Prof. Dr. Dr. Carsten Müller

Tag der mündlichen Prüfung:
27.04.2018

Abstract

The focus of this thesis was the investigation of the ion acceleration from laser interactions with underdense gaseous targets. The experimental campaigns were performed at the ARCTURUS laser facility at Heinrich Heine University Düsseldorf. The capability of a double beam configuration allows the interaction of two high intensity (up to $\sim 10^{20}\,\mathrm{W/cm^2}$), ultrashort ($\sim 30\,\mathrm{fs}$) laser pulses with a target. A third low intensity probe beam can be used for diagnostic purposes.

The ion acceleration was studied in two main experimental setups. In both arrangements Hydrogen or Helium ions were accelerated up to 400 keV energy by a single or double beam interaction with a 1 mm gas target ($0.01\,n_\mathrm{c} - 0.228\,n_\mathrm{c}$). The major diagnostics were two Thomson parabola spectrometers to detect the ions and to resolve their energy distribution. Besides that, accelerated electrons were detected via another magnetic spectrometer. Additionally, the laser interactions were investigated at different times by optical shadowgraphy, interferometry and charged particle probing. Various ion acceleration mechanisms were discovered and novel monoenergetic features in the ion spectra and transitions between different acceleration regimes were observed.

Ions were successfully accelerated in the transverse direction to the laser axis via Coulomb explosion (CE) by a single laser beam interaction of the Heater laser ($2.4 \cdot 10^{19}\,\mathrm{W/cm^2}$, f/10 off-axis parabola (OAP)) with the gas target up to a density of $0.12\,n_\mathrm{c}$. The interpretation is based on the experimental observations including additional diagnostics and numerical simulations. The conclusions about the acceleration mechanism are supported by analytical calculations.

By adding a second beam, the Driver ($1 \cdot 10^{20}\,\mathrm{W/cm^2}$, f/2 OAP), to the experimental arrangement in perpendicular direction to the Heater axis, the acceleration of ions was extended to high target densities (above $0.12\,n_\mathrm{c}$). The acceleration was based on a TNSA-like mechanism of the Driver interacting with a pre-formed plasma of the Heater beam. By a Driver-only interaction with the target, no ions were detected. However, ions were successfully accelerated by the double laser beam interaction in the longitudinal direction of the Driver axis. Numerical simulations and analytical calculations indicated the TNSA-like acceleration mechanism.

Finally, a stable, high repetition rate monoenergetic ion source was developed. The TNSA-like acceleration mechanism by the double beam interaction had to be adapted in order to generate a homogenous and directional electric field to accelerate narrowband ions. This regime was reached by a reduction of the intensity of the Heater beam ($6.6 \cdot 10^{17}\,\mathrm{W/cm^2}$, f/25 OAP). A special preformed target was created and by means of certain laser and target specifications, monoenergetic ion features were detected. By small changes in the experimental parameters, broadband energy spectra were observed.

Zusammenfassung

Ziel dieser Arbeit war die Untersuchung der Ionenbeschleunigung aus verschiedenen Laserinteraktionen mit unterdichten gasförmigen Targets. Die experimentellen Kampagnen wurden in der ARCTURUS Laseranlage der Heinrich-Heine-Universität Düsseldorf durchgeführt. Die Möglichkeit der Zwei-Strahl-Konfiguration erlaubt die Interaktion zweier hoch intensiver (bis zu $\sim 10^{20}\,\mathrm{W/cm^2}$), ultrakurzer ($\sim 30\,\mathrm{fs}$) Laserpulse mit einem Target. Ein dritter Laserstrahl mit niedriger Intensität kann zu Diagnosezwecken verwendet werden.

Die Ionenbeschleunigung wurde in zwei verschiedenen Versuchsaufbauten untersucht. In beiden Anordnungen wurden Wasserstoff- oder Heliumionen durch eine Einzel- oder Doppelstrahl-Wechselwirkung mit einem 1 mm Gastarget ($0.01\,n_\mathrm{c} - 0.228\,n_\mathrm{c}$) auf 400 keV Energie beschleunigt. Zwei Thomson-Parabelspektrometer, die Hauptdiagnostiken, detektierten die Ionen und ihre Energieverteilung wurde aufgelöst. Zusätzlich wurden beschleunigte Elektronen über ein weiteres magnetisches Spektrometer detektiert. Außerdem wurden die Laserinteraktionen durch eine optische orts- und zeitaufgelöste Diagnostik untersucht und elektromagnetische Felder im Plasma wurden mittels eines Diagnostikstrahls bestehend aus geladenen Teilchen identifiziert. Verschiedene Ionenbeschleunigungsmechanismen wurden entdeckt und neuartige monoenergetische Merkmale in den Ionenspektren und Übergänge zwischen den verschiedenen Beschleunigungssystemen beobachtet.

Zunächst wurden Ionen erfolgreich durch Coulomb-Explosion (CE) während einer Einzel-Laserstrahl Wechselwirkung des Heizlasers ($2.4 \cdot 10^{19}\,\mathrm{W/cm^2}$, f/10 off-axis parabola (OAP)) mit dem Gastraget in Querrichtung der Laserachse beschleunigt bis zu einer Dichte von $0.12\,n_\mathrm{c}$. Die Interpretation basiert auf den experimentellen Beobachtungen einschließlich zusätzlicher Diagnostiken und numerischer Simulationen. Die Schlussfolgerungen über den Beschleunigungsmechanismus werden durch analytische Berechnungen gestützt.

Durch Hinzufügen eines zweiten Strahls, des Treibers ($1 \cdot 10^{20}\,\mathrm{W/cm^2}$, f/2 OAP), in senkrechter Richtung der Heizlaserachse, wurde die Beschleunigung der Ionen bis zu hohen Targetdichten (über $0.12\,n_\mathrm{c}$) verlängert. Die Beschleunigung basiert auf einem TNSA-artigen Mechanismus des Treibers, der mit einem durch den Heizstrahl vorgeformten Plasma wechselwirkt. Durch eine reine Treiber-Interaktion mit dem Target wurden keine Ionen detektiert. Die Ionen wurden jedoch erfolgreich durch die Doppellaserstrahl-Wechselwirkung in Längsrichtung der Treiberachse beschleunigt. Numerische Simulationen und analytische Berechnungen wiesen den TNSA-ähnlichen Beschleunigungsmechanismus hin.

Schließlich wurde eine stabile monoenergetische Ionenquelle mit hoher Wiederholrate entwickelt. Der TNSA-ähnliche Beschleunigungsmechanismus durch die Doppelstrahl Wechselwirkung musste angepasst werden, um ein homogenes und gerichtetes elektrisches Feld zu erzeugen, um schmalbandige Ionen zu beschleunigen. Dieses Regime wurde durch eine Verringerung der Intensität des Heizstrahls erreicht ($6.6 \cdot 10^{17}\,\mathrm{W/cm^2}$, f/25

OAP). Ein speziell vorgeformtes Target wurde entwickelt und mittels bestimmter Laser- und Targetspezifikationen wurden monoenergetische Ionenmerkmale detektiert. Durch kleine Änderungen der experimentellen Parameter wurden Breitband-Energiespektren beobachtet.

Contents

Chapter 1

Introduction

Within the last two decades the development of ultra-short, high-intensity lasers became a promising tool for compact novel particle accelerators and sources of high energetic photons. During the interaction of a high-intensity laser pulse with a plasma, multi MeV protons, ions [1, 2] and high energy electron beams with monoenergetic features [3, 4] can be successfully accelerated. In addition, high brilliant gamma-ray sources [5] are realised as a product of different particle acceleration schemes.

In order to get a better understanding of the underlying physics, it is important to investigate both, experimentally and via simulations, the fundamental processes of the interaction and the plasma properties. Thus, these novel sources can be further improved for feasible applications e.g., in inertial confinement fusion [6], cancer therapy [7] or x-ray microscopy [8].

Target Normal Sheath Acceleration (TNSA) [9] is one of the best understood processes to accelerate ions from solid targets. At laser intensities above $10^{18}\,\mathrm{W/cm^2}$ a plasma is created at the front surface of a thin solid target. Originating from this point, relativistic electrons are accelerated through the target and finally pushed out of the solid material close the target rear side. A strong sheath field occurs by the electron cloud. Moreover, this charge separation between the positively charged target and the electron cloud induces a strong longitudinal electric field, which accelerates ions from the rear side of the target. Protons are preferentially accelerated (due to their high charge to mass ratio) from a hydrocarbon contaminant layer desorbed of the target surface. In addition, heavy ions such as carbon ions are also accelerated. Specially structured targets can be possibly applied to achieve single species ion acceleration, e.g [10].

In this regard, underdense gas targets offer potential advantages such as single species ions, less debris and the capability to run with a high repetition rate. So far, *Krushelnick et al.* observed ion acceleration at 90° with respect to the laser propagation axis up to a few MeV using different gases at the high-power VULCAN laser at Rutherford Appleton Laboratory. A plasma channel is generated by the high intensity laser interaction due to the ponderomotive expulsion of electrons in the transverse direction to the laser axis. A charge separation is induced causing the acceleration of the ions as described in [11]. This process is called Coulomb explosion [11]. *Wei et al.* measured an increase of the maximum ion energy with higher plasma densities by additional collisionless shock acceleration at the VULCAN PW laser facility [12]. By means of the same laser *Willingale et al.* were able to measure the acceleration of ions in laser propagation direction applying a specific gas density threshold. A TNSA-like mechanism occurs in addition to the Coulomb explosion for a longitudinal acceleration [13]. Recently, *Lifschitz et al.* achieved an acceleration of non-thermal ion bunches in 90° to the laser axis by means of the high intensity Salle Jaune laser at Laboratoire d'Optique Appliquèe. In this case a combination of TNSA and Coulomb explosion has contributed to the acceleration process [14].

In our recent experiments at the ARCTURUS laser facility at Heinrich Heine University Düsseldorf we observed acceleration of protons or Helium ions up to 400 keV from an underdense gas target. First, ions were accelerated in the transverse direction via Coulomb explosion by a single laser beam interaction. Second, ions were accelerated in the longitudinal direction via a TNSA-like mechanism by a novel double beam interaction scheme. Furthermore, it turned out, that this interaction was capable to achieve monoenergetic ion features. Several different experimental conditions, such as different gases at various densities, different laser energies and intensities and numerous relative time delays between the beams were investigated in order to control the laser plasma interactions in each configurations. Numerical simulations of the experimental conditions indicated the acceleration regimes, supported by analytical calculations.

The general experimental setup included two high power, 30 fs short pulse laser beams, which were focused orthogonal to each other into a 1 mm gas jet. The Driver laser beam focused by an f/2 off-axis parabola (OAP) had an intensity of $1 \cdot 10^{20}\,\mathrm{W/cm^2}$ and the Heater laser beam reached intensities of about $2.4 \cdot 10^{19}\,\mathrm{W/cm^2}$, focused by an f/10 OAP and in a second setup $6.6 \cdot 10^{17}\,\mathrm{W/cm^2}$, focused by an f/25 OAP. As main diagnostics two Thomson parabola spectrometers equipped with micro channel plate

(MCP) detectors were employed along 0° and 10° relative to the driver laser beam axis. Hydrogen and Helium gas jet densities of $n_e \sim 10^{19} - 10^{20}\, cm^{-3}$, corresponding to about $0.01\, n_c - 0.228\, n_c$, were applied.

Thesis structure:

Chapter 2 gives an overview of the underlying theory and fundamentals in laser plasma physics. First of all, basic principles of the ionisation processes of atoms by electromagnetic waves are described, e.g. multi-photon ionisation and tunnel ionisation. Furthermore, the effect of electromagnetic waves to a single charged particle is discussed. Then, fundamental laser plasma characteristics and non-linear effects in underdense plasmas are outlined. The most important ion acceleration mechanisms in order to understand the physical process, discussed in this thesis, are summarised: Target Normal Sheath Acceleration, Coulomb Explosion and Collisionless Shock Acceleration. Moreover, some previous experimental results of ion acceleration from underdense gas targets are presented.

Chapter 3 illustrates the ARCTURUS laser facility from the oscillator to the various amplification stages leading to the high intensity beam focused by a parabola in the radiation shielded target area. All three laser beams of the ARCTURUS were employed in the experimental campaigns. The topic of this thesis is the investigation of the ion acceleration due to the interaction of the lasers with an underdense gas target. This target was characterised by means of an interferometric measurement at different gas pressures and different interaction heights. Finally, a pressure to neutral density relation was defined.

Chapter 4 describes all the diagnostics operated in the experimental campaigns. In order to detect and spectrally resolve the accelerated ions, two main spectrometers were used in the configuration of Thomson parabolas at two different observation angles. The deflected ions were detected by micro channel plates. For the investigation of the laser plasma interaction, associated with the plasma densities and the electric and magnetic fields in the plasma, optical probing with shadowgraphy and interferometry and charge particle probing were employed. Furthermore, the acceleration of electrons was observed by a magnetic spectrometer resolving the electron energies. Finally, descriptions of the experimental setups and laser parameters relevant for the experimental campaigns of this thesis are introduced.

Chapter 5 outlines ion acceleration via Coulomb explosion in underdense targets. A single laser beam, called Heater, was employed to interact with Helium or Hydrogen gas. Accelerated ions were detected in the transverse direction to the laser axis up to a certain density. The acceleration process is validated by numerical simulations and supported by analytical calculations. Furthermore, results of a magnetic spectrometer, optical probing and charge particle probing are discussed and brought into connection with the acceleration mechanism.

Chapter 6 presents ion acceleration via a TNSA-like mechanism in underdense targets. In addition to the Heater laser, a short focal length, high intensity Driver laser was employed normal to the Heater axis. By means of this double beam interaction, the ion acceleration was extended up to very high target densities. The ions were detected along the Driver laser axis. Numerical simulations indicated the TNSA-like acceleration process in this novel experimental regime, strengthened by analytical calculations. Moreover, results of the electron acceleration and of shadowgraphy images of the Driver-only interaction are discussed.

Chapter 7 introduces a stable, high repetition rate monoenergetic ion source. The ion acceleration by the double beam interaction via the TNSA-like mechanism was further developed. The target has to be manipulated in order to generate a steep density gradient leading to a spatially homogenous localised electric sheath field. A reduction of the Heater intensity led to a specially pre-formed plasma for the Driver interaction in favour of the desired source. At a certain target density with a defined laser intensity and temporal delay between the beams, monoenergetic protons were generated. Different parameters of the target and the laser were changed in order to control the conditions for the novel monoenergetic ion source. Ions were detected only along the Driver axis. This was confirmed by the absence of accelerated ions in the spectrometer in the transverse direction to the Driver beam.

Chapter 8 summarises all the results and trends of the laser plasma interaction and gives an outlook on further experimental campaigns.

Role of the author:

The author had the leading role in designing and executing the experiments presented in this thesis performed at the ARCTURUS laser facility (Düsseldorf). The body of work described in this thesis is original and was undertaken by the author, except where indicated by references to other work. The subsequent data processing and analysis was carried out by the author, under the guidance of Professor Dr. Oswald Willi. Some ion energy spectra were analyzed by means of a Matlab routine written by A. Alejo of the Queens University Belfast. 2D PIC simulations were performed by Dr. T. Liseykina of the University of Rostock with additional guidance of Professor Dr. A. Macchi of the University of Pisa in the context of the project ISCRA B "PULPICS" granted by CINECA by means of the supercomputer MARCONI (CINECA, Bologna).

Chapter 2

Theoretical basics of laser plasma interactions

Basic processes of ionisation and interaction of electromagnetic waves with charged particles are described in this chapter. Furthermore some basic concepts of laser plasma physics and important non-linear effects, which play a role in the experiments, are lined out. Moreover, important ion acceleration mechanisms are discussed and at the end of this chapter some previous experiments of ion acceleration from underdense targets are summarised. The theoretical explanations are based on several laser plasma physics books, like those written by *Macchi* [15], *Chen* [16], *Gibbon* [17] and *Kruer* [18].

2.1 Ionisation processes

Different ionisation processes need to be investigated in order to get a deeper understanding of laser plasma interactions. Therefore, different basic mechanisms of plasma generation, due to light-matter interaction, are explained in the following, based on [17].

For all following processes, the simplest version is the ionisation of a Hydrogen atom. The first approximation is the matching of the electrostatic potential, which bounds the electron to the proton, with the electric field of the laser in order to ionise the atom. The electrostatic field within the Hydrogen atom is

$$E_{\mathrm{H}} = \frac{e}{4\pi\epsilon_0 a_{\mathrm{B}}^2} \approx 5.1 \cdot 10^9\,\mathrm{V/cm}, \tag{2.1}$$

with e as electron charge, ϵ_0 as vacuum permittivity and a_{B} as *Bohr* radius. The intensity at which the laser field strength matches the atomic electrostatic field and therefore the binding strength can be defined via

$$I_{\mathrm{L}} \geq \frac{\epsilon_0 c E_{\mathrm{H}}^2}{2} \approx 3.51 \cdot 10^{16}\,\mathrm{W/cm^2}. \tag{2.2}$$

Consequentially with a laser intensity of approximately $10^{16}\,\mathrm{W/cm^2}$ every target material can be ionised. However, ionisation can take place even with a lower laser field strength, as described in the following sections.

2.1.1 Multi-photon ionisation

Since the 19th century, ionisation due to radiation exposure is a well known phenomenon. In the photoelectric effect an electron is ejected of the atom by a single photon transferring its energy to the atom. The radiation energy has to be larger or equal to the ionisation energy of the atom. Later, it was found, that the ionisation can be achieved even by lower energy radiation, capturing multiple photons, necessary for the ionisation [19]. The ionisation rate for the non-resonant n-photon ionisation is

$$\Gamma_n = \sigma_n \Phi_n. \tag{2.3}$$

σ_n is the generalised cross section and Φ_n the photon flux, which is calculated by $\Phi = I_{\mathrm{L}}/E_{\mathrm{Photon}}$, ($I_{\mathrm{L}}$: Laser intensity; E_{Photon}: Photon energy). From the multiple photon ionisation (MPI) conclusions can be drawn about the atomic features, affected by the electromagnetic radiation, and the laser characteristics.

The photon energy of the ARCTURUS laser radiation is: $E = h\nu \approx 1.55\,\mathrm{eV}$, at the central wavelength of $\lambda = 800\,\mathrm{nm}$. However, the ionisation energies, E_{ion}, for Hydrogen are 13.6 eV and for Helium atoms 24.6 eV and 54.4 eV for the full ionisation. These energies are higher than the photon energy of the ARCTURUS laser. Therefore, an absorption of multiple photons (MPI) is necessary to ionise these atoms, compare plot

(a) of figure 2.1. The minimum necessary number of photons n to ionise Hydrogen is about 9 and for He^+ it is about 16 and for He^{++} 36. These values are much lower than the number of photons in one laser pulse. Therefore the multiple photon ionisation threshold is easily exceeded, as seen in plot (b).

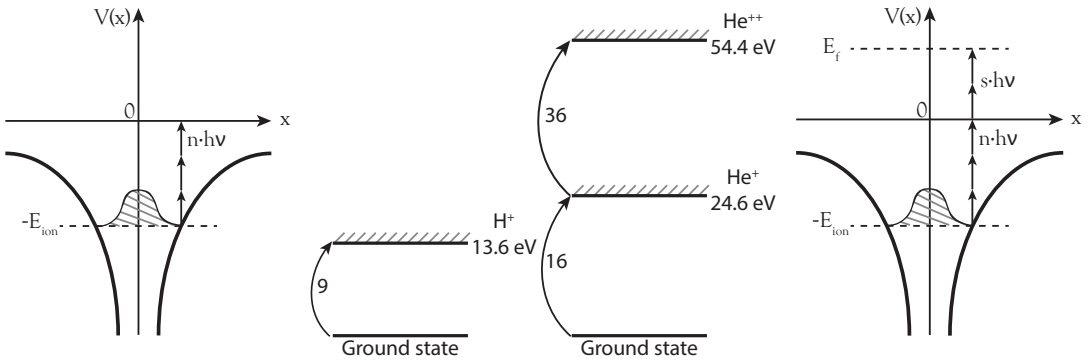

(a) MPI (b) MPI at ARCTURUS (c) ATI

Figure 2.1: Schematic illustration of multiple photon ionisation (MPI) and above threshold ionisation (ATI). To release an electron from an atom, the Coulomb potential has to be exceeded. This could happen by absorbing multiple photons until the binding energy E_{ion} of the electron can be balanced (MPI), plot(a). This numbers are calculated for the ionisation of Hydrogen and Helium ions by means of $\lambda = 800\,\mathrm{nm}$ photons, i.e. the central wavelength of the ARCTURUS laser, in plot(b). The electrons, however, can gain even more energy by absorbing more photons than necessary to be freed (ATI), plot(c).

The electron can gain even a higher kinetic energy than needed for ionisation, by absorbing more photons than necessary to eject it from the atom. This process is called above threshold ionisation (ATI), see plot (c). The energy can be calculated to

$$E_\mathrm{f} = (n+s)h\nu - E_\mathrm{ion}, \tag{2.4}$$

with the minimum number of photons n, which are needed to overcome the ionisation threshold and the much larger number s of the additional absorbed photons, while E_ion represents the ionisation energy for each atom. The ARCTURUS pulse energy in a focal spot of $d_0 = 12\,\mu\mathrm{m}$ was measured around 0.8 J, which corresponds to a number of photons of about $3 \cdot 10^{24}/\mathrm{cm}^2$. Even if the laser energy is reduced drastically, the

photon flux and the number of photons is still high. This values are much larger than the number of photons needed in a certain time for the MPI. Consequently, also the threshold for the ATI is easily exceeded even by a very low intensity laser beam.

2.1.2 Tunnel ionisation

The laser field does not disturb the Coulomb potential of the atom in MPI. However, for high intensity lasers ($I_{\mathrm{L}} \geq 10^{14}\,\mathrm{W/cm^2}$) the atomic binding potential of the electron to the atom is distorted and a new mechanism of ionisation takes place, the tunneling ionisation process (TI). In order to get an estimation, if the ionisation mechanism is MPI or TI, the Keldysh parameter γ can be considered.

$$\gamma = \omega_{\mathrm{L}} \frac{\sqrt{2E_{\mathrm{ion}}}}{eE_0} \sim \sqrt{\frac{E_{\mathrm{ion}}}{\Phi_{\mathrm{P}}}}, \tag{2.5}$$

where E_0 is the electric field strength of the laser pulse and Φ_{P} is the ponderomotive potential, which will be discussed later in this chapter. If $\gamma > 1$ MPI will dominantly take place, while for $\gamma < 1$ the TI will prevail the process.

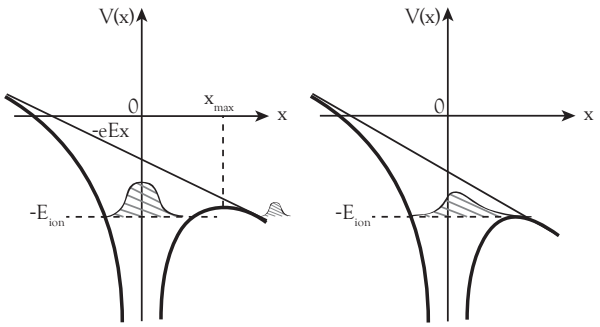

(a) TI (b) BSI

Figure 2.2: Scheme of the tunnel ionisation (TI), as well as the barrier suppression ionisation (BSI). The laser field is strong enough to disturb the atomic binding potential in a way that electrons can escape from the Coulomb potential spontaneously.

The classical Coulomb potential, modified by the laser field for TI to occur can be written as

$$V(x) = -\frac{Ze^2}{x} - eEx, \tag{2.6}$$

where E is the electric field of the laser, linearly polarized along the x-axis. The reshaped barrier has been suppressed on one side. The electron may tunnel through this barrier with a certain probability, as illustrated in plot (a) of figure 2.2. If E_{ion} is above the barrier, the electron will escape spontaneously, which is called barrier suppression ionisation (BSI), pictured in plot (b). The maximum position of the barrier can be expressed as

$$x_{\text{max}} = \frac{Ze}{E}. \tag{2.7}$$

If the potential at this point is set to the ion binding energy: $V(x_{\text{max}}) = E_{\text{ion}}$, the field threshold of the BSI can be calculated with

$$E_{\text{c}} = \frac{E_{\text{ion}}^2}{4Ze^3}. \tag{2.8}$$

By means of equation 2.8 an intensity for the ionisation threshold

$$I_{\text{BSI}} = \frac{c}{8\pi}E_{\text{c}}^2 = 4 \cdot 10^9 \frac{E_{\text{bind}}[eV]^4}{Z^2}\,[\text{W/cm}^2], \tag{2.9}$$

is needed. The required laser intensity for the BSI process for Hydrogen and Helium atoms can be defined as

$$\begin{aligned} I_{\text{BSI}}^{\text{H}} &\approx 1.4 \cdot 10^{14}\,\text{W/cm}^2, \\ I_{\text{BSI}}^{\text{He}^+} &\approx 1.4 \cdot 10^{15}\,\text{W/cm}^2, \\ I_{\text{BSI}}^{\text{He}^{++}} &\approx 8.8 \cdot 10^{15}\,\text{W/cm}^2. \end{aligned} \tag{2.10}$$

Therefore, the target can already be ionised by a relatively low intensity laser beam.

The temporal contrast of the laser is defined by a pedestal level due to amplified spontaneous emission (ASE) in the pico second time range, as discussed later on in subsection 3.1.3. This pedestal level is above the ionising threshold and could ionise the target before the main laser pulse arrives. This should be taken into account for further analysis of the results discussed in this thesis.

2.2 Single charged particle motion

In order to understand different processes in laser plasma interaction, the motion of a single charged particle of the plasma in the electromagnetic field of a laser has to be investigated. This section is based on books [15] and [16].

2.2.1 Particle motion in electromagnetic waves

An electron interacting with a magnetic field will carry out a circular gyration motion due to the magnetic Lorentz force. With an additional electric field, the guiding centre of the electrons will also have a drift. The equation of motion can be written as

$$m_\mathrm{e}\frac{d\boldsymbol{v}}{dt} = -e\left[\boldsymbol{E}(\boldsymbol{r},\boldsymbol{t}) + \frac{\boldsymbol{v}}{c}\times\boldsymbol{B}(\boldsymbol{r},\boldsymbol{t})\right]. \tag{2.11}$$

Where $\boldsymbol{r} = x\hat{\boldsymbol{x}} + y\hat{\boldsymbol{y}} + z\hat{\boldsymbol{z}} = \boldsymbol{r}(t)$ is the particle position with $d\boldsymbol{r}/dt = \boldsymbol{v}$, while the electric and magnetic fields of a plane wave, propagating in x direction, are

$$\begin{aligned}\boldsymbol{E} &= \boldsymbol{E}(\boldsymbol{x},\boldsymbol{t}) = E_0\hat{\boldsymbol{\epsilon}}\exp\left(\mathrm{i}(kx-\omega t)\right) = E_0\hat{\boldsymbol{\epsilon}}[\cos(kx-\omega t) + \mathrm{i}\sin(kx-\omega t)],\\ \boldsymbol{B} &= \boldsymbol{B}(\boldsymbol{x},\boldsymbol{t}) = \hat{\boldsymbol{x}}\times\boldsymbol{E} = \hat{\boldsymbol{x}}\times E_0\hat{\boldsymbol{\epsilon}}[\cos(kx-\omega t) + \mathrm{i}\sin(kx-\omega t)].\end{aligned} \tag{2.12}$$

The wave vector is $k = \omega/c$ with ω as angular frequency and c as speed of light. $\hat{\epsilon}$ is the complex polarization vector, which is $\hat{\boldsymbol{\epsilon}} = \hat{\boldsymbol{y}}(\hat{\boldsymbol{z}})$ for linear polarized light along $y(z)$ and $\hat{\boldsymbol{\epsilon}} = (\hat{\boldsymbol{y}} \pm \mathrm{i}\hat{\boldsymbol{z}})/\sqrt{2}$ for circular polarization.

In a linear approximation the $\boldsymbol{v}\times\boldsymbol{B}$ term of equation 2.11 can be neglected in the case of weak fields and for $|\boldsymbol{v}| \ll c$. A solution via a first order approach is obtained as

$$\begin{aligned}\boldsymbol{v}_1 &= -\frac{\mathrm{i}e}{m_\mathrm{e}\omega}\boldsymbol{E},\\ \boldsymbol{r}_1 &= \frac{e}{m_\mathrm{e}\omega^2}\boldsymbol{E}.\end{aligned} \tag{2.13}$$

Assuming no additional force in the $\hat{\boldsymbol{x}}$ direction, the electron trajectory is line-shaped for linear and a circle for circular polarized light.

A new parameter can be defined to distinguish between the non-relativistic and relativistic regimes of the interaction. The normalised and dimensionless amplitude of the laser field or normalised vector potential a_0, which can be expressed as

$$a_0 = \frac{v_1}{c} = \frac{eE_0}{m_e \omega c}. \tag{2.14}$$

If $a_0 > 1$, which means the electron velocity is comparable to the speed of light c, the electron motion will be relativistic. a_0 can also be written in practical units for a convenient description (for linear polarization) as

$$a_0 = \frac{e}{m_e c}\frac{\lambda}{2\pi c}\sqrt{\frac{8\pi I}{c}} = 0.85\sqrt{\frac{I\lambda_\mu^2}{10^{18}\mathrm{Wcm}^{-2}}}. \tag{2.15}$$

At the Düsseldorf ARCTURUS laser facility, peak intensities in the range of $10^{20}\,\mathrm{W/cm^2}$ can be reached. This corresponds to an $a_0 \approx 8$, which means relativistic effects have to be taken into account.

In the relativistic approximation ($a_0 \geq 1$), the equations 2.13 are not valid anymore. Now, the magnetic field has to be included. The next order term is considered as: $\boldsymbol{v} = \boldsymbol{v}_1 + \boldsymbol{v}_2$ and the equation of motion changes to

$$m_e \frac{d(\boldsymbol{v}_1 + \boldsymbol{v}_2)}{dt} = -e\left[\boldsymbol{E}(\boldsymbol{r},\boldsymbol{t}) + \frac{\boldsymbol{v}_1 + \boldsymbol{v}_2}{c} \times \boldsymbol{B}(\boldsymbol{r},\boldsymbol{t})\right]. \tag{2.16}$$

With $\boldsymbol{E} = E_0\hat{\boldsymbol{y}}\sin(\omega t)$ and $\boldsymbol{B} = E_0\hat{\boldsymbol{z}}\cos(\omega t)$ the trajectory of the electrons can be reduced to

$$16X^2 = Y^2(1 - Y^2), \tag{2.17}$$

with the dimensionless coordinates $X = (\omega x/c)/a_0^2$ and $Y = (\omega y/c)/a_0$. This movement represents the *figure-of-eight* in the rest frame with no average movement along the propagation direction x, figure 2.3.

The relativistic equation of motion, expressed by the momentum, can be defined as

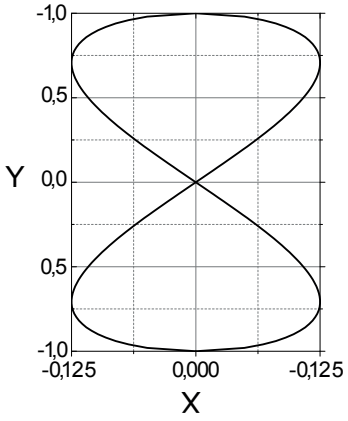

Figure 2.3: Trajectory of an electron in a plane electromagnetic wave in the average reference frame moving with the drift.

$$\frac{d\boldsymbol{p}}{dt} = -e\left[\boldsymbol{E} + \frac{\boldsymbol{v}}{c} \times \boldsymbol{B}\right], \tag{2.18}$$

with the momentum $\boldsymbol{p} = m_\mathrm{e}\gamma\boldsymbol{v}$. γ is the relativistic factor, which can be defined by means of a_0: $\gamma = 1/\sqrt{1 - v^2/c^2} \approx 1/\sqrt{1 - a_0^2}$. For a summary of the relativistic particle motion in an electromagnetic field see [15] p. 9.

2.2.2 Ponderomotive Force

The calculations above are only valid for plane electromagnetic waves. This, however, is not the case for interactions of ultra short laser pulses with a plasma. For example, an intensity gradient is caused by the tight focusing of the laser with a Gaussian intensity profile. In the following it is described how this fact will affect the particle motion in the field of an electromagnetic wave. If there is no energy transferred from the wave to the particles, electrons and ions just oscillate in the field. However, if the perturbation due to the wave gets bigger, non-linear terms have to be considered. Due to that the electron motion consists of a slowly varying part superposed by the fast oscillating term.

With equation 2.11 and the limit $v/c \ll 1$, the equation of motion is

$$\frac{d\boldsymbol{v}_1}{dt} = -\frac{e}{m_\mathrm{e}}\boldsymbol{E}(\boldsymbol{r}_\mathrm{s}(t), t). \tag{2.19}$$

In contrast to the calculations before, the amplitude of the electric field is now dependent on the radial component. A Taylor expansion leads to

$$\boldsymbol{E}(\boldsymbol{r}_\mathrm{s}(t),t) = \boldsymbol{E}(\boldsymbol{r}_\mathrm{s}(t)+\boldsymbol{r}_0(t),t) \approx \boldsymbol{E}(\boldsymbol{r}_\mathrm{s}(t),t) + (\boldsymbol{r}_0(t)\cdot\boldsymbol{\nabla})\boldsymbol{E}(\boldsymbol{r}_\mathrm{s}(t),t). \tag{2.20}$$

The first order solution at the initial position $\boldsymbol{r}_0$, neglecting the $\boldsymbol{v}/c\times\boldsymbol{B}$ term is reduced to

$$\begin{aligned} \frac{d\boldsymbol{v}_1}{dt} &= -\frac{e}{m_\mathrm{e}}\boldsymbol{E}(\boldsymbol{r}_0)\cos\omega t, \\ \boldsymbol{v}_1 &= -\frac{\mathrm{i}e}{m_\mathrm{e}\omega}\boldsymbol{E}_\mathrm{s}(\boldsymbol{r}_\mathrm{s}(t))\sin\omega t, \\ \boldsymbol{r}_1 &= \frac{e}{m_\mathrm{e}\omega^2}\boldsymbol{E}_\mathrm{s}(\boldsymbol{r}_\mathrm{s}(t))\cos\omega t. \end{aligned} \tag{2.21}$$

By using Maxwell's equation

$$\begin{aligned} \boldsymbol{\nabla}\times\boldsymbol{E} &= -\frac{\partial\boldsymbol{B}}{\partial t}, \\ \boldsymbol{B}_1 &= -\frac{1}{\omega}\boldsymbol{\nabla}\times\boldsymbol{E}_\mathrm{s}(\boldsymbol{r}_0)\sin\omega t, \end{aligned} \tag{2.22}$$

and the next order term, the equation of motion can be written as

$$\frac{d\boldsymbol{v}_2}{dt} = -\frac{e}{m_\mathrm{e}}\left[(\boldsymbol{r}_1\cdot\boldsymbol{\nabla})\boldsymbol{E}(\boldsymbol{r}_\mathrm{s}(t),t) + \frac{\boldsymbol{v}_1}{c}\times\boldsymbol{B}_1\right]. \tag{2.23}$$

By means of equation 2.21 and 2.22 and averaging over time, the non linear force on a single electron can be calculated with

$$m_\mathrm{e}\left\langle\frac{d\boldsymbol{v}_2}{dt}\right\rangle = -\frac{e^2}{m_\mathrm{e}\omega^2}\frac{1}{2}\left[(\boldsymbol{E}_\mathrm{s}(\boldsymbol{r}_\mathrm{s}(t))\cdot\boldsymbol{\nabla})\boldsymbol{E}_\mathrm{s}(\boldsymbol{r}_\mathrm{s}(t)) + \boldsymbol{E}_\mathrm{s}(\boldsymbol{r}_\mathrm{s}(t))\times(\boldsymbol{\nabla}\times\boldsymbol{E}_\mathrm{s}(\boldsymbol{r}_\mathrm{s}(t)))\right], \tag{2.24}$$

and finally summarised as

$$\boldsymbol{F}_\mathrm{P} = m_\mathrm{e}\left\langle\frac{d\boldsymbol{v}_2}{dt}\right\rangle = -\frac{e^2}{4m_\mathrm{e}\omega^2}\boldsymbol{\nabla}\left\langle\boldsymbol{E}_\mathrm{s}(\boldsymbol{r}_\mathrm{s}(t))^2\right\rangle. \tag{2.25}$$

The ponderomotive potential or the energy of the averaged cycle oscillation is calculated by integrating equation 2.25 to

$$\Phi_{\mathrm{P}} = \frac{1}{2} m_{\mathrm{e}} \left\langle \boldsymbol{v}_2^2 \right\rangle = \frac{e^2}{2 m_{\mathrm{e}} \omega^2} \left\langle \boldsymbol{E}(\boldsymbol{r}_{\mathrm{s}}(t))^2 \right\rangle . \tag{2.26}$$

The ponderomotive force is dependent on the negative gradient of the square of the electric field amplitude, which is proportional to the gradient of the laser intensity ($\langle \boldsymbol{E}(\boldsymbol{r}_{\mathrm{s}}(t))^2 \rangle \propto I_{\mathrm{L}}$). In the relativistic case the ponderomotive force can be expressed by means of the normalised vector potential a_0 as

$$\boldsymbol{F}_{\mathrm{P}} = -m_{\mathrm{e}} c^2 \boldsymbol{\nabla} \gamma = -m_{\mathrm{e}} c^2 \boldsymbol{\nabla} \sqrt{1 + a_0^2}. \tag{2.27}$$

As a consequence, charged particles will just oscillate and gain no energy in a plain homogenous electromagnetic wave. As soon as the laser has passed the interaction region, the oscillating electron, for example, will remain in its original position. But if a laser intensity gradient is present, the particles will be pushed by the ponderomotive force (equation 2.25) to areas with a lower field amplitude or laser intensity. Positive, as well as negative charged particles are affected in the same direction by this force, because of the square of the charge. But due to the heavy mass of the ions, they are less affected than the light electrons. Considering this mechanism, the electrons are accelerated radially away from the laser axis. At this point, the laser intensity is smaller and therefore also the ponderomotive force. The electrons cannot react with the same strength, so that they are forced to stay in the outer regions. A charge displacement takes place. In each half laser pulse cycle the electron is further accelerated and gains more and more kinetic energy. This process recurs until the energy of the electron is high enough to exit the laser region.

2.3 Laser plasma interaction

Characteristic parameters in order to describe and compare different laser plasma interactions are presented, followed by a summary of some non-linear effects occurring during the interplay. This section is based on [15, 16, 17, 18].

2.3.1 Characteristics of laser plasmas

A different approach to characterise the laser plasma interaction is, to assume a plasma as a collective cloud of electrons. The heavy ions can be assumed to be stationary over the pulse duration of the laser.

The electron density in a thermal equilibrium with a quasi-static electric field can be written as

$$n_{\mathrm{e}} = n_{\mathrm{e0}} \exp\left(\frac{e\Phi}{k_{\mathrm{B}} T_{\mathrm{e}}}\right). \tag{2.28}$$

It shows the characteristics of a Boltzmann distribution, with n_{e0} as electron density far away from the electrostatic potential Φ. k_{B} is the Boltzmann constant and T_{e} the electron temperature.

A field, induced by charged particles, is shielded by the plasma electrons with the characteristic distance of the Debye length, λ_D

$$\lambda_{\mathrm{D}} = \sqrt{\frac{\epsilon_0 k_{\mathrm{B}} T_{\mathrm{e}}}{n_{\mathrm{e0}} e^2}}. \tag{2.29}$$

Assuming a plasma with a homogenous density and no magnetisation, a dispersion relation for the electromagnetic wave, propagating through the plasma, can be expressed by

$$\omega_{\mathrm{L}}^2 = \omega_{\mathrm{P}}^2 + k^2 c^2, \tag{2.30}$$

with wave number k, laser frequency ω_{L} and plasma frequency ω_{P}.

The plasma frequency, ω_{P}, is another important parameter to describe the plasma. The ions are assumed to be stationary, but the electrons get an offset to their original location. An electric field is generated to restore the electric neutrality of the plasma. However, the light electrons will overshoot due to their initial motion and an oscillating motion is created. This oscillation around the equilibrium position of the electrons is characterised by the plasma frequency

$$\omega_{\mathrm{P}} = \sqrt{\frac{n_{\mathrm{e}0} e^2}{\epsilon_0 m_{\mathrm{e}}}}. \tag{2.31}$$

From the dispersion relation (equation 2.30) follows: If the frequency ω_{L} of the electromagnetic wave, traveling into the plasma, is smaller than the plasma frequency ($\omega_{\mathrm{L}} < \omega_{\mathrm{P}}$), the laser will be able to penetrate the plasma. Otherwise the electrons will shield the laser field by their oscillations. Therefore a density is defined to which the laser can penetrate the plasma. It is called critical density n_{c}

$$n_{\mathrm{c}} = \frac{\epsilon_0 m_{\mathrm{e}} \omega_{\mathrm{L}}^2}{e^2} \cong \frac{1.1 \cdot 10^{21}}{(\lambda[\mu m])^2} \quad [cm^{-3}]. \tag{2.32}$$

The plasma is defined as overdense, if $n_{\mathrm{e}} > n_{\mathrm{c}}$, typically for solid targets, or as underdense, if $n_{\mathrm{e}} < n_{\mathrm{c}}$, which are mostly gas targets or very thin metal targets, depending on the laser parameters.

Furthermore, there are low frequency oscillations in the plasma beside the high frequency electron plasma oscillations. It is called ion acoustic wave, determined by the heavy mass of the ions. The dispersion relation is defined by

$$\omega_{\mathrm{L}} = k c_{\mathrm{s}}. \tag{2.33}$$

c_{s} is the ion sound speed, with $c_{\mathrm{s}} = \sqrt{(Z k_{\mathrm{B}} T_{\mathrm{e}} + 3 k_{\mathrm{B}} T_{\mathrm{i}})/m_{\mathrm{i}}}$. If the temperature of the ions is small, compared to the electron temperature, the sound speed can be reduced to

$$c_{\mathrm{s}} = \sqrt{\frac{Z k_{\mathrm{B}} T_{\mathrm{e}}}{m_{\mathrm{i}}}}. \tag{2.34}$$

The ions are assumed to be fixed in the electron plasma oscillations. Here, the electrons are bunched with the ions in order to reduce the electric fields of the accumulated ions, however, this shielding is not perfect. The ions oscillate longitudinally as an acoustic wave in regular gases. Because of the thermal motion and electric fields, the ions are pushed from dense regions to areas with less ions and the ion acoustic wave propagates. The ion frequency of the oscillation is determined by

$$\omega_{\mathrm{Pi}} = \omega_{\mathrm{P}} \sqrt{\frac{Z m_{\mathrm{e}}}{m_{\mathrm{i}}}} = \sqrt{\frac{n_{\mathrm{e0}} Z e^2}{\epsilon_0 m_{\mathrm{i}}}}. \tag{2.35}$$

A further parameter is the refractive index η of the plasma, which can be calculated by means of the plasma frequency or the critical density.

$$\eta = \sqrt{1 - \frac{\omega_{\mathrm{P}}^2}{\omega_{\mathrm{L}}^2}} = \sqrt{1 - \frac{n_{\mathrm{e}}}{n_{\mathrm{c}}}} < 1. \tag{2.36}$$

In the relativistic case ω_{P}^2 changes to $\omega_{\mathrm{P\text{-}rel}}^2 = \omega_{\mathrm{P}}^2/\gamma$ and the electron mass also has to be multiplied by the relativistic factor to $m_{\mathrm{e\text{-}rel}} = m_{\mathrm{e}}\gamma$.

2.3.2 Non-linear effects in underdense plasmas

If a high intensity laser beam is focused tightly to a Gaussian intensity profile, some non-linear effects could occur in special cases. Relativistic self-focusing, Ponderomotive channeling and filamentation effects are described in detail in the following.

Relativistic self-focusing is one of the non-linear effects. It occurs, if a high intensity laser propagates through a fully ionised gas with an initial laser power, above a critical value P_{c}

$$P_{\mathrm{c}} \approx 17.5 \left(\frac{\omega_L}{\omega_{\mathrm{P}}}\right)^2 \mathrm{GW}. \tag{2.37}$$

Due to the radial intensity profile of the laser pulse, the refractive index (equation 2.36) of the plasma medium is different at every point. The highest refractive index is on the central laser axis, resulting in a refraction towards the axis. The laser beam will be focused over several Rayleigh lengths, because of the relativistic self-focusing effect.

If $P_{\mathrm{L}} = P_{\mathrm{c}}$, the beam should propagate unperturbed through the medium without any instabilities. $P_{\mathrm{L}} > P_{\mathrm{c}}$ is the threshold for the above mentioned self-focusing condition and $P_{\mathrm{L}} < P_{\mathrm{c}}$ is causing a beam spreading due to diffraction.

By the simple analytical model of *Bulanov et al.* [20, 21] based on [22], the normalised vector potential and the focal spot diameter, affected by the self-focusing effect, can be calculated with

$$\begin{aligned} a_{\mathrm{sf}} &= \left(\frac{2}{K}\frac{P_{\mathrm{L}}}{P_{sf}}\frac{n_{\mathrm{e}}}{n_{\mathrm{c}}}\right)^{1/3}, \\ d_{\mathrm{sf}} &= 2 * \sqrt{a_{\mathrm{sf}}}\frac{c}{\omega_{\mathrm{P}}} = \frac{\lambda}{\pi}\sqrt{a_{\mathrm{sf}}\frac{n_{\mathrm{c}}}{n_{\mathrm{e}}}}. \end{aligned} \tag{2.38}$$

$K = 0.074$ is based on [21], assuming a pulse duration of $\tau = 30\,\mathrm{fs}$ and an integration over the transverse coordinates. P_{sf} is taken as static typical power of self-focusing, $P_{\mathrm{sf}} = 2m_{\mathrm{e}}^2c^5/e^2 = 17\,\mathrm{GW}$.

Ponderomotive channeling appears, if $\tau\omega_{\mathrm{P}} \gg 1$. In this case, the plasma-wave creation can be neglected, but there will be an adiabatic electron response transverse to the incoming electromagnetic wave. Due to the ponderomotive force and the radial profile of the laser intensity, electrons are expelled from the laser axis. The high laser intensity on the laser axis results due to the already mentioned tight focusing or even because of the relativistic self-focusing effect. Therefore the electron density and the plasma frequency are lowest at the laser axis ($x = 0$) and higher in the transverse direction ($x = r$) to the laser propagation ($n_{\mathrm{e}}(0) < n_{\mathrm{e}}(r)$ and $\omega_{\mathrm{p}}(0) < \omega_{\mathrm{p}}(r)$). Because of that, the refractive index in the centre will be higher ($\eta(0) > \eta(r)$) and the focusing effect can occur, while creating a channel on the laser axis by moving electrons out from the centre during the interaction of the pulse.

Filamentation of a laser beam in space is the breaking up of the beam to multiple filaments. The laser intensity must be above a certain threshold [23] in order to have filamentation. With nowadays lasers, this threshold can be easily reached

$$I_{\mathrm{p}} = 2 \cdot 10^{15} L_{\mu}^{-1}\lambda_{\mu}^{-1}\frac{n_{\mathrm{c}}}{n_{\mathrm{e}}}T_{\mathrm{keV}}, \tag{2.39}$$

where L_{μ} is the plasma length and λ_{μ} the laser wavelength, both in microns, with T_{keV} as the electron temperature in keV. Depending on the electron temperature and plasma length, the intensity threshold for underdense targets is about $10^{13} - 10^{17}\,\mathrm{W/cm^2}$.

2.4 Ion acceleration mechanisms

Three different ion acceleration mechanisms, Target Normal Sheath Acceleration, Coulomb explosion and Colissionless Shock Acceleration, are presented in this section, which are important to understand the experimental results discussed in this thesis.

2.4.1 Target Normal Sheath Acceleration

The most investigated ion acceleration mechanism for solid targets is the Target Normal Sheath Acceleration (TNSA), which was introduced by *Wilks et al.* in 2001 [9]. To achieve an acceleration of ions to energies of several MeV, a very high intensity laser has to interact with a thin ($\sim$ μm-thick) solid target. This process is shown in figure 2.4. Highly energetic electrons are generated at the front surface and are passing through the target up to the rear surface without a significant energy loss. At this point the relativistic electrons can exit the target and a negative space-charged field is created. This field is nearly normal to the target surface. Because the field acts over a longer distance than the Debye length λ_D and in the order of TV/m, atoms will be ionised and the ions will be accelerated. The particles can originate from the target material itself or more likely from a hydrocarbon contamination layer on top of the target. Protons are the lightest ions and will move faster than heavier ions. They may shield the electric field of the hot electrons. This fast process from a cold surface to a plasma with a strong electric current in the forward direction, creating a sheath field of hot electrons, leads to a highly collimated and low emittance source of protons.

The energy spectrum of TNSA protons is typically braodband with a specific cut-off energy. This maximum energy can be calculated, as in [24] described,

$$E_{\max} = 2T_{\text{hot}} \left[\ln \left(t_{\text{p}} + \sqrt{t_{\text{p}}^2 + 1} \right) \right], \tag{2.40}$$

with the normalised acceleration time $t_{\text{p}} = \omega_{\text{Pi}} t_{\text{acc}} / \sqrt{2\text{exp}}$. ω_{Pi} is the ion plasma frequency $\omega_{\text{Pi}} = \sqrt{n_{\text{e0}} Z e^2 / \epsilon_0 m_{\text{p}}}$, and $T_{\text{hot}} = k_{\text{B}} T_{\text{e}}$ is the hot electron energy with n_{e0} as density of the hot electrons. The effective acceleration time was found to be $t_{\text{acc}} \sim 1.3 \tau_{\text{Laser}}$ in [24]. The hot electron temperature or energy is the cycle oscillation energy gained by the laser field and can be written as ([2, 25])

$$T_{\mathrm{hot}} = m_{\mathrm{e}}c^2(\gamma - 1) = m_{\mathrm{e}}c^2\left(\sqrt{1 + a_0^2} - 1\right) \approx m_{\mathrm{e}}c^2\left(\sqrt{1 + I_{W/cm^2}\lambda_\mu/1.37 \cdot 10^{18}} - 1\right). \tag{2.41}$$

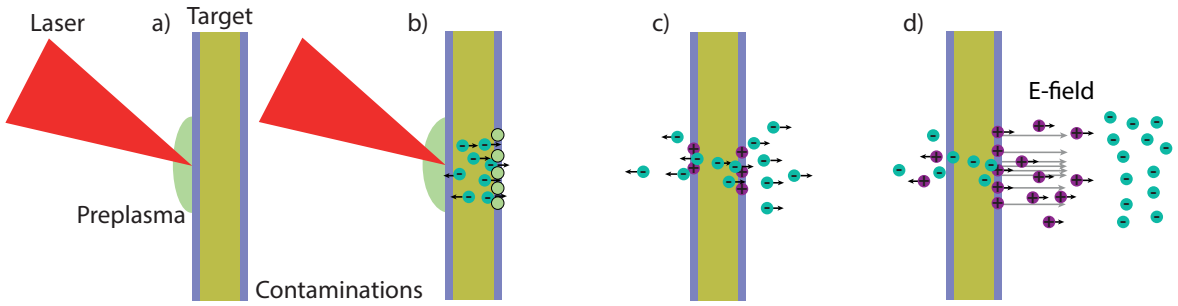

Figure 2.4: Schematic drawing of the TNSA process. The laser pulse including its pedestal level impinge on the target and create a preplasma, a.). When the main pulse interacts with the target, relativistic electrons are accelerated, b.). Most of these electrons are pushed towards the rear surface of the target, c.). The electric field, which is build up by the hot electrons is strong enough to accelerate protons or ions from a hydrocarbon contamination layer of the solid foil, d.). The acceleration process is normal to the target and highly collimated.

2.4.2 Coulomb explosion

Coulomb explosion [15, 17] is directly connected to the self-focusing and ponderomotive focusing effects (see subsection 2.3.2). The channel built around the central laser axis is depleted of electrons. This condition will persist, if the ponderomotive force F_{P} is bigger or equals the electric field from the immobile ions inside the channel. At this condition the Coulomb explosion can take place, and the ions are pushed radially outwards of the channel by the large space charge. After the laser pulse has passed, the ions and some low energy electrons will move further away from the laser axis. However, most of the high energy electrons will return to their initial position on a time scale of about $1/\omega_{\mathrm{p}}$ [11]. A sketch of the Coulomb explosion process is shown in figure 2.5.

This process depends on some limiting factors [26]. The laser frequency ω_0 has to be bigger than the electron plasma frequency ω_{p} and the laser pulse duration τ has to be longer than the electron response time $1/\omega_{\mathrm{p}}$ in order to push the electrons out of the

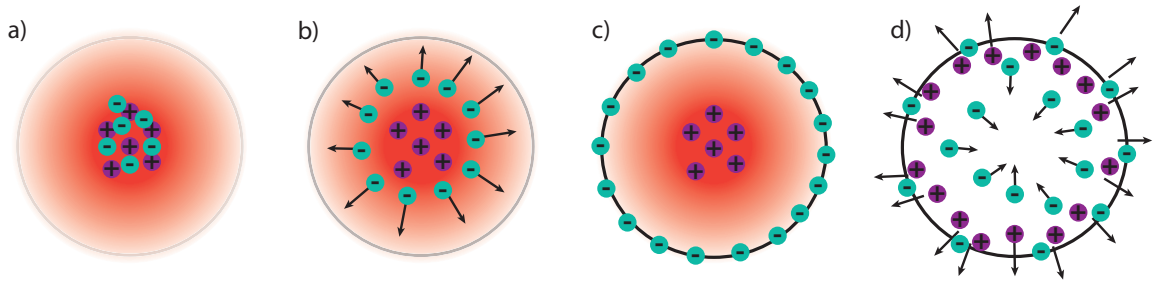

Figure 2.5: Schematic drawing of the Coulomb explosion process. The laser (red) hits the gas target, a.) and the electrons will be pushed radially outwards of the laser axis due to the self-focusing and ponderomotive channeling, b.). The electrons are completely depleted out of the channel up to a point, where the ponderomotive force equals the attractive electric field, c.). If this condition is fulfilled, the ions are pushed outwards as so-called Coulomb explosion, d.), while most of the electrons return to their original location.

channel, before they react to the field. If these conditions are fulfilled, the electrons could be assumed as a fluid, affected by the ponderomotive force. The electrons will respond in average over the laser period. Furthermore, the pulse length $c\tau$ has to be larger than the laser pulse radius r_0, in order to accelerate the ions in the transverse direction by the radial component of the ponderomotive force.

Therefore, the ponderomotive force and the corresponding electric field are dependent on the distance r from the central laser axis. The following 1D cylindrical calculations are based on [27]. The electric field in the region of the laser axis is

$$E_{\mathrm{D}}(r) = 2\pi Z e n_{\mathrm{i}0} r = 2\pi e n_{\mathrm{e}0} r, \tag{2.42}$$

by assuming, that the ion density equals to its original value and all electrons are pushed out. The ponderomotive force can be written as

$$F_{\mathrm{P}}(r) \approx \frac{m_{\mathrm{e}}c^2}{r_0}\frac{r}{r_0}\frac{a_0^2}{\sqrt{1+a_0^2}}. \tag{2.43}$$

The condition for the depletion is $F_{\mathrm{P}} > eE_{\mathrm{D}}$. $r \to 0$ results in

$$\frac{m_e c^2}{r_0^2}\frac{a_0^2}{\sqrt{1+a_0^2}} > 2\pi e^2 n_{e0}, \tag{2.44}$$

which can be written dependent on the normalised vector potential a_0 to

$$\begin{aligned} a_0 &> \sqrt{\frac{k^2}{2}+\sqrt{\frac{k^4}{4}+k^2}}, \\ k &= 2\pi\left(\frac{e^2}{m_e c^2}\right) n_{e0} r_0^2 = 2\pi r_e n_{e0} r_0^2, \end{aligned} \tag{2.45}$$

with $r_e = 2.82 \cdot 10^{-13}\,\mathrm{cm}$ as classical electron and r_0 as laser focal spot radius in cgs units.

If this condition is fulfilled, the ions will be pushed radially outwards of the channel axis. This ion displacement Δx_i after the time interval Δt_i needed to reach the outer part of the evacuated channel (Δx_i) is calculated in [17] to

$$\begin{aligned} \Delta x_i &= \frac{Z m_e}{m_i}\Delta t_i^2 c^2 \nabla_\perp \gamma, \\ \Delta t_i &\approx \sqrt{\frac{m_i}{Z m_e}}\frac{2^{1/4} r_c}{c\sqrt{a_0}}. \end{aligned} \tag{2.46}$$

r_c is the channel radius, which might be smaller than the vacuum focal spot size, because of the self-focusing effect. $\nabla_\perp \gamma$ is the ponderomotive force term, which is dependent on the laser intensity or the normalised vector potential

$$\begin{aligned} \nabla_\perp \gamma &\approx \frac{a_0^2}{4 r_c}, \quad a_0 \ll 1 \\ \nabla_\perp \gamma &\approx \frac{a_0^2}{\sqrt{2} r_c}, \quad a_0 \gg 1. \end{aligned} \tag{2.47}$$

For example, a Ti:Sapphire laser, e.q. the ARCTURUS laser, with an intensity of about $2.4 \cdot 10^{19}\,\mathrm{W/cm^2}$ with an $a_0 = 3.3$ focused into a Hydrogen gas target ($Z = 1, m_i/m_e = 1836$) and assuming a channel radius of about $r_c = 2\,\mu\mathrm{m}$, gives an acceleration time of $\Delta t_i = 0.186\,\mathrm{ps}$. A 30 fs laser pulse will be gone, when the ion channeling occurs and the electrons will be fully evacuated from of the channel at that time. But the ions will

still be pushed out due to their high inertia. This depleted channel can be detected via optical probing, which will be discussed later in this thesis.

The maximum cut-off energy of the accelerated ions in the ponderomotive potential can be calculated via $v_\mathrm{i} = \Delta x_\mathrm{i}/\Delta t_\mathrm{i}$ to

$$E_\mathrm{max} = Z m_\mathrm{e} c^2 \frac{a_0}{2\sqrt{2}}. \tag{2.48}$$

In [27, 11] the maximum energy is calculated more precisely:

$$E_\mathrm{max} = Z m_\mathrm{e} c^2 (\gamma - 1) = Z m_\mathrm{e} c^2 \left(\sqrt{1 + a_0^2} - 1 \right). \tag{2.49}$$

It is highly dependent on the laser beam radius, which affects the intensity and therefore a_0. The radius can be smaller than expected due to self-focusing effects. If the energy of the accelerated ions, the laser energy and pulse duration are known, the laser spot size inside the plasma can be calculated and the enhanced laser intensity can be deduced.

2.4.3 Collisionless shock acceleration

A well known phenomenon of a supersonic shock wave is an airplane travelling faster than the speed of sound. But as well, the laser light can be a source of a shock wave inside the plasma [15, 16, 27, 28]. A supersonic, high Mach-number collisionless electrostatic shock can be generated. Due to the radiation pressure of the laser field, which acts as a piston [28], an ion front is driven into the target with a velocity of ([15])

$$v_\mathrm{piston} = \sqrt{\frac{I}{m_\mathrm{i} n_\mathrm{i} c}} = \sqrt{\frac{Z}{A} \frac{m_\mathrm{e}}{m_\mathrm{p}} \frac{n_\mathrm{e}}{n_\mathrm{c}}} a_0 c. \tag{2.50}$$

If $v_\mathrm{piston} > c_\mathrm{s}$, a shock will propagate into the hot plasma with $v_\mathrm{shock} \approx v_\mathrm{piston}$. Ions, which are at rest at the beginning, gain a velocity due to a reflection of the electrostatic potential barrier Φ_max at the shock front. The reflection is dependent on the barrier height and the initial ion energy. If $Ze\Phi_\mathrm{max} > m_\mathrm{i} v_\mathrm{i}^2/2$, the final ion velocity v_i will be $v_\mathrm{i} = 2v_\mathrm{shock}$, while the ion front is totally reflected by the shock front. Therefore

the maximum energy of the reflected ions by the moving shock front with a supersonic Mach-number $M = v_{\mathrm{shock}}/c_{\mathrm{s}} > 1$ is

$$E_{\mathrm{max}} = \frac{1}{2} m_{\mathrm{i}} (2 v_{\mathrm{shock}})^2 = 2 m_{\mathrm{i}} v_{\mathrm{shock}}^2 = 2 Z M^2 T_{\mathrm{hot}}. \tag{2.51}$$

Another shock acceleration in underdense targets was investigated in [29], [30] and [31], the Low Density Collisionless Shock Acceleration (LDCSA). The acceleration regime was studied by exploding very thin foils by means of a secondary longer and low intensity laser or by the ASE pedestal level of the laser pulse itself. An undercritical density profile of a minimum width of about 100 μm up to millimetres is needed to be in this acceleration regime. Therefore, different laser foil interactions were investigated in order to get the best density profile as precondition. LDCSA is a combination of an initial CSA and a TNSA-like sheath field in the decreasing density ramp of the gas target. Several necessary steps can be discussed for the acceleration mechanism: In a first step, the ions are accelerated due to an electric field generated by hot electrons. The electric field consists of two components: An electrostatic field created by hot electrons in the expanded sheath front and an inductive field produced by a long living quasistatic magnetic field at the backside plasma vacuum interface. This combined electric field decreases constantly with growing distance to the high-density area. Therefore, ions of the low-density region are less affected by a lower electric field, than ions of the high-density region. This leads to a formation of an electrostatic shock front generated by fast ions of the high-density area overtaking the slow ions located in the low-density area. As a result, an ion density spike propagates within the decreasing density ramp. Ions, which are ahead of the moving shock front, are reflected. Finally, these ions are accelerated up to twice the shock velocity. In the case of LDCSA the ions are even further accelerated by the expansion inhomogeneous electrostatic TNSA-like field, contributing to a broadband energy spectrum.

2.5 Summary of previous experiments of ion acceleration from underdense gas targets

In 1999 ***Krushelnick et al.*** [11] published results about MeV ions accelerated by the interaction of the Nd:glass *VULCAN* laser with a gas target at the *Rutherford Appleton*

Laboratory (*RAL*). The high intensity laser beam (E= 50 J, $\tau_L = 0.9$ ps, $\lambda = 1.054\,\mu$m, I$\approx 6.6 \cdot 10^{19}$ W/cm^2) was focused by an f/4 off-axis parabola (OAP) into an underdense gas jet with a nozzle diameter of 4 mm and target densities of $n_e < 0.005 n_c$. Krushelnick et al. used Deuterium, Helium and Neon gases as possible targets. CR-39 nuclear detectors and Thomson parabolas (with CR-39) (see chapter 4) were used to detect accelerated ions in different angles around the interaction area. In addition, electrons could be observed in the longitudinal direction to the laser axis. The most significant emission of ions was detected transverse to the laser axis, while electrons, around 100 MeV, were identified only in the longitudinal direction. Maximum ion energies (with a sufficient high flux) of 1.0 MeV for Deuterium, 3.6 MeV for Helium and 6.0 MeV for Neon were seen. Both species of Helium ions were detected via the Thomson parabola, although the laser intensity was high enough to ionise nearly the total gas. Therefore He^{++} must undergo a charge exchange or recombination at the plasma edge, in order to become He^{+}. Krushelnick et al. refered to the classical charge exchange cross section: $\sigma \cong \pi(Z_1 Z_2 e^2)^2/\Delta E^3$. ΔE is the difference in the kinetic energy of the two species with charge states Z_1 and Z_2. For that reason, low energy ions have a higher probability of charge exchange with neutrals, which corresponds to a higher peak energy of He^{++} ions than for He^{+}. Furthermore, they described the fact, that there must be self-focusing inside the gas, enhancing the laser intensity. The ion acceleration in 90° to the laser axis was claimed to be due to Coulomb explosion.

Wei et al. presented results in 2004 of an experiment with the Nd:glass *VULCAN Petawatt* laser beam at *RAL* [12]. Helium ions were accelerated up to energies of 13.2±1.0 MeV by the interaction of the high intensity laser beam (E= 180 J, $\tau_L = 0.7$ ps, $\lambda = 1.054\,\mu$m, I$= 3 \cdot 10^{20}$ W/cm^2), focused by an f/3 OAP, with a gas target. The nozzle diameter was 2 mm and the electron density of the gas target was $0.01 - 0.14 n_c$. A Thomson parabola at 100° to the laser axis was used as main diagnostic. In addition, there were several radiochromic films placed around the interaction area to observe the angular spread of the accelerated ions. Two main major features were observed in the Helium ion-energy spectra: At high gas densities, the maximum ion energy and flux of the ions were increased, compared to the low density case. Furthermore, at high gas target densities, a plateau in the spectra in the high energy ions was detected. Both ion charge states were observed over the whole density scan, while He^{++} ions reached higher energies. Another difference was identified in the angular spread of the accelerated ions: In the low density case, the major direction of the acceleration

was transverse to the laser axis, while at high target densities the angular spread was shifted and increased. Furthermore, it was identified in simulations and by numerical calculations, that the laser beam intensity was increased due to self-focusing effects. The acceleration mechanism was described as ponderomotive expulsion or Coulomb explosion in the low density regime with additional enhancement in the high density regime. This enhancement, visible as plateau in the energy spectra, was declared as a collisionless shock acceleration.

Willingale et al. published results in 2006 about a collimated ion beam, accelerated due to the interaction of the intensive Nd:glass *VULCAN Petawatt* laser (*RAL*) (E= 340 J, $\tau_{\mathrm{L}} = 1.0\,\mathrm{ps}$, $\lambda = 1.054\,\mu\mathrm{m}$, I= $5.5{\cdot}10^{20}\,\mathrm{W/cm^2}$) with an underdense gas target [13]. A supersonic nozzle with a diameter of 2 mm was used. The possible Helium gas target density reached about $0.01 - 0.04 n_{\mathrm{c}}$. Thomson parabola spectrometers in 45° and 90° to the laser axis were used and additional magnetic spectrometers to detect electrons and ions in 10° and 0°. They detected most of the accelerated ions from low density targets in the transverse direction. The favourable direction was changed at the highest density. In the latter case, electrons with a maximum energy of 65 MeV and Helium ions of about 40 MeV ($\mathrm{He^{++}}$) and 10 MeV ($\mathrm{He^{+}}$) were accelerated in the longitudinal direction. The maximum energy of the ions, leaving the interaction in the transverse direction was around 7.8 MeV ($\mathrm{He^{++}}$) and 3.4 MeV ($\mathrm{He^{+}}$). At the same time, the spectrometer at a 45° detection angle showed lower maximum ion energies than in all other directions. The authors conclusion was, that they had a highly collimated ion acceleration. Based on simulations they claimed the transverse low density acceleration as Coulomb explosion and the longitudinal acceleration at high densities as an acceleration mechanism similar to TNSA. A hot expanding electron sheath front, expelled by the laser, accelerates the ions in the forward direction. Bulanov commented on the discussed mechanism [32]. He pointed out, that the longitudinal acceleration and collimation of the ions was a result of quasistatic magnetic fields at the plasma edge, produced of vorticose motion of electrons. The reply of Willingale [33] built on new simulations. The main acceleration mechanism was due to time changing magnetic fields and the corresponding hot electrons forming a sheath field. The quasistatic magnetic field enhanced the charge separation and therefore the ion acceleration, which is, however, not necessary for these experimental conditions.

Lifschitz et al. published results of ion acceleration from the laser interaction with an underdense Helium plasma in 2014 [14]. The Ti:sapphire *Salle Jaune* laser of the *Labora-*

toire d'Optique Appliquèe (E= 800 mJ, $\tau_L = 35$ fs, $\lambda = 0.8\,\mu$m, I= $1.3 \cdot 10^{19}$ W/cm^2) was focused into a Helium jet with a nozzle size of 700 μm and a density of $0.005 - 0.035 n_c$. Two Thomson parabola spectrometers in 0° and 80° related to the laser axis were used to detect the accelerated ions. No ion signal was observed in the longitudinal direction, but both He^{++} and He^{+} were identified in 80° up to a maximum energy of about 200 keV. They recognised a gap in the low energy He^{+} spectra, nevertheless both spectra of each species are in the range of 60 to 200 keV. By means of simulations, they explained the acceleration of the low energy branch by radial fields in the wakefield in the centre of the jet. In contrast, the high energy part was accelerated at the plasma edge in the decreasing density profile. Here, a TNSA-like sheath field was produced. This field caused a longitudinal acceleration, which was however not strong enough to overcome a focusing electric field, which was pinching a small channel or filament of ions with a high density. The channel reached its minimum after a few ps and a stronger Coulomb explosion happened, which accelerated ions in the radial direction. The acceleration was directed in 80° and not fully perpendicular to the axis, because of the small coexisting longitudinal field.

A further paper in 2016 by ***Kahaly et al.*** [34] builds on the experiment by Lifschitz et al.. Two new conditions were highlighted: The laser pulse duration (τ) was shorter than the ion plasma period ($1/\omega_{Pi}$) and the interaction length inside of the gas jet was comparable with the laser Rayleigh length (z_R). Furthermore, self-focusing effects were confirmed via simulations. The detected ion spectra for different densities were presented. There were some quasi-monoenergetic features in the spectra of He^{++} for low densities, which vanished out at higher gas densities. Here, the spectra of the He^{+} were more pronounced by a higher particle number, than for He^{++}. This fitted with the theory, that more surrounding gas, offers a higher potential of an electron capture. But in total the number of accelerated ions decreased with the density. A fast increasing trend following by a saturation level was visible in the scaling of the maximum cut-off energy versus gas density. As a consequence, an optimum target density presented the best conditions for an ion acceleration with the highest energies.

Chapter 3

Laser and Target characteristics

The experiments of ion acceleration of underdense gas targets were performed at the ARCTURUS laser facility established at the Heinrich Heine University Düsseldorf. The two main interaction beams were employed in the experiments in different configurations. In addition a laser pulse with lower energy was used for probing the interaction. The main modules of the ARCTURUS laser architecture will be presented in this chapter. Moreover, a characterisation of the underdense gas target used in the experiments follows. Using interferometric measurements at different gas pressures and different interaction heights, a relation between backing pressure and neutral density was determined.

3.1 The Düsseldorf ARCTURUS Laser Facility

ARCTURUS is the name of the $2 \times 200\,\mathrm{TW}$, dual beam Ti:Sapphire laser facility at Heinrich Heine University Düsseldorf. It is a commercial system of the *Amplitude Technologies* (*AT*) company, based on the chirped pulse amplification (CPA) technique. CPA is nowadays the best option to amplify a short laser pulse leading to an ultra-high intensity laser beam [35]. The ARCTURUS laser system has three main outstanding features: Dual beam configuration, ultra-short pulse duration and double CPA mode with a very high temporal contrast.

In the CPA technique, a laser pulse from a mode-locked oscillator (with a predetermined bandwidth) is stretched in time to reduce significantly its intensity without reducing

the pulse energy. Thus, the beam can be amplified, while avoiding nonlinear effects in the optical components, as well as the break down of the laser pulse by propagating long paths in the air. In the last step, the beam is temporally compressed, almost close to its initial value. Relativistic intensities of the order of $10^{20}\,\mathrm{W/cm^2}$ can be achieved by focusing the laser in the interaction area. A schematic of the CPA process is shown in figure 3.1.

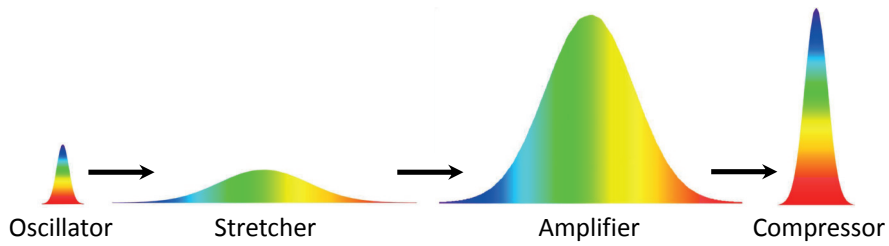

Figure 3.1: Technique of chirped pulse amplification (CPA): An existing short laser pulse is stretched, amplified and re-compressed to almost the original pulse length.

The ARCTURUS laser system consists of two high power main beams and one low power probe beam. The energy of the oscillator seed pulse is 5 nJ with a pulse duration of 25 fs and a repetition rate of 75 MHz. As a result of the CPA technique, each main pulse is amplified up to about 5 J with a pulse duration of 27 fs at a repetition rate of 10 Hz. The energy of the probe pulse is about 40 mJ and it is also compressed to a pulse duration of 27 fs. The Ti:Sapphire crystals are pumped by frequency doubled (green) Nd:YAG lasers in each amplification stage. The pulse is cleaned in the nano second range with two pulse pickers (*Pockels cells*), a saturable absorber, the cross-polarized wave module (XPW) and in the pico second range with a plasma mirror [36]. Therefore, a very high temporal contrast is achieved, which suppresses unwanted preheating of the target.

The laser beam is guided through four main stages, which are essential to achieve suitable parameters for the laser plasma interaction. These four main parts of the facility are: 1. the double CPA front-end, where the seed pulse is generated and preamplified up to a few mJ energy. 2. after a split, the two main beams are further amplified up to a final energy of 5 J by the last amplifier stages. 3. the main laser beams are ultimately and separately compressed up to 27 fs in two big grating compressors and the probe beam is separately compressed in a smaller grating compressor. Moreover, the laser contrast is enhanced by a plasma mirror system in each beamline. 4. all beams are guided into the radiation shielded target area (see figure 3.2).

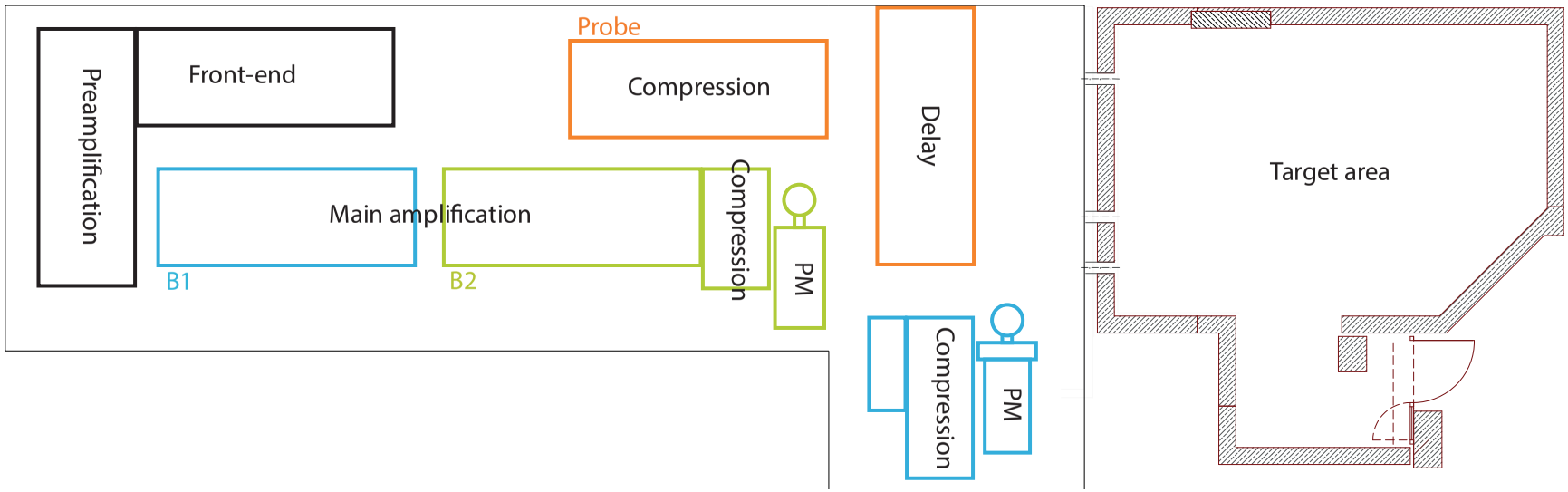

Figure 3.2: Scheme of the ARCTURUS laser facility. The seed pulse is amplified, stretched and compressed at the front end of the laser system (black). Afterwards it is split into three laser beams before it is guided to the main amplifiers (blue for beam 1 and green for beam 2). The probe laser is guided to a delay table (orange) and its own compressor unit (orange). Both main beams are also separately compressed and a contrast enhancement system (plasma mirror) can be included for each beam. All three beams are guided into the target area through vacuum beam lines after the amplification and compression in the laser laboratory.

3.1.1 The Front-end

The front-end of the ARCTURUS laser system consists of several different sections, like amplification, stretching, compression and cleaning. Each of this section, from the source of the laser up to the main amplifiers is described in the following section. A scheme of all the components is shown in figure 3.3.

Oscillator A Ti:Sapphire laser oscillator of *Femtolasers GmbH* generates pulses of nJ energies with a duration of 25 fs at a repetition rate of 75 MHz. It is pumped by a continuous wave 5 W - 532 nm frequency doubled diode laser. The central wavelength of the pulse spectrum is 780 nm with a bandwidth of around 100 nm. The oscillator pulse is the seed pulse for further amplification stages.

Booster The beam is amplified up to μJ level by a 14-pass-amplifier, which is pumped by one arm of a 33 mJ Nd:YAG laser *CFR Ultra* of the company *Quantel* in the Booster module. A pulse picker (*Pockels cell*, PC) lowers the pulse repetition rate to 10 Hz. Furthermore the pulse is cleaned by a saturable absorber to reduce the amplified spontaneous emission (ASE).

Stretcher 1 The stretcher (for the CPA technique) is the first module of a laser upgrade in 2013. It introduces a frequency chirp to the pulse, increasing the pulse duration to roughly 500 ps by passing four times through an Öffner stretcher. Furthermore an acusto optical modulator (*Dazzler*, *Fastlite*) is included in the optical stretcher setup, in order to shape the spectral phase of the pulse for the best performance of the final compression at later stage.

Regenerative Amplifier 1 and Preamplifier 1 The stretched, low intensity beam can now be further amplified. The first amplification stage is a regenerative amplifier (Regen), which consists of a cavity with a Ti:Sapphire crystal. It is pumped by the same *CFR Ultra* as the Booster. The seeding and maximum outcoupling of the cavity are controlled by two PCs at both ends of the amplifier. After passing through the Regen, the beam is amplified in a five-pass butterfly-amplifier, which is also pumped by the *CFR Ultra*.

Compressor 1 After the preamplifier stage, the beam is compressed up to a pulse duration of roughly 40 fs (corresponding to a spectral bandwidth of $\sim$40 nm) by a double pass grating compressor. There are two main free parameters, which control the

compression: The incidence angle on the gratings, the angle of the two gratings to each other and the distance between them. At the exit of the compressor the beam energy is about 1 mJ .

Wizzler and Beam stabilisation In order to maintain the laser contrast and spectral phase, the laser pulse can be diagnosed by a *Wizzler* (*Fastlite*). It measures the beam characteristics, e.g. spectrum, phase and pulse duration. Next, the laser is guided through a beam stabilisation system to improve the pointing into the hollow core fiber of the XPW system.

XPW To improve the temporal contrast, a nonlinear temporal filter was installed in the laser upgrade phase in 2013. It is based on the nonlinear effect of the generation of cross-polarized waves (XPW) in a BaF_2 crystal [37]. The crystal is sandwiched between two polarizers. The first one returns the original linear polarization, while the second one is orientated to let the cross-polarized wave pass. The conversion efficiency of the crystal (depending on $|\hat{E}|^2 \sim I$) is adequate for high intensity parts of the beam, while the prepulses are not intense enough to generate cross polarized light by nonlinear effects. That is why the XPW module cleans the temporal contrast of the beam. Another advantage of the XPW is the spectral broadening of the beam to about 60 nm bandwidth, which compensates a part of the spectral gain narrowing in the following amplification steps. Moreover, there is a small hollow core fiber included in the system in front of the XPW to spatially filter the beam. The whole module has an efficiency of about 10 %, which corresponds to an outcoupling energy of about 100 μJ (compare [37]).

Stretcher 2 A 2nd stretcher - *Dazzler* module follows after the XPW with the same operation mode as stretcher 1. A pulse duration of about 500 ps is achieved.

Mazzler, Regenerative Amplifier 2 and Preamplifier 2 The second regenerative amplifier, pumped by means of an additional *CFR Ultra* with 33 mJ energy, is almost the same like the one before, but in addition there is a *Mazzler* device implemented, produced by *Fastlite*. The spectral gain is controlled and filtered by the *Mazzler*. Furthermore, there are two Pockels cells for the cavity of the regenerative amplifier and another one in front of the preamplifier for cleaning the temporal profile of the pulse. Afterwards, the laser pulse is amplified up to 25-30 mJ by use of a second five-pass-preamplifier. This module is pumped by a *CFR 200 (Quantel)*, which has an energy of

about 133 mJ. Before being coupled in the next amplifier stage, the beam is expanded by a telescope.

Multipass amplifier 2A, 2B1 and 2B2 and probe beam The multipass amplifier (2A) is a four-pass butterfly amplifier, which is pumped by a frequency doubled *Propulse* Nd:YAG 1 J laser of *AT*. The energy of the seed laser beam reaches roughly 300 mJ. Then, the seed beam is expanded and guided through a combination of polarizers and a Pockels cell, which cleans the prepulses in the ns range. In fact, this system acts like an optical isolator, blocking the possible laser back reflections from the target area. The PC is open only for 10 ns, which corresponds to 3 m of travel, which is much shorter than the distance to the target area and back to the front-end. While it is off, the crystal of the Pockels cell has changed its polarization plane and the main part of the reflected beam would not be able to pass through. Afterwards, the laser is split up in two arms. 70 % is used for the two main beams and 30 % for the probe beam. The probe is guided to a delay setup to keep the same beam path length compared to the main beams, before it is guided through its own compressor. These 70 % of the full beam is further divided into equal parts for both beams. Each beam (beam 1 and beam 2) is again amplified in four-pass butterfly amplifiers (named 2B1 and 2B2), which are pumped by a green Nd:YAG *Propulse* laser of *AT* with 2 J energy. The beams are amplified up to about 300 mJ and are further expanded by a telescope.

3.1.2 Main Amplification

Each main beam is amplified by a four-pass butterfly amplifier pumped by six Nd:YAG *Propulse* lasers by *AT*. All pump lasers can reach an energy up to 2.5 J, which allows to amplify the seed beam up to about 5 J laser energy. The Ti:Sapphire crystal is cooled down in a vacuum vessel by a Helium gas cryostat. After the amplification, both beams are expanded to a final diameter of roughly 8 cm to keep the fluence below the damage threshold of the compressor gratings ($<$100 mJ/cm^2) and to avoid any nonlinear effects and damages due to the high intensity beam in the beamline on the way to the target area. Beamline 2 is equipped with a motorised one metre delay stage to adjust the timing between both beams for the desired interaction. In figure 3.3 a schematic drawing of this main amplification stages is shown.

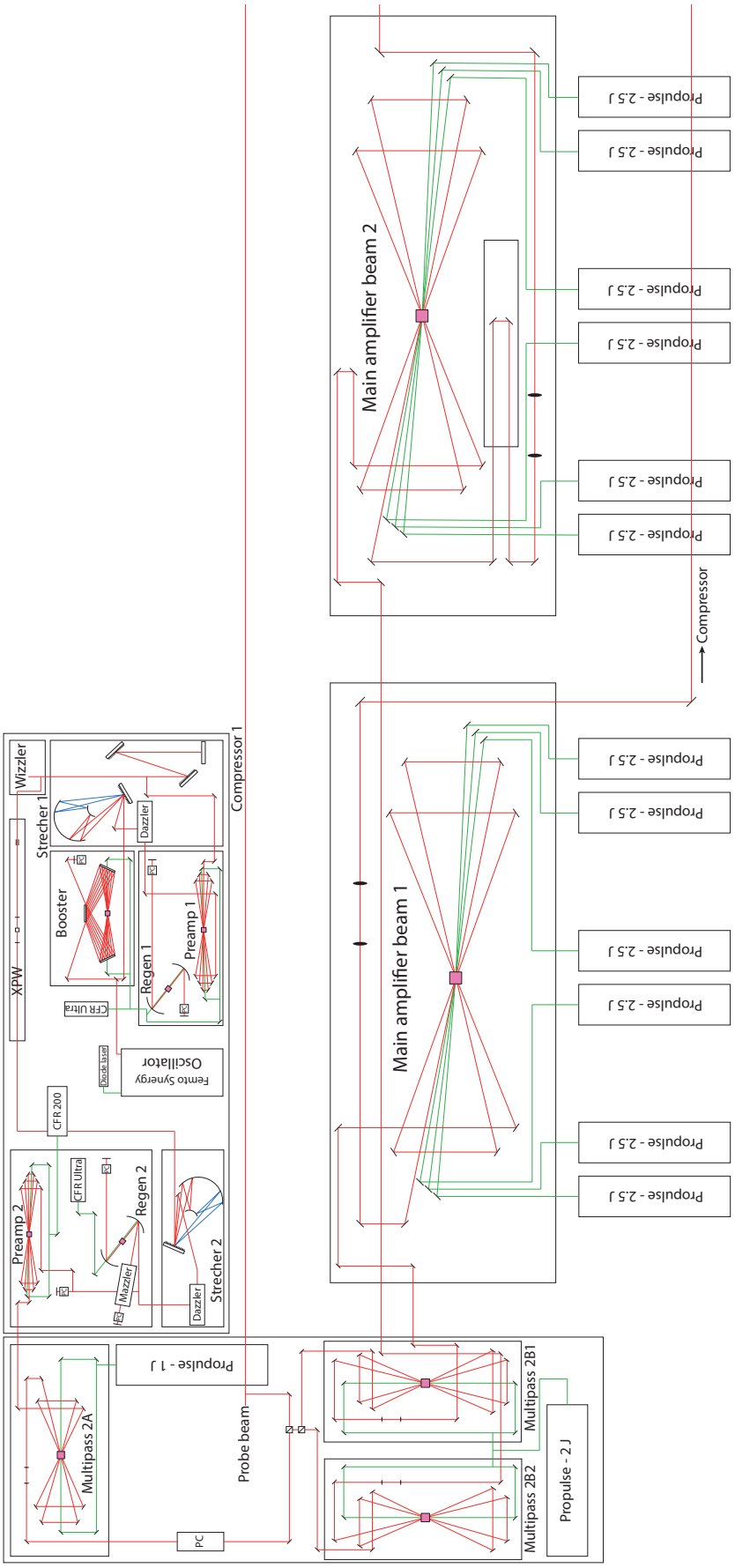

Figure 3.3: Scheme of the front-end and the two main amplifiers of the ARCTURUS laser facility.

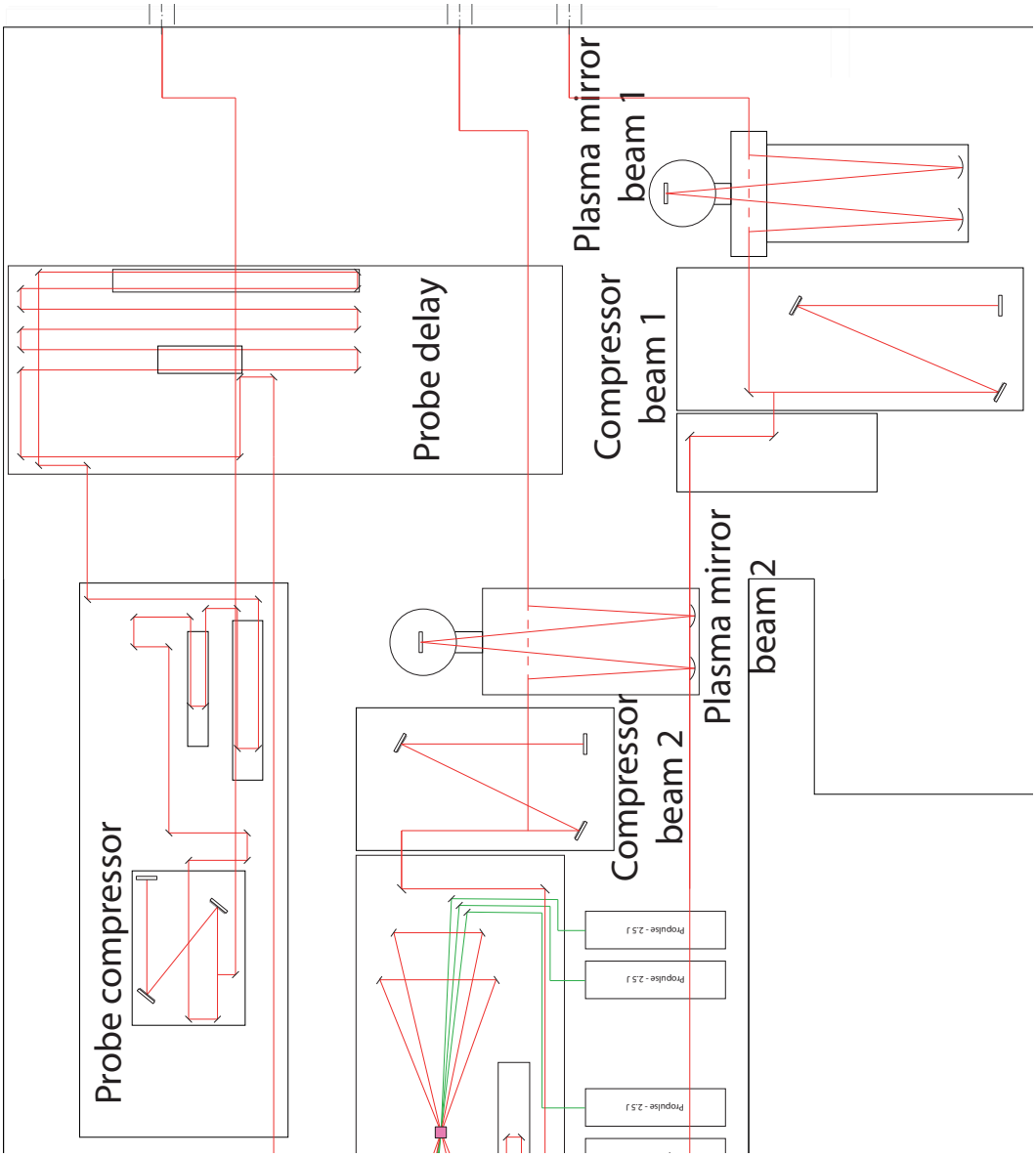

Figure 3.4: Scheme of the compressors of beam 1, 2 and probe as well as the plasma mirrors of beam 1 and 2 of the ARCTURUS laser facility.

3.1.3 Compression and contrast enhancement

Figure 3.4 shows sketch of this module.

Compressors All three beams are compressed by their own compressor module. The beam is entering into a vacuum vessel to be guided to a set of gold gratings. A rooftop mirror is folding the beam to pass the gratings a second time in a different level. With an optimum angle and distance of the gratings to each other, every beam is compressed to about 27 fs pulse duration. The energy transmission of the module is rougly 50-60 %. Now, the intensity of the beams is high enough to ionise the air, therefore the beams are guided in vacuum up to the interaction point.

Plasma mirrors The temporal contrast of the laser in the nano second range is cleaned by the Pockels cells and the XPW in the front-end. But in addition there could be a pedestal of ns to some tens of ps before the main pulse and the amplified spontaneous emission (ASE) as background level in the pulse left. Figure 3.5 shows the laser contrast of both main beams. An intensity of $10^{20}\,\mathrm{W/cm^2}$ on the target is reachable (focused by an f/2 parabola), if the main pulse is amplified and compressed. In that case, the pedestal level of the main pulse (of about $10^{14}/10^{16}\,\mathrm{W/cm^2}$) is strong enough to ionise the target.

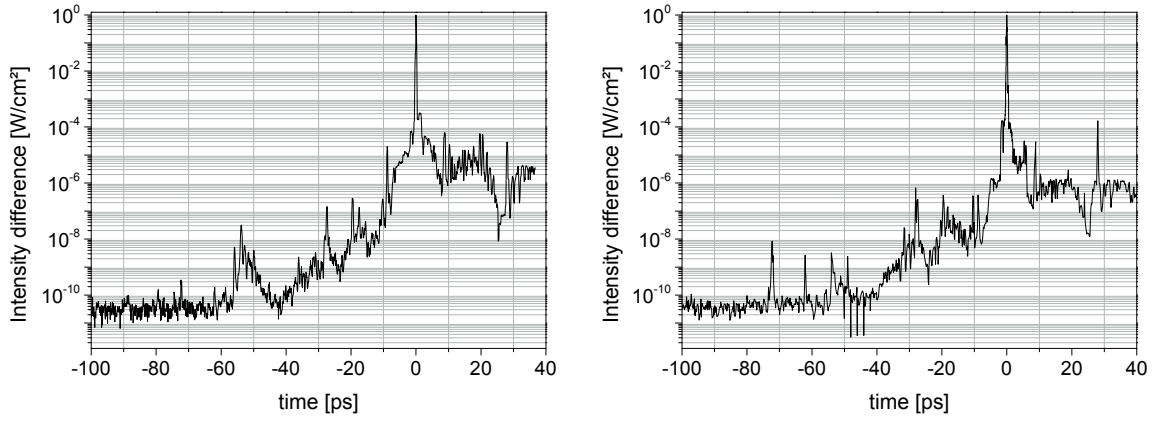

(a) Beam 1 contrast

(b) Beam 2 contrast

Figure 3.5: ARCTURUS laser contrast of beam 1 and beam 2 without a plasma mirror measured with the *Sequoia* (*Amplitude technologies*).

There is the possibility to insert a plasma mirror system in each main beam, in order to have a higher temporal contrast. The working principle of the plasma mirror is based on

the critical plasma density. If this density is reached, the laser is not able to propagate inside the plasma anymore. The light will be reflected. The laser is focused by an off-axis-parabola onto a transparent, anti-reflective coated glass substrate. The ASE part and the lower intensity prepulses are transmitted through the glass. However, as soon as the laser intensity is high enough to create an overdense plasma on the surface, most of the beam is reflected. In other words, the temporal contrast of the laser is enhanced during this process to a level of 10^{12} instead of 10^{10} (compare figure 3.5). Further details of the plasma mirror are described in [38, 39, 40]. Afterwards, the reflected beam is recollimated by an additional off-axis parabola and reinjected into the beamline to be further guided into the target area.

3.1.4 Target Area

The target area (figure 3.6) is a radiation shielded bunker made of special concrete walls. During the high-intensity laser shots, the bunker is a restricted area to avoid any exposure of the ionising radiation, which could be generated during the interaction. In order to achieve different kinds of experimental configurations, three different target chambers are available. All three laser beams can be coupled into target chamber 1 and 2. The third chamber (mostly for medical applications) is only operated by beam 2.

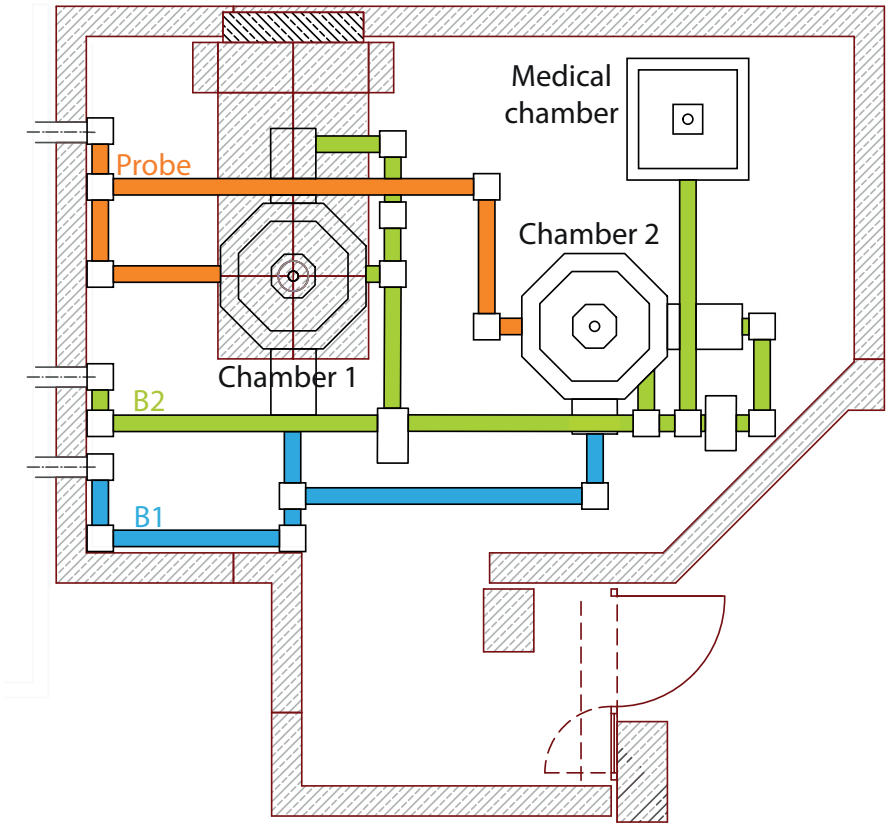

Figure 3.6: ARCTURUS target area; A bunker which is built of special concrete walls (grey) to shield against ionised radiation and an additional lead part (black) to protect against high energy electrons, accelerated with beam one (blue). Beam 2 (green) can be guided to chamber 1, 2 and the medical chamber. The probe (orange) can be used only in the main target chambers.

3.2 Target characterisation

A gas target was used in these experimental campaigns to accelerate ions by an intense laser pulse. Underdense gas targets offer potential advantages compared to solid targets: easy adjustment, single species ions, less debris and the capability to run with a high repetition rate. But there are some requirements on the gas target, in order to have an efficient laser-gas interaction. The aim is to have a supersonic gas flow with a plateau density profile and a sharp decreasing and increasing ramp at the edges [41, 42]. The opening and response time of the valve has to be short and adjustable to preserve a good surrounding vacuum during the interaction. A detailed characterisation of the gas target is necessary to provide information about the neutral density of the target. Thereby, a deeper analysis of the laser plasma interaction is possible. The neutral density of the target will change, while varying the backing pressure of the gas. By changing the type of the nozzle with a different geometrical construction, the gas jet shape will be different. The neutral gas density profile is adjustable up to a stable optimum by modifying the opening time of the gas valve. For that reason, different parameters are considered for the target characterisation.

During all the experimental campaigns described in this thesis, the same physical parameters of the nozzle and the same valve were used. The solenoid valve (suitable up to 200 bar) is commercially available by *Parker Hannifin*, while a self-made de Laval nozzle was used as the head. For further details see figure 3.7.

3.2.1 Supersonic nozzles

As discussed in [41] and [42], a supersonic *de Laval* nozzle is the best option for a proper flat-top gas target profile. Here, a gas reservoir with a predetermined temperature T_0, pressure p_0, and density n_0 is followed up to the throat by a convergent section of the nozzle. This is connected to a divergent section up to the nozzle top into the vacuum chamber with a given backing pressure p_b. In the first convergent part of the nozzle, the gas flow is subsonic (Mach number $M < 1$) up to the nozzle throat. It is accelerating and expanding, while the temperature and pressure are decreasing. At the thinnest part of the nozzle head the Mach-number equals one ($M = 1$). Then, in the divergent section, the gas is further expanded, accelerated and cooled down. Therefore, it is supersonic,

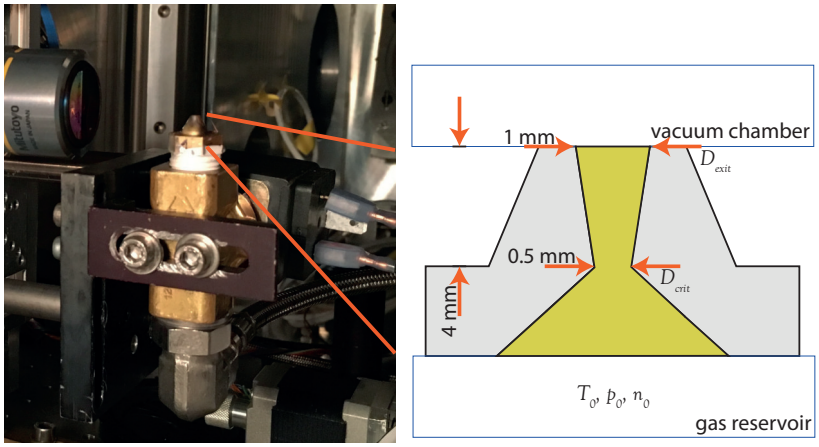

(a) Gas valve and nozzle real (b) Gas nozzle drawing

Figure 3.7: a.) image of the gas valve and nozzle mounted inside of the target vacuum chamber. In drawing b.) the nozzle parameters are shown.

which means, the Mach number increases ($M > 1$). This leads to a slow transverse expansion in the vacuum, which is a good requirement for laser-plasma interactions (compare [41, 42]).

The Mach number is defined as ratio between the speed of the gas flow v and the sound velocity a by $M = v/a$. The speed of sound is defined as $a = \sqrt{\gamma p/n} = \sqrt{\gamma RT}$, with pressure p, density n, γ as specific heat ratio (ratio between heat capacity at constant pressure and constant volume, c_p/c_v), specific gas constant R and temperature T. The specific heat ratio for Helium is $\gamma_\mathrm{He} = 5/3$ and for H_2 it is $\gamma_\mathrm{H2} = 7/5$. The gas constant is: $R_\mathrm{He} = 2.077\,\mathrm{kJ/(kgK)}$ and $R_\mathrm{H2} = 4.124\,\mathrm{kJ/(kgK)}$. Another important factor is the refractive index of the gases, which is: $\eta_\mathrm{He} = 1.0000348$ and $\eta_\mathrm{H2} = 1.0001424$ at standard temperature and pressure for a wavelength of 400 nm [43]. Considering these parameters, a calculation of the Mach number, temperature, pressure and density inside the *de Laval* nozzle with the following equations is possible [41, 42].

$$\begin{aligned} \frac{A_\mathrm{crit}}{A} &= M\left[1+\frac{\gamma-1}{\gamma+1}(M^2-1)\right]^{-\frac{\gamma+1}{2(\gamma-1)}} \\ &= \frac{216M}{(M^2+5)^3}\Bigg|_{\gamma_\mathrm{H2}=7/5} \quad \text{and} \quad = \frac{16M}{(M^2+3)^2}\Bigg|_{\gamma_\mathrm{He}=5/3} \end{aligned} \tag{3.1}$$

$$\begin{aligned} \frac{T}{T_0} &= \left(1+\frac{\gamma-1}{2}M^2\right)^{-1} \\ &= \frac{5}{M^2+5}\ \Big|_{\gamma_{\mathrm{H2}}=7/5} \quad \text{and} \quad = \frac{3}{M^2+3}\ \Big|_{\gamma_{\mathrm{He}}=5/3} \end{aligned} \tag{3.2}$$

$$\begin{aligned} \frac{p}{p_0} &= \left(1+\frac{\gamma-1}{2}M^2\right)^{-\frac{\gamma}{\gamma-1}} \\ &= \frac{125\sqrt{5}}{(M^2+5)^{7/2}}\ \Big|_{\gamma_{\mathrm{H2}}=7/5} \quad \text{and} \quad = \frac{9\sqrt{3}}{(M^2+3)^{5/2}}\ \Big|_{\gamma_{\mathrm{He}}=5/3} \end{aligned} \tag{3.3}$$

$$\begin{aligned} \frac{n}{n_0} &= \left(1+\frac{\gamma-1}{2}M^2\right)^{-\frac{1}{\gamma-1}} \\ &= \frac{25\sqrt{5}}{(M^2+5)^{5/2}}\ \Big|_{\gamma_{\mathrm{H2}}=7/5} \quad \text{and} \quad = \frac{3\sqrt{3}}{(M^2+3)^{3/2}}\ \Big|_{\gamma_{\mathrm{He}}=5/3}, \end{aligned} \tag{3.4}$$

with the cross section area $\mathrm{A_{crit}} = \pi(D_{\mathrm{crit}}/2)^2$ at the nozzle throat, and $T_0 \approx 293\,\mathrm{K}$, $p_0 = 5-95\,\mathrm{bar}$ and $n_0 = (p_0 V)/(k_B T_0)$ as initial values. A, T, p and n can be calculated at the point of interest, for example at the nozzle exit. A supersonic mach number of $M_{\mathrm{H2}} = 2.94$ for molecular Hydrogen and $M_{\mathrm{He}} = 3.44$ for Helium at the nozzle top is reachable by solving equation 3.1 with a nozzle width of $D_{\mathrm{crit}} = 0.5\,\mathrm{mm}$ and $D_{\mathrm{exit}} = 1\,\mathrm{mm}$ and a throat length of $l_{\mathrm{throat}} = 4\,\mathrm{mm}$ (cp. figure 3.7). According to this, both gases have different pressure to density ratios.

The density for different gases at the nozzle exit can be calculated by means of equation 3.4. A gas flow with a divergence angle of φ with $\varphi = \alpha + \theta$, and α as Mach cone half-angle ($\alpha = \arcsin(M^{-1})$) and $\theta = \arctan((D_{\mathrm{exit}}/2)/(l_{\mathrm{throat}}+x))$ as nozzle expansion angle are assumed [44]. The radius of the density profile in cylindrical coordinates is: $r = r_{\mathrm{exit}} + h\tan(\varphi)$, with h as height above the nozzle exit. In this experiment, the interaction took place at a height $h = 600\,\mu\mathrm{m}$ (target chamber centre (TCC)), where all main lasers were focused into the gas jet. Theoretically assuming, that φ is constant, the gas density can be calculated at a specific height by: $n = n_{\mathrm{exit}}(r_{\mathrm{exit}}/r)^2$.

In figure 3.8 the neutral gas density to pressure relation for this explicit nozzle is calculated by the above formulas. Considering the same pressure, Helium has a higher density compared to Hydrogen. The density at the nozzle exit is of course higher than at the interaction height of 600 μm.

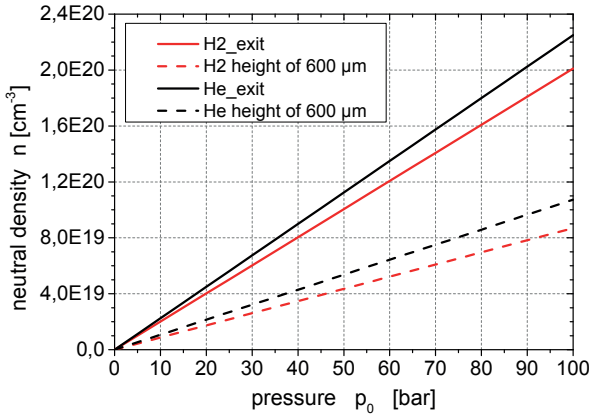

Figure 3.8: Theoretical calculation of the density to pressure relation for H_2 (red) and He (black) gas at the nozzle exit and in the interaction height of 600 μm above the nozzle.

3.2.2 Density measurement

An interferometer is used to determine experimentally the neutral gas density n_{gas} for a specific pressure p_0. A fringe pattern of a reference image without gas flow and a pattern of an image with gas flow are compared. The phase shift between the two images is extracted via Fast Fourier Transformation. Using this phase shift, the neutral gas density is calculated by an *Abel* inversion. Further details, how to analyze interferograms, are given in section 4.3.

The changes in density in this nozzle characterisation, were detected by using a *Mach-Zehnder* interferometer [45]. A sketch of the setup is pictured in figure 3.9. Two beam splitters divide and combine the probe beam, in order to have two beamlets overlapping to get a fringe pattern. No short-pulse laser is necessary for this investigation, because it is sufficient to have a millisecond resolution (The gas flow and density do not change very fast), which can be provided by the detecting camera shutter. Therefore, a continuous blue laser ($\lambda = 405\,\text{nm}$) with a maximum power of $P = 50\,\text{mW}$ was installed. The beam was spatially cleaned by a pinhole and afterwards expanded and collimated. The laser traveled through the gas jet and then to the *Mach-Zehnder* with additional lenses to magnify the image of the jet. The beam is split into two beamlets with two adjustable arms, to set a delay between the beams and to change the fringe orientation and width. Next, the two beams are guided to a CCD camera, where the disturbed part of the laser beam overlaps the undisturbed reference part of the beamlets (further details in

section 4.3). The gas nozzle was operated in the vacuum chamber ($\sim 10^{-2}$ mbar). The fringe pattern was aligned parallel to the nozzle (compare figure 3.10), in order to get the fringe shift in the direction of the gas flow.

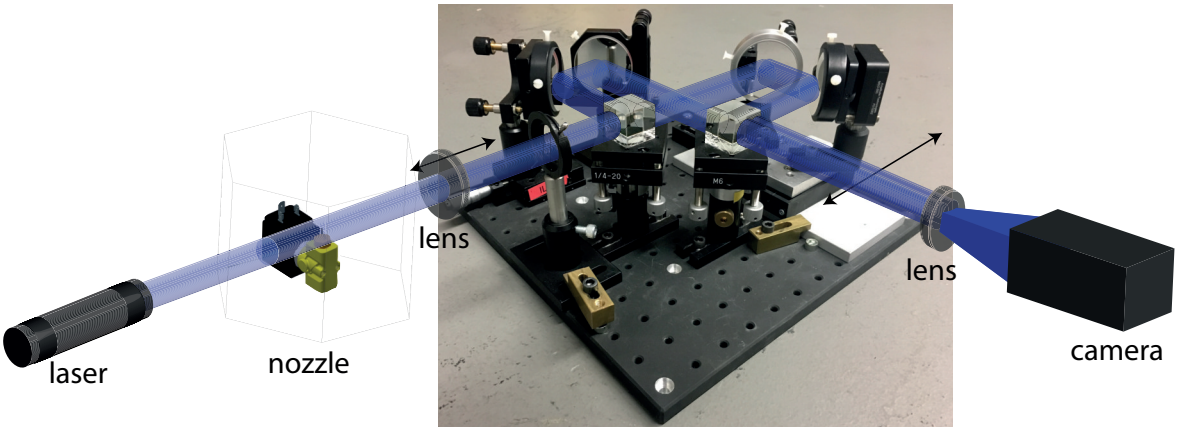

Figure 3.9: The *Mach-Zehnder* setup, which was used in the experiment, is shown in the centre. A blue laser passes through the gas target and is split into two arms/beamlets in the interferometer. Both beams are imaged and magnified onto a camera. A fringe pattern is produced. By adjusting the arms of the *Mach-Zehnder*, the fringe orientation and distance is flexible.

3.2.3 Characterisation results

In the following subsection presents a characterisation of the gas density profile at different pressures and different trigger times. All resulting images and line-outs are analysed in the interaction height of 600 μm above the nozzle. It was a compromise between reaching a good density profile and not hitting the nozzle edge with the laser.

Figure 3.10 shows two recorded images. The tip of the nozzle with an outer diameter of 2 mm is visible at the bottom of each image (black shadow). The left image (a) shows the reference image with undisturbed straight fringes. A shift in the centre of the nozzle, due to the H_2 gas flow, is visible in image (b). A comparison of the fringe pattern is highlighted in the the magnified squared details. Every corresponding phase shift is calculated by help of the interference pattern of each full image. The phase of the disturbed image is subtracted of the reference phase in order to get a net phase shift. Consequently, the neutral gas density can be calculated by means of the net phase and the refractive index of the gas.

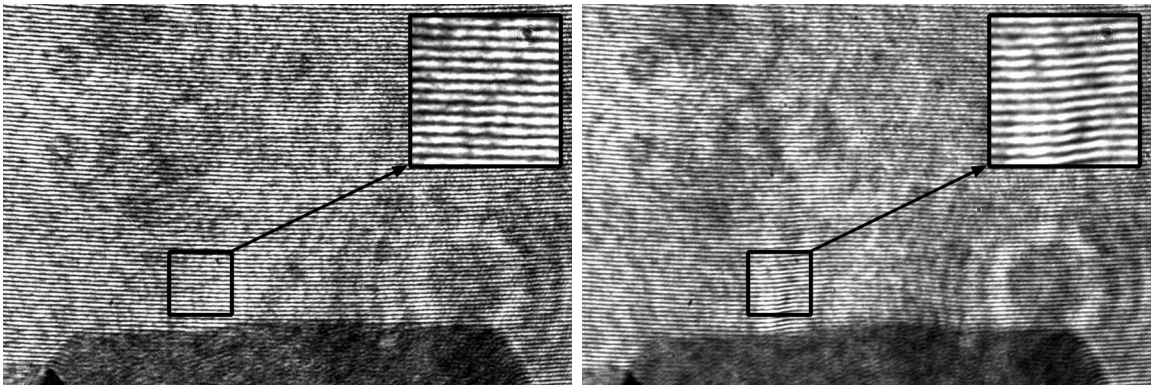

(a) Gas nozzle fringes reference (b) Gas nozzle fringes

Figure 3.10: The detected images of the *Mach-Zehnder* interferometer are shown. The black shadow at the bottom of the images is the top of the nozzle. Picture (a) illustrates the reference image, without gas. In picture (b) a fringe shift due to the gas flow is visible. The shift is highlighted in the magnified square planes (H_2 gas with $p_0 = 70\,\text{bar}$ and the image is taken 6 ms after the valve is triggered).

The calculated phase shift is displayed in figure 3.11 (a). An image of the neutral gas density, determined from the phase shift, is presented in figure 3.11 (b). Both images are 2D pseudo-colour plots, corresponding to the complete interferograms above (figure 3.10).

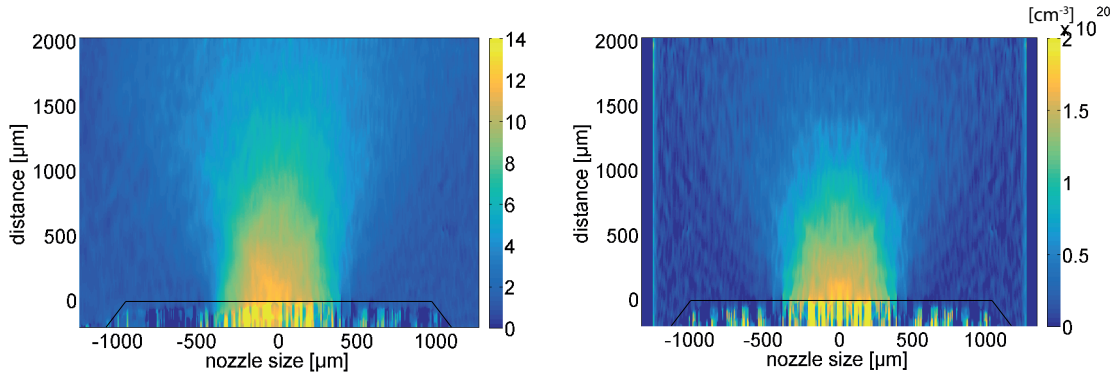

(a) Gas nozzle phase shift (b) Gas nozzle neutral density

Figure 3.11: Phase shift calculated via Fourier transformation (a) and the extracted neutral density (b). (The images/calculations correspond to the interferograms in fig. 3.10)

A corresponding line-out at a specific height (horizontal line-out) and a line-out along

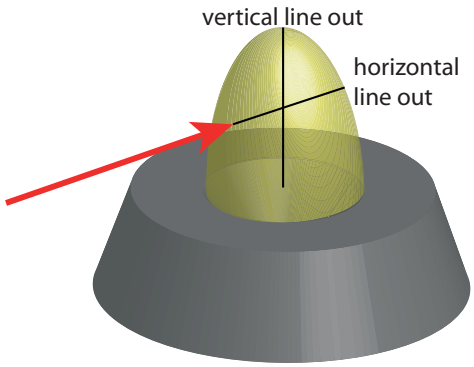

Figure 3.12: Two different line-outs were observed to get a better understanding of the gas profile. The horizontal line-out proceeds in the laser direction in a specific height, while the vertical line-out shows the central evolution of the gas jet normal to the top of the nozzle.

the symmetry axis of the gas jet (vertical line-out) can be extracted (see figure 3.12). The density profile at the height of 600 μm is of particular interest, because the laser propagates through the gas with a width of 1 mm at that height. The line-out along the symmetric axis normal to the nozzle edge gives an evolution of the gas jet. For both line-outs, compare figure 3.13. The horizontal line-out in this figure is fitted by a superposition of two super-Gaussian functions, as for example:

$$\begin{aligned} n_{\text{gas}} &= g_1(x) + g_2(x) + y \qquad [cm^{-3}] \\ &= 5.7 \cdot 10^{19} exp\left(-\left(\frac{x}{325}\right)^4\right) + 5.2 \cdot 10^{19} exp\left(-\left(\frac{x}{575}\right)^6\right) + 5 \cdot 10^{18} \end{aligned} \tag{3.5}$$

Timing-density relation Directly after the opening of the valve, the gas yet profile is not jet stable. That is why different trigger times for one pressure were tested. This means, the valve was opened at different times before the laser was hitting the gas target and the interaction took place. The gas profile and the peak gas density are different for a short time after triggering the valve. Finally, the line-outs of figure 3.14 (a) and (b) show that the gas flow becomes stable 6 ms after the triggering of the valve.

Pressure-density relation Different pressures lead to different peak densities and slightly different density profiles. Four different pressure scans were measured and analysed for the same valve opening time in order to get a dependence between pressure and peak density. The horizontal and vertical line-out for the different pressures are demonstrated in figure 3.15 (a) and (b).

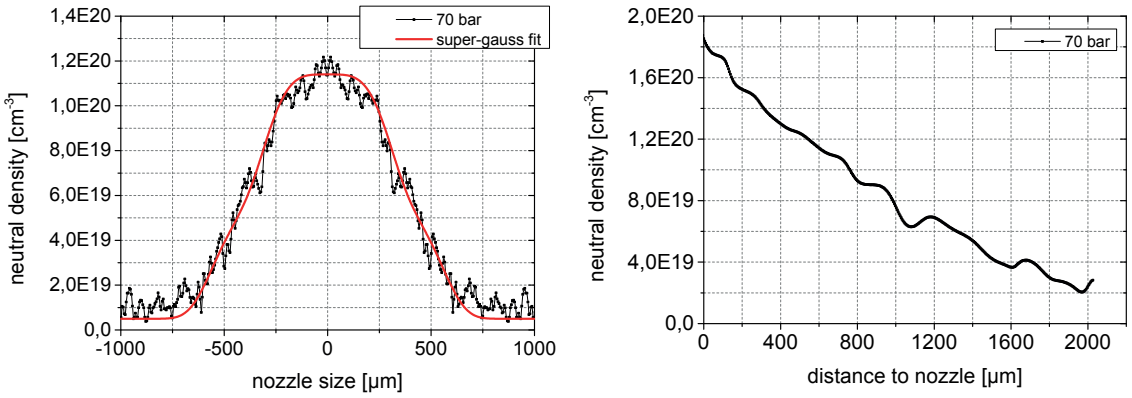

(a) Gas nozzle TCC line-out

(b) Vertical gas nozzle line-out

Figure 3.13: Image (a) and (b) are line-outs of the 2D plot in figure 3.11 (b). Plot (a) is a horizontal line-out at a height of 600 μm, the interaction height of the lasers. Line-out (b) is normal to the nozzle edge along the central symmetry axis.

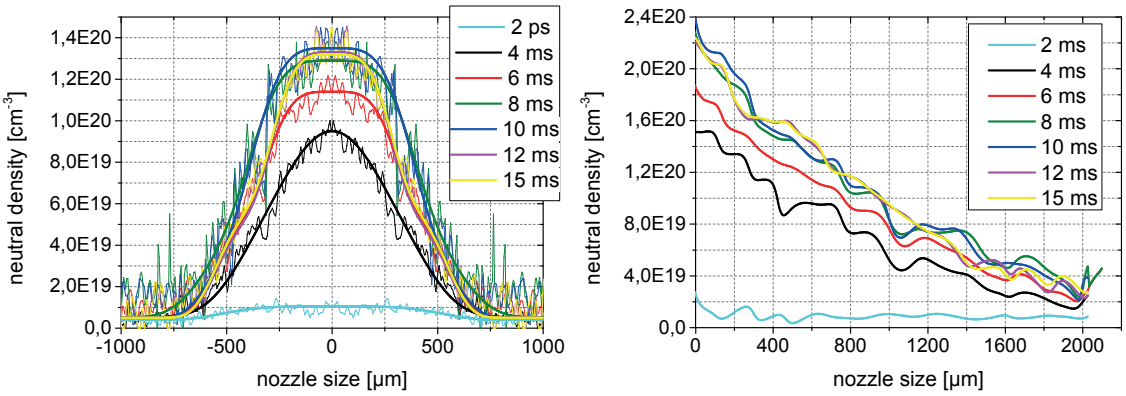

(a) Gas nozzle TCC line-out

(b) Vertical gas nozzle line-out

Figure 3.14: Horizontal line-out (a) at TCC height and vertical line-outs (b) of the H_2 density profile at 70 bar backing pressure at different times of the valve opening.

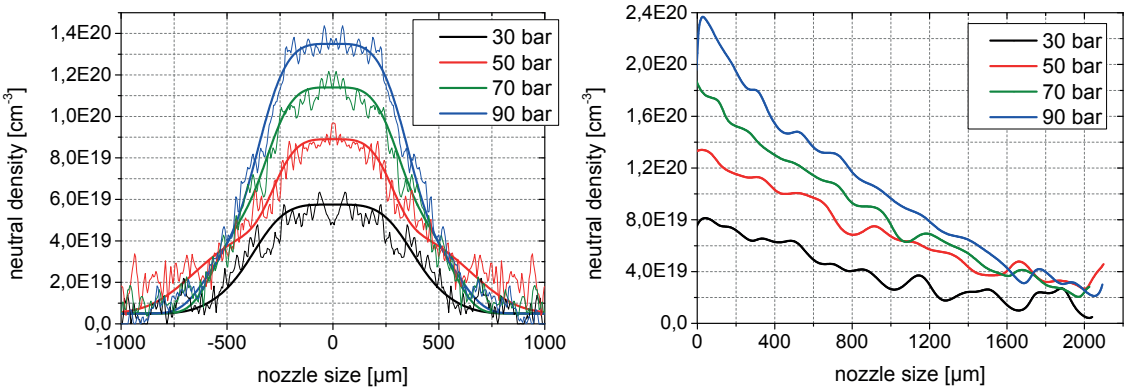

(a) Gas nozzle TCC line-out

(b) Vertical gas nozzle line-out

Figure 3.15: Horizontal line-outs (a) at TCC height and vertical line-outs (b) of the H_2 density for different pressures at the same valve opening time.

The peak value of the horizontal line-outs was considered, to set a pressure to density ratio. Figure 3.16 presents a linear distribution, which can be fitted to estimate density values for different pressures. Moreover, knowing the neutral density, the relation of the gas electron density to the non-relativistic critical density ($1.72 \cdot 10^{21}\,\mathrm{cm}^{-3}$) is set. The linear fit matches well with the theoretical calculations in figure 3.8. But in order to get the density profiles along the line-outs and to evaluate, if it is flat-top, the experimental data is necessary.

3.3 Summary

All experiments described in this thesis, were performed at the ARCTURUS laser facility in Düsseldorf. The facility, consisting of the laser laboratory and the radiation shielded target area, is presented in this chapter. There are three main units in the laser laboratory: The double CPA front-end, where the seed pulse is preamplified and split into three parts, one laser beam is the low energy probe beam and the other two are the main beams. The last two are amplified in the second step to a few Joule of energy. In the third step all three beams are separately temporally compressed to 27 fs. In addition, a plasma mirror system is integrated for further improvement of the temporal contrast in each main laser path. After all these steps, the laser beams are guided into the target area, where the interaction of laser and target takes place.

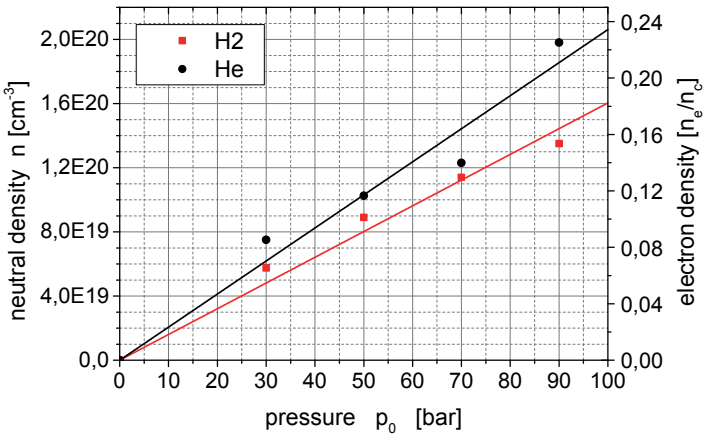

Figure 3.16: Pressure to neutral density relation of H_2 (red) and He (black) gas. Four different pressures were measured in the interaction height of 600 μm above the nozzle. The solid lines are linear fits to the data points anchored in the coordinate origin. This agrees well with the theoretical calculations shown in figure 3.8.

Moreover, the gas target for the laser plasma interaction was investigated in detail for further analysis steps. The advantages and the theory of supersonic nozzles are described. Furthermore, the gas target was experimentally characterised via interferometry. The neutral gas density was studied with regard to different backing pressures and different nozzle opening times.

Chapter 4

Diagnostics, investigation methods and experimental setups

Ion acceleration due to the interaction of a high power laser with a gas target is experimentally investigated. Therefore, several diagnostics were employed. The main diagnostic to detect the ions and to analyse their energy distribution were Thomson parabolas (section 4.2) with multi channel plate detectors (subsection 4.2.2), which were cross-calibrated with CR-39 nuclear track detectors (section 4.1). The temporal evolution of the plasma was investigated via optical probing (section 4.3). Another way to investigate the interaction, including electric and/or magnetic field structures inside the plasma channel, is charged-particle-probing via a secondary source of accelerated protons (section 4.5) observed by radiochromic film detectors (section 4.4). As a minor diagnostic a spectrometer was employed to resolve the energy distribution of the accelerated electrons (section 4.6).

4.1 CR39

CR-39, Columbia Resin #39, is a transparent stiff plastic polymer $[(C_{12}H_{18}O_7)]_n$ with a density of $1.3\,\mathrm{g/cm^3}$. It can be used as a solid state nuclear track detector. CR-39 plates are not sensitive to electromagnetic waves and electrons. That is why they are used to detect charged ions and protons with mostly energies above $100\,\mathrm{keV/nucleon}$. Penetrating particles create a track of broken molecular chains and free radicals along their path through the material. The track depth is determined by the path length

of the particle. Moreover, the amount of damages along the track is proportional to the rate of energy loss of the particle [46]. The CR-39 has to be etched in a sodium hydroxide (NaOH) solution to evaluate and to make these tracks of each single particle visible. The damaged polymer structure has a faster etching rate compared to the intact one. Because of that, conical pits with sharply defined circular holes arise out of the irradiated parts of the CR-39 during etching [46, 47, 48].

The CR-39 plates used in these experimental campaigns were etched at 80 °C in a $\sim$6 mol/l NaOH solution for 20 to 30 minutes. After etching, the CR-39 is scanned with a microscope with different magnifications for further investigations. In figure 4.1 two different scans of the same CR-39 plate are shown. All round spots with the same size are tracks of ions, which can be counted to determine the actual number of the particles.

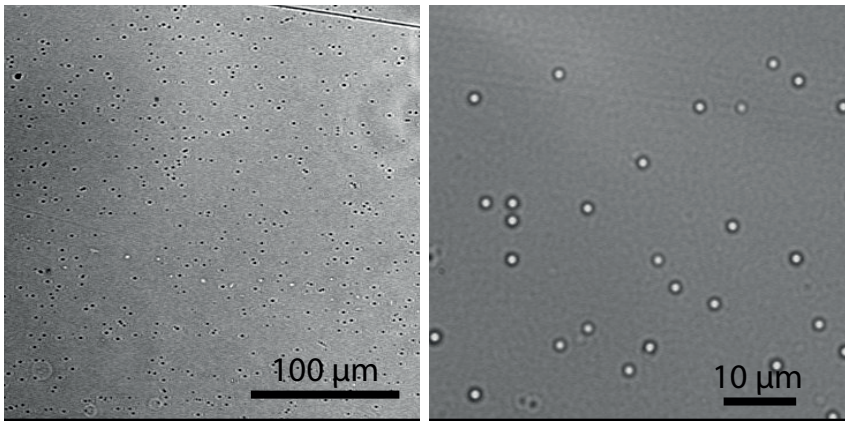

(a) CR-39 20x magnified (b) CR-39 100x magnified

Figure 4.1: Two microscope images of an irradiated and etched CR-39 plate are shown. (a) is 20 times magnified. Some dirt and lots of tracks are visible. Image (b) is 100 times magnified and the single tracks are clearly distinguishable.

In these experimental campaigns the CR-39 ion detectors were used for two different purposes. First, to calibrate the detector (micro channel plate (MCP)) of the Thomson parabola spectrometer (see. subsection 4.2.3), obtaining information about the absolute number of the particles by counting all single tracks. Second, to resolve the divergence of the accelerated ion beam. Moreover, especially for low energy ions, the surface of the CR-39 was over-saturated, resulting in overlapping tracks and pits, so that counting of the particles was not possible anymore.

4.2 Thomson parabola spectrometer

A Thomson parabola spectrometer [49] is a well established diagnostic for laser plasma experiments. It provides a high-resolution energy spectrum and a charge-to-mass separation of the accelerated ion species. Moreover, it is easily adjustable for different purposes of investigations. It consists of several components: A pinhole is used to observe a small part of the accelerated ions. This provides a better resolution in all dimensions for an improved spatial (between the tracks) and energy determination of the ions. Due to the laser plasma interaction, x-rays are emitted in 4π and the laser light could be reflected from the target chamber all over the experimental setup. This light would overlay with the deflected ions on the detector. With a pinhole, these disturbing effects are just present in the zero point of the experimental arrangement of the Thomson parabola. The collimated particle beam propagates then through a pair of permanent magnets, which deflect the ions in one dimension, according to their energy and mass. Followed by an electric field, the particles are deflected in the orthogonal direction by their charge state and mass. This combination acts like a Wien-filter, separating the different ions by their charge-to-mass ratio in the parabolic traces. The last part of the setup of the Thomson parabola diagnostic is a detector to visualise these traces. In these experimental campaigns, the detectors were two micro channel plates (MCPs) observed by CCD cameras. More details of the MCPs are given in subsection 4.2.2.

4.2.1 Basics of the spectrometer

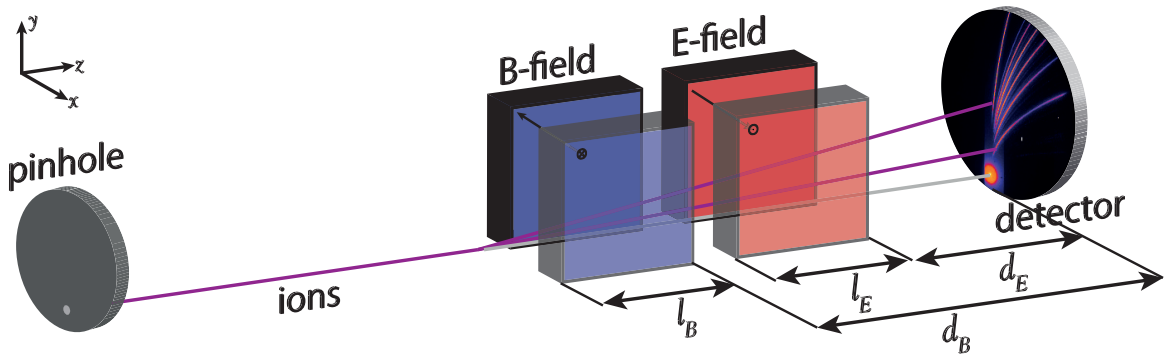

Figure 4.2: Schematic drawing of the Thomson parabola spectrometer with an experimentally investigated raw image at the detector.

A simple drawing of the spectrometer is illustrated in figure 4.2. The deflection and position of the ion at the detector can be exactly calculated by the assumption of a homogenous and box-shaped magnetic (B_0) and electric field (E_0) and a non-relativistic motion of the particles. In the first part of the spectrometer (B-field), the particle motion is on a circular orbit due to the Lorentz force F_L. The corresponding Larmor radius can be derived from the balance between F_L and the centrifugal force F_Z to: $r_\mathrm{L} = (mv_0^2)/(qB_0)$. The coordinates of the detector plane can be summarised according to [50, 51] in a non-relativistic case, with the circular motion of $r_\mathrm{L} = \sqrt{(y(z) - r_\mathrm{L})^2 + z^2}$ and the electric force $F_\mathrm{e} = qE_0 = m\frac{d^2x}{d^2t}$, to:

$$\begin{aligned} x &= \frac{q}{mv_0^2} E_0 l_\mathrm{E} \left(d_\mathrm{E} + \frac{l_\mathrm{E}}{2} \right), \\ y &= \frac{q}{mv_0} B_0 l_\mathrm{B} \left(d_\mathrm{B} + \frac{l_\mathrm{B}}{2} \right), \end{aligned} \tag{4.1}$$

where v_0, q and m are the velocity, charge and mass of the ion and l_E, d_E, l_B and d_B are the distances between the components of the diagnostic (compare figure 4.2). The final parabolic trajectory depends on the relation of q/m [52] and can be expressed by:

$$y^2 = \frac{q}{m} \frac{B_0^2}{E_0} \frac{l_\mathrm{B}^2}{l_\mathrm{E}} \frac{(d_\mathrm{B} + l_\mathrm{B}/2)^2}{(d_\mathrm{E} + l_\mathrm{E}/2)} x. \tag{4.2}$$

High energy ions are less deflected than low energy ions (in vertical direction, y) and particles with a high q/m ratio are more deflected in horizontal direction, x. An image of traces of different ion species on a MCP detector captured by a CCD camera is shown in figure 4.3.

The energy spectrum is extracted from the raw data and further evaluated for a proper data analysis. An energy interval, ΔE, is chosen and all particles in this area are summed up and normalised by the interval. This value is then divided by the solid angle of the source size, which can be calculated by:

$$\frac{D}{P} = \frac{l_\mathrm{D}}{l_\mathrm{P}}, \tag{4.3}$$

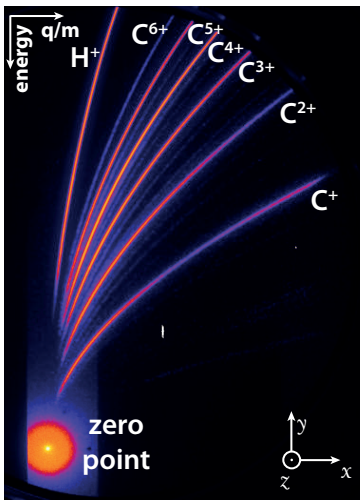

Figure 4.3: An example of an experimentally detected ion spectra by the Thomson parabola spectrometer.

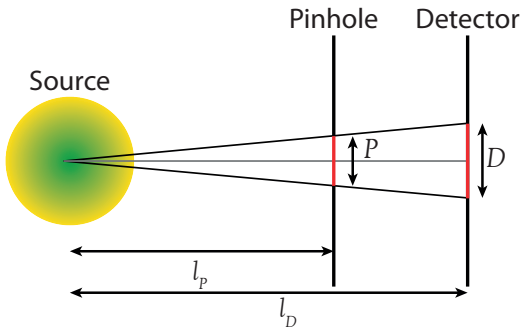

Figure 4.4: Sketch for the calculation of the solid angle: The ion source is reduced by a pinhole at the entrance of the Thomson parabola spectrometer for a better spatial (between the tracks) and energy (within one track) resolution.

with the diameter of the Detector D, the pinhole P and the distances l_{D} and l_{P}, as shown in figure 4.4. The solid angle is defined as relation between the circular area and the surface of a sphere multiplied by 4π:

$$\Delta\Omega = \frac{\pi\frac{D^2}{4}}{4\pi l_{\mathrm{D}}^2}4\pi \tag{4.4}$$

Using equation 4.3 and 4.4 the definition is reduced to:

$$\begin{aligned}\Delta\Omega &= \frac{\pi\left(\frac{P^2}{2}\right)^2}{l_{\mathrm{P}}^2} \\ &= \frac{A_{\mathrm{P}}}{l_{\mathrm{P}}^2},\end{aligned} \tag{4.5}$$

with A_{P} as the two-dimensional circular area of the pinhole. Considering all these calculations, the flux count is normalised by the energy interval and the solid angle, to: particles/ΔE/$\Delta\Omega$.

In these experimental campaigns, two Thomson parabola spectrometers were used in two different positions of the setup. One along 0° to the driver beam and a second one along 10° to the driver (a detailed description of the setup is given in section 4.8). Both were installed in the same vacuum chamber, but with two slightly different configurations and each one with a micro channel plate as detector. In table 4.1 all relevant parameters of the Thomson parabola spectrometers and the minimal energy, which can be detected from these geometrical setups, are listed. The magnetic field was measured with a Hall probe. The electric field was supplied by a voltage source.

4.2.2 Micro channel plate detector

A micro channel plate (MCP) detector is easy to handle and a efficient way to detect the deflected ions of the Thomson parabola spectrometer. The advantage of the MCP over other detectors, like image plates or track detectors (CR-39), is, that it can be used with a very low flux of accelerated ions. In addition to that, the Thomson parabola, including the MCP detector, is an online diagnostic, which can be used for the whole

	Spectr. 0°	Spectr. 10°
B [T]	0.5	0.17
E [kV/cm]	2	4
l_B [mm]	50	50
l_E [mm]	50	50
d_B [mm]	130	148
d_E [mm]	124.5	130
pinhole ⌀ [mm]	1	1
$\Delta\Omega$ [μsr]	1.58	1.79

species	H^+	
E_{min} [keV]	180	30
species	He^+	
E_{min} [keV]	50	10
species	He^{++}	
E_{min} [keV]	200	30

Table 4.1: Parameters and minimal energy of the Thomson parabola spectrometers used in these experimental campaigns.

experimental campaign without any maintenance and/or changes, which makes it easy to handle.

In figure 4.5 the working principle of the MCP is demonstrated. As soon as a single particle (ion, electron or photon) enters a small electron multiplier tube of an array of around $10^4 - 10^7$, bundled together, it will emit secondary electrons out of the wall. These are accelerated along the channel by an electric field, generated by a voltage, which is applied between front and rear side of the MCP. While travelling along, they collide with the opposite inner channel wall, emitting more electrons by every impact (avalanche effect). It is a cascade process until an exponentially increased amount of electrons reach the rear site of the multiplier. These electrons are further accelerated by an additional voltage to a phosphor screen. Impacting on the phosphor, the kinetic energy of the electron is converted into luminescence, generating a visible trace. The screen can be imaged by a CCD camera without any ambient light around. Further details of the working principle of the MCP are described in [53].

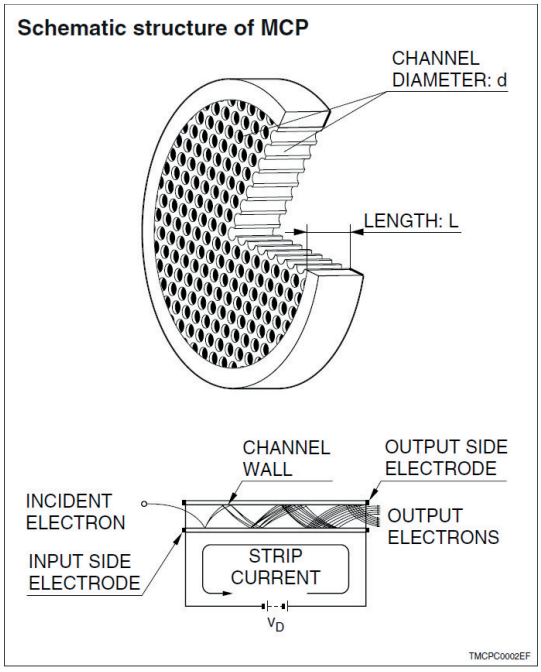

Figure 4.5: Schematic structure and working principle of a micro channel plate [54].

In these experimental campaigns two types of MCP detectors were used. One for the 0° Thomson parabola and the other one for the 10° Thomson parabola. The main specifications are listed in table 4.2. Both of them are equipped with a Phosphor screen, which emits light with a peak intensity at a wavelength of around 545 nm.

4.2.3 Flux calibration

For a comparison within different experiments and between experiments and simulations, the detected counts on the CCD have to be converted in an absolute ion particle number. Therefore, the signal on the phosphor screen of the MCP, detected by the CCD, has to be calibrated. CR-39 solid state nuclear detectors (see section 4.1) offer a great potential to extract the matching absolute particle track number.

It is important to know all the settings of the MCP, as well as the CCD camera settings for the calibration. For example the MCP voltage (plates and Phosphor screen) and the internal camera gain mode have to be read out. A slotted CR-39 plate, with stripes and gaps of 1 mm, is placed in the Thomson parabola between the electric field and the MCP detector. In figure 4.6 a sketch of the arrangement of the detectors is shown. In

	MCP 0°	MCP 10°
company	tectra GmbH (MCP-88-D-R-VF-P43)	Hamamatsu Photonics (F2226)
assembly	double stage	single stage
effective diameter [mm]	77	77
phosphor screen	P43	P43
channel diameter [μm]	21	25
gain factor	10^6	10^4
bias angle [°]	6	8
length to diameter ratio	40	40
thickness [mm]		1
channel length [mm]	0.840	1
MCP voltage [kV]	1.4	0.95
Screen voltage [kV]	3.3	3.9

Table 4.2: Main specifications of both types of MCP detectors, which were used in these experimental campaigns.

this configuration the CR-39 plate and the MCP are exposed at the same time by the ions, which allows a direct comparison between the signal on the MCP or rather on the CCD camera and the absolute particle number on the CR-39 detector for each energy.

The calibration is made for both types of MCPs. The analysis of the double stage MCP is described in detail in the following. The calibration is performed with protons, accelerated by the laser interaction with the Hydrogen gas. Each ion species has a different stopping power dE/dx in the MCP [55] and it was experimentally proven, that Carbon ions have a different calibration response than protons. But in these experimental campaigns only Hydrogen and Helium ions were investigated. Therefore, the assumption of a similar response is made, because of the similar atomic mass of Helium to Hydrogen. Which means the signal to particle number is comparable for all accelerated species of ions.

Both proton energy spectra are calculated for the CR-39 arrangement and the MCP configuration, see figure 4.7 (a) and (b). The signal of the MCP is integrated over the whole width of the detected trace. Several laser shots were performed to accumulate a

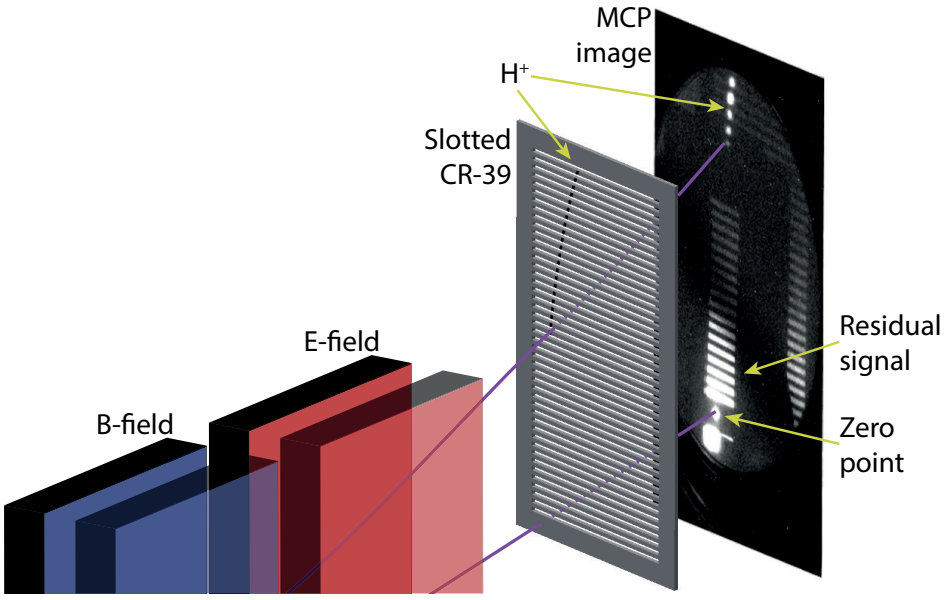

Figure 4.6: Sketch of detector arrangement for the calibration of the Thomson parabola. By means of the CR-39 plates the absolute number of particles can be compared with the signal of the MCP, detected by a CCD camera. The ion signal deflected by the Thomson parabola can be detected at the same time by the inserted CR-39 plate and the MCP detector.

decent number of ions or tracks on the CR-39 plate. Therefore, the signal in the two presented graphs is a sum of all accelerated protons. Both graphs should be complementary to each other, because protons, which pass through the gaps of the CR-39 plate, are detected by the MCP and recorded by the CCD camera (see figure 4.6). However, the energy resolution, especially in the low energy range, on the MCP image is more correct than on the CR-39, because the nuclear detector is 6 cm closer to the Thomson parabola as the MCP detector. The energy spread is wider over a larger distance on the parabola trace. That is why there are some overlaps in the corresponding energy to the detected signal of the CR-39 and the MCP proton-energy spectra. In the further analysis steps the signal is averaged over two sections and the resolution error can be neglected.

The particle tracks and the corresponding counts of the camera image are counted and summed up for each slot or gap of the CR-39 and all laser shots. This number is normalised by the unit energy interval in each corresponding area (counts/ΔE or particles/ΔE). In every analysis two signal sections are interpolated for the comparison of the trends of the particle/counts to energy evolution of MCP signal and CR-39 tracks.

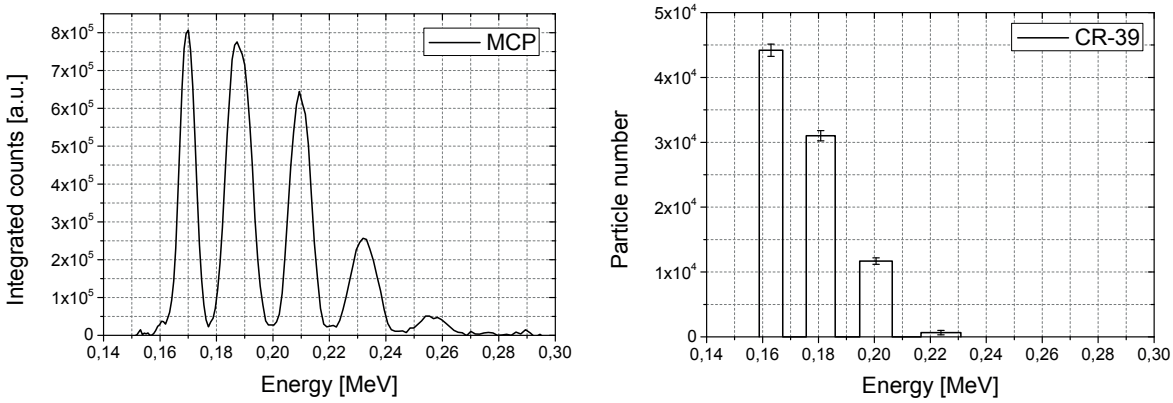

(a) MCP proton-energy spectrum

(b) CR-39 proton-energy spectrum

Figure 4.7: Energy spectra detected via the MCP (a) and via CR-39 (b). In order to calibrate the recorded MCP images, the absolute number of particles, detected by CR-39 plates, has to be compared with the corresponding signal of the MCP. A CR-39 plate with slots was used to record the tracks and at the same time a trace on the MCP. The graph is valid for the detection of protons on the double stage MCP of the 0° Thomson parabola.

This ratio is pictured in figure 4.8. The error bars are small and the similarity in the trend lines is clearly distinguishable.

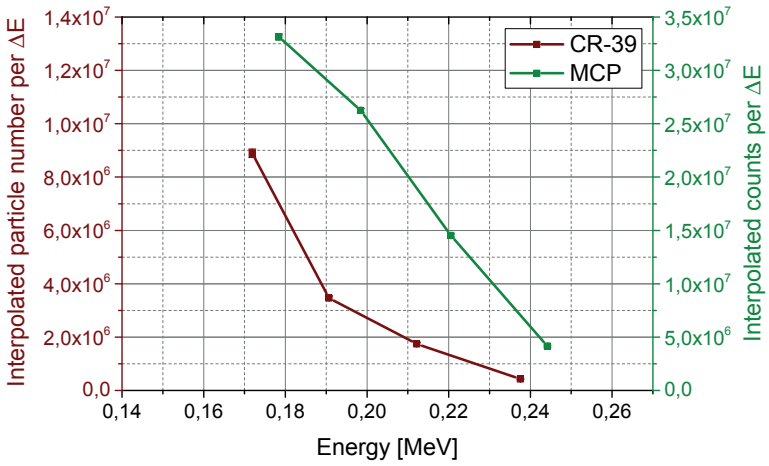

Figure 4.8: Ratio between particle number and MCP signal per unit energy interval, interpolated over two connected energy sections. The graph coressponds to the graphs (a) and (b) of figure 4.7.

The final calibration is shown in figure 4.9. Graph (a) is valid for the double stage

MCP as detector for the 0° Thomson parabola, while Graph (b) is valid for the single stage MCP, exposed by the ions of the 10° Thomson parabola. Both calibrations are made from the same laser shots. The first data point in (b) for the energy of 45 keV is much higher than the average. In the low energy section on the CR-39 less particles were found and the error to distinguish between actual tracks and noise was increasing. Therefore, this point was neglected for further calculations. By choosing the average number for the ratio counts to particle number, around ∼7.32 counts for one proton were calculated for the double stage MCP and ∼5.4 counts per proton for the single stage MCP.

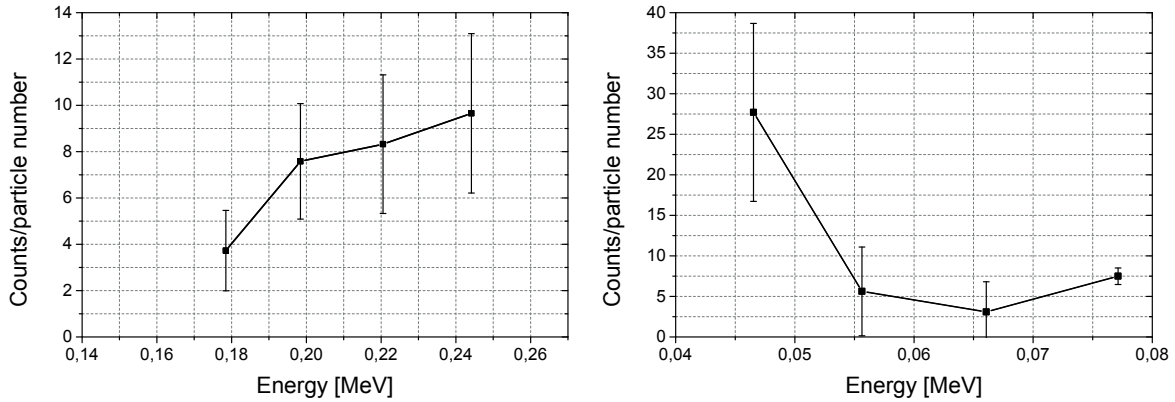

(a) Response of the double stage MCP

(b) Response of the single stage MCP

Figure 4.9: Response curve (counts per particle) of the double stage MCP (a) and single stage MCP (b). The average number for (a) is 7.32 counts per proton and for (b) 5.4 counts per proton. The data point for the energy of 0.045 MeV in graph (b) can be neglected, because of large counting errors in the low energy region of the CR-39 plate.

4.2.4 Ion trace analysis

The ion spectra of the Thomson parabolas, detected by MCPs and recorded by CCD cameras, are analyzed by means of a Matlab routine, written by A. Alejo (QUB) [50]. All necessary parameters, like magnetic and electric field, solid angle and the corresponding distances between the elements of the Thomson parabola (see table 4.1) have to be considered in the program. The zero point and rotation of the image must be chosen. Moreover, charge and atomic mass of the investigated ion species need to be selected to

trace the deflected ions. A digital trace line is fitted on the raw image by the program. It can be adjusted until it fits with the trace of the camera image by adapting all free parameters. The width of this trace can be regulated and the background is subtracted for the calculation of the ion energy spectrum.

4.3 Optical probing

Optical probing of the laser-plasma interaction depends on the propagation of the laser pulse through the plasma. Angular deflections of the laser beam, due to changes in the plasma refractive index, reveal information of the observed area, like plasma density and plasma structure. The diagnostic is limited by the critical density of the plasma, related to the probe wavelength, whereas the temporal resolution is dependent on the pulse duration of the beam. The shorter the pulse, the less integrated is the recorded image of the observed interaction plane. That is why the ARCTURUS probe beam is separately compressed to a pulse duration of 27 fs. The relative time between the probe laser pulse and the interaction is adjusted by moving a delay stage in the probe beam path. Doing so, different time steps of the interaction can be visualised in consecutive laser shots.

After passing the interaction area, the probe beam is guided through an optical system to a detector. The setup consists of lenses to magnify and to image the interaction and of interference filters to spectrally select the probe light, in order to block scattered and/or emitted light of different frequencies generated by the plasma of the main interaction. At the end of the setup, the probe light is detected by CCD cameras. In these experimental campaigns, the beam is split into two arms. One sub-diagnostic to analyse the plasma structure is shadowgraphy. The other one is interferometry from a perturbed part of the probe beam overlying with an unperturbed reference part of the laser to get the plasma electron density. Shadowgraphy is dependent of deflections and displacements of the laser beams at the detection plane, while these effects are neglected in the interferometry. The latter relies on the changes of the optical path length due to variations of the refractive index inside of the plasma. Therefore interferometry is sensitive to small gradients, while the laser is only deflected and displaced by large gradients. The forming interferometry image is directly connected to changes in the refractive index ($\sim \eta$). The relatively change in intensity in the shadowgraphy is in contrast dependent on the second

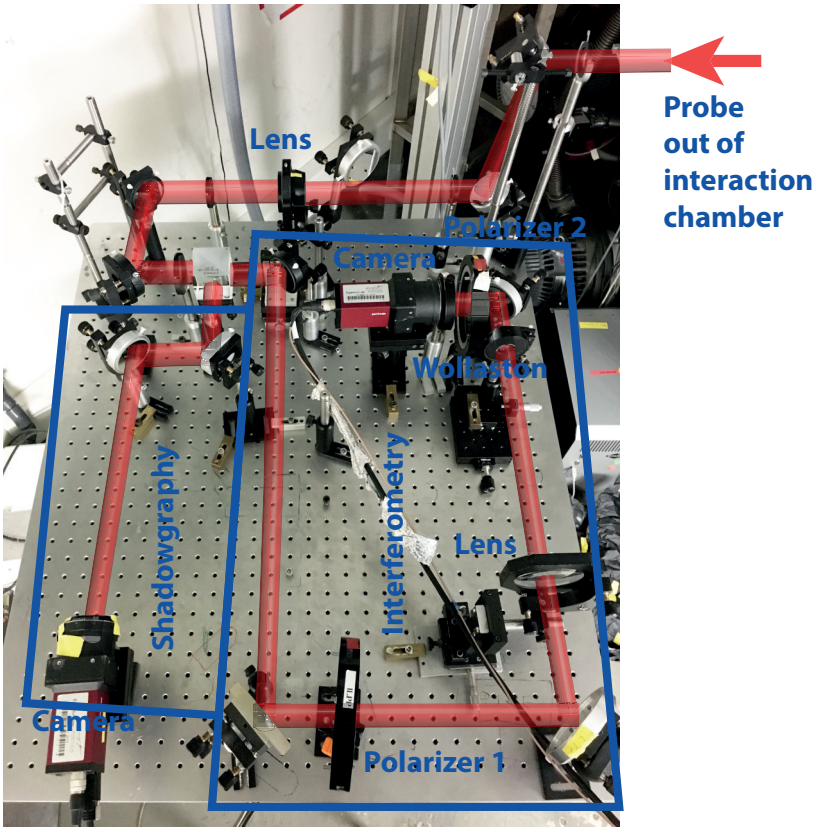

Figure 4.10: Setup of the optical probing diagnostic in these experimental campaigns. The probe beam passes through the interaction area and leaves the vacuum chamber. After that, it enters an optical table, as visible in the picture. An optical system is installed, consisting of lenses, filters, polarizers, CCD cameras and a *Wollaston* prism. The plasma evolution can be investigated with two different diagnostics, shadowgraphy and interferometry, which will be discussed in detail in the following sections.

derivative of the refractive index ($\sim \partial^2\eta/\partial y^2$). Therefore, small density changes can be better distinguished with interferometric images, than with the shadowgraphy images. In addition, the calculations for displacements and deflections are way more difficult to solve. In summary the shadowgraphy is a very easy to built diagnostic, which gives a first qualitatively impression of the plasma channel evolution, while by means of the interferometry the plasma density can be quantitatively extracted [56, 57, 58]. For more details of the setup, see figure 4.10. The following main theoretical description is based on [59].

4.3.1 Shadowgraphy

The interaction of the main laser with the target creates a plasma with different gradients in electron density. Because of that, the refractive index η (eq. 4.6) of the medium changes and the probe rays will be deflected.

$$\eta = \sqrt{1 - \left(\frac{\omega_\mathrm{p}}{\omega_0}\right)^2} \tag{4.6}$$

With $\omega_\mathrm{p} = \sqrt{n_\mathrm{e} e^2/\epsilon_0 m_\mathrm{e}}$ and $\omega_0 = \sqrt{n_\mathrm{c} e^2/\epsilon_0 m_\mathrm{e}}$ the refractive index is (assuming $n_\mathrm{e} << n_\mathrm{c}$):

$$\eta = \sqrt{1 - \frac{n_\mathrm{e}}{n_\mathrm{c}}} \approx 1 - \frac{n_\mathrm{e}}{2n_\mathrm{c}} \tag{4.7}$$

The critical plasma density n_c depends on the laser wavelength and consequently the refractive index. The probe rays are deflected due to the inhomogeneities in the plasma, corresponding to various refractive indices. Dark regions in the shadowgram correlate with areas in the plasma, where the probe rays are absorbed or deflected/reflected away from their original path. First clues of the density gradients and their evolution in time in the plasma [59] could be estimated due to the bright and dark parts of the shadowgram image (compare figure 4.11).

4.3.2 Interferometry

More details about the plasma properties can be extracted from the interferometry. A comparison of the interference pattern of the disturbed part of the probe beam with a reference beam leads to the determination of the local plasma electron density. The phase shift between both beams can be observed as fringe shift in the interference pattern. It is proportional to the integral of the refractive index along the beam propagation length (L) [60] and can be expressed by:

$$\Delta\Phi(x,z) = \int_\mathrm{L} (k_\mathrm{p} - k_0)\, dy = \frac{\omega_\mathrm{L}}{c} \int_\mathrm{L} [\eta(x,y,z) - 1]\, dy = \frac{2\pi}{\lambda} \int_\mathrm{L} [\eta(x,y,z) - 1]\, dy, \tag{4.8}$$

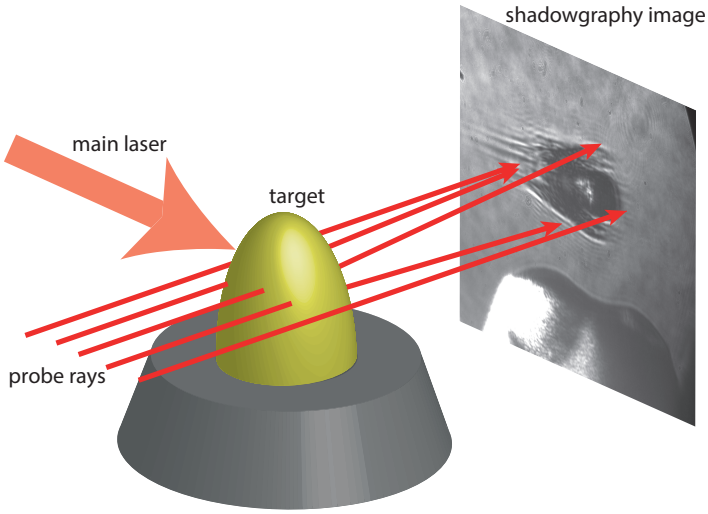

Figure 4.11: Sketch of the laser rays, which are deflected by the density gradient and therefore by the refractive index gradient in the plasma. The deflected light is detected and used as shadowgraphy diagnostic.

with the integral of the difference between vaccum wavenumber $k_0 = \omega_\mathrm{L}/c$ and the plasma wavenumber $k_\mathrm{p} = \eta\omega_\mathrm{L}/c$. With equation 4.7 the phase difference becomes:

$$\Delta\Phi(x,z) = \frac{2\pi}{\lambda}\int_\mathrm{L}\left[\sqrt{1-\frac{n_\mathrm{e}}{n_\mathrm{c}}}-1\right]dy. \tag{4.9}$$

It is difficult to solve this integral in order to know η at every point of interest in the plasma. The problem is easier to handle in two dimensions assuming a cylindrical symmetric plasma, as shown in figure 4.12.

Equation 4.8 is first converted from Cartesian (x,y,z) to cylindrical (x,r,z) coordinates. With $r = \sqrt{x^2+y^2}$ and $dy = rdr/\sqrt{r^2-x^2}$, it becomes:

$$\Delta\Phi(x,z) = \frac{2\pi}{\lambda}\int_x^{r_0}\frac{[\eta(r,z)-1]}{\sqrt{r^2-x^2}}rdr = -\frac{\pi}{\lambda n_\mathrm{c}}\int_x^{r_0}\frac{n_\mathrm{e}(r,z)}{\sqrt{r^2-x^2}}rdr. \tag{4.10}$$

The radial density profile is calculated by an analytical approach to invert the phase shift, which is the projection of the cylindrical symmetric equation of the refractive index, alias electron density. It is called *Abel* inversion [61] and the general expression is given by:

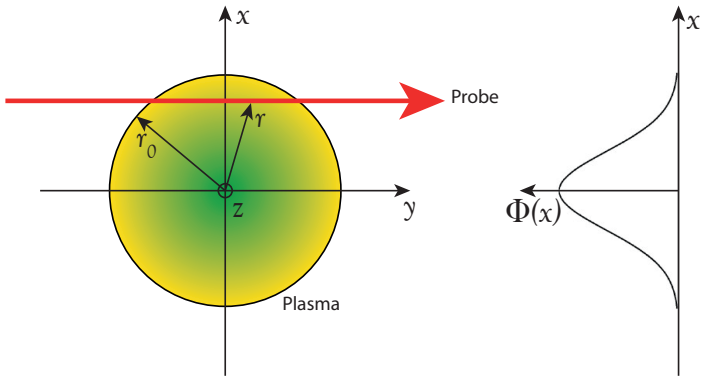

Figure 4.12: Schematic image of the plasma, which leads to the *Abel* inversion [61]. The main interacting beam propagates in z direction, while the probe beam passes along the y-axis. On the right sketch shows the evolution of the phase shift along the x-axis.

$$F(x,z) = 2\int_x^{r_0} f(r,z)\frac{rdr}{\sqrt{r^2-x^2}} \longleftrightarrow f(r,z) = -\frac{1}{\pi}\int_r^{r_o}\frac{\partial F(x,z)}{\partial x}\frac{dx}{\sqrt{x^2-r^2}}. \tag{4.11}$$

By applying this Abel inversion to the phase shift, the refractive index is calculated to:

$$\frac{2\pi}{\lambda}[\eta(r,z)-1] = -\frac{1}{\pi}\int_r^{r_0}\frac{\partial\Delta\Phi(r,z)}{\partial y}\frac{dx}{\sqrt{x^2-r^2}}, \tag{4.12}$$

which is dependent only on the location and the phase shift between the beam parts.

Equation 4.12 can be simplified to:

$$\begin{aligned}\eta(r,z) &= 1 - \frac{\lambda}{2\pi}\frac{1}{\pi}\int_r^{r_0}\frac{\partial\Delta\Phi(r,z)}{\partial y}\frac{dx}{\sqrt{x^2-r^2}} \\ &= 1 - \frac{\lambda}{2\pi}\kappa\vartheta(r),\end{aligned} \tag{4.13}$$

in which, according to [60] and [42], κ presents an experimental geometric scaling factor (conversion of pixel to the actual distance) and $\vartheta(r)$ is introduced as local phase at every point of interest. The electron density can now be calculated by means of the refractive index (eq. 4.7):

$$\begin{aligned} \eta(r,z) &= 1 - \frac{\lambda}{2\pi}\kappa\vartheta(r) = \sqrt{1-\frac{n_\mathrm{e}}{n_\mathrm{c}}} \\ \Leftrightarrow n_\mathrm{e} &= n_\mathrm{c}\left[1-\left(1-\frac{\lambda}{2\pi}\kappa\vartheta(r)\right)^2\right]. \end{aligned} \tag{4.14}$$

To characterise the target (see section 3.2), the neutral gas density can as well be calculated from eq. 4.12. With the definitions of [60], the neutral gas density can be defined as:

$$\begin{aligned} \eta(r,z) - 1 &= \frac{\lambda}{2\pi}\frac{1}{\pi}\int_r^{r_0}\frac{\partial\Delta\Phi(r,z)}{\partial y}\frac{dx}{\sqrt{x^2-r^2}} \\ &= \frac{\lambda}{2\pi}\kappa\vartheta(r) \\ &\stackrel{!}{=} (\eta_\mathrm{gas}-1)\frac{n_\mathrm{gas}}{n_0} \\ \Leftrightarrow n_\mathrm{gas} &= \frac{N_0}{(\eta_\mathrm{gas}-1)}\frac{\lambda}{2\pi}\kappa\vartheta(r), \end{aligned} \tag{4.15}$$

with $N_0 = 2.68 \cdot 10^{19}\,\mathrm{cm}^{-3}$ as atom density at standard temperature and pressure, as well as η_gas being the refractive index of a defined gas for a specific laser wavelength.

4.3.3 Experimental setup and analysis of the data

A *Normarski* interferometer [62] was used as probe diagnostic in the experiments. It is an easy method to measure the phase difference and therefore the electron density of a plasma. The interferometer is easily aligned, especially for the temporal overlap of ultra short beams. The working principle is based on one probe beam, which is first propagating through the interaction area, and then through an optical path up to a lens, where it is focused close to a *Wollaston* prism. Only now the beam is split into two beamlets in the *Wollaston* crystal (two virtual foci, F' and F", are created). The *Wollaston* crystal consists of two orthogonal prisms and optical axis. Consequently, the parallel polarized laser is divided into two perpendicular linear polarized beamlets with a predefined angle between each other. In order to get interference of the two beams, their polarization has to be adjusted by a polarizer in 45° to the original polarization. That is why no temporal alignment of the two beams is necessary. The only requirement is, that the beam diameter is bigger than the interaction area, to overlap a perturbed

part of the beamlet with an unperturbed part of the second beamlet. The fringe width i is calculated by (accordingly to [62]):

$$i = \frac{\lambda}{\alpha}\frac{L}{l}, \tag{4.16}$$

with a given wavelength λ, an opening angle α defined by the crystal and a variation between the distances of the focus of the lens to the *Wollaston* (l) and *Wollaston* to the image plane (L). A schematic view of the *Normarski* interferometer is shown in figure 4.13.

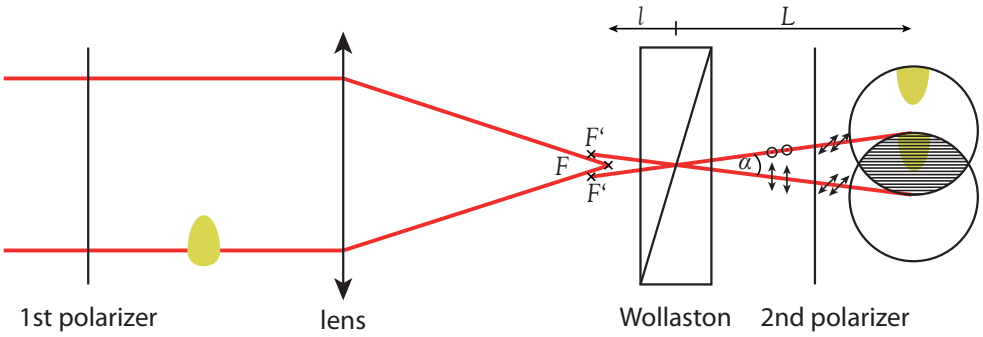

Figure 4.13: Sketch of the *Normarski* interferometer. A prepolarized probe beam propagates through an interaction area. It is focused close to a *Wollaston* prism, where it is split into two perpendicular polarized beamlets. A second polarizer is necessary for a proper interference between the two beams.

Some interference patterns of the experimental recorded images are manually traced by additional computer programs in order to get a better contrast of the fringes. The phase shift $\Delta\Phi(x,z)$ of the interference pattern is extracted by a method based on numerical *Fast Fourier Transform* (FFT) [63, 64], described in the following part. Based on [65], the intensity of the fringe pattern of the disturbed image can be calculated by:

$$\begin{aligned} g(x,z) &= a(x,z) + b(x,z)cos(2\pi f_u z + \Delta\Phi(x,z)) \\ &= a(x,z) + c(x,z)exp(2\pi i f_u z) + c^*(x,z)exp(-2\pi i f_u z), \end{aligned} \tag{4.17}$$

with $\Delta\Phi(x,z))$ as phase shift, as described before. $a(x,z)$ and $b(x,z)$ represent intensity fluctuations from irregular reflections and transmission of the light by the plasma. c depicts the contrast of the interference pattern and can be written as: $c(x,z) = 1/2 \cdot$

$b(x,z) \cdot exp(i\Delta\Phi(x,z))$, while c^* is the complex conjugate. f_u is the spatial carrier frequency of the unperturbed fringes. If equation 4.17 is Fourier transformed along z, three components result (capital letters represent the Fourier transform):

$$G(x,f) = A(x,f) + C(x,f-f_u) + C^*(x,f+f_u), \tag{4.18}$$

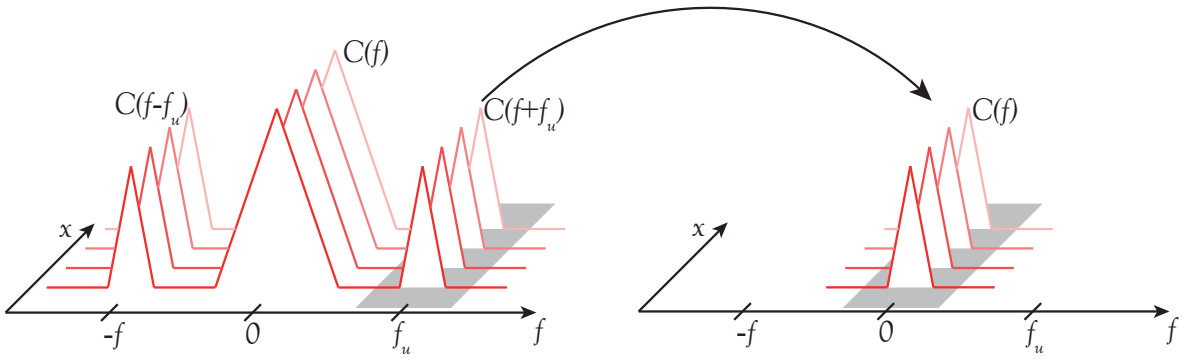

Figure 4.14: Method of the Fourier transformation to extract the phase from an intensity pattern of the recorded images of the interferometer. The Fourier spectrum consists of three parts, but only one is selected and shifted by $-f_u$.

while f is the spatial frequency of the interference modulation. $a(x,z)$, $b(x,z)$ and $c(x,z)$ change very slowly compared to the carrier frequency f_u, so that they are separated by f_u. $C(x,f-f_u)$ is selected in the Fourier transform and shifted by f_u (compare figure 4.14) towards $C(x,f)$. The variation in the background, stored in $a(x,z)$, is filtered and C or C^* can be inversely Fourier transformed to $c(x,z)$. From the complex part of the logarithm of $c(x,z)$, the phase $\Delta\Phi(x,z)$ can be calculated:

$$log[c(x,z)] = i\Phi(x,z) + log[1/2b(x,z)] \tag{4.19}$$

The phase extraction can be summarised as:

$$g(x,z) \overset{FFT}{\rightarrow} G(x,f) \rightarrow C(x,f-f_u) \rightarrow C(x,f) \overset{iFFT}{\rightarrow} c(x,z). \tag{4.20}$$

Phase $\Delta\Phi(x,z)$ can be calculated between 0 and 2π due to the periodicity of the imaginary logarithm. An unwrapping procedure is necessary in order to resolve the real phase.

Jumps are detected and eliminated to connect the phase. A more detailed description is mentioned in [66].

A *Matlab* routine was used to extract the phase via FFT and via *Abel* inversion the electron and neutral gas density from the recorded images.

4.4 Radiochromic films

Radiochromic films (RCFs) are self-developing films. They are sensitive to ionising radiation like electrons, ions, X-rays and Gamma rays and very easy to handle, because no post-exposure processing is necessary to extract further information. A film consists of at least one polyester plastic substrate and a layer of radiation-sensitive organic micro crystal monomer [67]. The active layer is changing its colour, while being irradiated, almost independent of the radiation energy. Therefore, the optical density (OD) of the exposed area changes. A high OD corresponds to a high deposited energy of the ionising radiation. It is directly proportional to the absorbed radiation dose (amount of energy absorbed per unit mass) in the active layer. A calibration of the colour change can therefore provide information about the flux of the particles. This could be one possible purpose of the RCFs, to measure the flux of the incident particles. The other one is to resolve structures by particles exposing the film, which are deflected in the plasma, as described in the following section 4.5.

A high spatial resolution up to sub-micron range is achievable, because the polymerisation reactions in the active layer do not spread between the micro crystals [68]. The biggest change in colour of the active layer takes place immediately after the irradiation, in a few milliseconds, but is not completed. Consequently, the films should be read out at least 24 hours after the illumination, even better after 48 hours [69]. Some older types of RCF films could be slightly pre-exposed by room light [70], which makes necessary a storage in the dark. Moreover, the exact thickness of the active layer varies from film to film [68, 71].

4.4.1 Composition of the RCFs

In these experimental campaigns, two different types of radiochromic films were used: the *Gafchromic* film HD-V2 with a dose range of 10 Gy to 1000 Gy [68] and the more sensitive *Gafchromic* EBT2 film, which has a working range of 0.01 Gy up to 40 Gy [72]. The composition of the two films is shown in figure 4.15. The active layers of both films have only slightly different chemical compositions [73]. The main characteristic is the thickness of this layer.

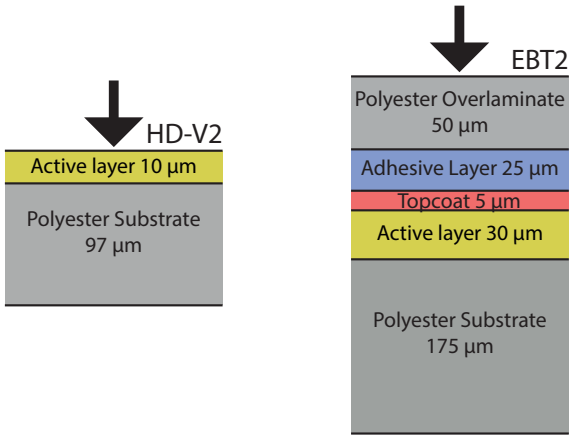

Figure 4.15: Two different types of radiochromic films. The left illustration shows the composition of the HD-V2 film with a thin 10 μm active layer and the right one the composition of the more sensitive EBT2 film with a thicker active layer.

Not only one single film were used during the laser plasma experiments, instead multiple layers of films were stacked together. Thus, information about the flux, transverse profiles of the particle energies and spatial structures can be obtained. The stack is always covered in an aluminum foil with a thickness of about 14 μm to secure the film of laser light and all low energy ions. In these experimental campaigns, a stack of five HD-V2 and two following EBT2 films was used (compare figure 4.16). Due to the high sensitivity, the EBT2 films are the last two of the stack to resolve the high energy particles with low flux. The high dose of the low energy particles would oversaturate the EBT2s.

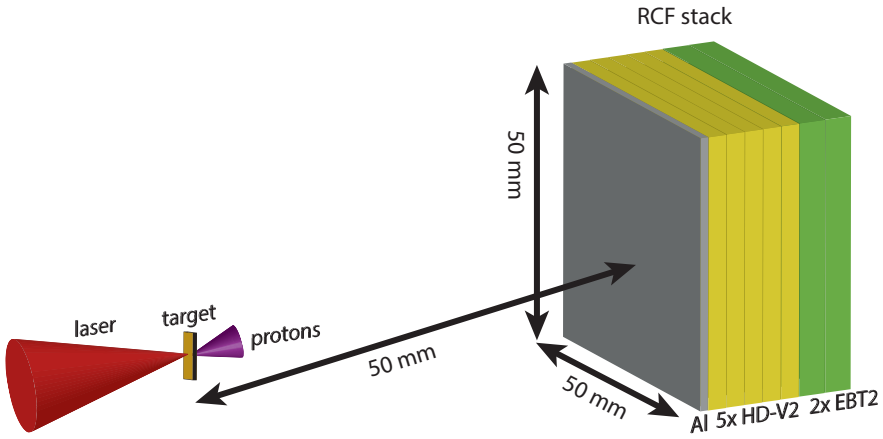

Figure 4.16: RCF stack composition and size used in these experimental campaigns.

4.4.2 Proton energies in each RCF layer

Ions propagat through matter until they are stopped. At this point the highest amount of energy is deposited in the material (Bragg-peak) described by the *Bethe-Bloch* formula [74, 75]. But until they are stopped, the protons deposit a considerable amount of their initial energy along their track (compare figure 4.17). Therefore, each layer of the RCF stack will contain information about a certain energy range of protons, like dose and spatial distribution.

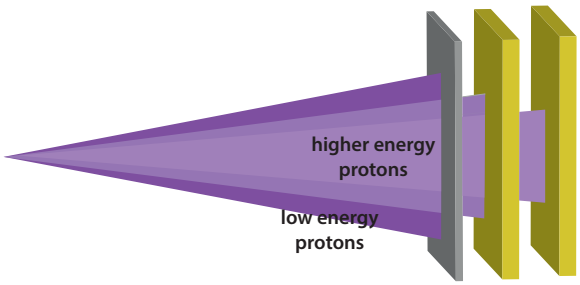

Figure 4.17: Protons of different energies reach different layers in the RCF stack. Low energy protons are blocked by the cover layer of aluminium, while higher energies can reach rear RCF films.

Figure 4.18 shows the energy loss of protons of a certain energy per target depth. The curves are calculated by the software package SRIM (Stopping and Range of Ions in Matter) [76, 77]. Each Bragg-peak corresponds to an active layer of the mentioned RCF stack. The black curve represents the cover layer. Protons of roughly 1 MeV

or less are stopped by the 14 μm aluminum layer. The traveling length of the protons through the stack from one active layer to the next is the same for all HD films. However, for the EBT films it is different. At this point the whole thickness of the film varies and the distance up to the following active layer changes. The correct composition and density of each layer [73] of each RCF type as target is taken into account in the SRIM calculations. Due to the active layer thickness, not only particles of one energy have their Bragg-peak in it, but also particles, which are stopped elsewhere in the 10 or 30 μm thick layer. Figure 4.18 is valid for the maximum energy, which is stopped at the end of the active layer. If the thickness is taken into account, there will be an uncertainty of the particle energy, which is stopped in that layer. In the active layer of the second HD-V2 the minimum energy of the stopped protons is for example 3.1 MeV and the maximum energy is 3.27 MeV. There is a difference of 170 keV, which however is not crucial. Therefore, an average value of the centre of the active layer is taken into account for further calculations.

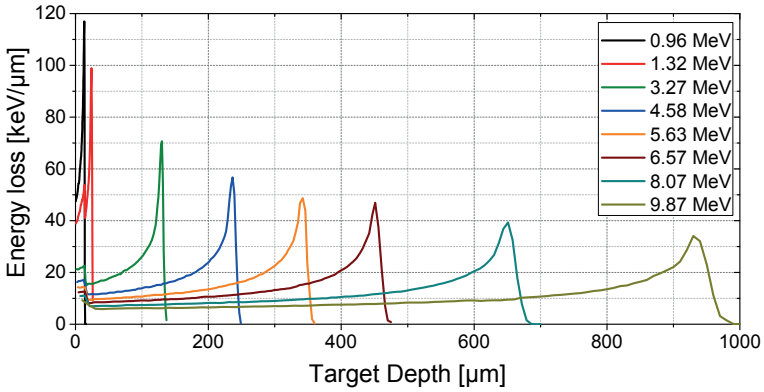

Figure 4.18: Stopping power curves of different energy protons in the RCF stack. The depth of the Bragg-peak corresponds to each active layer of the RCF films. The curves are simulated by the software package SRIM [76, 77].

Moreover, each active layer contains not only the deposited energy of the particles, which are stopped due to their Bragg-peak. Also higher energy protons deposit part of their energy in the active layers, less deep in the RCF stack compared to their stopping depth. The deposited energy in each active layer of the RCFs is calculated by TRIM (a tool of the SRIM software package). The corresponding curves are shown in figure 4.19.

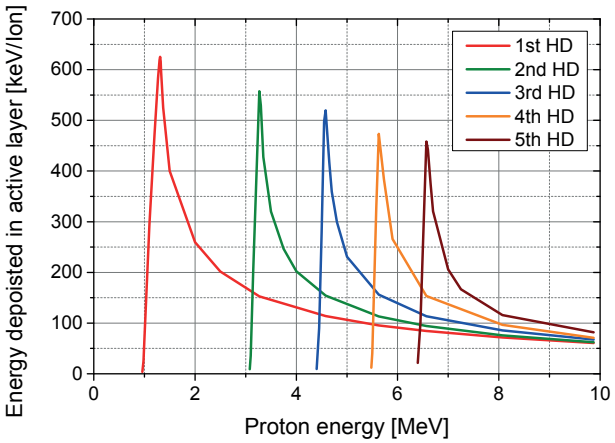

Figure 4.19: Deposited energy in each active layer of the RCF films. The curves are simulated by the software package SRIM with the tool TRIM [76, 77].

4.5 Proton probing technique

The employment of a beam of protons, produced by a TNSA interaction (compare subsection 2.4.1), for imaging was presented in [78] for the first time. Nowadays it is a common way to investigate the electric and magnetic fields, generated during different laser-plasma interactions. A typical setup of the proton probing technique is shown in figure 4.20. A high intensity laser beam impinges onto a target. A bunch of protons of different energies is accelerated due to the TNSA mechanism. The target is aligned in such a way, that the protons will pass a second laser-target interaction area. The point of interest is this interaction of the main laser with its own target. The protons used for the imaging are deflected of their original longitudinal beam path, because of electric and magnetic fields, generated by the latter interaction. A detector can highlight the protons and therefore the investigated interaction. Beam 1 of the of the ARCTURUS laser facility is focused to a spot of 4 μm in diameter with an intensity of roughly $1.5{\cdot}10^{20}\,\mathrm{W/cm^2}$ by an F/2 OAP in these experimental campaigns. The laser irradiated a 10 μm thick gold target to produce the protons.

A typical physical source size of the protons is more than about 10 μm in diameter (depending on the proton energy) at the rear (non-irradiated) surface of the target, which was experimentally measured in [79]. This size however would lead to bad spatial resolution in the imaging technique. Instead, the highly-laminar and diverging TNSA-driven proton beam could be assumed to originate from a point-like virtual source,

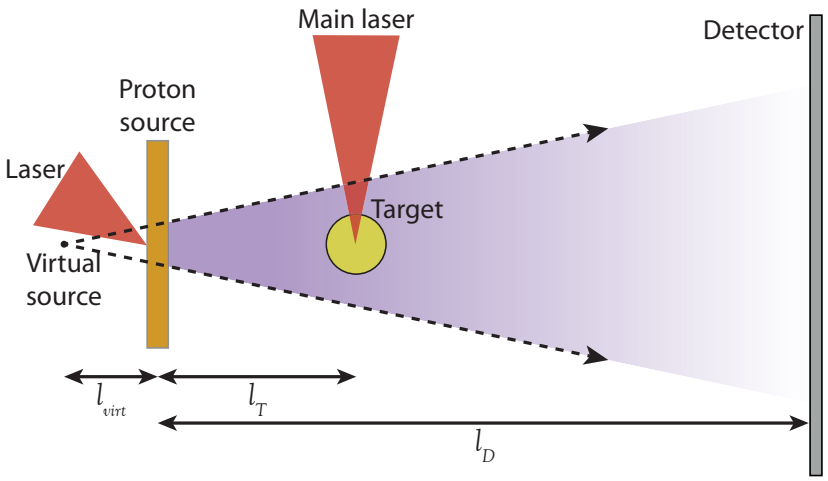

Figure 4.20: Drawing of a typical proton probing setup. A high intensity laser impinges a thin metal foil to accelerate protons due to the TNSA mechanism. These protons pass through a region of electric and/or magnetic fields. The protons are deflected off their original path on their way to the detector. The field region is produced by a second (main) laser beam hitting its target. This laser-plasma interaction is investigated by the charged particle beam.

several hundreds of microns away from the target surface [80]. In this case a geometrical magnification can be calculated as follows:

$$M = \frac{l_{\mathrm{virt}} + l_{\mathrm{D}}}{l_{\mathrm{virt}} + l_{\mathrm{T}}} \simeq \frac{l_{\mathrm{D}}}{l_{\mathrm{T}}}, \tag{4.21}$$

with l_{D}, distance from the TNSA target to the detector and l_{T}, distance from the proton source to the investigated area of interest (main target). As long as the displacement of the virtual source is as small as described and the condition $l_{\mathrm{virt}} \ll l_{\mathrm{T}} \ll l_{\mathrm{D}}$ is satisfied, the proton source can be assumed as point-like and the magnification can be reduced to the expression above (equation 4.21). In these experimental campaigns l_{T} had a length of about 8.5 mm and l_{D} between 50.5 to 76.5 mm, which leads to a magnification between 6 and 9.

An advantage of the proton probing technique is a temporal resolution within a single laser shot with a capable detector, like the radiochromic films. Because the proton beam has a rather broad energy spectrum, all protons of different energies have a different time-of-flight until they reach the interaction area of the main laser beam. Low energy

protons will need longer time to reach the interaction compared to high energy protons. Therefore, they will be deflected by different fields inside the main laser plasma interaction, which evolves in time. That is why the interaction is probed at different times in one laser shot. RCFs (details in section 4.4) as detectors, can resolve the different time steps in a multi-frame arrangement.

4.5.1 Principles of proton imaging

The imaging is based on the deflection of the probing beam of charged particles at the area of interest. This area consists of electric and/or magnetic fields due to the laser-plasma interaction of the main laser pulse with its own target. In these campaigns beam 2 of the ARCTURUS laser facility was focused by an F/10 OAP into a gas jet, which acts as area of interest. More details about the setup and interaction will be discussed in subsection 4.8.5.

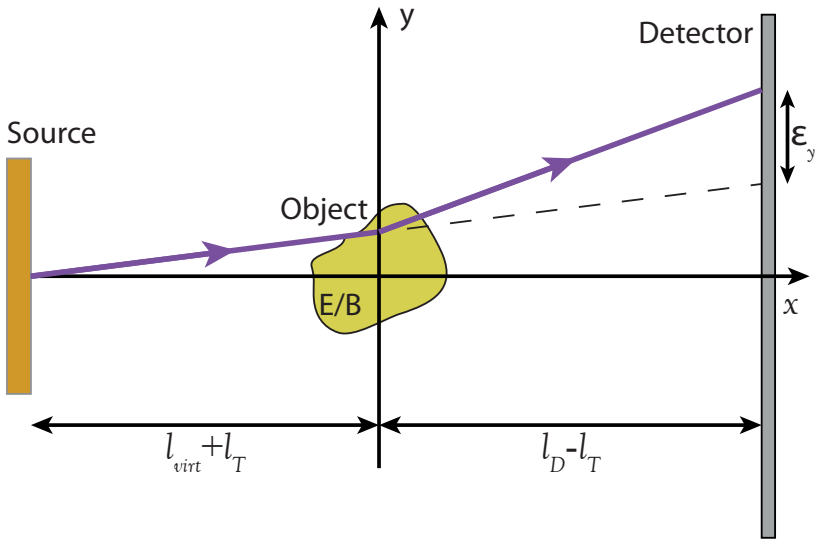

Figure 4.21: The principle of the proton imaging.

A single proton passing through the deflecting area (compare sketch 4.21) is affected by the Lorentz force of the electric and magnetic fields ($\boldsymbol{E}$ and $\boldsymbol{B}$):

$$\boldsymbol{F}_{\mathrm{L}} = m_{\mathrm{P}}\boldsymbol{a}_{\mathrm{P}} = m_{\mathrm{P}}\frac{d\boldsymbol{v}_{\mathrm{P}}}{dt} = -e(\boldsymbol{E}(t) + \boldsymbol{v}_{\mathrm{P}}(t) \times \boldsymbol{B}(t)), \tag{4.22}$$

where m_P and $\boldsymbol{v}_\mathrm{P}$ are the proton mass and velocity vector in the disturbed region. The fields are both time dependent, because the plasma evolves in time and the charged particles change their positions. By means of equation 4.22, the transverse velocity of the charged particles in the interaction area with a linear extension d can be written as:

$$\begin{aligned}\delta\boldsymbol{v_y} &= \frac{e}{m_\mathrm{P}}\int(\boldsymbol{E}(t)+\boldsymbol{v}_\mathrm{P}(t)\times\boldsymbol{B}(t))_y dt \\ &\simeq \frac{e}{m_\mathrm{P}v_\mathrm{P}}\int_d(\boldsymbol{E}(t)+\boldsymbol{v}_\mathrm{P}(t)\times\boldsymbol{B}(t))_y dx,\end{aligned} \tag{4.23}$$

in which the transverse motion of the laminar flow of the TNSA protons can be neglected, compared to the longitudinal motion with:

$$v_x = \frac{dx}{dt} \simeq v_\mathrm{P} \Leftrightarrow dt = \frac{dx}{v_\mathrm{P}}. \tag{4.24}$$

The transverse displacement at the detector is defined by the time-of-flight of the protons from the investigated interaction area to the detector, $\Delta t \simeq (l_\mathrm{D}-l_\mathrm{T})/v_\mathrm{P}$, and the initial proton energy $E_\mathrm{P} = (1/2)m_\mathrm{P}v_P^2$, as follows:

$$\begin{aligned}\epsilon_y \simeq \delta\boldsymbol{v_y}\Delta t &\simeq \frac{e(l_\mathrm{D}-l_\mathrm{T})}{2E_\mathrm{P}}\int_d(\boldsymbol{E}(t)+\boldsymbol{v}_\mathrm{P}(t)\times\boldsymbol{B}(t))_y dx \\ &= \frac{e(l_\mathrm{D}-l_\mathrm{T})}{2E_\mathrm{P}} d\left\langle(\boldsymbol{E}(t)+\boldsymbol{v}_\mathrm{P}(t)\times\boldsymbol{B}(t))_y\right\rangle_d.\end{aligned} \tag{4.25}$$

If the displacement is known or can be calculated from the detector images, the average field values of the investigated area can be assumed as:

$$\begin{aligned}\left\langle(\boldsymbol{E}(t)+\boldsymbol{v}_\mathrm{P}(t)\times\boldsymbol{B}(t))_y\right\rangle_d &= \frac{1}{d}\int_d(\boldsymbol{E}(t)+\boldsymbol{v}_\mathrm{P}(t)\times\boldsymbol{B}(t))_y dx \\ &\simeq \frac{2E_\mathrm{P}}{e(l_\mathrm{D}-l_\mathrm{T})d}\epsilon_y.\end{aligned} \tag{4.26}$$

In order to get more information about the main laser-plasma interaction area simulations of the plasma fields can be done and analysed by equation 4.26.

4.6 Electron spectrometer

An electron spectrometer to resolve the energy of the accelerated electrons was a secondary diagnostic in these experimental campaigns. It consists of a pair of permanent magnets and a detector. A schematic view of the spectrometer arrangement is shown in figure 4.22. In these experimental campaigns the detector for the spectrometer was a MCP (subsection 4.2.2) and in another setup a scintillating screen [81]. A commercially available *Carestream Kodak BioMax MS Intensifying Screen* was used. If the electrons deposit energy in the screen, a fluorescence of visible green light can be read out as live image with a CCD camera. In the MCP arrangement the spectrometer was equipped with a pinhole, as described in section 4.2, while in second case, the magnets were covered with a thin aluminum foil to insulate the scintillating screen from the laser light.

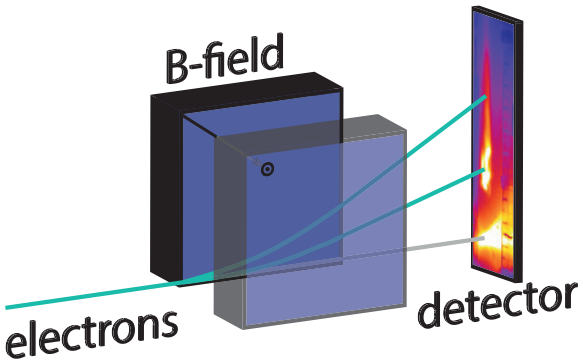

Figure 4.22: Schematic view of an electron spectrometer. Electrons enter the pair of magnets and are deflected by the magnetic B-field. Behind the magnet is a detector to resolve the energy distribution of the electrons.

As soon as the electrons enter the magnets, they are deflected on a circular path by the Lorentz force, as already described in section 4.2. Here, the relativistic motion of the electrons has to be taken into account, so that the relativistic Larmor radius of the electrons is:

$$r_{\mathrm{L}} = \frac{m_{\mathrm{e}}}{eB}\sqrt{\gamma^2 - 1}c, \tag{4.27}$$

with the relativistic γ factor, electron mass m_{e} and magnetic field B. The electron energy can be defined as:

$$E = E_0 \left(\sqrt{\left(\frac{eBr_\mathrm{L}}{m_\mathrm{e}c} \right)^2 + 1} - 1 \right). \tag{4.28}$$

In order to get the energy of the electrons the deflection on the detector can be calculated and compared with the detected images via geometrical calculations.

4.7 Summary of all diagnostic methods

In this chapter all diagnostics, which were used in these experimental campaigns, are described in detail. Two Thomson parabolas were the main diagnostics to detect the accelerated ions and to investigate their energy distribution. The MCP detector of the TPs was cross-calibrated by CR-39 nuclear track detectors in order to achieve an absolute particle number reaching the MCP. Moreover, optical probing was employed to study the temporal evolution of the plasma, including the electron density via shadowgraphy and interferometry. Charge particle probing was used to investigate the evolution of the magnetic and electric fields inside the interaction area. The RCFs in a multi-frame arrangement were utilised as a detector, which can resolve the deflected particles with different time-of-flights in one laser shot. Furthermore, an electron spectrometer was employed to explore the accelerated electrons as a byproduct of the laser plasma interaction.

4.8 Experimental setups

The experimental campaigns were performed at the ARCTURUS laser facility. Both main beams were employed for the laser plasma interaction. They were focused down into the gas target in the perpendicular direction to each other. The underdense gas jet, described and characterised in detail in section 3.2, was used for all experimental campaigns. While during the measurements, different laser and target parameters were changed in order to investigate various acceleration processes. The gas jet target was operated with Helium or Hydrogen gas with different neutral densities, respectively. Furthermore, the energy of the laser pulses and the time delay between the two pulses were also changed.

4.8.1 Laser beam parameters

The energy of beam 1 and beam 2 was about 3 J after the main amplifiers. Both beams were compressed to a pulse duration of ∼27 fs. Both beams were used without a plasma mirror. As a result the temporal laser contrast is as shown in subsection 3.1.3 in figure 3.5. Therefore, the target was probably preheated by the pedestal level of the laser. Each beam looses part of its energy in the compressor and in the vacuum beamline up to the target chamber. Thus, an energy of about 1.44 J, corresponding to a throughput of about 48 %, was measured inside the experimental chamber before the beams were further guided and focused by the parabolas.

Beam 1, which from now on is called "Driver", was focused to a $\sim 4\,\mu$m diameter focal spot (Full Width Half Maximum (FWHM)) by a gold coated 90° off-axis parabola (OAP) with a focal length of 152.4 mm (***f/2 OAP***). More details about the investigation of the focal spots are following in the next subsection. The FWHM consists of 38 % of the total energy of the beam, because the focus area is not entirely homogenous with some hot wings around the actual spot. An intensity of $1.5 \cdot 10^{20}\,\mathrm{W/cm^2}$ was reached on the target by a Driver energy of ~ 0.55 J in the focal spot.

Two different configurations were employed for beam 2, the "Heater", in the experimental setup. In one arrangement, the Heater beam was focused over a length of 0.8 m by a dielectric ***f/10 OAP***. This corresponds to a focal spot diameter of 12 μm and an energy of roughly $\sim 56\%$ FWHM, which correlates to 0.8 J on the target. Accordingly,

an intensity of $2.4 \cdot 10^{19}\,\mathrm{W/cm^2}$ was reached. A sketch of this setup is shown in figure 4.23.

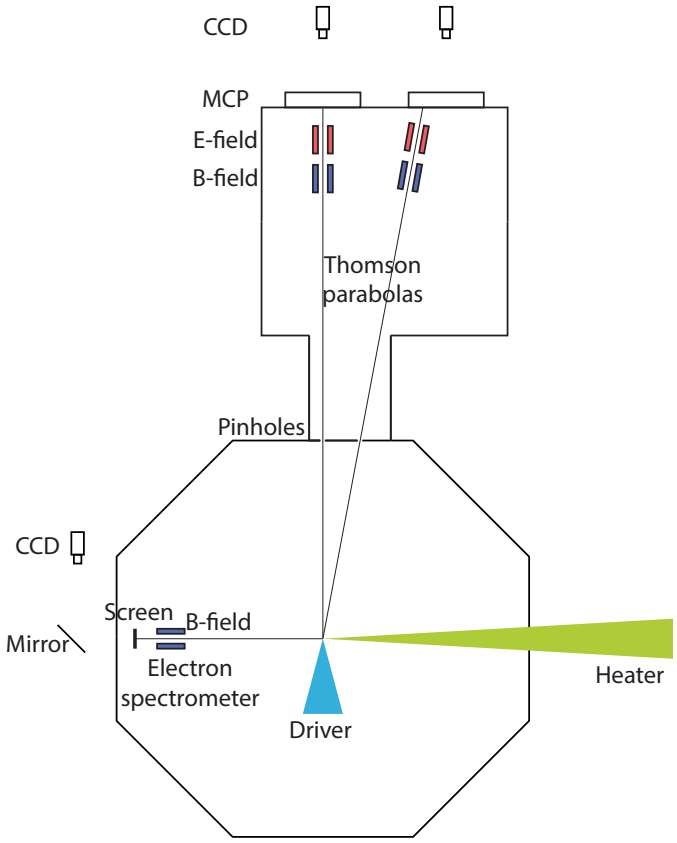

Figure 4.23: Sketch of the f/10 setup of the experimental campaigns employed for ion acceleration via Coulomb explosion (Heater-only) or via a TNSA-like mechanism (double beam). Driver- (Beam 1) and Heater lasers (Beam 2) are focused perpendicularly to each other into a gas target. The Driver is focused by an f/2 gold coated OAP and the Heater by a dielectric f/10 OAP. Two Thomson parabolas with MCP detectors along 0° and 10° related to the Driver beam were used to investigate accelerated particles as main diagnostics. A magnetic spectrometer with a scintillating screen was installed to observe the electron energy spectrum at 90° to the Driver.

Second, in contrast to the f/10 setup, the Heater was focused by an ***f/25 OAP*** (f=2 m) to a 75 μm focal spot (FWHM) with an energy of 61 % of the full beam reaching the parabola. This corresponds to roughly 0.87 J and $\sim 6.6 \cdot 10^{17}\,\mathrm{W/cm^2}$ on the target. This part is presented in figure 4.24.

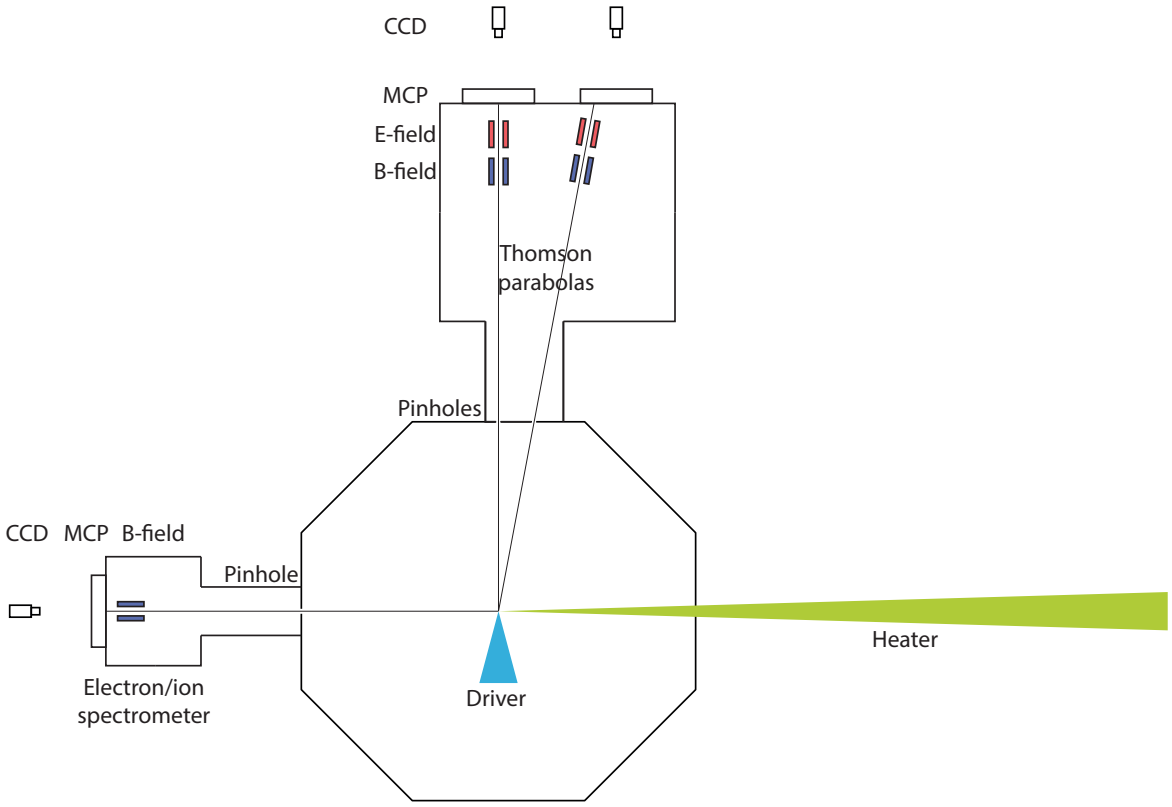

Figure 4.24: Sketch of the f/25 setup of the experimental campaigns employed for the acceleration of monoenergetic ions. Driver- (Beam 1) and Heater lasers (Beam 2) are focused perpendicular to each other into a gas target. The Driver is focused by an f/2 gold coated OAP and the Heater by a dielectric f/25 OAP. Two Thomson parabolas with MCP detectors along 0° and 10° related to the Driver beam were used to investigate accelerated particles as the main diagnostics. A magnetic spectrometer was installed to observe the ion and electron energy spectra 90° to the Driver. In addition, the probe beam was employed to perform shadowgraphy of the Driver beam.

4.8.2 Employed diagnostics

In the ***f/10-Heater, Coulomb explosion setup*** two Thomson parabola spectrometers were the main diagnostics. They were placed along 0° and 10° (related to the Driver), as shown in figure 4.23. For more details about the diagnostic, see section 4.2. In addition, there was an electron spectrometer inside the vacuum chamber with a scintillating screen as detector, monitored by a CCD camera from outside of the chamber.

The same two Thomson parabolas were the main diagnostics in the ***f/25-Heater setup***. One more spectrometer (magnet) was employed to observe possible accelerated ions 90° to the Driver. Later on it was used as an electron spectrometer (see section 4.6). Compare figure 4.24.

4.8.3 Focal spot characterisation

The focal spot was monitored and optimised in a daily routine for each beam. The aim was to get the highest possible intensity of each beam or at least to know the actual focal spot size in order to adjust the beam intensity for the best laser target interaction. The laser focus at the target chamber centre (tcc) is imaged and magnified outside of the vacuum chamber to a CCD camera by adjusting a high quality, infinity corrected, long working distance objective of the company *Mitutoyo*. The Driver with the short focal length is magnified 10x, while the Heater is magnified 5x. Each microscope objective and the outcoupling mirrors are mounted on motorised linear stages to move them remotely under vacuum in the experimental chamber. Three exemplary images of the focal spots are shown in figure 4.25, (a-c).

The radial profile is read out and averaged of several images of the focal spots. Plot (d-f) of figure 4.25 shows plots of the normalised integrated intensities around concentric circles as a function of distance from the centre of the circle. The graphs are correlated to the images in figure 4.25. The signal is the sum of all pixel values along a circle. The Full Width Half Maximum can be estimated from the graphs by finding the corresponding radius value for half of the maximum of the integrated intensity. The diameter of the focal spot and the area of the beam at the FWHM of the intensity can be calculated. A focal spot size of $4\,\mu$m $\pm$ $0.1\,\mu$m and an area with respect to the total beam profile of $38\,\% \pm 2\,\%$ for the Driver beam was determined by the evaluation of several images.

A spot size of 12 μm $\pm$ 1 μm with a FWHM area of 56 % $\pm$ 2 % is considered for the shorter focal length Heater beam. For the f/25 OAP a spot size of 75 μm and a focal area of 61 % is calculated.

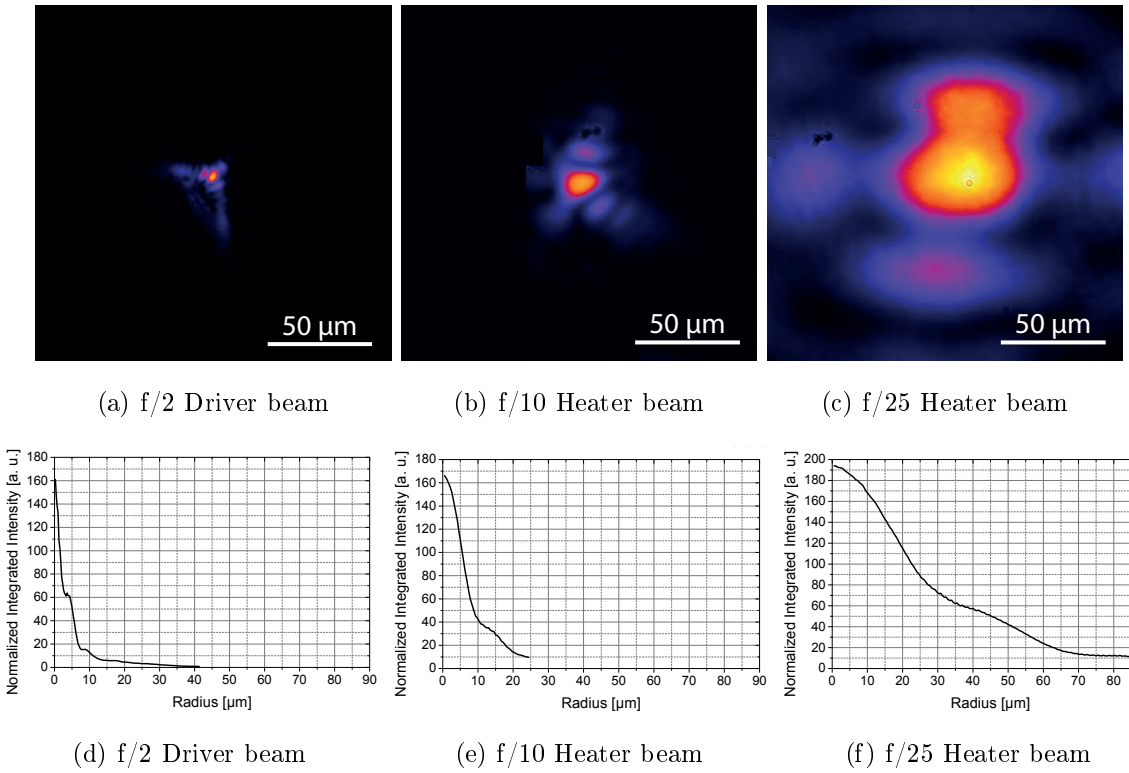

(a) f/2 Driver beam (b) f/10 Heater beam (c) f/25 Heater beam

(d) f/2 Driver beam (e) f/10 Heater beam (f) f/25 Heater beam

Figure 4.25: Focal spot images of the Driver (a) and the Heater beams (b) and (c). The spot at the target chamber centre is magnified by microscope objectives to a CCD camera outside the vacuum chamber. In order to have the radial profiles (d-f) of the focal spots, the intensity is integrated along concentric circles for each distance to the spot centre. The FWHM of the focal spot size and area can be estimated according to the graphs.

	Beam 1	Beam 2	
name	Driver	Heater	
OAP	f/2	f/10	f/25
FWHM focal spot diameter [μm]	4	12	75
FWHM focal spot area [%]	38	56	61
laser intensity [W/cm^2]	$1.5 \cdot 10^{20}$	$2.4 \cdot 10^{19}$	$6.6 \cdot 10^{17}$

Table 4.3: Summary of the laser parameters with focal spot characteristics and laser intensities for the two different main setups.

4.8.4 Spatial and temporal overlap of the beams

The laser beams had to be precisely aligned in a regular procedure, in order to ensure a ***spatial overlap*** in the centre of the gas target. Therefore, the target holder was motorised with linear x, y and z stages and a 80 μm thin wire was mounted on the nozzle head. Each beam was aligned on the same wire to achieve the spatial overlap, by means of the microscope objectives. Afterwards, the beam alignment was fixed and the nozzle was moved and adjusted to its centre.

A fast photodiode and an oscilloscope were used, to obtain a preliminary nanosecond ***temporal overlap***. This rough temporal overlap was adjusted by setting up a fixed delay in the Driver beam path. However, a more precise method had to be implemented in order to get an overlap of the ultra short pulses with femtosecond accuracy. For this reason, the Heater beam itself was employed as optical probe beam. The laser was sent into the target area with very low energy to observe the interaction of the Driver beam with the gas target. The Heater gets a homogeneous airy pattern and illuminates a bigger area in the focal plane by decreasing an aperture on the main amplifier in the laser laboratory. Consequently, the Heater beam could be used for a shadowgram, while the Driver was slightly amplified to about 25 mJ after the main amplifier, which coressponds to an intensity of roughly $10 \cdot 10^{18}$ W/cm^2 on the target. Due to that, an ionised plasma channel was formed in the target and probed by the Heater. The fine motorised delay stage of the Heater (beam 2) was moved in 500 femtosecond steps until the channel was just no longer visible. The evolution of the plasma channel starts within femtoseconds, as seen in other experiments [82, 83, 84] or later on in the results of this campaign. Laser intensities of about $10^{14} - 10^{15}$ W/cm^2 are needed for the ionisation, as discussed before.

The ionisation rate and therefore the duration of the process can be calculated by means of the formulas presented in [85]. The ionisation process of the neutral Hydrogen and Helium starts within the interaction of the laser pulse with the gas, that means on a femtosecond scale. In order to fully ionise He^+ to He^{++} a bit more time is needed. It takes about 50 fs with a laser intensity of $I_L = 5 \cdot 10^{15}\,W/cm^2$, 350 fs with $I_L = 4 \cdot 10^{15}\,W/cm^2$ and about 2 ps with $I_L = 3 \cdot 10^{15}\,W/cm^2$. If the laser contrast of this low energy Driver is considered, the shoulder of the peak, highlighted in figure 4.26, will have an intensity of about $10^{15}\,W/cm^2$ 500 fs before, which is in the scope of the temporal scan. A gas ionisation and creation of a plasma channel can occur only in this time range. Hence, the beams were timed with an adequate precision for these experimental campaigns.

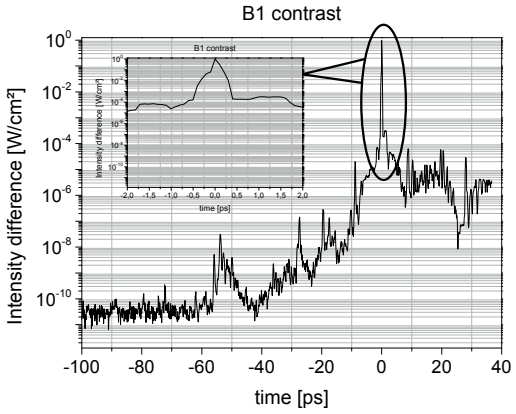

Figure 4.26: The temporal Driver laser contrast and a magnification of the peak.

4.8.5 Further experimental setups

In addition to the already described setups, two more major measurements were performed in the f/10 Heater beam configuration: Optical probing and charged particle probing.

For further investigations of the interaction of the Heater beam with the gas target, ***beam 1*** was used as an ***optical diagnostic probe beam*** for interferometry and shadowgraphy (see section 4.3). This setup is shown in figure 4.27, plot (a). The beam was guided to the tcc without any focusing optic. The OAP was changed with a mirror to have a homogenous laser beam with a beam diameter of several centimeters. The temporal overlap was achieved by using the ionisation method described before by means of the shadowgraphy diagnostic. The Heater was moved in time until no plasma channel was visible in the gas jet. Furthermore, ***optical shadowgraphy*** of the Driver interaction was performed by means of the ARCTURUS ***probe beam***, see plot(b).

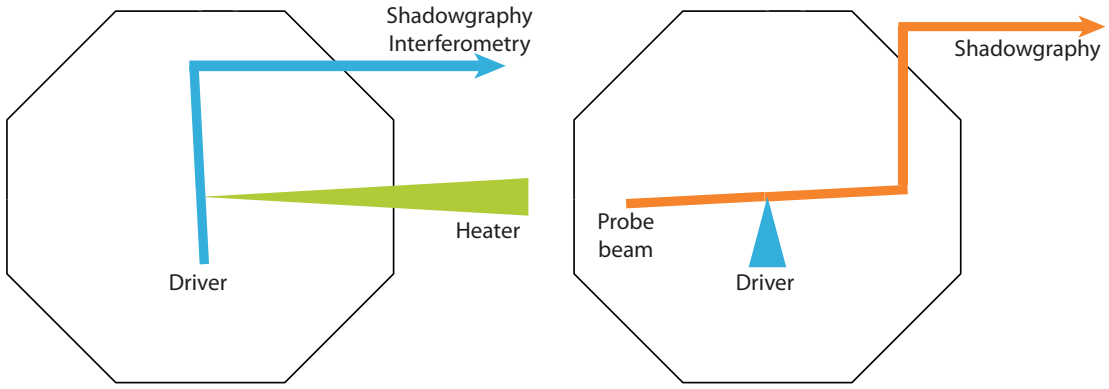

(a) Optical probing of the Heater (b) Optical probing of the Driver

Figure 4.27: Sketch of the first modification of the f/10 OAP setup. Plot (a): Beam 1 is used as optical diagnostic beam, while the Heater beam is still focused by the dielectric f/10 OAP into the gas target. Interferometry and shadowgraphy of the laser plasma interaction were employed as main diagnostics. Plot (b): Shadowgraphy of the Driver beam interaction was performed by means of the optical probe beam.

Furthermore, the interaction of the Heater with the plasma was studied by ***charged particle probing*** (see section 4.5). Therefore, ***beam 1*** was used to accelerate protons from a solid target in order to probe the plasma. These deflected protons were detected by a stack of radiochromic films. A 10 μm thin gold foil has turned out to be the best target for the interaction (highest proton energy and highest flux). A sketch of this setup is presented in figure 4.28. Two beams were timed inside the gas target, as described above. Afterwards, beam 1 was shifted a few millimeters away from the nozzle to hit the solid target, in order to have the ability to align the target without restrictions and to control the time-of-flight of the protons. Consequently, the timing between the laser beams is shifted in a range of a picosecond, which can however be neglected as small time uncertainty.

The probe source creates a proton bunch with a broad energy distribution. In each RCF layer a specific proton energy is stopped due to the Bragg-peak, as described in section 4.4. The time-of-flight of the protons can be calculated by knowing the proton energy, which is stopped in the specific stack layer. Therefore, the time of the charged particle probing related to the laser beam timing is known. Each film layer represents accordingly a different time of the laser plasma interaction. Moreover, the gold target was rotated 20° with respect to the Driver in order to have a time resolution in more

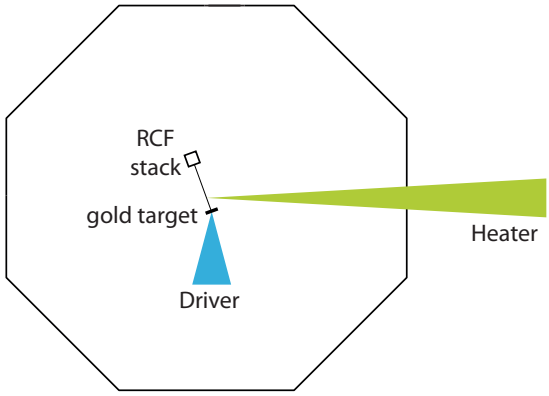

Figure 4.28: Sketch of the second modification of the f/10 OAP setup. Beam 1 is used to accelerate charged particles for proton probing, while the Heater beam is still focused by the dielectric f/10 OAP into the gas target. Beam 1 is focused with an f/2 gold coated OAP onto a solid target. Accelerated protons are deflected inside the interaction area and were detected by a stack of radiochromic films.

than one dimension. Compare figure 4.29 for an illustration of the 20° alignment. The central distance from the gold target to the centre of the nozzle is assumed to be fixed. If the different times-of-flight are normalised to that length, the most sidewise deflected particles will require a time delay of about 40 to 90 ps, depending on the proton energy. Instead, the vertical time delays are not much affecting the time resolution. The created plasma channel, detected by the RCF films, is on the source plane less than a millimeter wide, but more than 4 mm long, which shows the importance of the knowledge of the horizontal time delay. The different time delays are shown in the graphs in figure 4.30 for two line-outs: One in the horizontal x direction in the tcc height and one in the vertical y direction above the centre of the nozzle. Each line or rather each energy represents the protons, which are stopped in every single RCF layer. If the solid target would be centered and parallel aligned to the plasma channel, the time delay of each proton ray will be in the range of the vertical line out. This corresponds to a delay of 15 to 30 ps in a distance of 3 of the nozzle centre, which can be neglected, while investigating the actual plasma channel inside the gas jet. Figure 4.31 shows an overlay of a 3D image of the calculated normalised traveling time (see colourbar) of protons of 3.27 MeV (second RCF stack layer) and the corresponding exposed radiochromic film. The white shadow from the centre to the bottom is the nozzle, while a plasma channel can be seen above.

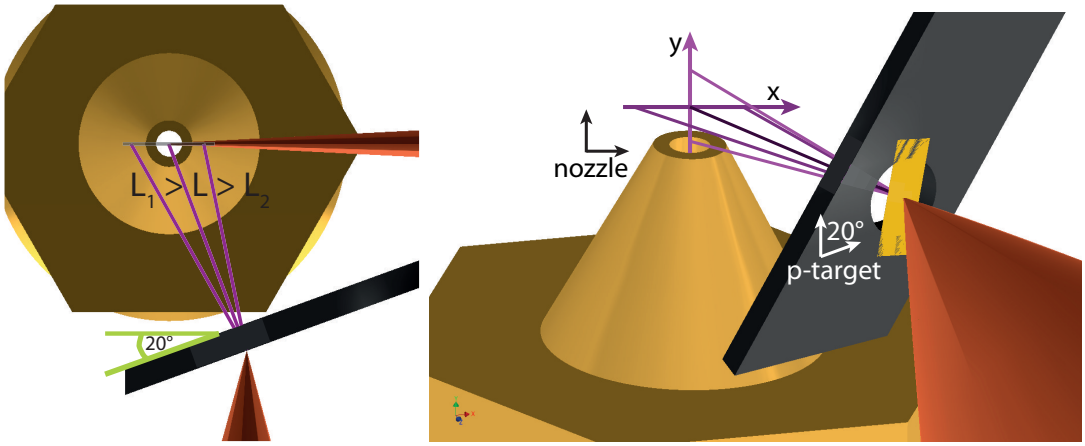

(a) Top view of PP setup (b) Side view of PP setup

Figure 4.29: Top view and side view of the proton probing setup. A time resolution for protons with the same energy is reached due to the 20° angle of the solid target. The time-of-flight for one single proton will be drastically longer, if it is reflected on the left side of the target. This means L_1>L>L_2 correspond to t_1>t>t_2.

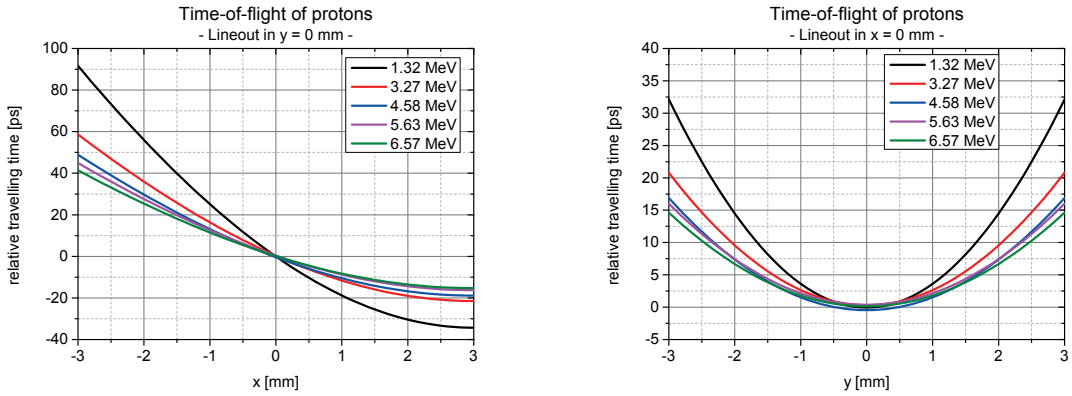

(a) X direction (b) Y direction

Figure 4.30: Evolution of the time-of-fligth of protons in x direction (a) and y direction (b). In order to have a time resolution in more than one dimension, the solid target was rotated. The graphs are normalised to the central ray of protons. Each line represents one proton energy, which is stopped in one RCF layer. Figure (a) represents a horizontal line-out at the tcc height and (b) depicts a vertical line-out in the centre of the nozzle.

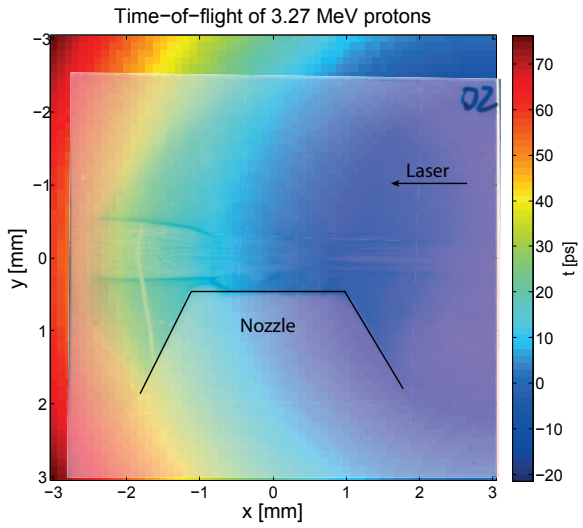

Figure 4.31: A 2D contour plot of the normalised traveling time (see colourbar) of 3.27 MeV protons is shown together with a sample radiochromic film. The white big shadow is caused by the gas nozzle. A plasma channel can be seen above.

Chapter 5

Ion acceleration via Coulomb explosion in underdense targets

In this chapter, the interaction of the Heater beam, as named before, focused by an f/10 OAP to an intensity of $2.4 \cdot 10^{19}\,\mathrm{W/cm^2}$, with a Hydrogen or Helium gas target (setup in figure 4.23) was investigated in detail. During the interaction, electrons were radially pushed away from the laser axis due to ponderomotive channeling and self-focusing effects by the laser beam. A non-neutral channel evacuated of electrons was created. Consequently, the ions were radially expelled and accelerated outwards in the transverse direction by their own space-charge field, which is called Coulomb explosion (CE).

Experimentally accelerated ions were detected in the transverse direction via Thomson parabola spectrometers. Target densities and the gas type, Helium or Hydrogen, were varied to fully optimise the interaction conditions. Furthermore, the physical concept of the acceleration mechanism was identified by numerical simulations, which reproduced well the experimental results. First insights into the particle distribution and electric and magnetic fields in the plasma area were given. Consequentially, the conditions for the nonlinear effects responsible for the CE and the necessary conditions for the CE, plus the maximum ion energies were calculated by means of analytical models.

Moreover, various diagnostics, electron spectrometer, optical probing and charge particle probing, were employed, which allowed a deep understanding of the physical processes at play. The electron acceleration by the Heater interaction at low target densities was investigated and discussed. Due to optical probing of the created plasma channel, the

evolution in longitudinal and transverse direction was analysed. Via charge particle probing, soliton structures were observed at the channel centre. These structures can explode and contribute to the low energy ion spectra.

5.1 Experimental results

Ions were accelerated along 0° and 10° (related to the Driver beam) by only the Heater (f/10) interacting with the gas target. The experimental setup can be seen in figure 4.23.

Figure 5.1 (a) shows the proton spectra of the best measurements, determined by the Thomson parabola along 0°. The protons were accelerated by the interaction of the f/10-Heater beam with the Hydrogen gas jet with different neutral densities. The spectral characteristics at different densities are almost similar. The background flux level is about $1.5 \cdot 10^8$ particles/sr/MeV. The minimum energy is related to the lower detection limit of the Thomson parabola. The maximum cut-off energy for each pressure is approximately 230 keV. Only at a low density ($0.019\,n_c$) a cut-off energy of about 310 keV is reached, which was an exception. Furthermore, the acceleration vanished at high densities (above $0.121\,n_c$), no protons were measured above this value. Protons were detected by the 10° Thomson parabola spectrometer for the whole density range, as visible in plot (b) and in the comparison between single and double beam configuration. The maximum cut-off energies were about half the value of the 0° TP.

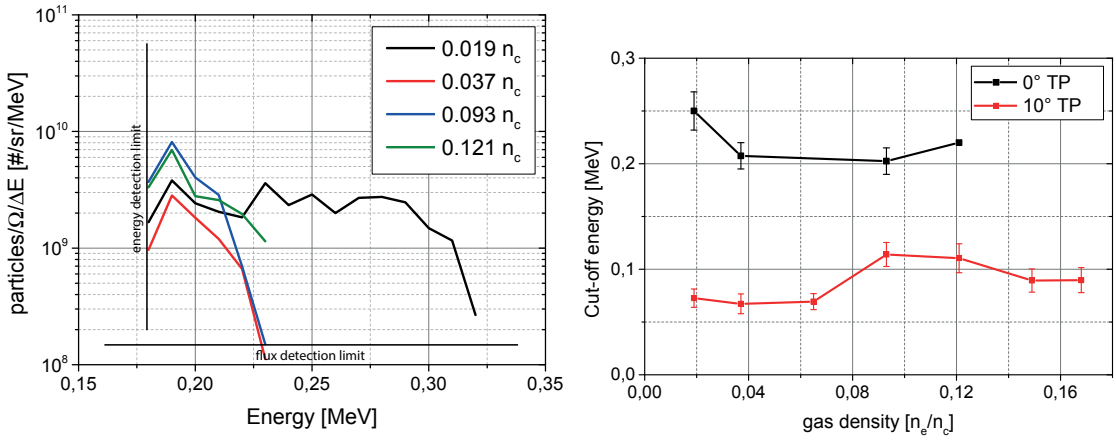

(a) Proton energy spectra

(b) Cut-off energies

Figure 5.1: Graph (a): Proton energy spectra for different neutral target densities in the single beam configuration, detected by the 0° Thomson parabola. The protons are accelerated transverse to the beam axis. Plot (b): Maximum cut-off energies of the protons detected by the 0° (black) and 10° (red) spectrometer.

The energy spectra, detected by the 0° Thomson parabola, of the accelerated He^+ ions can be seen in figure 5.2 (a). Particles were accelerated over the whole variety of possible target densities. Maximum energies of about 200 to 300 keV were achieved. Only at a very low target density ($0.012\,n_c$) and a very high density ($0.12\,n_c$) the maximum energy is low, circa 125 keV. Plot (b) shows the He^{++} energy spectra. He^{++} was only detected at high densities, like $0.084\,n_c$ or higher. The flux is more than 10 times lower, compared to the He^+ case, and the maximum achieved energies are about 250 keV. The minimum energy is limited to 210 keV due to the Thomson parabola configuration. Whereas, the 10° Thomson parabola was built in a way to detect very low ions. Here, He^+ and He^{++} were identified from a low target density on. This can be seen in graph (c), which illustrates the maximum cut-off energies versus target densities for the 0° and 10° detection angle. Besides, no ions were detected at target densities above $0.12\,n_c$.

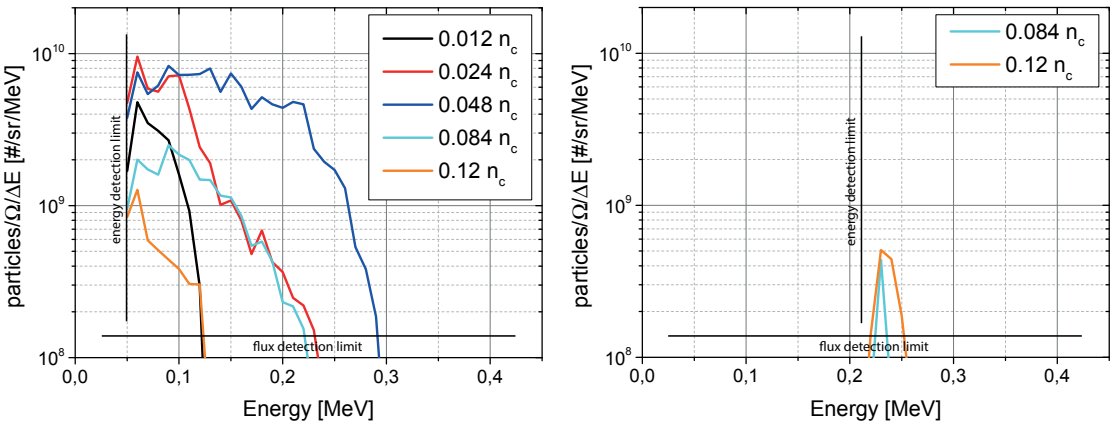

(a) He^{+} energy spectra

(b) He^{++} energy spectra

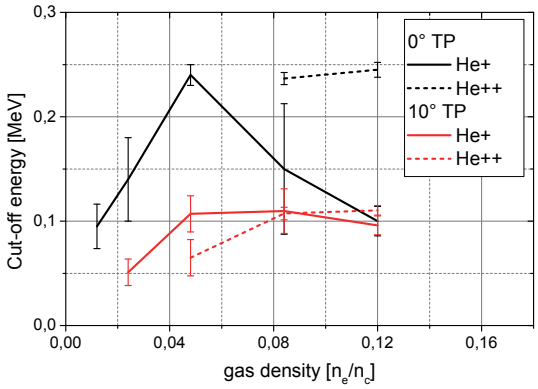

(c) Cut-off energies

Figure 5.2: He^{+}, graph (a) and He^{++}, graph (b) ion energy spectra of the 0° Thomson parabola for different target densities. Graph (c) shows the maximum cut-off energies for different target densities detected by the 0° and 10° TP spectrometer.

5.2 Numerical simulations

T. Liseykina of the university of Rostock provided ***2D PIC simulations*** of the Heater beam's interaction with the gas target. By means of the simulation results a first insight into the laser propagation, density and field distributions and acceleration of particles at different observation times can be investigated. In a *Particle-In-Cell* (PIC) code computational particles and electromagnetic fields are discretised in a grid representing a collisionless plasma. By means of this particle-grid numerical method the particle density can be calculated at every grid point by reconstructing the particle location and velocity, which leads to the electromagnetic fields accelerating the charged particles [86].

The advanced *Particle-in-Cell code UMKA* was employed. This code is operated by different numerical algorithms such as the Yee Cartesian lattice to calculate the electromagnetic fields, the Boris pusher to integrate the Lorentz force and the current reconstruction scheme to satisfy the continuity equation, as described in [87, 88]. The UMKA code has often been applied to compare experimental results or analytical models, see [89, 90, 91, 92, 93].

The experimental laser parameters were used as input for the UMKA code: $d_0 = 12\,\mu$m (FWHM), $\lambda = 800\,\mu$m, $\tau = 30\,$fs, $I_\mathrm{L} \approx 2.4 \cdot 10^{19}\,\mathrm{W/cm^2}$ ($a_0 = 3.4$) and p-polarization. All x and y dimensions are in the unit of λ. All time steps are in the unit of one laser cycle T, which is T $\approx 2.6\,$fs. The density profile of the gas was reduced in size in order to save computational time as illustrated in figure 5.3 with two 150 λ long edges on both sides adopted to a $\sin^2$ fit and a constant central density of a length of 300 λ. The density of the profile is normalised to the maximum target density.

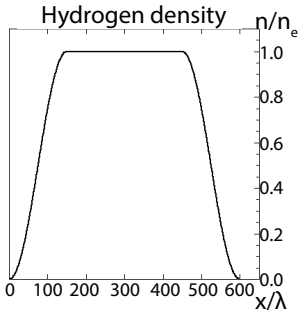

Figure 5.3: Gas density profile normalised to the maximum target density for the PIC simulations.

The simulations investigated an exemplary Hydrogen target with a density of $n_e = 9.9 \cdot 10^{19}\,\mathrm{cm^{-3}} \approx 0.056\,n_\mathrm{c}$. First of all, the laser intensity inside the plasma was observed in six different time steps, visible in figure 5.4. The intensity was plotted in logarithmic scale ($\lg(I/I_0)$)

and colour blue represents the vacuum intensity, while dark black illustrates an intensity enhancement. The black circles in $t = 120\,\mathrm{T} = 312\,\mathrm{fs}$ up to $t = 210\,\mathrm{T} = 546\,\mathrm{fs}$ highlight self-focusing effects with an increase of $\lg(I/I_0) = 0.5$, which corresponds to $I = 3I_0$. At $t = 300\,\mathrm{T} = 780\,\mathrm{fs}$ the laser pulse has nearly reached the centre of the nozzle at $x = 300\,\lambda = 240\,\mu\mathrm{m}$ and is depleted inside the plasma with a loss of almost its initial intensity.

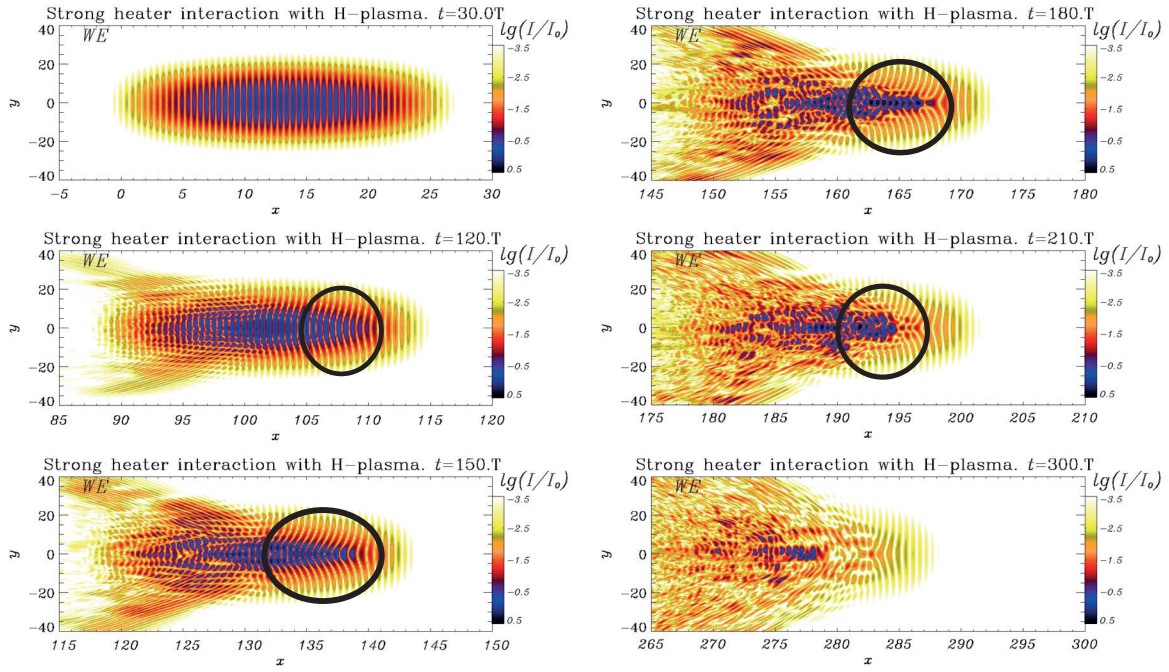

Figure 5.4: Laser intensity distribution inside the plasma from PIC simulations at different observation times.

Figure 5.5 shows two simulation results at times $t = 570\,\mathrm{T} = 1.482\,\mathrm{ps}$ (left) and $t = 810\,\mathrm{T} = 2.106\,\mathrm{ps}$ (right) of the ion density (top of each images) and electron density (bottom of each image). The colour scale is adopted to the units of $n_\mathrm{e}/n_\mathrm{c}$. A formation of a partly evacuated density channel along the laser axis can be observed. Electrons and consequently ions are expelled in the transverse direction, due to the ponderomotive channeling and self-focusing effects. Therefore, the plasma density inside the channel is lower compared to the density of the surrounding plasma. At the channel edges the density is more than a factor three higher than the density at the channel axis. The channel walls of the electron density distribution are less sharp than the walls of the ion distribution, because of vacuum heating effects at the edges. In addition, the channel width is slowly growing during 624 fs between the images, from about $25\,\mu\mathrm{m}$ to $35\,\mu\mathrm{m}$.

In the centre of the plasma ($x = 300\,\lambda = 240\,\mu$m), the laser beam is dispersed as seen in figure 5.4. Thus, the channel structure in the density distribution slowly vanishes in the longitudinal direction by a decreasing width.

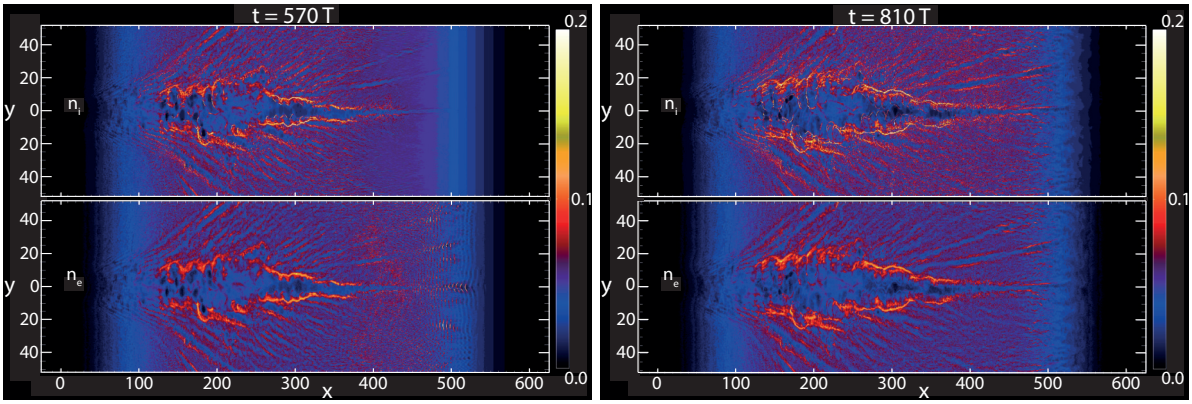

Figure 5.5: Channel ion (top) and electron (bottom) density distribution of PIC simulations at two different times of $t = 570\,\mathrm{T} = 1.482\,\mathrm{ps}$ (left) and $t = 810\,\mathrm{T} = 2.106\,\mathrm{ps}$ (right).

The electric (top) and magnetic (bottom) field distributions are illustrated in figure 5.6 for the same two simulation run times as before ($t = 570\,\mathrm{T} = 1.482\,\mathrm{ps}$ (left) and $t = 810\,\mathrm{T} = 2.106\,\mathrm{ps}$ (right). The channel edges are supported by electrical fields of the charged particles. In addition bubble-like field structures, especially at $t = 570\,\mathrm{T} = 1.482\,\mathrm{ps}$, can be recognised at about $x = 220\,\lambda$. Furthermore a quasistatic magnetic field is built up around the laser axis inside the channel, which exists over the whole time period. The channel and field structures were also simulated for the interaction of a Petawatt laser with an underdense gas target slab in [89, 94, 95].

The next step was to analyse the proton acceleration due to the fields inside the plasma. The phase space plots are pictured in figure 5.7. The longitudinal acceleration in the x-direction (top) and the transverse acceleration (bottom) in the y-direction were investigated. The integrated kinetic energy $E(P)$ of the ions, normalised to $m_\mathrm{i}c$, is plotted versus x for the two different times of the plasma evolution ($t = 570\,\mathrm{T} = 1.482\,\mathrm{ps}$ (left) and $t = 810\,\mathrm{T} = 2.106\,\mathrm{ps}$ (right)). The colour scale is set to be logarithmic of the particle density f_i, which is proportional to the number of particles in the interval $[\Delta x, \Delta P]$. The sharpest edges in the density and electric fields are visible in the centre of the nozzle, around $x = 300\,\lambda$. This indicates a radial acceleration of protons in this area, which can be seen in strong modulations in the transverse ion momentum distribution.

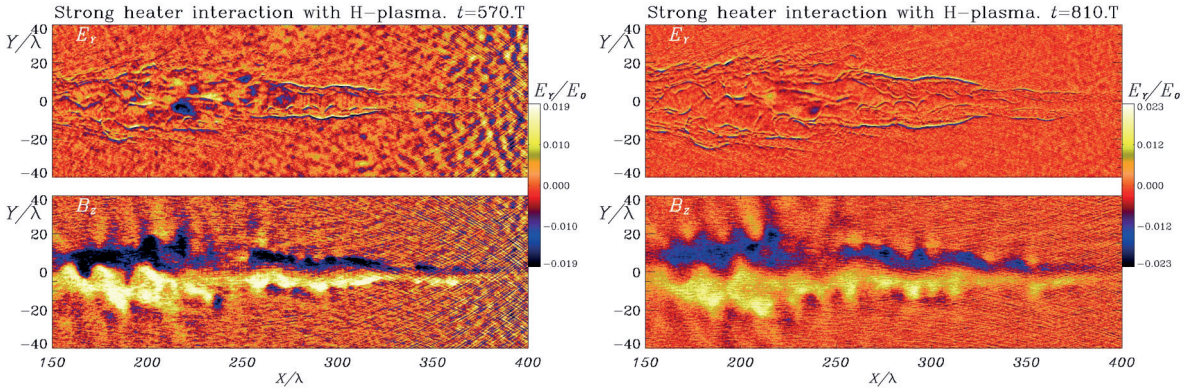

Figure 5.6: Electric field (top) and magnetic field (bottom) distribution in the plasma at two different time steps, $t = 570\,\mathrm{T} = 1.482\,\mathrm{ps}$ (left) and $t = 810\,\mathrm{T} = 2.106\,\mathrm{ps}$ (right).

Two local spikes at the beginning ($x = 0\,\lambda$) and at the end ($x = 600\,\lambda$) of the plasma are distinguishable in the longitudinal phase space plots, which occurred due to fast escaping electrons from the low density plasma/gas edges. The forward acceleration, originating from the central part of the plasma, is weaker in energy compared to the transverse acceleration.

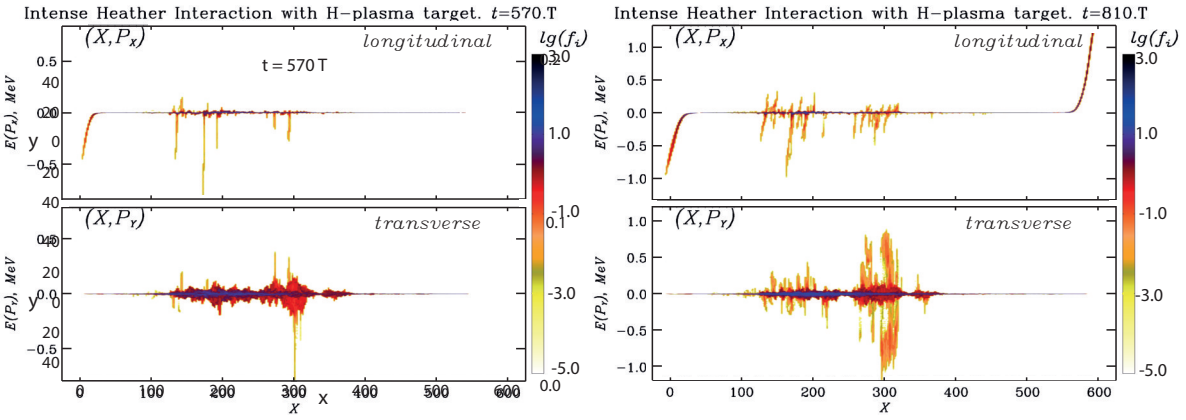

Figure 5.7: Proton phase space plots normalised to $m_\mathrm{i}c$ for the longitudinal (top) and transverse (bottom) distribution.

The ion spectra calculated by means of the phase space plot at $t = 810\,\mathrm{T} = 2.106\,\mathrm{ps}$ are illustrated in figure 5.8. The red line represents the spectrum of the longitudinal accelerated particles, while the green line represents the particles accelerated in the transverse direction. The particle number is normalised to the energy in keV. Particles accelerated in forward direction reach energies of about 200 keV to 300 keV. However, the particles accelerated in the transverse direction gain higher energies up to about 850 keV with a plateau in the particle flux. These energies are more than twice as high as the energy of the forward accelerated particles. A spectrum of all particles accelerated in every direction is illustrated by the black curve. Some ions are accelerated up to about 1.2 MeV, but the flux in the high energy area, however, is low.

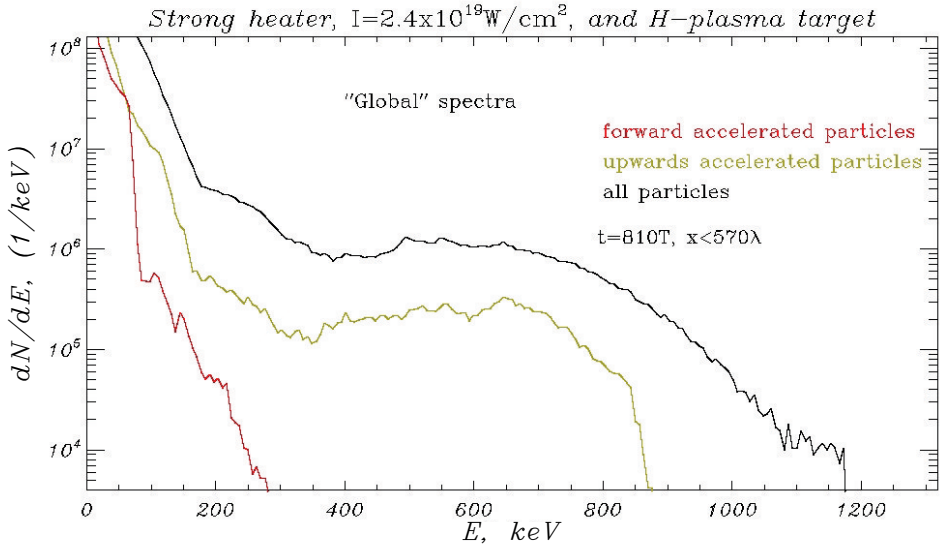

Figure 5.8: Energy spectra of the protons accelerated in longitudinal (red) and transverse (green) direction and the global spectrum of all particles in black.

Finally, the simulation results fit well with the experimental results. The particle flux is in the order of the experimentally evaluated proton flux (Simulation: $10^5\,1/\mathrm{keV}$, in comparison to the experiment: $10^5\,1/\mathrm{keV} = 10^{11}\,\#/\mathrm{sr/keV}$). The calculated energies are in the order of the experimental energies, but slightly higher, because of the 2D calculations. If, in the experiment, there have been particles accelerated in the longitudinal direction, their energies would have been even smaller than the calculated energies (red curve). In addition the particles number is fast decreasing. This two facts lead to no experimental observation of particles in the longitudinal direction.

Another simulation was performed with a higher intensity Heater beam with $I_L = 1.5 \cdot 2.4 \cdot 10^{19}\,\mathrm{W/cm^2}$, see figure 5.9. The channel density distribution, picture (a), shows a channel with really parallel high density walls at the edges, which leads to a better acceleration in the transverse direction, in comparison to a slightly weaker Heater laser beam in figure 5.5. The evacuation of the plasma channel is a bit stronger and more pronounced. The electric field distribution, plot (b), illustrates a similar field distribution in transverse y-direction (top image), while a very weak sheath field around $x = 600\,\lambda$ can be seen in longitudinal x-direction (bottom image). This sheath field accelerates protons in the longitudinal direction, as illustrated in the top phase space plots of picture (c). This sheath field is built up at late interaction times, later than $t = 626\,\mathrm{T} = 1.628\,\mathrm{ps}$. The phase space plots in the longitudinal direction are similar in strength and structure compared to the plots in figure 5.7 of the weaker Heater beam. The transverse acceleration (bottom images) is much stronger up to an ion momentum of 2 MeV. These phenomena lead to a stronger acceleration of protons in the transverse direction, see plot (d). Ions to about 2 MeV energy are accelerated.

A laser intensity enhancement with a factor of 1.5 doubles the energy of the transverse accelerated protons. Stronger electric fields at the channel edge lead to a stronger Coulomb explosion. As already mentioned, however, not only the fields are stronger, but also the channel structure is different. The channel edges in the first simulation are cloudy and not sharp at $x < 300\,\lambda$. Instead, the channel created by the interaction of the slightly stronger Heater has nearly straight boundaries at the channel edges, even from $x = 150\,\lambda$ onwards.

As a conclusion, there are two big differences when the Heater intensity is changed: The field strength and the field structure. These changes affect only the transverse acceleration, whereas the longitudinal proton acceleration is not affected by the Heater intensity. The interaction of a laser with the same focal characteristics with the same gas target, but with a higher intensity, will lead to higher ion energies, which can be seen in the previous experiments at the VULCAN laser.

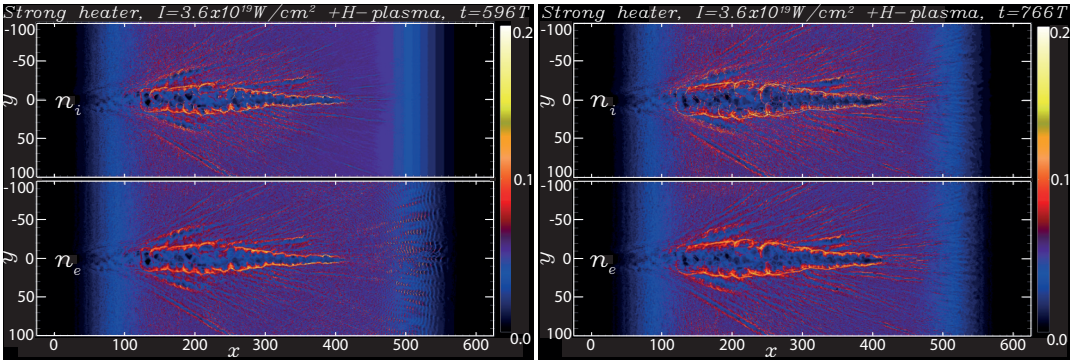

(a) Channel density distribution

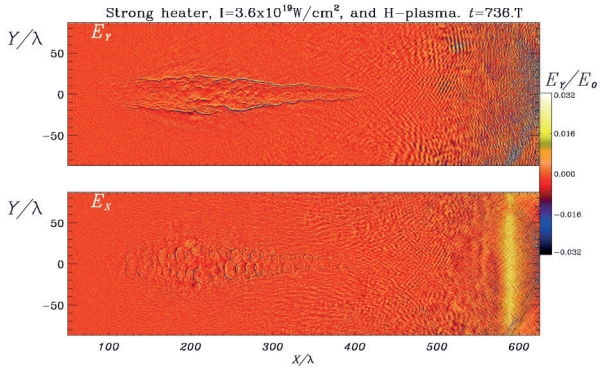

(b) Electric field distribution

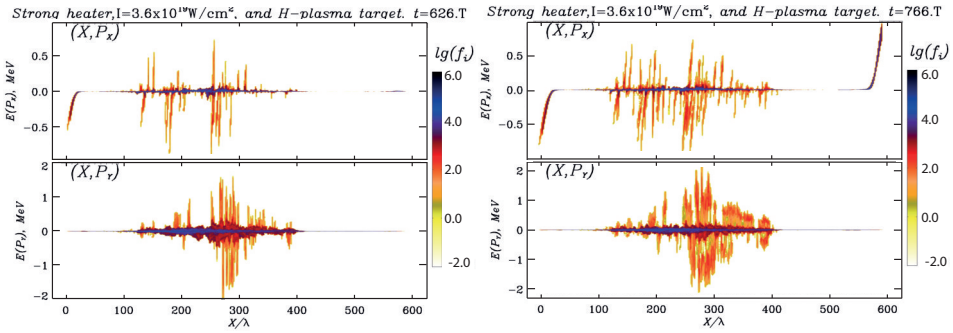

(c) Proton phase space plots

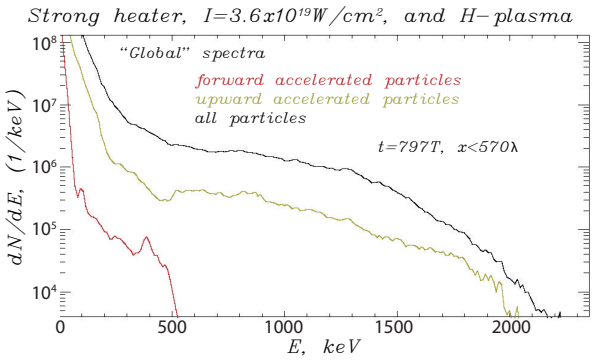

(d) Proton spectra

Figure 5.9: Results of PIC simulations with a stronger Heater intensity.

5.3 Analytical discussion

The ions were accelerated in the transverse direction from the laser axis. Different laser and plasma parameters were scanned for a detailed investigation and in addition numerical simulations recreated the experimental conditions. Mostly electrons were accelerated in the longitudinal direction, as discussed later in this chapter. Presumably, only a very weak space-charge field (created by the electrons) has acted on the ions, because the highest energy electrons have left the plasma before and the flux was too low, as discussed in the simulation results.

In order to explain the experimental and simulated observations, like the transverse acceleration of ions, the self-focusing effects and the field distributions different, analytical calculations and assumptions can be made. The following discussion starts with the analysis of non-linear effects and ends with a model of Coulomb explosion.

The requirements for several non-linear effects, as discussed in subsection 2.3.2, were fulfilled in the experimental conditions. The threshold for the filamentation (equation 2.39) was exceeded by the laser intensity in the f/10 OAP configuration, which is dependent on the hot electron temperature (equation 2.41), the plasma length (1 mm) and a certain target density. The calculated thresholds are listed in table 5.1.

		target density	min	max
		n_e [cm^{-3}]	$1.6 \cdot 10^{19}$	$3.92 \cdot 10^{20}$
		n_e/n_c	0.009	0.228
I_L [W/cm^2]	$2.4 \cdot 10^{19}$	I_p [W/cm^2]	$3.4 \cdot 10^{17}$	$1.39 \cdot 10^{16}$
		$\tau\omega_p$	6.78	33.56
P_L [TW]	26.88	P_c [TW]	1.88	0.08

Table 5.1: Thresholds for non-linear effects in the laser plasma interaction.

Ponderomotive channeling and self-focusing can affect the laser propagation inside the plasma, as well. The requirement for ponderomotive channeling ($\tau\omega_P \gg 1$) was fulfilled, as well as the requirement for self-focusing $P_L > P_c$ or $P_L/P_c > 1$ for the whole target density range, as calculated in table 5.1. Therefore, the laser beam was even more focused to a smaller spot size and higher intensity when passing through the gas jet. Figure 5.10 illustrates the development of the relation between the vacuum laser power

and critical power on the dependence of the nozzle size (plot (a)) and the target density range (plot (b)). It was calculated using the equation 2.37 and by means of the density profiles of figure 3.15 for 30 and 70 bar. The profile of the black curve in graph (a) is calculated with the density profile of 70 bar alias $0.131\,n_c$ and the red curve is for a target pressure of 30 bar alias $0.056\,n_c$. P_L starts to be significantly larger than P_c at a distance of 700 μm from the nozzle centre for the higher density curve and at a distance of 600 μm for the lower density curve. At these points the condition for self-focusing is fulfilled. Maximum values of about $P_L = 180P_c$ and $P_L = 100P_c$ are reached. This calculation is not completely accurate, but gives an approach of the dependence of the two parameters. The laser power inside the gas jet will be reduced, because the laser looses part of its energy during the interaction with the target. Nevertheless, the condition for self-focusing will still be fulfilled, even with a critical power of some TW, instead of the full laser power. Graph (b) shows the evolution of the power relation per target density. The dashed line represents the evolution with the assumption of a reduced laser power to half of its value, and still, the self-focusing condition is fulfilled.

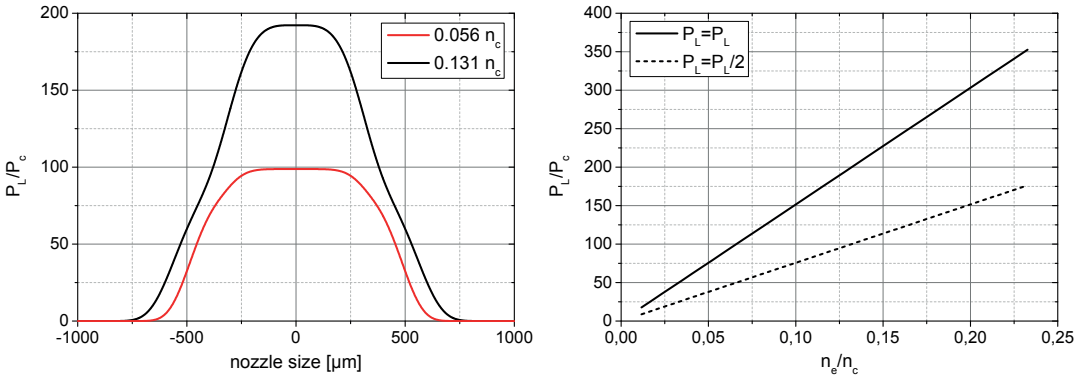

(a) P_L/P_c-relation per target profile

(b) P_L/P_c-relation per target density

Figure 5.10: Relation between laser power and critical power. If the laser power exceeds the critical power the condition for self-focusing effects is fulfilled. P_c is dependent on the target density, which has a certain profile along the nozzle opening. The relation is calculated for two different density line-outs in graph (a). The red curve represents a target density of $0.056\,n_c$ (H_2, 30 bar) and the black one a target density of $0.131\,n_c$ (H_2, 70 bar). Graph (b) illustrates the power evolution for the whole target density range.

Based on the fact, that the condition for self-focusing is fulfilled and an evacuated channel is assumed, the evolution of the normalised vector potential and the focal spot radius

in the self-focusing case can be roughly calculated by means of equation 2.38. Figure 5.11 shows the relation of the two values per target density. While the vector potential (red) is increasing with target density the focal spot radius (green) is decreasing. The dashed curves represents the calculations for a reduced laser power to half of its value, which might be even an underestimated value. However, the vector potential is still higher than the vacuum value of $a_0 = 3.3$. The focal spot radius is as well smaller than the vacuum spot size ($r_0 = 6\,\mu$m) over the whole density range.

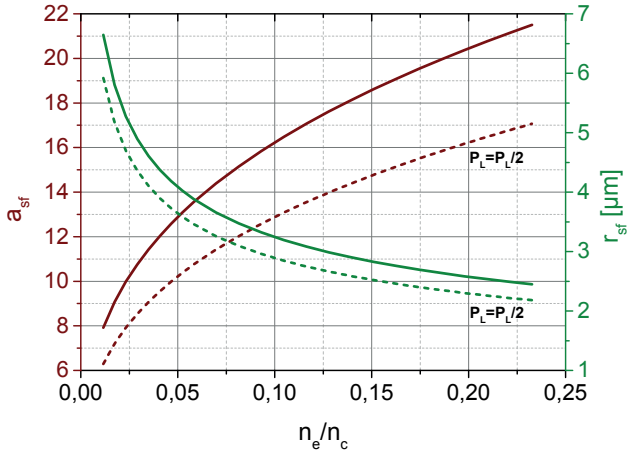

Figure 5.11: Evolution of the normalised vector potential (red) and focal spot radius (green) during self-focusing per target density. The dashed lines represents the trends calculated with half of the vacuum laser power. While the vector potential is increasing, the focal spot size is decreasing.

Self-focusing and ponderomotive channeling will lead to a transverse expulsion of the electrons due to the radial ponderomotive force. Ions on the other hand will be accelerated in the same direction by their own space-charge field due to the complete evacuation of electrons on the laser axis. The process is called Coulomb explosion. In order to reach this regime, the conditions: $\omega_0 > \omega_\mathrm{p}$, $\tau > 1/\omega_\mathrm{p}$ and $c\tau > r_0$ have to be fulfilled, as discussed in subsection 2.4.2 and summarised in table 5.2. The laser frequency $\omega_0 = 2.35 \cdot 10^{15}\,$Hz is larger than the plasma frequency and the laser pulse length $\tau = 30\,$fs is also longer than the electron response time for all target densities. The spatial plasma scale (width of the plasma channel) and the laser intensity scale are larger than the laser wavelength $\lambda = 0.8\,\mu$m. Hence, these conditions are satisfied and the electron response can be averaged over the laser pulse period. The radial ponderomotive force acts as leading effect on the electrons. In addition, the pulse length

$c\tau = 8.99\,\mu$m is larger than the pulse radius, which is even reduced due to the self-focusing. Therefore, ions are accelerated transverse to the laser axis due to evacuation of the electrons resulting in a strong space charge field.

As discussed in subsection 2.4.2, the electrons are radially expelled, if the force of the electric field in the depleted area is smaller than radial ponderomotive force. This condition results in the threshold for a_0 (see equation 2.45), which is in the range of $a_0 = [10 - 248]$, depending on the target density. These values are above the vacuum $a_0 = 3.3$. However, considering a reduction of the focal spot size ($r_0 = 6\,\mu$m) by 1/4 due to self-focusing effects to $r_{0\mathrm{sf}} = 4.5\,\mu$m, the minimum vector potential is already reduced to $a_0 = [6 - 140]$. According to [27] a complete electron expulsion can still take place at lower intensities than calculated by the equation. This threshold is a rough estimation via a 1D analytical model. *Macchi et al.* have presented in [27] also results of numerical simulations, which are more valid for the intensity threshold of a_0. Figure 5.12 shows the relation between the intensity threshold and $n_\mathrm{e} r_0^2$. The white diamonds describe the so-called ponderomotive regime with no complete electron depletion along the central axis. The ions are accelerated due to a force proportional to the ponderomotive force, which is almost exactly balanced with the attractive electrostatic field. The black diamonds indicate the fully evacuated channel, where ions are accelerated due to their own space charge field in the Coulomb explosion regime. Here the ponderomotive force exceeds the electric force of the depleted area. Gray markers represent a near-threshold data set, where the electron depletion appears only near the laser axis and the condition $F_\mathrm{P} > eE_\mathrm{D}$ is mostly fulfilled. The data points "a" and "b" have similar a_0 and $n_\mathrm{e} r_0^2$ values, but the laser pulse duration in case "b" is about two times the pulse duration of simulation "a". The electron evacuation in "b" is much stronger than in "a", which shows an important dependence on the variation of the laser parameters. The solid line shows the threshold calculated by the 1D equation 2.45, which is close to the transition region between the ponderomotive and Coulomb explosion regime. The red arrow indicates the target density of this experimental campaign in a height of the vacuum $a_0 = 3.3$. At least for a wide density range, the plasma channel is fully depleted of electrons and Coulomb explosion is the dominating acceleration mechanism.

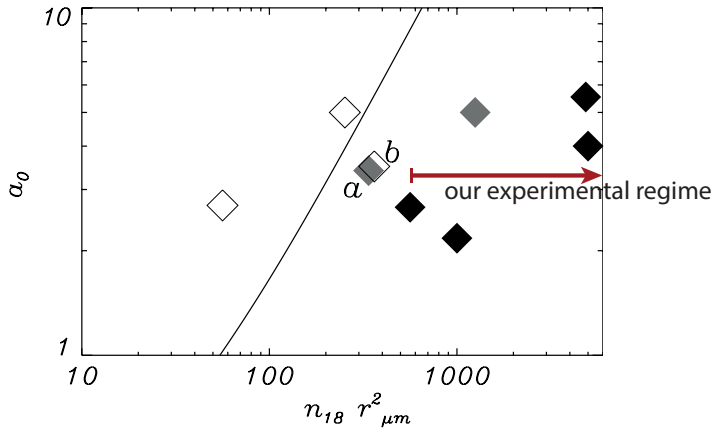

Figure 5.12: Laser intensity in terms of a_0 as a function of $n_e r_0^2$. White diamonds represents regions with no complete electron depletion, while the channel is fully evacuated of electrons in the black diamonds data points. There will be Coulomb explosion, while the region with the white markers will be in the ponderomotive regime. Gray diamonds depict the near-threshold regime, where the channel is not completely depleted, but the ponderomotive force is still bigger than the electrostatic force. The data points "a" and "b" have similar values, but the laser pulse duration in "b" is about two times the pulse duration of simulation "a". The red arrow corresponds to the intensity and density values of this experimental campaign. (Figure 5 of [27])

A summary of the conditions and their values is presented in table 5.2 for the minimum and maximum target density.

		target density	min	max
		n_e [cm^{-3}]	$1.6 \cdot 10^{19}$	$3.92 \cdot 10^{20}$
		n_e/n_c	0.009	0.228
ω_0 [Hz]	$2.35 \cdot 10^{15}$	ω_p [Hz]	$2.26 \cdot 10^{14}$	$1.12 \cdot 10^{15}$
τ [fs]	30	$1/\omega_p$ [fs]	4.42	0.9
$c\tau$ [μm]	8.99	r_0 [μm]	6	
a_0	3.3	a_{0max}(1D)	10	248

Table 5.2: Different conditions, which have to be fulfilled in order to accelerate ions due to Coulomb explosion at the minimum and maximum target density.

The ion displacement Δx_i and the time they need to dislocate Δt_i (equation 2.46) can be calculated by assuming a plasma channel radius r_c, smaller than the focal spot radius. Ions are pushed 6 μm away from the channel axis in 0.186 ps, if a channel radius of 2 μm is considered. The maximum energy calculated by the theoretical models for Coulomb explosion (equations 2.48 and 2.49) is between 600 keV and 1.2 MeV for protons and He^+ ions, while it is twice the value, 1.2 MeV to 2.4 MeV, for He^{++} ions (dependence on $\sim Z$), see table 5.3. These energies are slightly overestimated by the model compared to the experimental cut-off energies, which is an acceptable accuracy. If the plasma channel is not completely evacuated and the regime is in the transition region between the ponderomotive and Coulomb explosion regime, the space charge field will be smaller and therefore the energy of the accelerated ions is decreased compared to the pure Coulomb explosion. The laser intensity threshold is more difficult to fulfill for higher target densities, which is visible in figure 5.12. The acceleration of protons and ions was reduced at a density of about $0.12\,n_c$, which can be seen in figure 5.1 and 5.2. This corresponds to the fact of an increasing a_0 threshold for Coulomb explosion. In addition, the laser pulse might not be able to propagate to the center of the dense target. A partly evacuated channel can be generated in the increasing density gradient at the beginning of the target. The origin of the ion acceleration can be shifted.

E_H [MeV]	0.6 - 1.2
E_{He^+} [MeV]	0.6 - 1.2
$E_{He^{++}}$ [MeV]	1.2 - 2.4

Table 5.3: The maximum cut-off energies of the Coulomb explosion mechanism for Hydrogen and Helium ions.

The reason for the appearance of He^{++} ions for high target densities only at the 0° detection angle, compare figure 5.2, can be explained by the experimental arrangement of the spectrometer. The lowest detectable energy of the He^{++} ions is about 200 keV, while at the same time the maximum cut-off energy of the spectrum is marginal higher at about 250 keV. He^{++} ions are very likely accelerated also for low densities, but not above the threshold, limited by the Thomson spectrometer configuration. The laser intensity is high enough to ionise the gas target completely ($I \geq 10^{16}\,W/cm^2$) and He^{++} ions have to recombine or undergo charge exchange at the plasma edge in order to become He^+ ions. The higher the target density, the higher is the probability to recombine by an one-electron-capture. Therefore, the flux of the He^{++} spectrum is lower compared

to the He^+ spectrum. The phenomena of no acceleration at very high densities (above $0.12\,n_c$), compare figure 6.4 can be also explained by this theory. The He^+ can even be neutralised at the plasma edge.

This analytical discussion explains the transverse ion acceleration, visible in the experimental and simulated results. The laser pulse undergoes several non-linear effects, as seen in the numerical simulations. Electrons are pushed radially outwards and an evacuated channel is created. Electric fields from the channel edges and the expelling force of the remaining ions leading to a Coulomb explosion and a transverse acceleration.

The results of Coulomb explosion demonstrated by *Krushelnik et al.* [11] and *Wei et al.* [12] are very similar to the results presented in this thesis. They used a different powerful laser (VULCAN), as described in section 2.5, with different pulse energy and pulse duration, which has an immediate effect on the acceleration strength and self-focusing effects. Therefore they observed ions up to a few MeV in 1999 and several MeV in 2004. *Lifschitz et al.* [14] and *Kahaly et al.* [34] used a laser system very similar to the ARCTURUS laser. However, most important to mention is their target density range, which is much lower than in this campaigns. The acceleration and cut-off energy for higher densities due to Coulomb explosion is comparable to the results described here. They claim to have an additional sheath field in the longitudinal direction, which is not strong enough to overcome the electric fields inside the channel, but to push the accelerated ions a bit in the forward direction, to be mostly detected at 80° of the laser axis instead of 90°. In the ARCTURUS campaign a strong acceleration exclusively in the transverse direction to the laser axis was observed. The maximum ion energy at a 10° angle was drastically decreased in contrast to the *Lifschitz* and *Kahaly* data.

5.4 Results of the complementary diagnostics

As mentioned earlier various diagnostics such as an electron spectrometer, optical or charge particle probing, were employed in addition to the Thomson parabola spectrometer. These diagnostics greatly help to get an insight into the interaction processes taking place. First, the longitudinal acceleration of electrons due to the Heater interacting with the gas target will be analysed. Only at low target densities, electrons were able to exit the plasma region. Secondly, the results of the optical probing technique will be discussed. The plasma channel evolution in longitudinal and transverse direction was studied. Furthermore a pre-formed channel generated by the pedestal level of the beam was discovered. Finally, a different study of the insight into the laser gas interaction will be presented via the charge particle probing technique. Soliton structures were identified, which can contribute to the ion energy spectra by their exploding nature. In the following subsections the results of each diagnostic and their major role for a better understanding of the acceleration process will be discussed in detail.

5.4.1 Electron acceleration by the Heater beam

Accelerated electrons were detected at low target densities along 90° with respect to the Driver beam or in the longitudinal direction to the Heater beam, as illustrated in figure 4.23. Figure 5.13 shows the best four electron energy spectra from Hydrogen gas as well as the corresponding raw images. The results of the two beam configuration of Driver and Heater interacting together with the plasma, are as well included in this analysis and are marked in black, while the Heater-only shots are marked in red. The results of two various target densities are illustrated. High electron energies up to 160 MeV were reached at the lowest density of $0.009\,n_c$ (dashed lines). After all, electron energies of about 40 to 60 MeV were achieved at a slightly higher density ($0.019\,n_c$, solid line). The maximum energy is similar in both laser beam configurations at the very low target density. At the higher density the double beam interaction seems to be more effective for the acceleration of higher energy electrons with a slightly higher flux.

The two best energy spectra of the accelerated electrons from the Helium gas target are shown in figure 5.14. The relative particle flux is the most obvious difference between the two electron spectra of Hydrogen and Helium gas. The flux is higher in the interaction

with the Helium gas target, which is already visible in the raw images of the electron spectra. The maximum energy of about 50 to 60 MeV is exactly between the maximum energies in the Hydrogen gas analysis. The target density seams to be the reason for this effect, because the lowest tunable Helium density was $0.012\,n_c$, which corresponds to a medium Hydrogen target density (necessary for an electron acceleration).

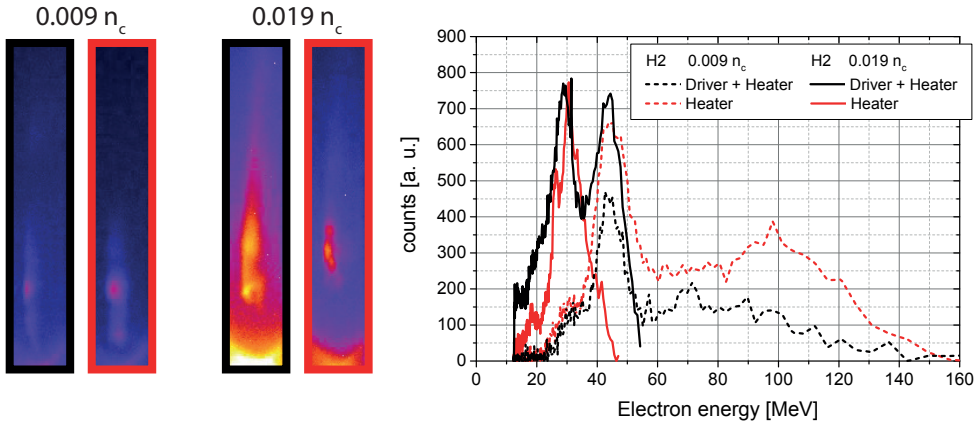

(a) Raw images (b) Electron spectra

Figure 5.13: Electron energy spectra from the interaction of the laser beams with a Hydrogen gas target. Signals detected during the double beam interaction are marked in black, while the Heater-only shots are marked in red. Image (a) shows the raw spectrometer images for two different target densities and the two laser configurations. Plot (b) illustrates the evaluated energy spectra. The dashed lines represents a very low target density of $0.009\,n_c$, while the solid lines display a density of $0.019\,n_c$. Lower target densities lead to higher cut-off energies.

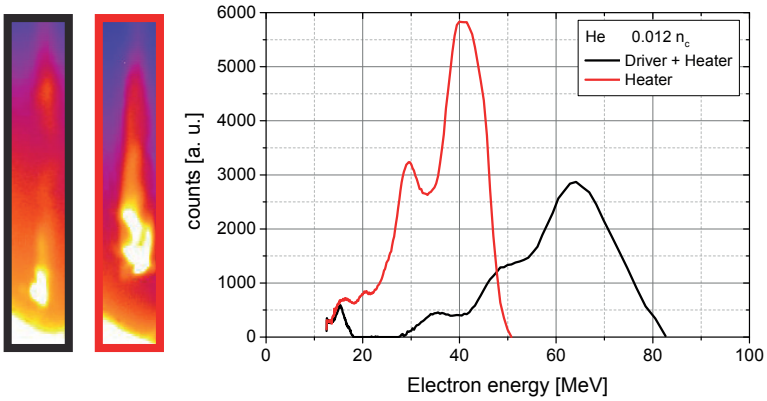

(a) Raw images

(b) Electron spectra

Figure 5.14: Electron energy spectra from the interaction of the laser beams with a Helium gas target at a density of $0.012\,n_c$. Signals detected during the double beam interaction are marked in black, while the Heater-only shots in red. Image (a) shows the raw spectrometer images for the two laser configurations. Plot (b) illustrates the evaluated energy spectra.

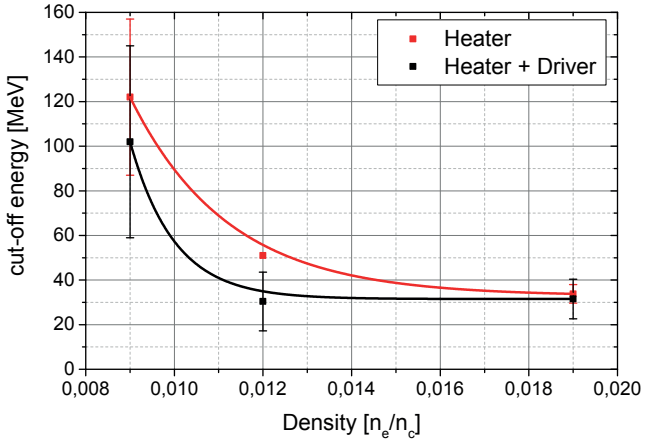

Figure 5.15: Evolution of the maximum cut-off electron energy in dependence of the target density for Hydrogen and Helium.

Figure 5.15 illustrates the evolution of the maximum cut-off electron energy in dependence of the target density. The values were averaged over all electron signals, including the presented spectra of Hydrogen and Helium. The data was fitted by an exponential decay, which serves well as the slope of the energy decrease with decreasing target density.

It was not the main investigative focus to study the electron acceleration. However, a significant flow of electrons was detected by a spectrometer at low densities up to $0.019\,n_c$ ($n_e = 3.2 \cdot 10^{19}\,\mathrm{cm}^{-3}$) as described before in the subsection 5.4.1. The acceleration of electrons is very sensitive towards a change of the laser parameters or the plasma density. Therefore, different acceleration regimes can be easily obtained. The laser pulse length, $c\tau$, can be compared to the plasma wavelength, $\lambda_P = 2\pi c/\omega_P$. The resonant condition $\lambda_P/2 < c\tau \approx \lambda_P$ is fulfilled for the Heater beam for the lowest target density, see table 5.4. This means, the acceleration mechanism can be self-modulated-laser-wakefield-acceleration (SMLWFA) or LWFA. The requirement for self-focusing ($P_L > P_c$) is as well fulfilled for these laser parameters and target densities, which can lead to wave-breaking and bubble structures. To explain all the features would go beyond the scope of this thesis. For further details about the acceleration mechanism see [96].

		target density	min	max
		n_e [cm^{-3}]	$1.6 \cdot 10^{19}$	$3.92 \cdot 10^{20}$
		n_e/n_c	0.009	0.228
$c\tau$ [μm]	8.99	λ_P [μm]	8.33	1.68

Table 5.4: Laser pulse length and plasma wavelength for the minimum and maximum target densities.

The difference between Heater and Heater plus Driver in the averaged maximum cut-off energies are marginal and can be neglected. The main electron acceleration happened due to the Heater laser. The observed effect of a decrease in electron energy with increasing gas density can be explained by the dephasing of the relativistic electrons. If the plasma length is longer than the dephasing length, $L_{dph} \propto n_e^{-3/2}$, the electrons will decelerate. Moreover, the energy gain can be assumed as $\nabla E \propto 1/n_e$. Therefore the electron acceleration is more promising in the low density regime. This dependence is described in [97] in detail and can be even seen in the analysis of this experimental campaign in figure 5.15.

5.4.2 Optical probing of the Heater interaction

Beam 1 of the ARCTURUS laser system was employed as optical probe beam, to investigate the interaction of the Heater with the gas target via shadowgraphy and interferometry, as seen in plot (a) of figure 4.27. Different delays and therefore different time steps of the plasma evolution were considered, as well as different target densities. Figure 5.16 shows the plasma channel of the interaction of the Heater beam with a Helium gas target at a density of $0.024\,n_c$. The laser interacted from the right to the left. The left column of images are from the shadowgraphy, while the central column are interferometry images. The processed fringe pattern is improved in contrast for a better analysis. The evaluated plasma electron density is illustrated in the right column of images and the dashed red line represents the centre of the nozzle. The interaction is investigated at four different time steps and the plasma channel can have a maximum expansion of roughly 1.8 mm, because of additional gas surrounding the main gas jet with a size of only 1 mm. The plasma channel evolves in length and width with time. At 3 ps after the Heater has reached the centre of the nozzle, a small plasma channel is spread out up to the beginning of a mentionable gas density (see gas profiles as a function of nozzle length in figure 3.15). At 5 ps, the channel is evolved up to the target centre and at a delay of 9 ps the plasma channel is visible over the full length. The most dense part of the channel is at the nozzle centre, as well as on the image with a delay of 5 ps. Maximum electron densities up to $0.024\,n_c$ are reached. At a delay of 2 ns, the channel is vanishing out and denser regions at the channel edge are developed.

Figure 5.17 shows the evolution of the plasma channel of the interaction of the Heater beam with a Helium gas target of $0.048\,n_c$ and $0.072\,n_c$. A similar expansion in time was observed, as shown in figure 5.16. The highest reachable electron densities are increased compared to the lower density plasma channel. The fringe pattern in plot (b) was not clearly distinguishable for later times. Therefore the electron density is retrieved before and after the overdense zones. The plasma channel 2 ns after the laser interaction was even too dense to analyse over the whole field of view.

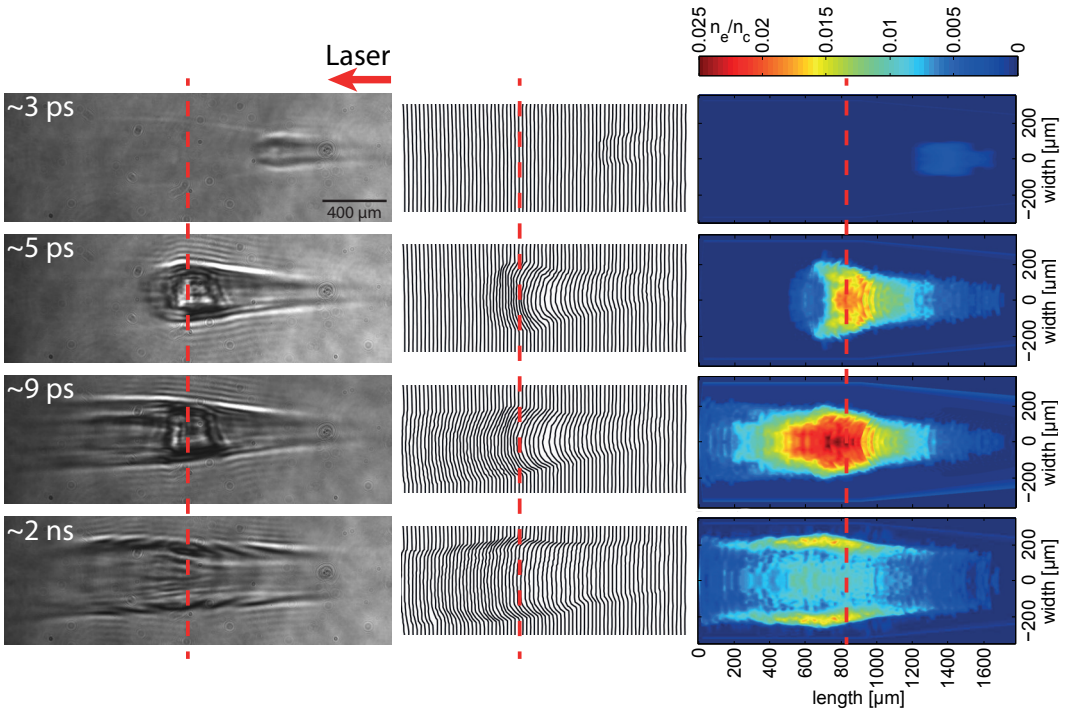

Figure 5.16: Optical probing of the Heater beam with a Helium gas target ($0.024\,n_c$). Left column: Shadowgraphy images; Middle column: Traced fringes of the interferometry images; Right column: Evaluated plasma density. The time delay after the laser has interacted with the target is increasing from top to bottom. And the Heater beam interacts from the right to the left. The vertical dashed red line stands for the centre of the nozzle.

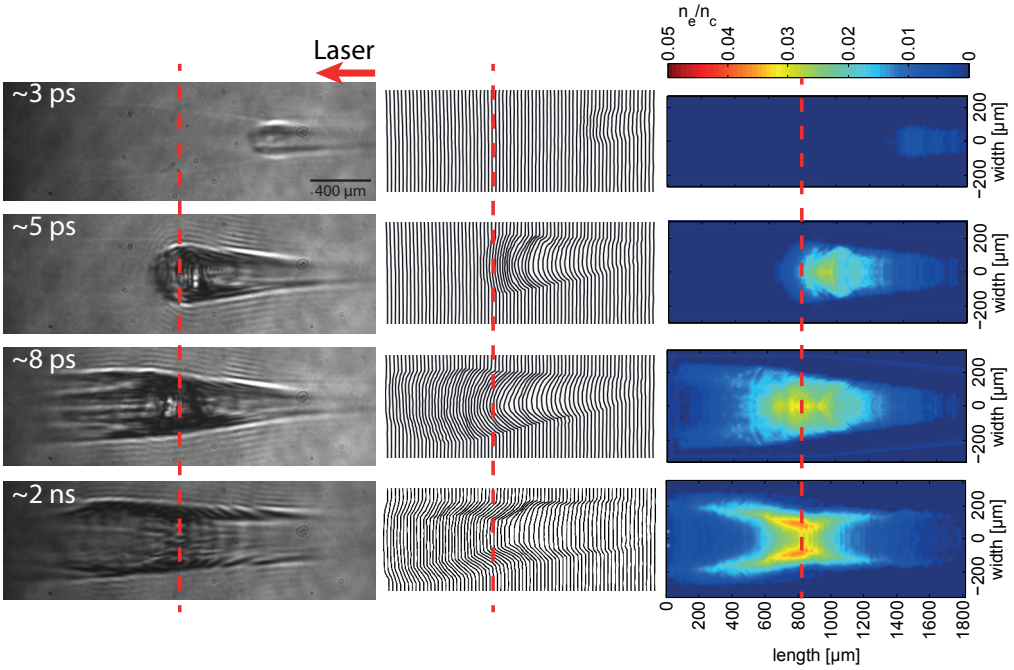

(a) Optical probing of the laser interacting with a gas target at $0.048\,n_c$

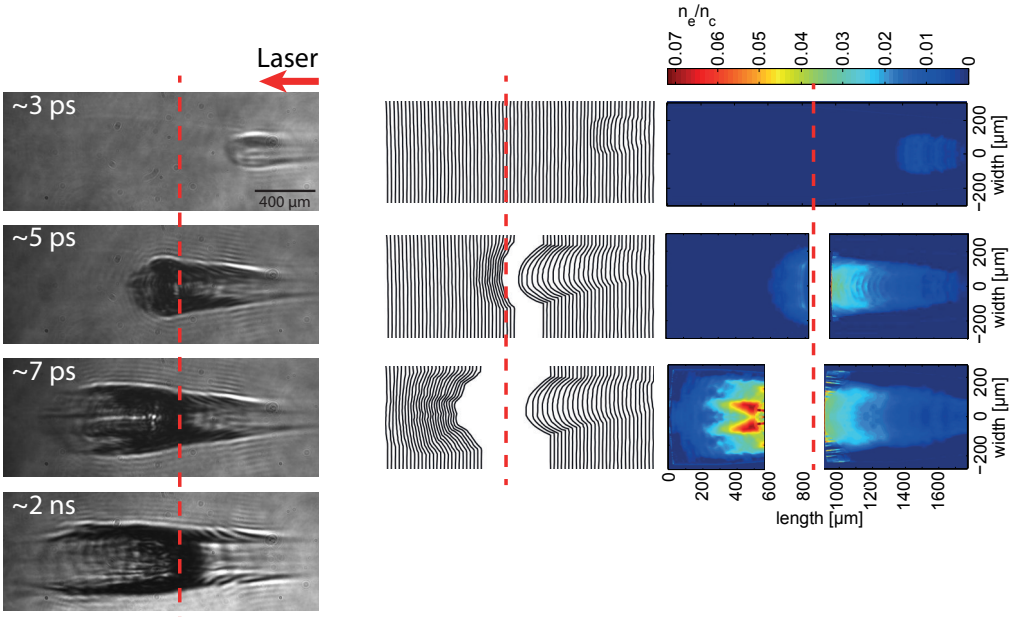

(b) Optical probing of the laser interacting with a gas target at $0.072\,n_c$

Figure 5.17: Optical probing of the Heater beam interacting with a Helium gas target at two different densities: $0.048\,n_c$ and $0.072\,n_c$ in (a) and (b) respectively. Left column: Shadowgraphy images; Middle column: Traced fringes of the interferometry images; Right column: Electron density. The time of probing increases from top to bottom, while the Heater beam propagated from right to left. The vertical dashed red line represents the centre of the nozzle.

The results of the shadowgraphy diagnostic show the plasma channel and the evolution in longitudinal and transversal direction. The whole channel, visible in the figures before, appears larger in width than the actual channel, created due to the laser interaction, caused by refracting effects of the probe beam. However, the actual inner plasma channel can be as well recognised in brighter areas in the images, which are highlighted due to self-emission from the nonlinear effects in the interaction. The transverse evolution of this channel is plotted in figure 5.18. The channel size increases fast in the first pico seconds from about 50 μm to 70 μm width at the lowest density. This fast increase is followed by a slow rise of the width up to about 210 μm after 2 ns. A higher target density leads to a slightly larger channel width, due to a higher charge density of the electrons. The channel evolution in the longitudinal direction develops with nearly speed of light, which will be discussed later in this subsection by means of figure 5.20. Therefore the channel is created almost instantaneously by the laser interaction. The propagation distance of the laser in 3 ps is about 900 μm, which is in good agreement with the shadowgraphy images. For this reason, the temporal overlap of the Heater and the probe beam was timed in a way, that at no temporal delay, the Heater laser was just about to enter the gas target. 3.5 ps later, the laser reached to focal point in the centre of the target. The images are not comparable one to one with the numerical results, however in good agreement.

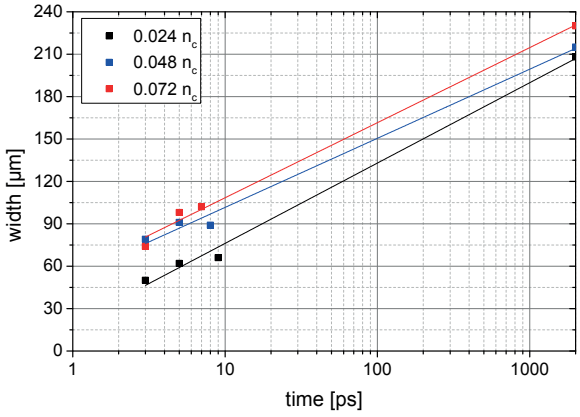

Figure 5.18: Widths of the inner laser plasma channel at three different densities, extracted from the shadowgraphy images above.

At the same time as the shadowgraphy images were recorded, interferometry data were as well recorded. The magnification of the diagnostic was too small in order to resolve the fine changes in the fringe pattern by the inner plasma channel. Due to huge gradients at the outer edges the electron density were overestimated for the whole channel. Only

at late temporal delays between the probing time and the interaction, a channel pattern was recognised.

These results show the generation of a plasma channel with sharp edges, which is a hint on the exploding channel structure in the Coulomb explosion mechanism. Furthermore, the simulation results reproduce the physical concept of a channel generation, which evolves in time in longitudinal and transverse direction. Moreover, a pre-channel structure can be recognised in the shadowgraphy images, which is important for the investigation of the following double beam interactions.

In the shadowgraphy images two outer channel edges of the same size as the plasma channel of the main interaction are visible, which are also evolving in time. They were just too weak or not dense enough to distinguish them via the interferometry. The lowest detectable density in the interferometry diagnostic is about $10^{17}\,\mathrm{cm}^{-3}$. It could be possible to identify them with a smaller fringe distance and therefore higher resolution. This pre-channel, which is formed by the laser pedestal level, is the most important result of the analysis of the optical probing images. As seen in figure 3.5, the pedestal level of the Heater beam has still an intensity of about $10^{14} - 10^{15}\,\mathrm{W/cm}^2$. These laser intensities are at the edge of the ionisation thresholds for Hydrogen and Helium (see section 2.1). Figure 5.19 shows several images of the pre-channel, detected by the shadowgraphy diagnostic. The edges of the pre-channel can easily be seen on the contrast enhanced digital version. But in order to make them visible even in the printed version, the edges are marked with white lines. The vertical dashed red line roughly represents the centre of the nozzle. The time is related to the channel of the interaction of the main laser pulse with the gas target. The late times images can be seen at the bottom, while the very

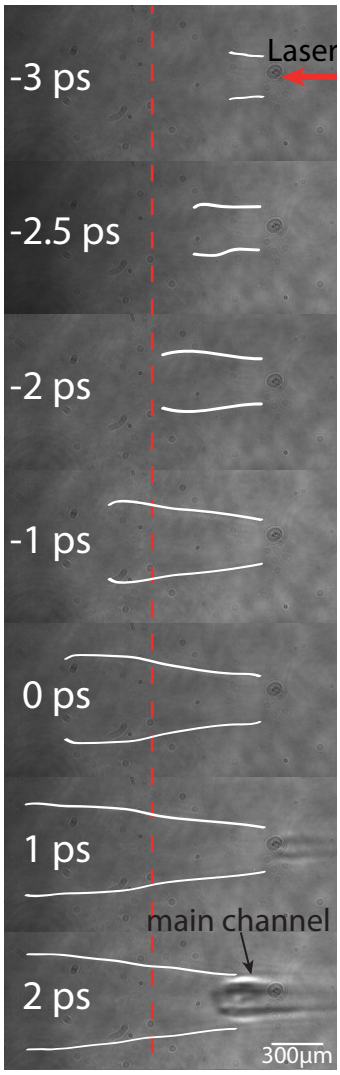

Figure 5.19: Plasma pre-channel detected by the shadowgraphy for different interacting times.

early evolution is presented on the top image. Within 4 ps the plasma pre-channel is fully extended over the whole nozzle area.

Figure 5.20 illustrates the longitudinal evolution of the pre-channel (black) and main-channel (red) versus the time of the optical probing. The pre-channel, as already described is hard to recognise on the shadowgraphy images. Therefore, it was not visible over the whole field-of-view and has not the same size as the main-channel. After 4 to 5 ps the maximum visible extension is reached and the pre-channel overlaps with the main channel. It took about 4 ps for the main channel to reach the size of the pre-channel and after 7 ps the main-channel was fully developed over the whole field-of-view. Again, the channel size is bigger than the actual gas jet width, > 2 mm compared to 1 mm. Gas molecules around the jet has to be considered in order to ionise the gas even besides the main gas target. For the best fit for each gas density profile (figure 3.15), densities of about $10^{18}\,\mathrm{cm}^{-3}$ were considered at the outer part of the nozzle head. After 7 ps, the channel was not growing anymore, but saturating and slowly vanishing in a time period longer than 2 ns. By means of linear fits of the data point, the evolution velocity can be calculated. The speed for both kind of plasma channels is nearly the speed of light c, $v_{\mathrm{pre}} = 2.97 \cdot 10^8 \pm 13\,\mathrm{m/s}$ and $v_{\mathrm{main}} = 2.99 \cdot 10^8 \pm 9\,\mathrm{m/s}$. Therefore, an instantaneously ionisation had to take place, as similarly shown in [98].

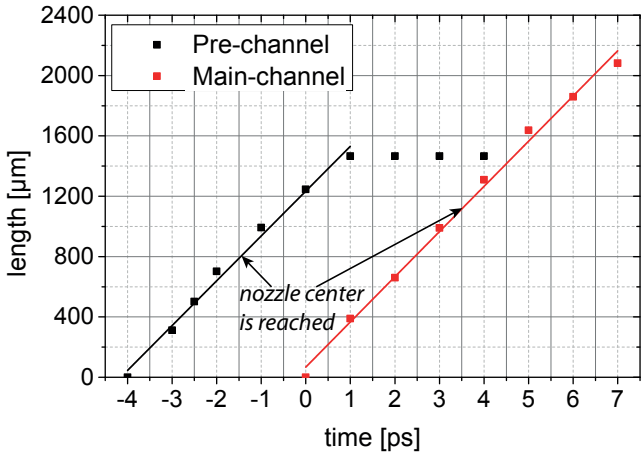

Figure 5.20: Length of the pre (black) and main (red) plasma channel per time. The measurements are fitted linearly to analyse the longitudinal evolution of the plasma channel.

These investigated results are important for a better understanding of the double beam interaction. The pre-channel is still present at later times and the main plasma chan-

nel has reached the centre of the nozzle 5 ps after the interaction. As a consequence the Driver beam interacts with the pre-formed plasma channel and not with the main channel. Only a weak ionisation took place, but preserving two density barriers in the direction to the Heater beam.

5.4.3 Charged particle probing of the Heater interaction

As discussed before, the interaction of the Heater beam with the gas target was as well investigated by charged particle probing. Long-living electric and magnetic fields inside the plasma can be observed. Figure 5.21 shows the radiochromic films exposed by the deflected protons for three different Helium target densities, $0.024\,n_c$, $0.048\,n_c$ and $0.072\,n_c$ (same densities, as in the results of the optical probing). The laser, indicated by a red arrow, interacted from the right to the left with the target. Protons of a certain energy, as written in the figure, were stopped in each RCF layer. The bottom images were the first films in each RCF stack, in which the lowest energy protons were stopped. Lowest energy implies longest time-of-flight. Therefore, the time of the probing of the interaction decreases from bottom to top. t_0, which is labeled in the figure, corresponds to the time of probing the interaction at the centre. Each row in figure 5.21 represents the same proton energy and accordingly the same probing time. The possibility of 20° rotation gives an additional time spread in one single film layer. By means of figure 4.30 in subsection 4.8.5 the time shift can be analysed: for example the time at the location ± 1 mm around the centre of the nozzle (central time, t_0) is illustrated in figure 5.21.

Different structures due to electric and magnetic field dynamics inside the plasma can be determined in the charged particle probing than in the optical probing. A more magnified image of the second film of the $0.072\,n_c$ RCF stack is presented in figure 5.22. The white shadow at the bottom shows the gas nozzle, while the actual cone-shaped gas jet can be also identified. The laser impinges from right to left onto the gas target. A multiple filament channel can be recognised outside of the gas jet at the right (1) and left side (3). The right outer channel (1) has a width up to about 400 μm and three main clear straight line-structures can be seen on every image. The left outer channel (3) is bigger with a width up to about 800 μm and a diffracting filament structure. In the central main gas region (2) a bubble-like structure is visible, accentuated by two red arrows, which is most pronounced at this higher target density of $0.072\,n_c$. A more

kind of smeared channel form can be seen in this area for example in the RCF stack of $0.024\,n_c$.

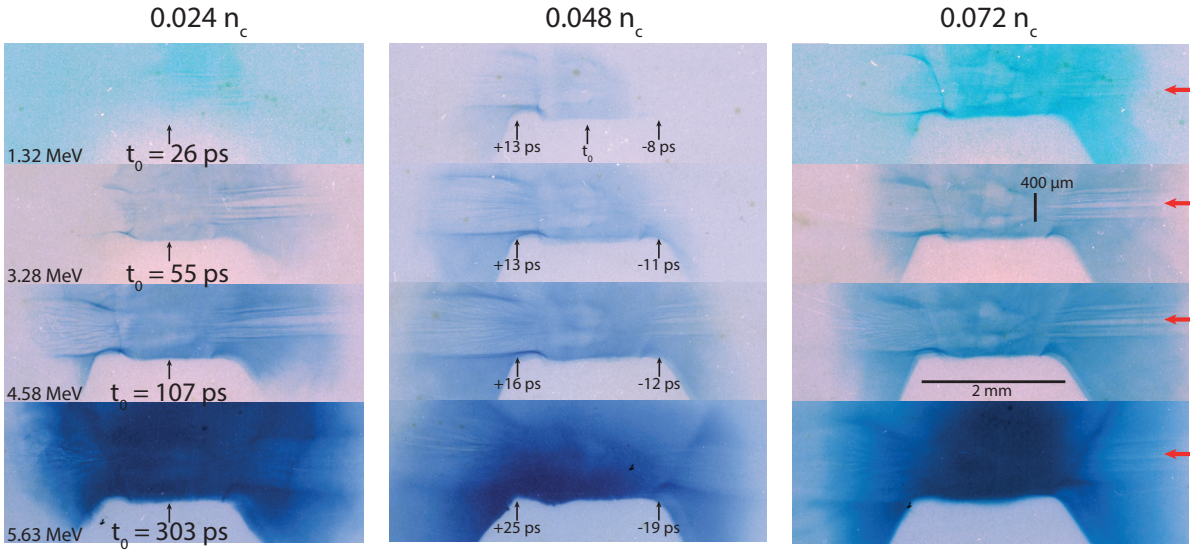

Figure 5.21: Results of the charged particle probing of the Heater interacting with the gas. Different RCF layers with different times of probing at different target densities are shown.

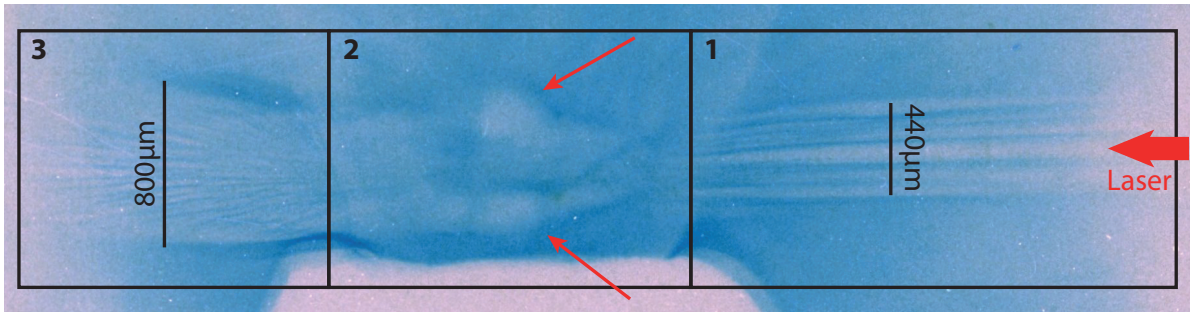

Figure 5.22: Second RCF film of the scan at $0.072\,n_c$. The Heater impinged from the right to the left. The gas nozzle, the jet, and three different areas can be distinguished.

The filamentary structures in (1) and (3) of figure 5.22 are caused by hot electrons ejected from the central area of the target in the longitudinal direction. Electromagnetic heat flow instabilities [99] by the return current of the electrons [100] deflected the protons of the charged particle probe beam. The filaments were magnetised and the inside radial electric fields affected the probing particles, leading to this special imprint on the RCFs, which is as well seen in [101, 102, 103].

Two bubble-like structures can be seen in the centre of the target in area (2) of figure 5.22. They have a vertical extend of about 700 μm and a horizontal width of about 250 μm. Each bubble had a diameter of about 250 μm. These bubble-like structures correspond to regions, where the probing particles have been deflected because of electric and magnetic fields inside the plasma. *Bulanov et al.* showed the appearance of long-lived solitons in the wake of the laser pulse in an underdense plasma [104]. A soliton is defined as electromagnetic radiation, which is trapped in small cavitated overdense areas of the plasma. As a result of the ponderomotive expulsion of the electromagnetic wave, electrons are expelled from the core, leaving protons behind. Therefore, localised electric fields acted transverse to the probing proton propagation direction deflecting the protons from the inner part of the bubble, contributing to enhanced edges of the solitons in the imprint on the RCF. More general information about solitons can be found in [105]. Ions can be considered to rest during the formation of solitons, which last less than the ion response time. The frequency of a soliton ω_s is connected to the maximum field amplitude a_m of the electromagnetic waves inside, $a_\mathrm{m} = 2\sqrt{\omega_\mathrm{p}^2 - \omega_\mathrm{s}^2}/\omega_\mathrm{s}$. The amplitude can reach the maximum value of a_m, otherwise the soliton structure will be unstable and might break [106]. The typical width of a soliton on the electron time scale is in the order of the electron skin depth: $d_\mathrm{e} = c/\omega_\mathrm{p}$, which is below one micrometre in the target density range of this experimental campaign.

The propagation velocity of a soliton is below the group velocity of the laser and is almost zero in homogenous plasmas. Due to the evacuation of electrons inside the solitons, the Coulomb repulsion of the ions leads to a radial expansion of the structure. Therefore, solitons expand and merge together, forming larger post-soliton structures [107], which include a transverse outwards directed electrostatic field. This field deflects the charge particle probe beam and circularly shaped formations occur on the detection plane. The appearance and merging are simulated and as well experimentally observed in [83, 108, 109]. As calculated in [107], the ions inside the post-soliton can be assumed to be fixed during $\sqrt{m_\mathrm{i}/m_\mathrm{e}}$ oscillation periods ($\sim 2\pi\omega_\mathrm{p}^{-1}$) of the trapped electromagnetic

field inside the soliton. Nevertheless, the ions will be affected by the ponderomotive force after about 240 fs. However, the slowly expanding post-soliton nature remains intact including the captured electromagnetic waves packet. This repulsive process is similar to the Coulomb explosion mechanism. In [107] the interaction of a laser pulse ($I_\mathrm{L} = 1.37 \cdot 10^{18}\,\mathrm{W/cm^2}$, $\lambda = 1\,\mu\mathrm{m}$, $\tau = 13.3\,\mathrm{fs}$, $a = 1$) with an underdense target ($n_0 = 0.36\,n_\mathrm{c}$) is investigated via 2D simulations. Relativistic strong electromagnetic solitons evolve into post-solitons, leading to an ion acceleration. During the Coulomb explosion-like process low energy ions are radially accelerated. By means of a 3D simulations with the same laser and gas parameters enhanced ion energies up to 30 keV were calculated in [110]. In the 2D simulations in [104], the electric field inside the soliton is 1.5 times stronger with laser parameters very close to the ARCTURUS Heater laser beam, $I_\mathrm{L} = 2 \cdot 10^{19}\,\mathrm{W/cm^2}$, $\lambda = 1\,\mu\mathrm{m}$, $\tau = 40\,\mathrm{fs}$, $a = 3$ and a plasma density of $n_0 = 0.2025\,n_\mathrm{c}$. Hence, the ions originating from the solitons gain an energy of about 45 keV.

Preliminary simulations of the Heater-gas interaction indicate some long-living electric structures, which can be seen in figure 5.6 as dark blue and yellow spots inside the plasma channel. These field structures can hint at the soliton structures visible in the charge particle probing. Consequently, also the solitons observed in the Heater channel can explode and contribute to the ion acceleration. In comparison to the previous results of *Bulanov et al.*, *Naumova et al.* and *Esirkepov et al.*, the ion energy will be less than 100 keV and the mechanism starts later than the Coulomb explosion of the plasma channel. Since the ion detection via the CCD camera in combination with the MCP is time integrated, the acceleration due to different mechanism at different times could not be distinguished. However, the ion energy spectra can be enhanced in the low energy regime due to the exploding solitons.

5.5 Summary

Ions of several hundred keV energy were accelerated via the Coulomb explosion mechanism by a single laser pulse interacting with a gas target. Electrons were pushed away from the laser axis by the radial component of the ponderomotive force, which has to be larger than the electric field force of the immobile ions. Under this condition the ions were pushed in the transverse direction from the channel due to a Coulomb repulsion.

The interaction of the Heater beam with an intensity of $2.4 \cdot 10^{19}\,\mathrm{W/cm^2}$ with a Hydrogen or Helium target with different densities was experimentally investigated. Ions of different energies were detected by means of two Thomson parabola spectrometers. In addition, numerical simulations of the experimental conditions showed comparable results and gave a deep insight into the laser, density, field and accelerated ion distributions in the plasma. Via analytical models, thresholds for self-focusing effects and conditions for a Coulomb explosion mechanism were calculated in order to discuss the results.

Furthermore, three different diagnostics, besides the Thomson parabola spectrometer, were employed for an additional investigation of the physical processes inside of the laser plasma interaction. Electrons were accelerated in the longitudinal direction by the Heater beam at low target densities. However, these electrons were not energetic enough and left the plasma too fast in order to set up an electrostatic field to accelerate ions in this direction. By observing the interaction with optical probing, the inner plasma channel of the interaction was visible in the shadowgraphy. The evolution in longitudinal and transverse direction is in good agreement with the downsized numerical simulations. Interferometry images were analysed to reconstruct the density profile at late temporal delays. Moreover, a pre-plasma channel was visible in the shadowgraphy before the main channel started to evolve, which was important to investigate the physics of a double beam interaction in the following chapter. Due to charge particle probing soliton structures were observed, which existed for hundreds of picoseconds. Low energy ions, radially accelerated by a Coulomb expulsion from these small structures, can contribute to the low energy ion spectra in combination with the Coulomb explosion of the full plasma channel.

Chapter 6

Ion acceleration from underdense targets via a TNSA-like mechanism

This chapter is dedicated for further development of an ion source from underdense targets. Thanks to the unique capability of the ARCTURUS laser, a novel acceleration scheme was investigated. By means of a TNSA-like mechanism, ions were accelerated in the longitudinal direction of a Driver laser beam.

It was described in the chapter before, that protons or Helium ions were accelerated in the transverse direction by the interaction of a single laser beam with the gas target by the Coulomb explosion mechanism. However, the ion acceleration was efficient up to gas densities of about $0.12\,n_c$. The Heater laser beam was not intense enough to generate an evacuated plasma channel in order to start the CE above this density at the optimum target position. A strong plasma channel resulting in the acceleration mechanism might occur in the increasing lower density ramp of the target. These ions cannot be detected by the Thomson parabola spectrometers aligned to the center of the nozzle. However, by employing a second laser beam, the Driver, focused by an f/2 OAP to an intensity of about $1.5 \cdot 10^{20}\,\mathrm{W/cm^2}$, the acceleration mechanism was extended to a target density of about $0.18\,n_c$. The experimental setup can be seen in figure 4.23. Instead of accelerating ions in the transverse direction by the generation of a plasma channel in the gas target due to the single beam interaction, a novel target design was implemented. The Driver interacted with a pre-formed plasma profile created by the Heater consisting of two density spikes combined with a density gap in between. It should be mentioned, that no ions were accelerated neither in transverse, nor in the longitudinal direction by a

single Driver interaction. The results were experimentally observed and reproduced by numerical simulations, helping to investigate the laser plasma interaction. A TNSA-like acceleration process was identified by studying the density and field distributions. Finally, analytical calculations supported the conclusions about the interaction processes. Moreover, these results, observed for the first time, helped to understand the crossover of the interaction physics.

In addition, a magnetic spectrometer was employed in the setup in the transverse direction to the Driver laser axis. The main purpose of the diagnostic was the detection of ions in this direction. However, only electrons were detected by the interaction of the Driver with the target. No ions were observed in this direction during the various target and laser adjustments. Moreover, the Driver interaction was investigated by optical shadowgraphy. The plasma channel blasted in the target centre, consistent with the result, that no ions were accelerated in the transverse direction by the Driver interaction.

6.1 Experimental results

Figure 6.1 illustrates the proton spectra of the interaction of Heater and Driver, impinging onto the Hydrogen target at the same time. If this figure is compared to figure 5.1 in section 5.1, higher cut-off energies and a flux about 8 times higher is clearly distinguishable. Moreover, the acceleration took place even at very high target densities above $0.121\,n_c$. The cut-off energy is higher than in the single beam case and slightly increasing with increasing target density.

Figure 6.2 shows a comparison of the cut-off energy of the accelerated protons of the single beam (red) versus the double beam (black) configuration. The values are averaged over several shots and therefore represent a statistics of the evolution of the maximum energy of the protons from the Hydrogen gas target. The graph illustrates the trends of the cut-off energy for both Thomson parabolas: 0° - solid line and 10° - dashed line. The trend line in the double beam configuration shows a slight increase with increasing target density in both detection angles. Whereas the maximum energy of the protons in the single beam setup remains nearly the same or is even decreasing again for high

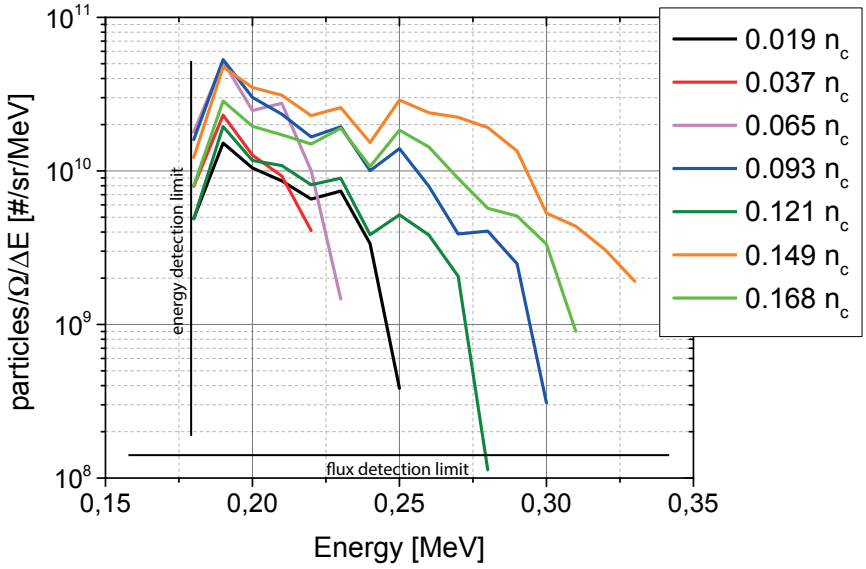

Figure 6.1: Proton energy spectra for different gas target densities in the double beam configuration, detected by the 0° Thomson parabola. The protons are accelerated transverse to the beam axis.

target densities. In the gap at $0.065\,n_c$ (0° angle) the proton energy is probably below the detection threshold of 160 keV.

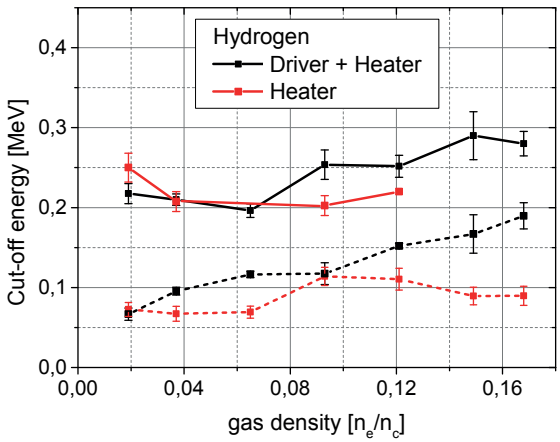

Figure 6.2: The graph demonstrates the evolution of the cut-off energy of the proton spectra for a given gas density. The black curve represents the slowly increasing trend of the energy in the double beam configuration, while the red curve represents the maximum energy for the single beam, Heater-only shots. The solid line represents the 0° Thomson parabola and the dashed line the 10° Thomson parabola.

The He^+ ion energy spectra in the double beam configuration are almost similar to the

single beam spectra (see figure 6.3 (a)). The particle flux is slightly increased and the maximum energy cut-off however is at about 200 to 300 keV. Only the acceleration at $0.12\,n_c$ is an outlier, reaching a maximum energy of approximately 400 keV. Moreover, an acceleration was observed even at a very high gas density of $0.18\,n_c$. The latter is also valid for the detected He^{++} signal (6.3 (b)). He^{++} is again detected only at high densities. The maximum energies are slightly higher than in the Heater-only case, around 300 to 400 keV.

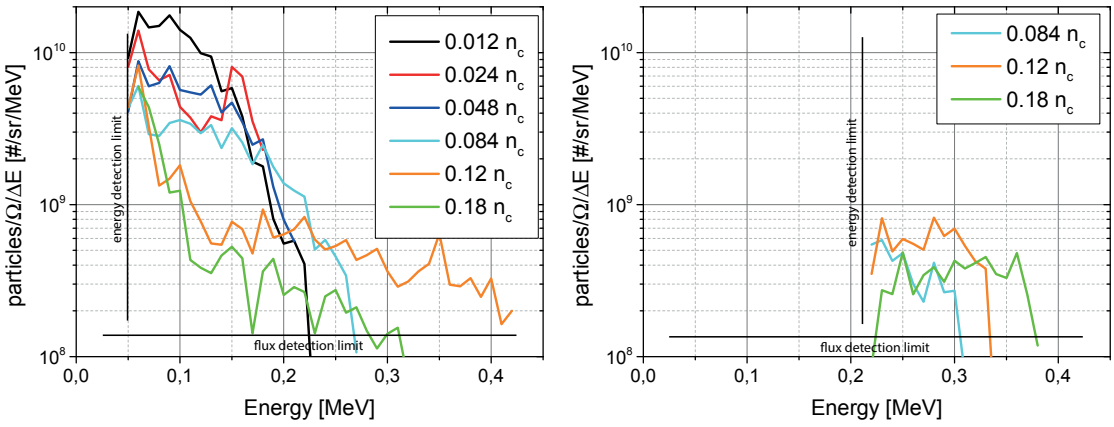

(a) He^{+} energy spectra

(b) He^{++} energy spectra

Figure 6.3: He^{+} and He^{++} ion energy spectra for different gas target densities in the double beam configuration, detected by the 0° Thomson parabola. The ions are accelerated and detected transverse to the beam axis.

Figure 6.4 presents the cut-off energies in the double beam configuration versus the single beam setup. The Heater-only analysis is drawn in red and the double beam configuration in black. Moreover, He^{+} ions are illustrated by full square labels and He^{++} ions by white framed squares. The maximum energies (Graph (a) 0° TP and (b) 10° TP) remained more or less the same in any setup and angle for low target densities. While above a density of $0.12\,n_c$ the acceleration stopped in the single beam configuration the cut-off energy in the double beam setup is very high about 300 to 350 keV. Furthermore, it is clearly visible in the results of the 0° Thomson parabola, that He^{++} ions were only detected above a certain target density ($0.084\,n_c$) in both laser configurations. Below this density, only He^{+} ions were detected. In the 10° detector all ion species are visible for the whole density range with nearly two times lower maximum cut-off energy.

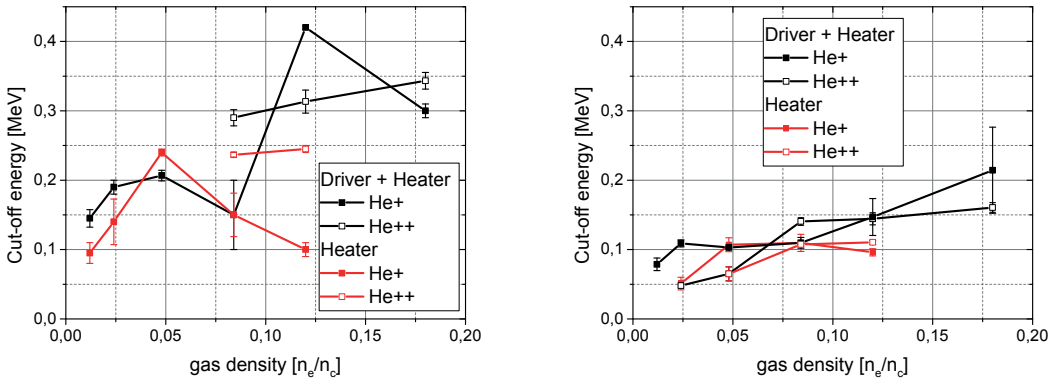

(a) Maximum energy - 0° TP

(b) Maximum energy - 10° TP

Figure 6.4: Plot (a) reveals the evolution of the cut-off energy of the Helium ion spectra for a given gas density. The black curve represents the trend of the energy in the double beam configuration, while the red curve represents the maximum energy for the single beam, Heater-only shots. He^{+} ions are labeled by full square markers, while He^{++} is illustrated by white framed squares. The same illustration is used for plot (b), which shows the results of the 10° Thomson parabola.

6.2 Numerical simulations

In order to get a better understanding of the plasma and the acceleration processes and to corroborate the experimental findings, numerical 2D PIC simulations were performed by *T. Liseykina* with the same simulation setup as discussed in section 5.2. However, instead of running a complicated two beam simulation, a preformed density profile was assumed for the Driver interaction. The Heater interacted already with the target and created a channel structure. Two dense walls surround a low density area, evacuated of particles due to the ponderomotive push of the Heater interaction. A density profile, as shown in plot (b) in figure 6.5, was employed in the simulations for a Hydrogen plasma with an average density of $0.056\,n_c$. Plot (a) shows the electron density distribution of the Heater-only interaction and a vertical line-out. This plot is taken as model for the density structure implemented in the code. The channel walls or density spikes in the Driver simulation had a thickness of about $2.7\,\mu$m and a gap of about $32\,\mu$m, placed at $x = 280\,\lambda = 224\,\mu$m and $x = 320\,\lambda = 256\,\mu$m. A Driver laser with two different intensities was employed in two different runs.

The experimental laser parameters were $d_0 = 4\,\mu$m (FWHM), $\lambda = 800\,\mu$m, $\tau = 30\,$fs, $I_\mathrm{L} \approx 5 \cdot 10^{19}\,\mathrm{W/cm^2}$ ($a_0 = 3.4$) and p-polarization. The Driver intensity was reduced, because the fully amplified Driver beam in the experimental arrangement had hot wings around the focal spot, which reduced the beam quality and the laser intensity. In the second run the intensity was changed to the original $I_\mathrm{L} \approx 1.5 \cdot 10^{20}\,\mathrm{W/cm^2}$ ($a_0 = 8.2$). The results of the first lower intensity simulation run are shown in detail in the following.

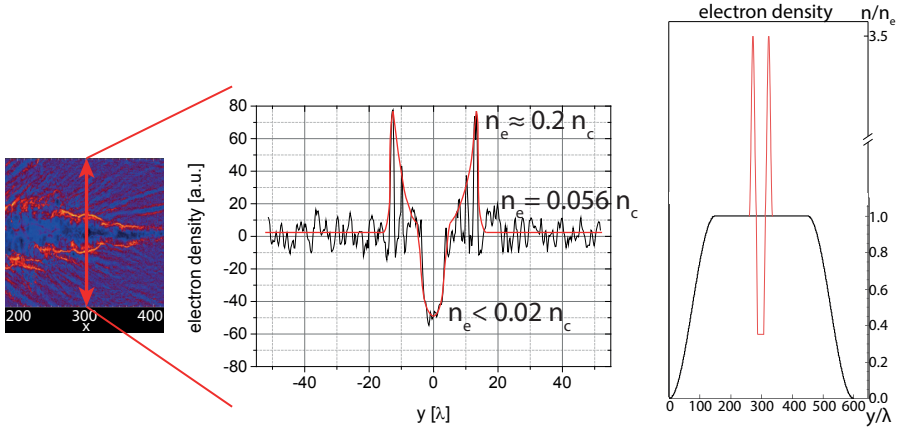

(a) Line-out of simulated n_e profile after Heater interaction

(b) Expected n_e profile for Driver simulation

Figure 6.5: Pre-formed density profiles for the interaction of the second Driver laser. Graph (b) shows a vertical line-out of the Heater-only simulations and (c) illustrates the total modified density profile for the Driver simulation.

Figure 6.6 illustrates the evolution of the laser pulse and its intensity inside the plasma at different times and locations. The Driver beam interacted from left to right with the target. The black circles highlight the areas of self-focusing effects, where the laser intensity was increased up to $I = 3I_0$. The last pictures shows, that the laser pulse can be seen even behind the channel structure at $x = 375\,\lambda = 300\,\mu$m.

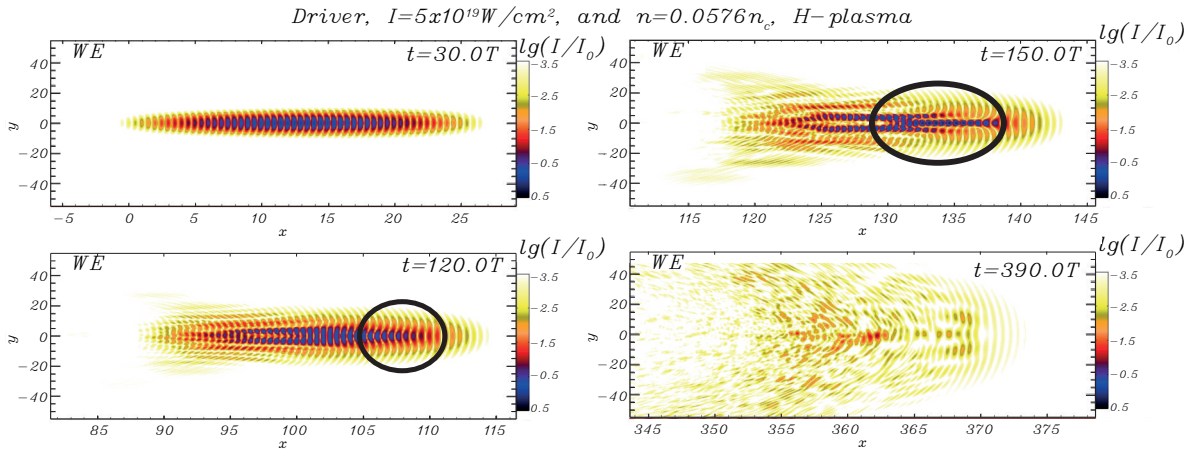

Figure 6.6: Driver intensity distribution inside the plasma from PIC simulations for different observation times.

The ion (top) and electron (bottom) density distributions are shown in figure 6.7. The first image shows the distributions over the full length of the target. At $x = 280\,\lambda$ and $x = 320\,\lambda$ the two density wall can be clearly distinguished. A channel structure and filamentations are visible in $50\,\lambda < x < 280\,\lambda$. However, the novel interaction happened at the preformed dense walls. The six lower images show magnified plots of the distributions around the density spike profile at different interaction times. At the time $t = 360\,\mathrm{T} = 936\,\mathrm{fs}$ electrons were already pushed out of the first density wall ($x = 280\,\lambda$) into the low density region. Especially at the center ($y = 0\lambda$) the biggest amount of accelerated electrons can be found. Later on, a whole layer of electrons and ions originating from the first density wall moved in the longitudinal x-direction (visible as vertical line in the density profile). When the first particles hit the second density wall ($x = 320\,\lambda$), it started to disperse clearly, already at $t = 420\,\mathrm{T} = 1.092\,\mathrm{ps}$. However, the most important phenomena are the particles accelerated around $y = 0\lambda$ at early times ($t \leq 480\,\mathrm{T} = 1.248\,\mathrm{ps}$), distinguishable by the moving central layer of electrons followed by the ions.

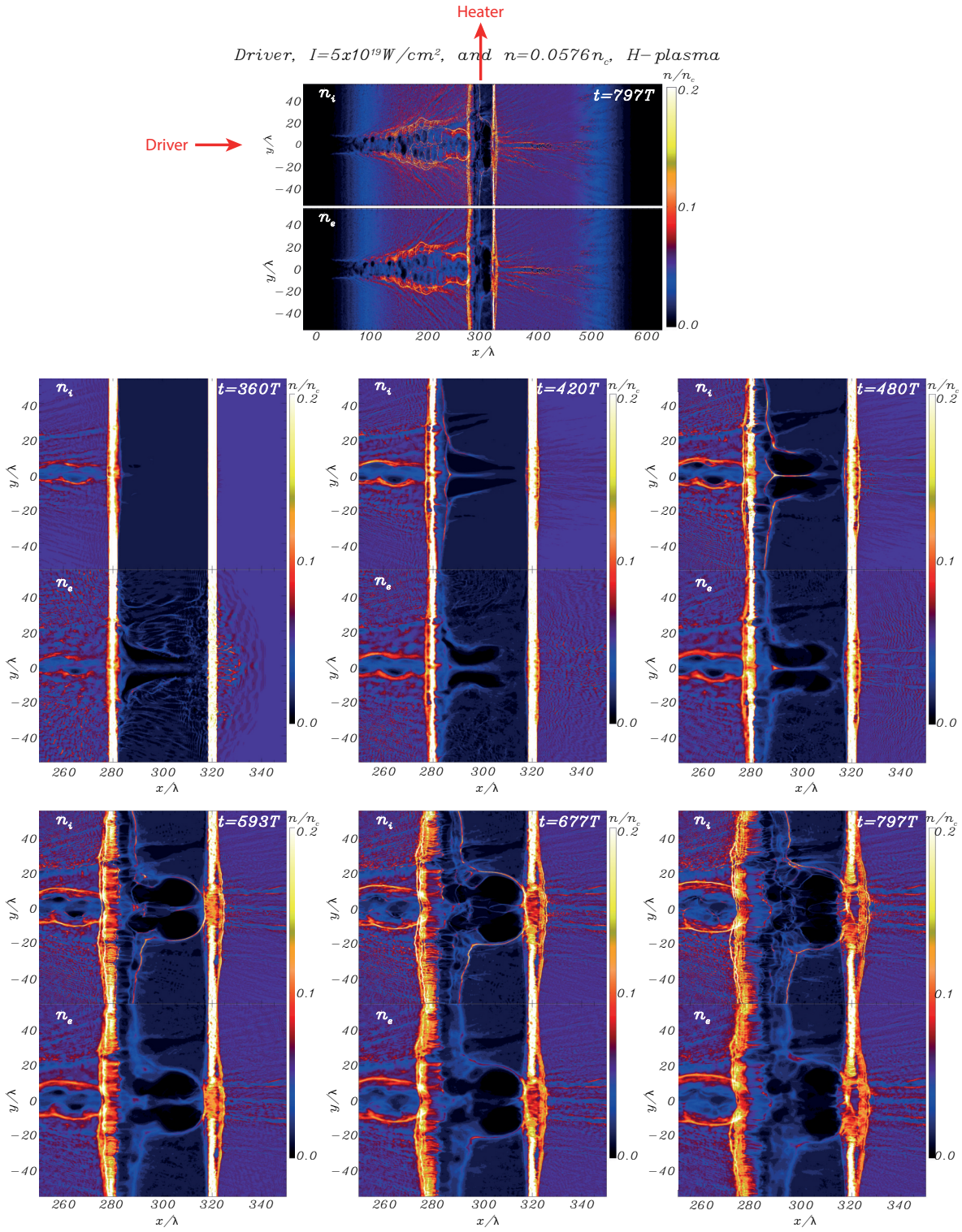

Figure 6.7: Channel ion (top) and electron (bottom) density distribution of PIC simulations at different times of the interaction. The top image shows the whole interaction area, whereas the six bottom images present a magnification of the density distributions around the channel structure.

In Figure 6.8 the magnetic and electric fields are illustrated. The top two images show the electric field in the transverse y-direction (E_y) and the magnetic field in the z-direction (B_z) for two different times of the interaction. The channel structure created by the Driver beam interaction can again be recognized in $50\,\lambda < x < 280\,\lambda$, surrounded by a low transverse electric field and the quastistatic magnetic field. In between the preformed density walls ($280\,\lambda < x < 320\,\lambda$) a transverse electric field and a strong bipolar magnetic field can be observed. The longitudinal acting electric field distributions (E_x) are shown in the six bottom images. The field strength is twice as high as of E_y, which is in favour of the longitudinal acceleration. Along the moving particle front (of figure 6.7) and especially around $y = 0\lambda$ an accelerating electric field can be identified, especially at $t = 420\,\mathrm{T} = 1.092\,\mathrm{ps}$ and $t = 480\,\mathrm{T} = 1.248\,\mathrm{ps}$. This strong sheath field will accelerate the ions in forward direction. Moreover, no strong sheath field can be recognised around the second density wall at $x = 320\,\lambda$. Although, this second wall vanished in the density distribution, it is not an origin of a strong ion acceleration. Only due to the interaction of the Driver laser with the first density wall, an accelerating sheath field was created.

Furthermore, the ion phase space was plotted in figure 6.9 at two different interaction times. A strong longitudinal acceleration started at $t = 360\,\mathrm{T} = 936\,\mathrm{fs}$ at the location of the first preformed density wall at $x = 280\,\lambda$. Particles were transverse accelerated before and in the gap of the preformed structure. At later time ($t = 797\,\mathrm{T} = 2.072\,\mathrm{ps}$) the longitudinal particles were further accelerated to energies of roughly 4 MeV, however still originating from the first density wall. As already discussed before, at the second wall at $x = 320$ only a weak longitudinal acceleration happened. The energy of the transverse accelerated particles increased to roughly 1.5 MeV, which originated from the gap of the density formation ($280\,\lambda < x < 320\,\lambda$).

By means of the phase space plot, the integrated ion energy spectra were calculated at $t = 798\,\mathrm{T} = 2.075\,\mathrm{ps}$. Longitudinal accelerated ions (red curve) reached an energy of about 3.2 MeV, while a lower number of transverse accelerated ions (green curve) reached an energy of about 1.5 MeV. The ion energies are one order of magnitude higher than the experimental ion energies and the simulations resulted in a transverse acceleration of ions, which was not distinguished in the experimental campaigns. Further simulation runs have to be carried out with different laser and target parameters in order to reproduce the exact experimental conditions. However, the physical concept of a laser pulse propagating through an underdense target and interacting with a density spike at the centre of the plasma was successfully investigated via the 2D PIC simulations. It was

proven, that ions were accelerated in the longitudinal direction via a TNSA-like sheath field, visible in the density and field distributions.

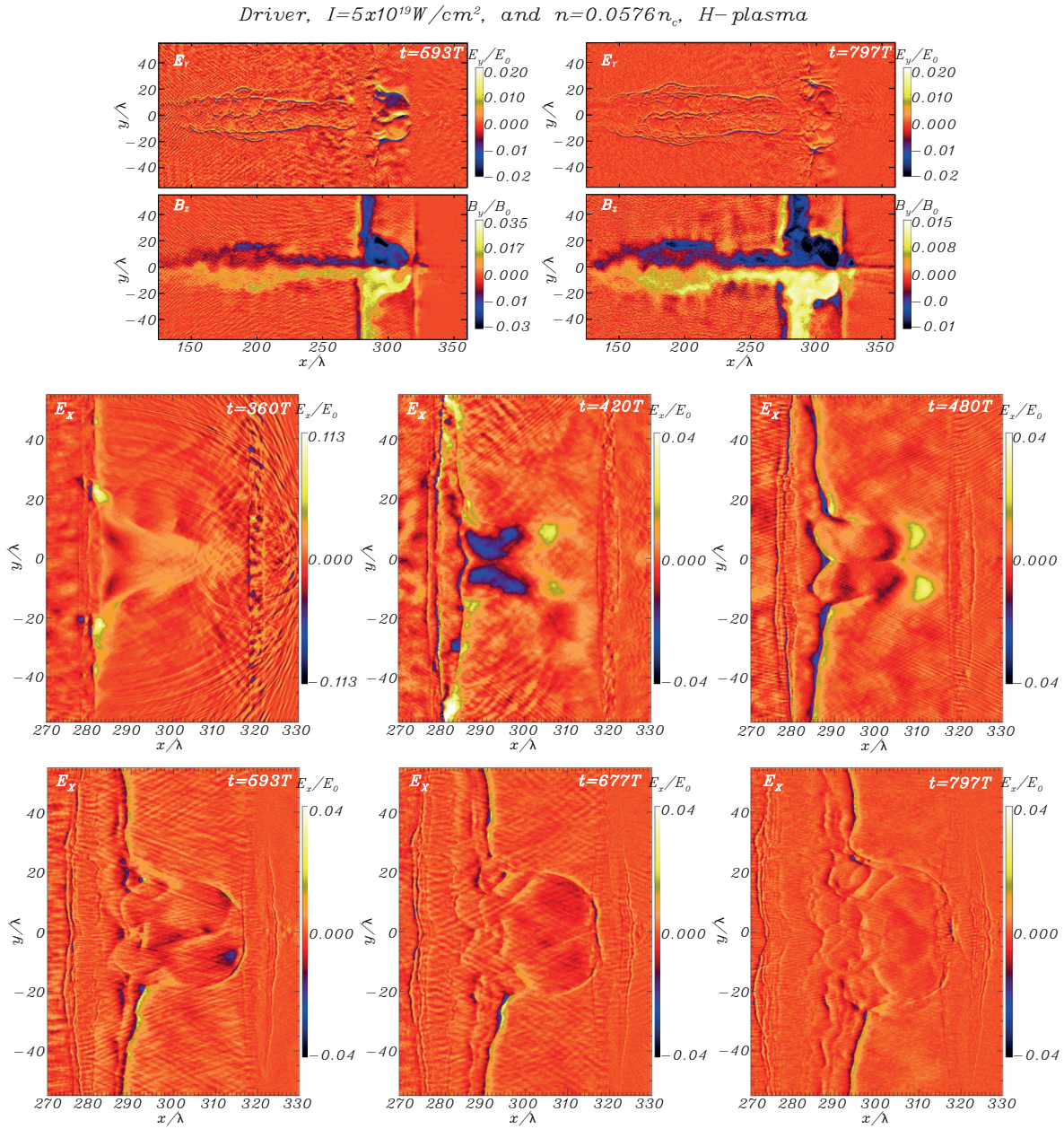

Figure 6.8: Channel ion (top) and electron (bottom) density distribution of PIC simulations at different times of the interaction. The top image shows the whole interaction area, whereas the six bottom images present a magnification of the density distributions around the channel structure.

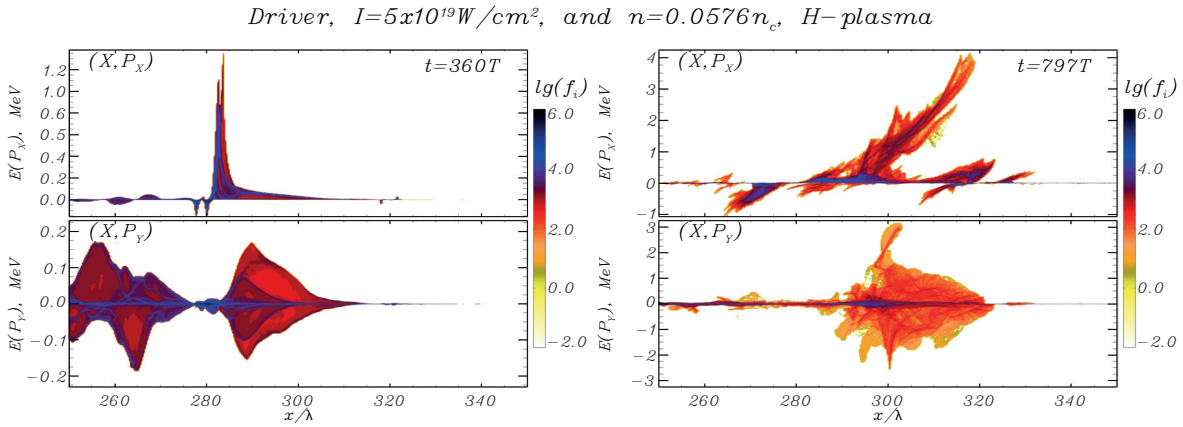

Figure 6.9: Proton phase space plots normalised to $m_{\mathrm{i}}c$ for the longitudinal (top) and transverse (bottom) distribution.

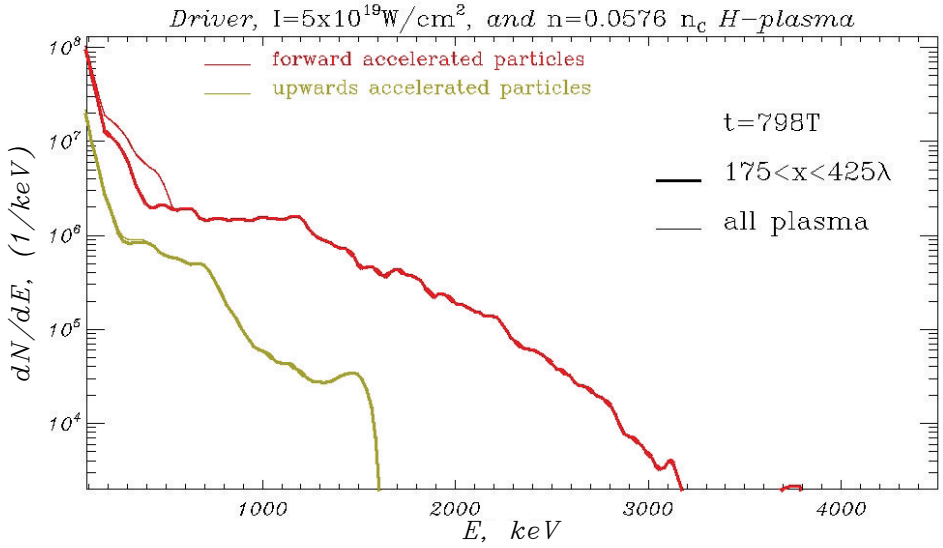

Figure 6.10: Energy spectra of the protons accelerated in longitudinal (red) and transverse (green) direction.

A second simulation was performed employing a higher intensity Driver, corresponding to the calculated intensity of $I_{\mathrm{L}} \approx 1.5 \cdot 10^{20}\,\mathrm{W/cm^2}$. This Driver interacted once with the preformed density structure and in another run with the normal undisturbed density profile. In figure 6.11 are two density distributions and two images of the phase space shown. On the left images is the Driver interacting with the target, described before, including the preformed density spike structure, visible. The right images match with a Driver interacting with an undisturbed target profile. The white line illustrates the location of the first density spike ($x = 280\,\lambda$) of the left simulation results. The right

density image is more magnified in the y-direction, which explains the differences in the channel size and filaments.

The Driver created a plasma channel in both simulations. However, the obvious difference in the density profiles is the disruption at $x = 280\lambda$ at the location of the first density spike, where a layer of particles moved in the longitudinal direction, as described before. As seen in the low intensity simulation, the laser pulse was capable of propagating through the spikes, which will be even stronger in this higher intensity simulation. Therefore, the higher intensity laser was able to generate a plasma channel even behind the second spike ($x > 320\lambda$). The bottom phase space plots show the direction and strength of the acceleration over the entire target length. On the left image (Driver + preformed plasma) a transverse and a strong longitudinal acceleration can be recognised, while due to the interaction of the Driver with an undisturbed target, the transverse acceleration exceeds the longitudinal one.

Clearly two facts can be highlighted. First, a stronger Driver interaction induced a stronger transverse ponderomotive push leading to a stronger transverse acceleration of ions. Moreover, the energy of the longitudinal accelerated ions was as well stronger induced by a stronger electric sheath field. Second and the most important fact, the Driver interacting with the specially preformed target induced an enhancement of the longitudinal acceleration in comparison with the results of the Driver interacting with a undisturbed density profile. These PIC simulations show the physical concept of the interaction with a special gas target, although the experimental results were slightly different. No transverse accelerated ions were detected, which can be due to the fact, that the experimental target had a size of one millimetre. The Driver could have created a plasma channel in the very beginning of the gas. Only particles originating from the centre of the target could have been detected. Furthermore, the fully amplified laser pulse had a focal spot surrounded by hot wings, leading to a weaker intensity as predicted in the analytical calculations, which is again leading to a weaker transverse acceleration. However, the simulations show the basic principle of a laser interacting with a specially preformed gas target and predict a TNSA-like acceleration mechanism of the ions in longitudinal direction.

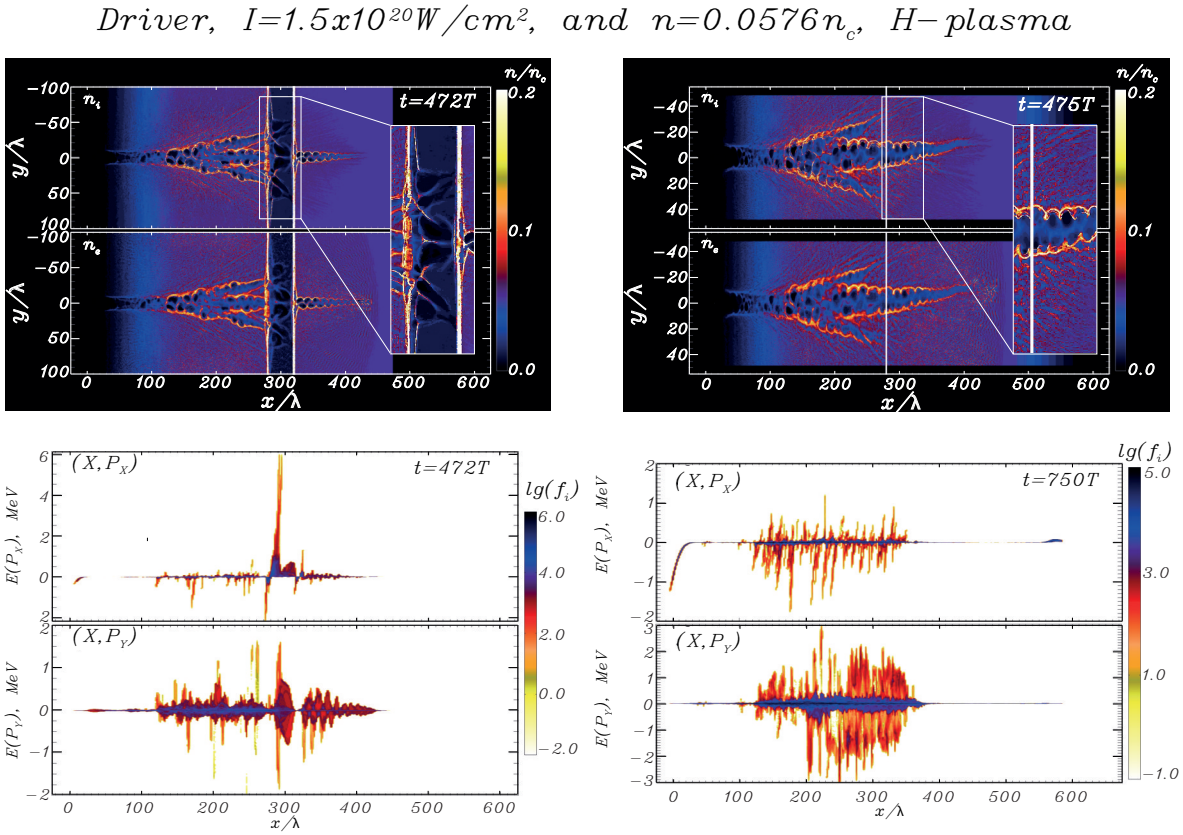

Figure 6.11: Results of PIC simulations of the intense Driver interacting with a preformed special target (left images) and of an interaction with a undisturbed target profile (right images). The density distributions are shown in the top and the phase space plots of the acceleration are shown in the bottom.

6.3 Analytical discussion

The slowly increasing trend in the maximum particle energy with the target density is one significant difference in the acceleration features compared to the single beam configuration. Another difference is the acceleration even at very high densities, above $0.12\,n_c$. A Driver-only interaction with the target was not able to produce any ions at any gas density. Both beams together, Driver with Heater, must play a role in this acceleration mechanism, as already reproduced by the numerical simulations.

In the low density regime, the Coulomb explosion by the Heater was probably the dominant method to accelerate the particles. Moreover, there could be as well an ion

acceleration by the interplay of Driver and Heater together in the low density regime. But the CCD camera, recording the ion traces on the MCP detector, integrates the image over several milliseconds. Therefore, even if there was an ion acceleration of the double beam interaction, it was superimposed with the accelerated ions of the Heater-only interaction. Certainly, only in the high density regime the pure ion signal of the double beam interaction was detected, because of the missing signal in the single beam configuration.

The conditions to accelerate ions by a Driver-only interaction in the transverse direction via Coulomb explosion are fulfilled, see table 6.1. However, no ions were detected in this direction. The short Rayleigh length of the Driver, focused by the f/2 OAP is not taken into account by the analytical model calculations of the thresholds. As discussed in the following chapter about the shadowgraphy results (subsection 6.4.2), the laser pulse was not able to propagate through the full plasma and to create a proper plasma channel. Rather the plasma channel bursts in the centre of the target. However, in the simulations, the laser was able to create a plasma channel. The reason can be, that gas target was reduced in size, which means for the experiment, that the laser created a channel only in the first hundreds of micrometers of the target. Furthermore, a homogenous focal spot with a high intensity was assumed for the simulation, while the fully amplified laser was focused to a spot including hot wings leading to a reduction in intensity and homogeneity of the profile.

		target density	min	max
		n_e [cm^{-3}]	$1.6 \cdot 10^{19}$	$3.92 \cdot 10^{20}$
		n_e/n_c	0.009	0.228
ω_0 [Hz]	$2.35 \cdot 10^{15}$	ω_p [Hz]	$2.26 \cdot 10^{14}$	$1.12 \cdot 10^{15}$
τ [fs]	30	$1/\omega_p$ [fs]	4.42	0.9
$c\tau$ [μm]	8.99	r_0 [μm]	2	
a_0	0.6	a_{0max}(1D)	1	29

Table 6.1: Different conditions, which have to be fulfilled by the Driver laser in order to accelerate ions due to Coulomb explosion, at the minimum and maximum target density.

For densities higher than $0.12\,n_c$ the theoretical condition for collisionless shock acceleration due to the Driver beam is fulfilled. The piston velocity (equation 2.50) has

to be bigger than the sound velocity (equation 2.34), $v_{\text{piston}} > c_s$, in order to have a shock propagating inside the plasma and the Mach-number $M = v_{shock}/c_s$ has to exceed one. This conditions are fulfilled from this density threshold on, as shown in table 6.2. Nevertheless, the Driver-only interaction did not accelerate any ions and the simulation results hint to a TNSA-like acceleration mechanism.

		target density	min	intermediate	max
		n_e [cm^{-3}]	$1.6 \cdot 10^{19}$	$2.06 \cdot 10^{20}$	$3.92 \cdot 10^{20}$
		n_e/n_c	0.009	0.12	0.228
c_s [m/s]	$9.45 \cdot 10^6$	v_{piston} [m/s]	$2.78 \cdot 10^6$	$9.98 \cdot 10^6$	$1.38 \cdot 10^7$

Table 6.2: Sound speed and piston velocities for different target densities, calculated for the Driver beam.

However, ion acceleration from a gas target due to Collisionless Shock Acceleration (CSA) was observed only in overcritical gas jets by *Palmer et al.* [111], *Haberberger et al.* [112] and Chen et al. [113]. A CO_2 laser was employed in order to easily reach an overdense target density in a Hydrogen gas jet and *Chen et al.* employed a high pressure, high density gas nozzle combined with a Ti:Sa laser system. In these experiments, the radiation pressure pushes electrons into the target, which launch an electrostatic shock wave in an overcritical plasma. Ions are overtaken and reflected by the wave into the expanding plasma leading to an narrowband acceleration.

A different mechanism to accelerate ions from underdense targets is Low Density Collisionless Shock Acceleration (LDCSA) experimentally observed by *Gauthier et al.* [29] and *Antici et al.* [30] and theoretically simulated by *d'Humieres et al.* [31]. The acceleration mechanism is discussed in subsection 2.4.3. These results show that there could appear not only a pure electrostatic field to accelerate the ions, but also a shock mechanism can occur, depending on the target profile with different gradients and on the density itself. Figure 6.12 (a) shows the different underdense target profiles of the Livermore experiment [30]. On the left of Picture (b) is the density profile of the f/10-Heater simulations reported before. A vertical line-out (red arrow) illustrates the density profile for the Driver interaction. However, the target conditions for the LDCSA mechanism are not given in this experimental arrangement presented here. *Fiuza et al.* have calculated analytical thresholds for a successful ion acceleration due to a shock acceleration in underdense targets [114]. A target profile of several hundred microme-

tres and a higher Mach number would be necessary to reach the conditions. Therefore, LDCSA was not the accelerating process in the results investigated in this thesis.

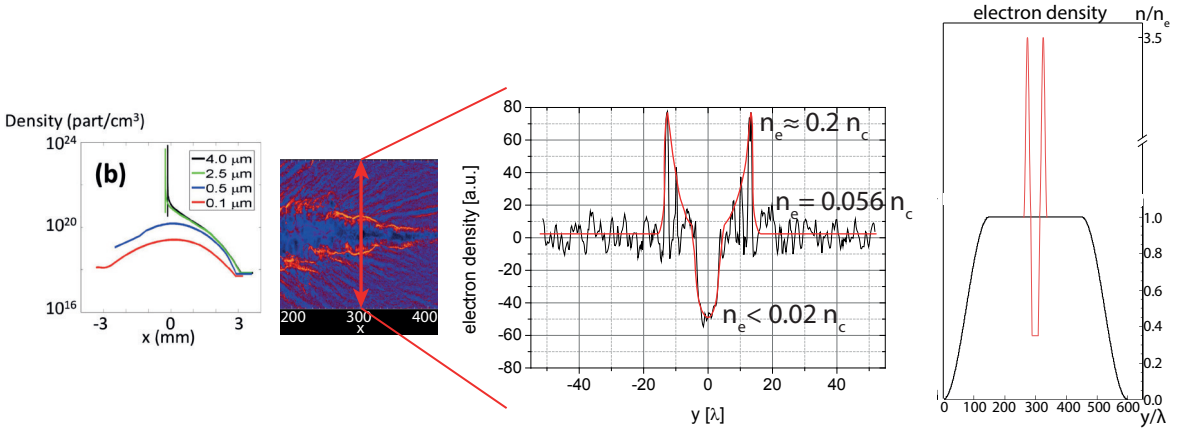

(a) Modeled n_e profiles [30]

(b) Line-out of simulated n_e profile

(c) Expected n_e profile

Figure 6.12: Pre-formed density profiles for the interaction of the second laser or rather the Driver laser. Graph (a) shows the different underdense target profiles for different initial foil target thicknesses, plot of [30]. (b) contains a vertical line-out of the Heater-only simulations and (c) illustrates the total modified density profile.

Willingale et al. [13] published results about a longitudinal ion acceleration due to an electric field acting as sheath field for a TNSA-like acceleration. 2D PIC simulations were performed to further investigate the experimentally observations. The laser parameters were different to the ARCTURUS laser, with $\tau = 500\,\text{fs}$, $d = 8\,\mu\text{m}$ and a peak vector potential of $a_0 \sim 13$. It was discussed, that the electrons were accelerated by fields inside the plasma and direct laser acceleration. A longitudinal electric field can be seen in the simulations, which acted as an accelerating sheath field for the slowly responding ions at the plasma-vacuum interface. Further simulations showed a time varying magnetic field, which was all the time smaller compared to the electric field (build up by a charge separation), compare figure 6.13. However, due to this magnetic field the electrons were pinched, which led to a collimated electric field. As a summary, Willingale et al. observed an ion acceleration from an underdense gas target in the longitudinal direction, caused by a charge separated field supported by a quasistatic magnetic field. The difference to the experimental data in this thesis were the laser and target parameters.

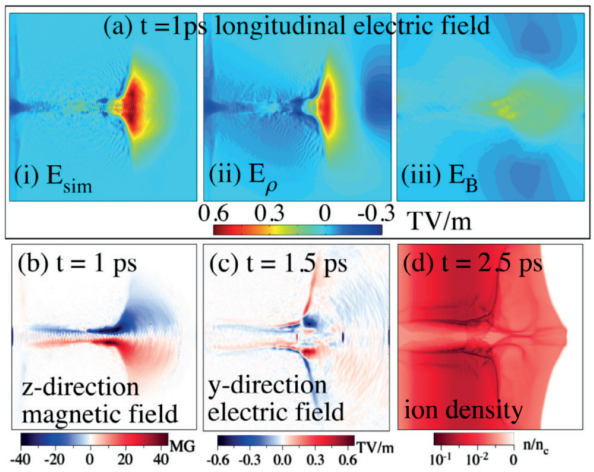

Figure 6.13: Simulation results of *Willingale at el.*. Picture (a) shows the longitudinal electric field (i) and its contributing parts of the charge separation (ii) and the varying magnetic field (iii). Picture (b) and (c) illustrate magnetic and electric field at the plasma edge and (d) the ion density including the pinching effect (Figure 1 of [33]).

Further publications by *Bulanov et al.* about ion acceleration from underdense targets in the longitudinal direction refereed to this quasistatic magnetic field at the plasma-vacuum interface as the mechanism to accelerate and collimate the ions [32, 89, 115, 116]. The magnetic field was build up by a vorticose motion of the electrons along the plasma channel. At the same time, electrons were pushed out into the vacuum by the magnetic fields and were redistributed into the plasma in order to form a positively charged area. Therefore, a long living electrostatic sheath was build up, due to which a collimated ion beam originating from the central channel axis is accelerated, compare figure 6.14. The big disagreement in this scenario were as well the laser parameters, which have reached PW-intensities with a huge normalised vector potential, even more diverse compared to the *Willingale et al.* data.

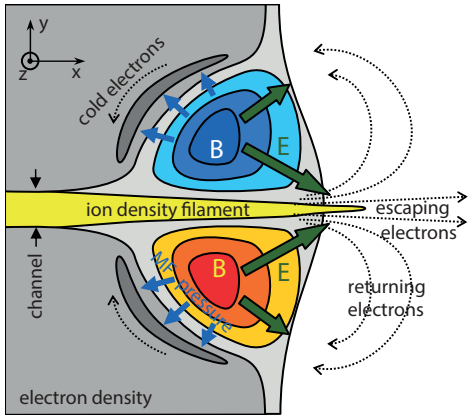

Figure 6.14: Sketch of *Bulanov et al.* about the ion acceleration due to a vorticose electron motion. The quasistatic magnetic field assists to keep up an electric field to collimate and accelerate ions from the channel axis (Figure 1 of [32]).

A more promising interpretation is an acceleration due to a TNSA-like mechanism, as already indicated by the simulations. The pedestal level of the Heater beam creates a pre-plasma-channel, which is evolved up to the centre of the nozzle when the Driver beam interacts with this high density barrier. Electrons gain energy of the laser field and are accelerated in the forward direction. A sheath field is created, due to which the ions of the density barrier are also accelerated in the forward direction. The higher the target density, the higher the amount of accelerated electrons and therefore the higher the ion energy, because of a higher correlated electric field. The prechannel is still created by the Heater even at very high densities, because the intensity level is still high enough to do multiphoton ionisation. However, only the double beam interaction is effective at very high densities, as already discussed. The target is too dense for the Heater beam in order to create a fully evacuated channel for CE, but the interaction is still able to produce a necessary density spike in the target of the Driver beam.

target density	min	max
n_e [cm^{-3}]	$1.6 \cdot 10^{19}$	$3.92 \cdot 10^{20}$
n_e/n_c	0.009	0.228
E_H [keV]	278	1313
E_{He^+} [keV]	140	675
$E_{He^{++}}$ [keV]	197	943

Table 6.3: The maximum cut-off energies of the TNSA mechanism for Hydrogen and Helium ions at the minimum and maximum target density.

The plasma expansion into vacuum was simulated for the ion acceleration caused by electrostatic sheath fields for example by *Mora* [117]. By assuming an TNSA-like acceleration mechanism, the maximum achievable energy can be calculated as described before in equation 2.40. By inserting the laser parameters of the Driver beam and the minimum and maximum target density, the cut-off energies with a hot electron temperature of $T_{hot} = 3.73\,\text{MeV}$ can be calculated, see table 6.3. These energies are slightly higher than in the experiment, but they fit well within the range of the measured values. In addition, the theoretical calculated maximum energy is reduced due to the profile of the density wall. A solid target with no plasma scale length is assumed for the calculation of the accelerating field in the TNSA mechanism. However, as shown in [118, 119] the electric field is drastically reduced by increasing the density scale length at the target rear surface to: $E = T_e/(eL_n)$, with L_n as local plasma scale length. The

experimentally observed channel barrier (in this thesis) was larger, about 10 μm, than the plasma Debye length (equation 2.29), which was in the order of 0.42 to 2 μm, depending on the target density. This should lead to a reduction of the maximum ion energy compared to the calculated values of table 6.3. Therefore, the maximum energy of around 200 keV at the lowest target density (refer table 6.3), would be even less, due to the density profile effect. Thus, the energy of these accelerated ions was below the ion energy of the transverse accelerated ions via CE. As a consequence only the ions accelerated from high density targets were detected. In other words, the TNSA-like acceleration of the double beam interaction is dominant at high target densities, while at lower target densities the Coulomb explosion of the Heater interaction dominates the acceleration.

6.4 Results of the complementary diagnostics

A different magnetic spectrometer was employed in the transverse direction to the Driver laser axis. The main purpose of the spectrometer was the detection of ions. However, no ions were observed, rather, electrons were detected during a Driver-only interaction or a double beam interaction. Furthermore, it was confirmed by means of shadowgraphy images of the Driver laser interaction, that the laser was only able to propagate to the target centre. The channel burst and filamented, afterwards. Therefore, no plasma channel, necessary for a Coulomb explosion was generated by the Driver laser.

6.4.1 Electron acceleration by the Driver interaction

A different magnetic spectrometer also in 90° direction to the Driver laser axis was installed, as shown in figure 4.24. The spectrometer had two purposes in the setup of the f/25 Heater beam. A magnet with an average field strength of $B = 0.178\,\mathrm{T}$ and geometrically aligned to the centre of the laser axis was used in order to spectrally resolve electrons and ions at the same time. Electrons with a minimum energy of about 5 MeV and ions respectively, deflected in the opposite direction, with a minimum energy of about 5 to 30 keV depending on the ion species could be detected. In all interaction with different laser and target parameters, no ion signal was detected via the spectrometer.

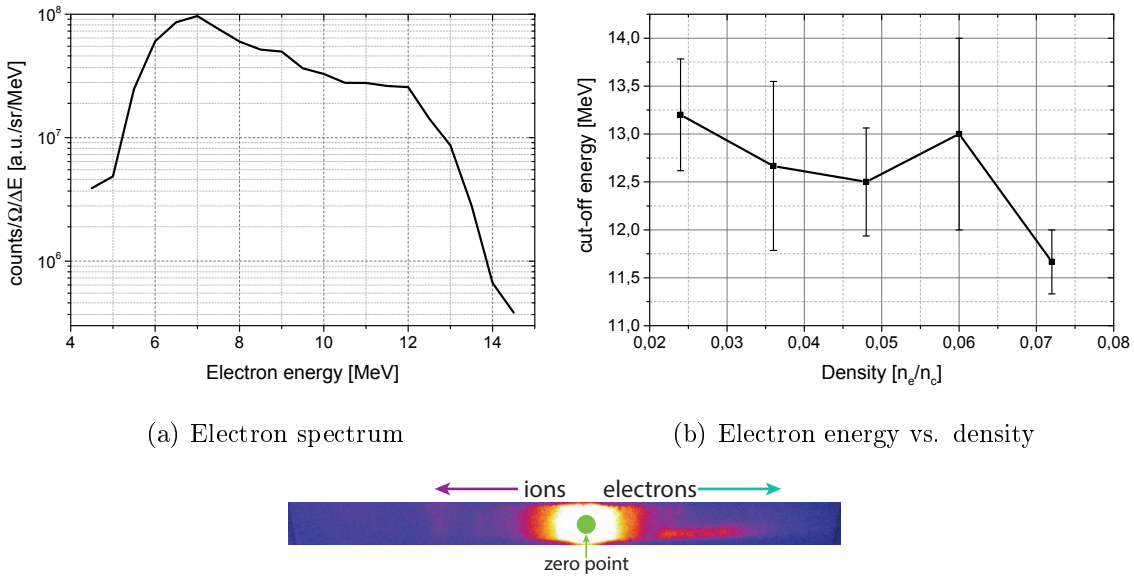

(a) Electron spectrum

(b) Electron energy vs. density

(c) Raw images

Figure 6.15: Electron energy spectrum from the interaction of the Driver with a Helium gas target at a density of $0.024\,n_c$. Image (a) shows the electron energy spectrum, graph (b) the evolution of the maximum energy versus target density and graph (c) illustrates the raw spectrometer image.

Figure 6.15, plot (c), shows the raw CCD camera image of the MCP screen. The zero point is illustrated by a green dot. Ions would be deflected by the magnet to the left and electrons to the right. This image and the trace visible on the right corresponds to the electron spectrum in plot (a). The electrons were accelerated by a Driver-only interaction with a Helium target at a density of $0.024\,n_c$. A cut-off energy of about 14 MeV was achieved. Plot (b) illustrates a statistics of the maximum cut-off energy versus target density for an interaction of the Driver with an Helium target. The maximum cut-off energy of the accelerated electrons slightly decreased with density from about 13.5 MeV to around 11.5 MeV at a density of $0.072\,n_c$.

Before, in subsection 5.4.1 (electron acceleration due to the Heater) no electrons accelerated by a Driver-only interaction were distinguished, because of the sensitivity of the detection medium and the spectrometer configuration. The detection efficiency of the MCP, which actively amplifies the signal, is much higher compared to the passive Kodak scintillator screen. As a result, the flux of the electrons, described in here, must be very low, compared to the LMFA acceleration by the f/10-Heater beam. Secondly the

spectrometer configuration was different: The lower detection limit was about 11 MeV. For that reason, the low energy electrons accelerated by a Driver-only interaction could not be discovered in the subsection 5.4.1.

These low flux and low energy electrons were accelerated normal to the Driver axis. The electrons were pushed by the transverse acting ponderomotive force. However, as discussed later in subsection 6.4.2, it is visible in the shadowgraphy images of the Driver interacting with the target, that no plasma channel was created. Therefore, there was no fully evacuation of the electrons in the transverse direction and accordingly no ion acceleration due to Coulomb explosion. Only a few electrons could escape the Coulomb potential and be detected by the spectrometer.

6.4.2 Optical probing of the Driver-target interaction

Shadowgraphy of the Driver beam was performed by means of the ARCTURUS probe beam, as seen in the illustration of the setup, plot(b) of figure 4.27. Images of different times of the interaction of the laser beam with a Helium target at a density of $0.024\,n_c$ are shown in figure 6.16. The red dashed lines represent the centre of the gas nozzle. The laser interacted from the left to the right with the gas jet, as illustrated by the red arrow in the first image.

As already discussed before, in Figure 5.4.2, the plasma channel needed about 3 ps to reach the centre of the gas target. However, the difference in the plasma channel, created by the Driver beam, is an explosion of the channel after 2.5 ps. The channel filamented in the central part of the nozzle.

The Driver was focused by the f/2 OAP to a very high intensity of $a_0 = 8$ and a tight focal spot radius of $r_0 = 2\,\mu$m. The interaction length with the plasma was short, due to the very short Rayleigh length of $z_{\text{r-f/2}} \sim 4\,\mu$m, instead of $z_{\text{r-f/10}} \sim 102\,\mu$m. Therefore, no plasma channel could be created and a burst at the target centre took place. This indicates, that no Coulomb explosion could happen by means of the Driver beam, as already discussed.

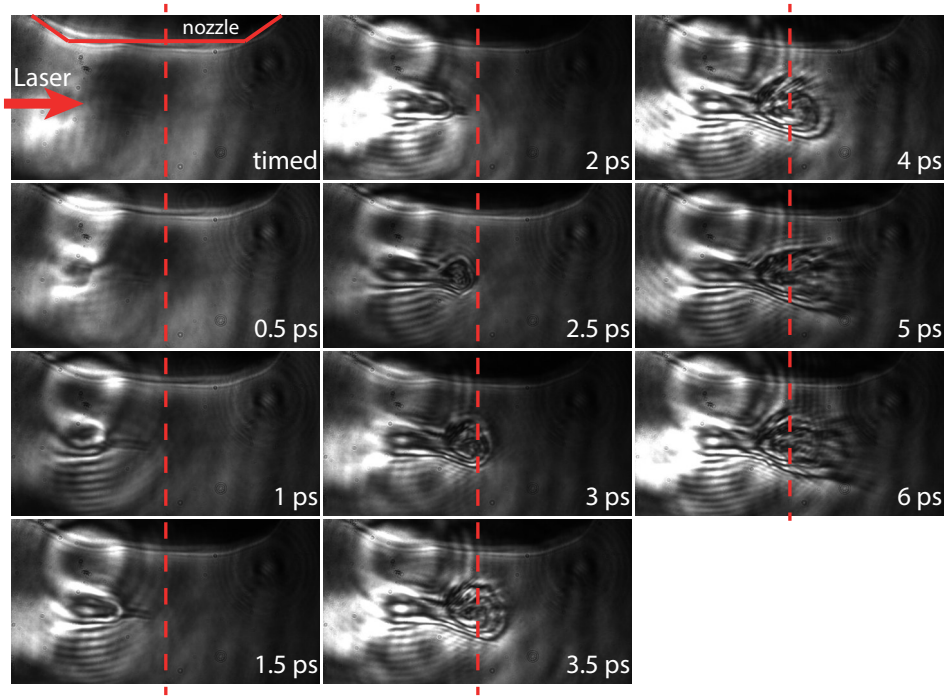

Figure 6.16: Shadowgraphy of the Driver laser beam at different times of the interaction with a Helium gas target with a density of $0.024\,n_c$. The laser comes from left to right and the dashed red line represents the centre of the nozzle.

6.5 Summary

A novel experimental scheme leading to an ion acceleration from underdense targets is presented in this chapter. By the unique capability of the ARCTURUS double beam configuration ions were accelerated via a TNSA-like mechanism.

A high intensity short focal length Driver beam (f/2 OAP, $1.5 \cdot 10^{20}\,\mathrm{W/cm^2}$) was employed normal to the Heater (f/10 OAP) axis in addition to the single beam configuration, where ions were accelerated in the transverse direction via Coulomb explosion. Both beams were overlapped in time and space. While the acceleration due to CE was not sufficient enough at target densities higher than $0.12\,n_\mathrm{c}$, ions were detected up to $0.18\,n_\mathrm{c}$ by means of the double beam interaction. The acceleration process was still in the same direction, transverse to the Heater axis or longitudinal to the Driver axis. A Driver-only interaction was not able to accelerate any ions neither in the longitudinal direction nor in the transverse direction. The experimental results showed, that CE was the dominating process at low target densities, whereas at high densities, a TNSA-like process took place. A novel transition of the leading acceleration mechanism in a new experimental scheme took place. The plasma was pre-formed by the interaction of the pedestal level and the main pulse of the Heater laser beam, forming a pre-channel structure. The Driver laser interacted with this channel edge, appearing like a density spike close to the centre of the underdense target. Ions were accelerated via an electric field in a TNSA-like process. Experimental results reproduced by numerical simulations allowed the identification of the acceleration method. Analytical calculations excluded various other processes and strengthened the conclusion about the TNSA-like mechanism.

A magnetic spectrometer was employed as an additional diagnostic in order to detect ions and electrons at the same time in the transverse direction to the Driver axis. The most important result of the diagnostic was, that no ions were detected. Only low energy electrons were identified during a Driver interaction. Moreover, the interaction of the Driver was investigated via optical shadowgraphy. No plasma channel was created by the Driver laser. The channel burst in the centre of the target, which indicates that a CE by a Driver-only interaction was not possible.

Chapter 7

Development of a monoenergetic ion source from underdense targets

In this chapter, the development of a monoenergetic ion source from underdense targets is described. The TNSA-like acceleration mechanism by the double beam interaction with the gas target led to a novel applicable source of a stable, high repetition rate monoenergetic ion beam. These sources are desirable in many applications schemes such as isochoric heating [120], medical physics [121] and inertial confinement fusion [122].

As discussed in chapter 6, the interaction of a Driver beam with a preformed target profile including density boundaries led to an ion acceleration via a TNSA-like process. Clearly the density spike at the wall of the depleted channel enabled a sheath field formation and consequently ion acceleration took place. Nevertheless, the plasma channel created by the strong f/10 Heater, as described before, expanded in time, because of the expelling nature of the Coulomb explosion mechanism. The depleting channel walls were pushed radially away from the laser axis.

Based on the previous experimental studies across various laboratories, the ion acceleration was mostly observed via Coulomb explosion of the plasma channel or ponderomotive acceleration in underdense targets. At the same time, various studies show a steep density gradient in overdense targets as precondition for monoenergetic ion acceleration via a TNSA process. Therefore, the idea was conceived of creating a specially preformed plasma profile in order to generate a spatially homogenous localised electric field in the TNSA-like process. Thanks to the availability of the second short femtosecond, high

power laser pulse of the ARCTURUS laser a preformed target was attained, which will most likely help to generate a monoenergetic ion source. For this reason, the interaction strength of the Heater beam was reduced by focusing the beam by means of an f/25 OAP to about $6.6 \cdot 10^{17}\,\mathrm{W/cm^2}$, going along with an increased Rayleigh length (setup in figure 4.24). This beam was not strong enough to initiate an ion acceleration via CE, but still adequate intense to generate a plasma channel for the double beam interaction. Therefore, unlike to the case of the previous chapter, a setup was designed, where a long focusing parabola was employed to create sharp density spikes, while the Driver beam, however, remained the same. Furthermore, an arrangement with a lower intensity Heater beam allows a very flexible and compact source, which can be developed at university scale laboratories.

In the following, the interaction of the Driver beam with a suitably tailored density profile generated with the help of Heater beam is investigated via varying numerous laser and target parameters. Ion acceleration from Helium or Hydrogen gas was investigated via two Thomson parabola spectrometer in the longitudinal direction to the Driver axis. In addition, a magnetic spectrometer was employed in the setup in the transverse direction to the Driver laser axis. The main purpose of this diagnostic was the detection of ions in this direction. However, only electrons were detected by the interaction of the Driver and of Driver plus Heater with the target. No ions were observed in this direction during the various target and laser adjustments. Moreover, no ions were detected in a single beam interaction neither along 90° nor along 0° with respect to the Driver. Only due to the double beam interaction, ions were successfully accelerated by a variation of the TNSA-like mechanism, identified by the investigations described in the last chapter. However, the preformed target was more expanded, less evacuated of electrons, but the depletion of the density spikes was slower due to the intensity reduction of the Heater laser. At a certain density range ($0.056 - 0.103\,n_\mathrm{c}$) with defined laser parameters and a specific temporal delay between the beams, the pre-formed plasma was generated in a specific way. As a result, a spatially homogenous localised electric field was created in order to accelerate monoenergetic ions due to the Driver interacting with a specially shaped target. Small variations in the target and laser parameters resulted in broadband spectra. A large range of laser and target parameters were explored in order to optimise the novel, high repetition rate, monoenergetic source, required greatly in many potential applications.

7.1 Acceleration of monoenergetic protons from Hydrogen gas

The proton acceleration due to the laser interaction with a Hydrogen gas target is investigated in detail by changing different parameters of the target and the lasers. First some characteristic proton energy spectra are shown. Then the evolution of the maximum cut-off energy versus relative laser time delay and target density is illustrated. Moreover, the appearance of a monoenergetic feature in the proton spectra is further studied by changing the laser energy and the relative time delay between the two beams.

Proton energy spectra

Four selected proton spectra at four different Hydrogen gas target densities, recorded by the 0° Thomson parabola, are shown in figure 7.1. The flux of the protons in the spectra is above the flux detection limit of $1.5 \cdot 10^8$ particles/sr/MeV. At a density of $0.056\,n_c$ (black) and of $0.103\,n_c$ (red) sharp monoenergetic features can be recognised. The ions of the lower density feature ($0.056\,n_c$) had an energy of about 225 keV and a spectral width of 25 keV, while the monoenergetic ions at $0.103\,n_c$ reached an energy of around 340 keV and also a spectral width of about 25 keV. However, the ions, accelerated at higher target densities ($0.14\,n_c$, blue and $0.177\,n_c$, green) had broadband energy spectra and higher cut-off energies of about 400 keV. Consequentially: The higher the target density, the higher the cut-off energy. Figure 7.2 presents the raw images of the energy spectra of the 0° and respectively of the 10° Thomson parabola spectrometer of the evaluated spectra of figure 7.1. The monoenergetic features were only identified along 0° and not by the spectrometer along 10°. Therefore the acceleration of the protons in this regime was not only monoenergetic, but as well highly collimated.

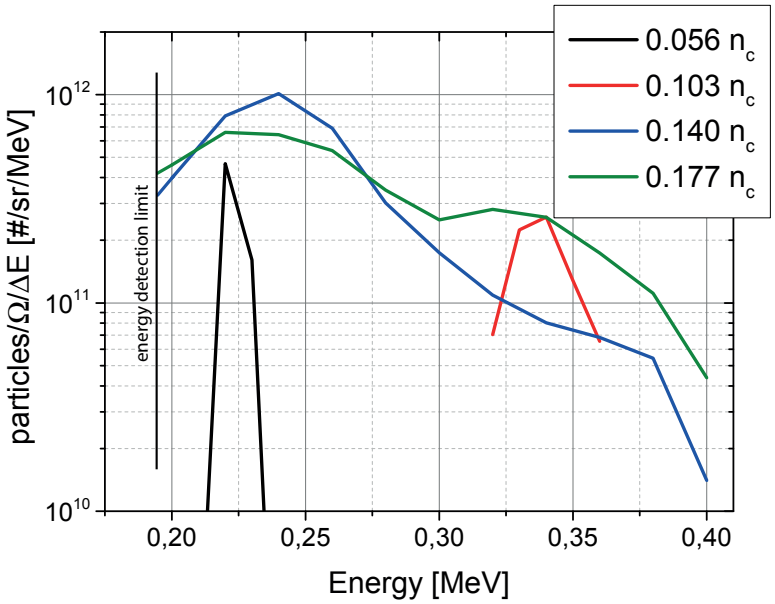

Figure 7.1: Proton energy spectra for different neutral target densities, detected by the 0° Thomson parabola spectrometer. Monoenergetic features can be recognised up to about $0.103\,n_c$, while the energy spectra is broadband at higher target densities.

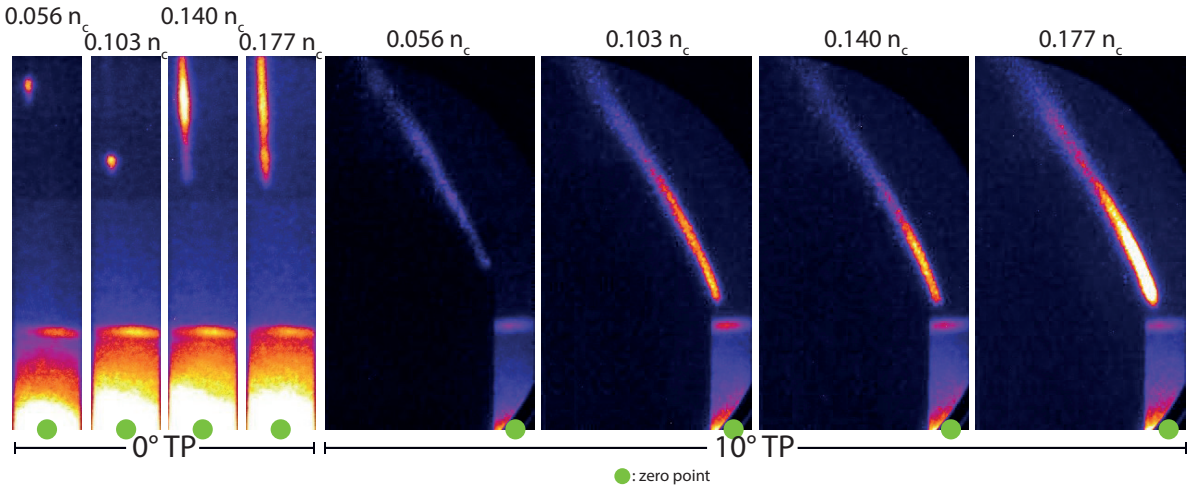

Figure 7.2: Raw images of the proton traces of the 0° and 10° spectrometers (related to the Driver beam). Monoenergetic features are only visible along 0°. The corresponding energy spectra along 10° reveal only broadband energy distributions.

Spectral features versus target density

The spectral features versus target density, detected by the 0° Thomson parabola spectrometer, can be summarised in a simple statistics. Nearly no proton signal was detected for low gas densities. Monoenergetic particles were observed in a mid range density and broadband spectra appeared at high target densities. A change in the density of a factor of two or even less changed the proton energy profile drastically.

Figure 7.3 illustrates the evolution of the energy spectral characteristics. The small numbers below the x-axis show the absolute number of laser interactions counting for that histogram column. For target densities below $0.056\,n_c$ no ion signal was detected in 90% of 74 laser interactions. At densities above this value and below $0.103\,n_c$ the probability of a monoenergetic acceleration (∼70% of 34 interactions) exceeds the one having a broadband (∼20%) energy spectrum or even no ion signal (∼10%). Most of the time the spectral characteristics were transformed to broad spectra (in 75% of 53 recorded spectra) at higher densities.

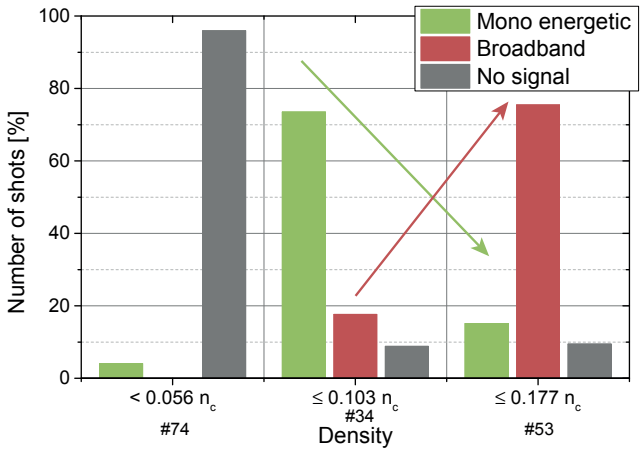

Figure 7.3: Statistics of the spectral characteristics of the protons for different density regimes.

Maximum cut-off energy versus relative delay and target density

The maximum proton energy, excluding the spectral characteristics in the analysis, was mainly dependent on the target density, the delay between the beams and the detection angle.

In conclusion both spectrometers showed that the higher the target density, the higher the cut-off energy. However, protons accelerated by the interaction with the lowest

density target were not identified along 0°, because the energy was below the detection limit of about 180 keV, while in the 10° TP ions to about 30 keV could be resolved.

A Driver interacting earlier than the Heater with the target was inefficient for the acceleration, while the best condition was at ±10 ps of the two laser pulses. A long relative delay between Heater and Driver (with Heater first) led to a lower energy acceleration. This effect was seen in the 0° and 10° spectrometer.

Worth mentioning is, that the cut-off energy along 0° was nearly twice that high as in a 10° detection angle.

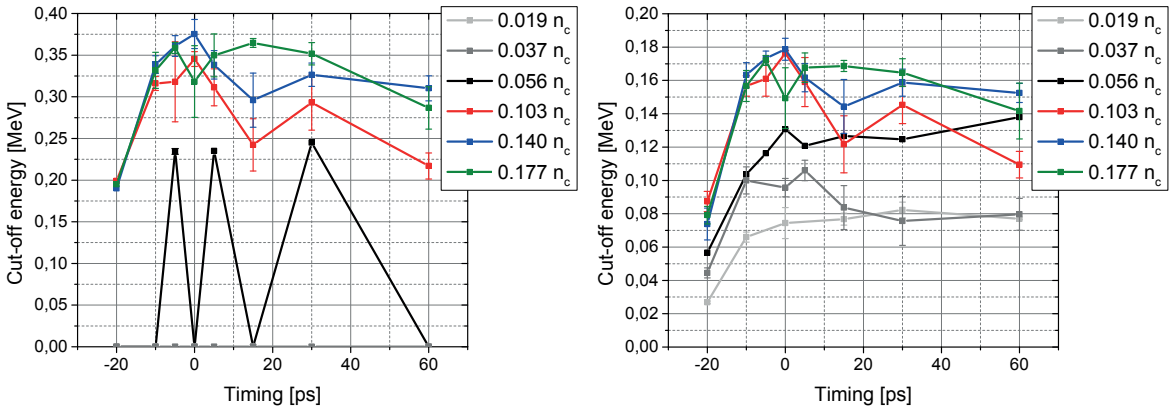

(a) Maximum energy - 0° TP

(b) Maximum energy - 10° TP

Figure 7.4: Dependence of the maximum proton energy on the different target densities and time delays between the two laser pulses. Plot (a) represents the values detected by the 0° Thomson parabola spectrometer and plot (b) by the 10° TP.

Figure 7.4 shows the dependence of the cut-off energies along 0°, plot (a), and 10°, plot (b), for different target densities and different relative time delays between the two laser pulses. The Driver beam was impinging earlier in the negative x-direction, the Heater in the positive x-direction. Both graphs demonstrate a similar trend for each target density. When the Driver beam reached the target 20 ps before the Heater, the cut-off energy was decreased drastically to about 180 keV along 0° and about 80 keV along 10°. In comparison, the cut-off energies at zero delay were about 350 keV along 0° and 170 keV along 10°, which were about twice as high as the values at the negative time delay. For positive timings, Heater before Driver, the cut-off energy was decreasing slowly, but was more or less constant up to minimum values of about 220 keV and 130 keV. In conclusion, the higher the target density, the higher the cut-off energy, is mainly valid for a positive

time delay. Ions accelerated from a low target density ($\leq 0.037\,n_c$) were not detected by the 0° Thomson parabola spectrometer, but along 10°. The cut-off energy at the densities of $0.037\,n_c$ and $0.019\,n_c$ were much lower than for higher values.

Monoenergetic features

The highlight of the novel acceleration features, the monoenergetic spectra, were investigated in more detail for a better understanding by varying the laser energy and the relative time delay between the two beams. These parameter changes were performed at a target density of $0.103\,n_c$, where most of the time monoenergetic features were observed.

Spectral features versus laser energy

In order to investigate the dependence of these monoenergetic features on the laser parameters, both beams were successively reduced in energy and the spectral features were observed. Only with a strong Driver of about 70% of its initial energy, the feature could still be distinguished at 0°. This means, the Driver beam had to have an intensity at a minimal value of about $10^{20}\,\mathrm{W/cm^2}$, with an $a_0 > 6$, otherwise broadband energy protons were accelerated by the interaction. In contrast, the combination of a high energy Driver beam and a reduced Heater energy was still leading to a monoenergetic proton acceleration even with a Heater beam of 43% of its initial energy. Therefore, a Heater with an intensity of $3 \cdot 10^{17}\,\mathrm{W/cm^2}$ was still able to set the right condition for a successful monoenergetic proton acceleration.

Figure 7.5 shows the evolution of the spectral characteristics over all laser target interactions at only one target density of $0.103\,n_c$ detected by the 0° TP. Plot (a) pictures this evolution with reducing the Driver laser energy from 100% to less than half of its initial energy, while the Heater energy remained at 100%. The probability of having monoenergetic features decreased with decreasing laser energy from ∼70% (of 34 interactions) down to zero (in 16 interactions), while the probability of having broadband energy proton spectra increased from ∼20% (of 34 interactions) up to 50% (of 16 interactions). But at the same time, the whole ion acceleration process occurred less frequently from ∼10% (of 34 shots) up to 50% (in 16 laser interactions).

Plot (b) shows the changes of the spectral characteristics, while reducing the Heater energy from 100% to only 8.7%. The probability of having monoenergetic spectral features decreased from ∼70% (of 34 interactions) down to ∼30% (of 19 interactions) and

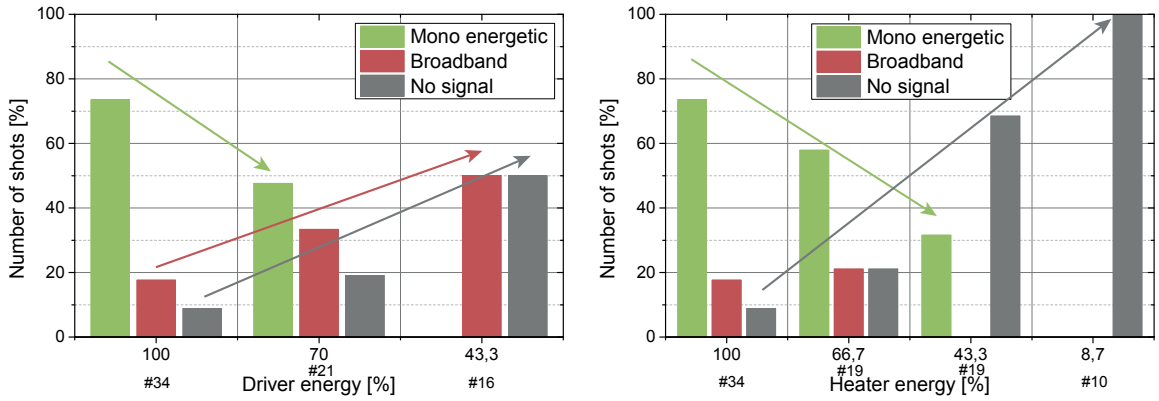

(a) Reduction of the Driver energy 100% Heater energy

(b) Reduction of the Heater energy 100% Driver energy

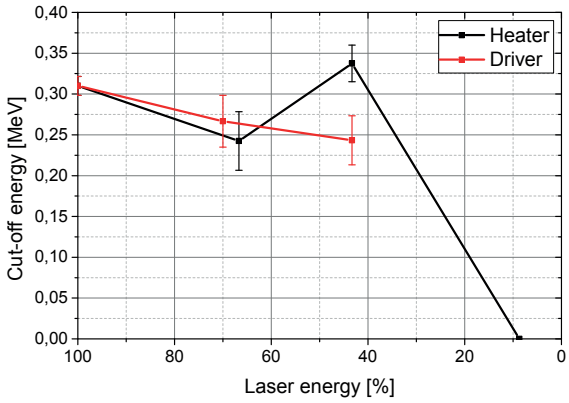

(c) Cut-off energy vs laser energy

Figure 7.5: Statistics of the spectral characteristics of the proton energy for a reduction of the Heater and Driver laser energy for one target density of $0.103\,n_c$ (observation along 0°).

further down to 0% (of 10 laser shots). In this case, the spectral characteristics did not shift towards a broadband energy spectrum, rather towards an inefficient acceleration.

Plot (c) illustrates the evolution of the maximum cut-off energy by reducing the Heater and Driver laser energy. Although the spectral characteristics of the accelerated ions changed noticeably, the maximum cut-off energy did not vary drastically. However, the ion energy was slightly increased with a Heater energy of only 43% of its initial value, while by reducing the Driver energy, the maximum cut-off ion energy decreased.

Spectral features versus relative temporal delay

Furthermore, the effect of the relative delay of the two laser beams on the acceleration was investigated at the same target density of $0.103\,n_c$. Clearly, only by a timed or slightly delayed interaction, the sharp monoenergetic features were observed in most of the interactions. The assumption, Driver first or Heater much earlier than the Driver, was leading to a broadband spectrum.

Figure 7.6 shows a Histogram broken down into single time steps. Each delay was measured over three laser interactions at maximum initial laser energy. By means of this graph, however, it is visible, that the acceleration of monoenergetic protons took place predominantly around $-10\,\mathrm{ps}$ to $0\,\mathrm{ps}$. Negative x-values represent the Driver beam, which reached the target before the Heater, positive values vice versa, Heater before Driver. The larger the time delay between the Heater and the Driver in the positive direction, the higher was the probability of getting a broadband spectrum.

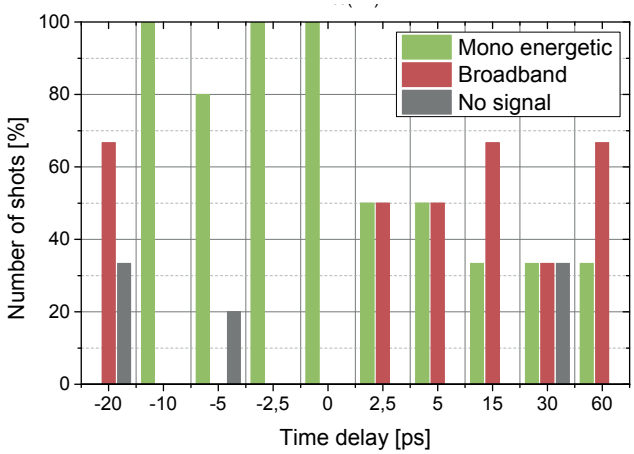

Figure 7.6: Statistics of the spectral characteristics of the proton energy for different relative delays between the two laser pulses for on target density of $0.103\,n_c$.

7.2 Acceleration of Helium ions

Both ion species of Helium were accelerated by the interaction of the Heater and Driver laser with the Helium gas target. The ion energy distribution and spectral characteristics are discussed in the following. First of all, four characteristic Helium ion energy spectra are shown. Afterwards, the detection of the different ion species and spectral features are illustrated. Then, the evolution of the maximum cut-off energy versus relative laser time delay and target density is presented. Moreover, the appearance of the two different ion species in the spectra was further investigated by changing the Heater laser energy.

Helium ion energy spectra

Four typical ion spectra detected by the 0° Thomson parabola spectrometer are presented in figure 7.7. He^+ ions were accelerated from a low density gas, $0.024\,n_c$ (black), up to an energy of about 210 keV. At a target density of $0.060\,n_c$ (red) a monoenergetic He^+ ion spectrum was visible, with a maximum energy of about 350 keV and a spectral width of 60 keV. Moreover, the spectrum was broadband again at a density of $0.084\,n_c$ (blue) with a maximum energy of about 200 to 220 keV. With the highest density of $0.228\,n_c$ (green), He^+ up to 120 keV and at the same time fully ionised Helium, He^{++}, up to 260 keV were identified. The detection limit of the Thomson parabola spectrometer for He^{++} was at about 170 keV, while He^+ ions could be distinguished to a minimum energy of about 50 keV. The corresponding raw images of the spectra are shown in figure 7.8. The images of the 0° Thomson parabola spectrometer are illustrated on the left side, whereas the raw images of the 10° Thomson parabola spectrometer on the right-hand side. The traces of the two species are labelled and can be clearly distinguished to each other. He^{++} traces were visible even at low target densities in the 10° direction.

Spectral features and ion species versus target density

The observed ion species changed with respect to the target density. The probability to detect He^+ decreased over the whole density range, while He^{++} only appeared at very high densities. Monoenergetic features were exclusively observed in the He^+ spectrum at a specific density.

The histogram in figure 7.9 shows the evolution of the spectral features and detected Helium species in 0° direction versus target density. The probability to detect He^+ decreased over the whole density range, while He^{++} appeared from a high density of

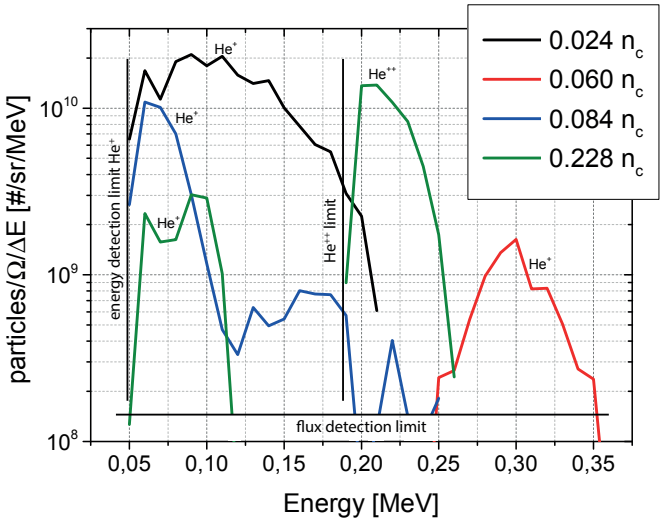

Figure 7.7: Helium ion energy spectra at different neutral target densities, detected by the 0° Thomson parabola spectrometer. A monoenergetic feature can be recognised at a certain target density, while broadband energy spectra were distinguished at all other target densities. Fully ionised Helium was detected at the highest densities.

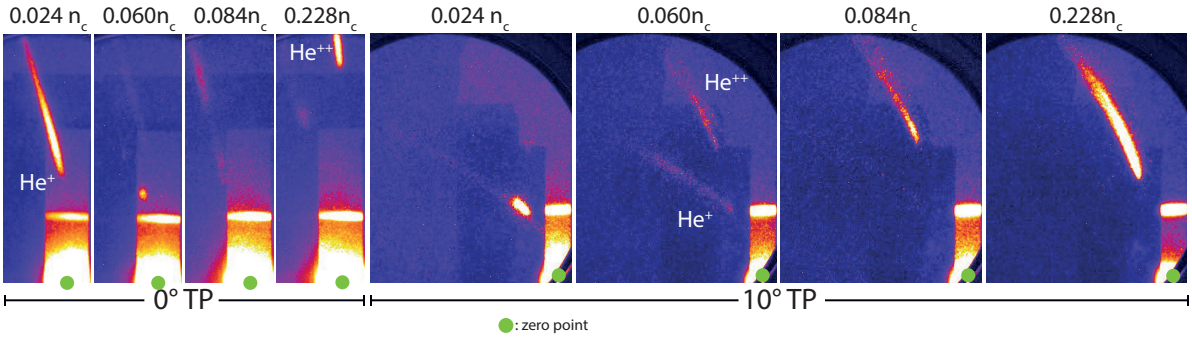

Figure 7.8: Raw images of the Helium ion energy spectra in 0° and 10° direction, related to the Driver beam.

$0.132\,n_c$ on. This effect had nothing to do with the actual appearance of the species in the plasma, rather the detection was limited due to the specific configuration of the spectrometer setups. The energy of the accelerated He^{++} probably decreased below $< 170\,keV$ (the detection limit) at low target densities, which was too low to be resolved by the Thomson parabola spectrometer. However, at the same time both species were detected by the TP spectrometer along 10°. Monoenergetic features were only visible in the spectra of the He^{+} ions and mostly at a target density of $0.060\,n_c$ in over 60% of 30 recorded spectra. At the target density of $0.132\,n_c$ the chance was low to detect any ion signal. In 50% of 8 laser interactions no ion signal was identified.

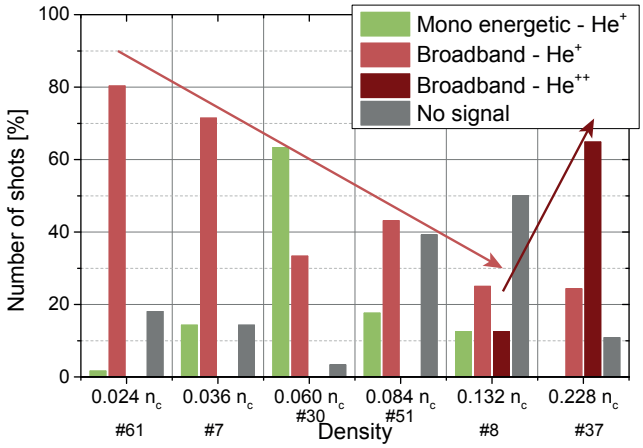

Figure 7.9: Statistics of the spectral characteristics of the Helium ion energy for different density regimes.

Maximum cut-off energy versus relative delay and target density

The trend of the maximum ion energy versus delay between the laser pulses was similar to the evolution of the proton energy distribution described before (see figure 7.4). The ion energies in the 0° direction were also about twice as high as in 10° direction. Worth mentioning, however, is: The higher the density, the higher the He^{++} energy and the lower the He^{+} ion energy.

By adjusting the relative time delay between the Driver and the Heater a difference in the maximum energy of the accelerated ions can be found, see figure 7.10, plot (a). Driver before Heater (negative timing) led to lower cut-off energies of the Helium ions until the acceleration vanished completely. Maximum energies were reached at around $+10\,ps$ (Heater before Driver) from around $100\,keV$ up to $325\,keV$, depending on the target density. At higher delays (later timing) the cut-off energies were constant over

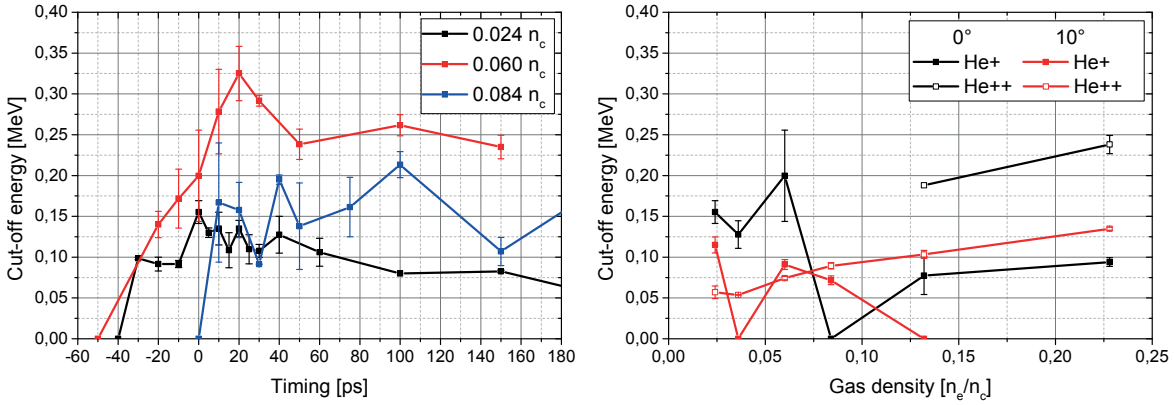

(a) Maximum He^+ energy - 0° TP

(b) Maximum energy - at zero laser time delay

Figure 7.10: Dependence of the maximum Helium ion energy on the different target densities and time delays between the two laser pulses. Plot (a) represents the values detected by the 0° Thomson parabola and plot (b) the maximum cut-off energy at zero time delay between the laser pulses along 0° and 10°.

the whole time period, between 75 and 250 keV, on average. Plot (b) shows the cut-off energy versus target density for a zero relative time delay between the two lasers in 0° (black) and 10° direction (red) at all target densities. The evolution was not as clear as for Hydrogen in the low density regime. Only at high target densities the maximum ion energies of He^+ and He^{++} increased with the density in the 0° observation angle. The trend in 10° direction turned out to be: The higher the density, the higher the cut-off energy, only valid for He^{++} ions. The maximum energy of He^+ ions decreased with density.

Spectral features and ion species versus Heater laser energy

Moreover, the effect of the Heater laser energy on the acceleration mechanism was further investigated at two different target densities. At a low target density, the Heater energy could be reduced down to 2.8% of its initial value, which corresponds to an intensity of approximately $1 \cdot 10^{16}\,\mathrm{W/cm^2}$, while He^+ ions were still observed with more or less the same maximum energy. By reducing the Heater energy at the highest target density, the probability of the appearance and the energy of the He^{++} decreased. At the same time the probability to detect He^+ ions increased, while the energy of the He^+ ions was about to stay constant at a value of about half the He^{++} energy.

Figure 7.11 shows the statistics at the two different densities, $0.036\,n_c$ and $0.228\,n_c$,

along the 0° detection angle. In plot (a) the spectral features at a density of $0.036\,n_c$ are illustrated, while reducing the Heater laser energy from 100% to 0.6% and keeping a Driver energy of 100% of its initial value. Broadband He^+ ion energy spectra were the main detected features (in over 70% of all interactions) to a Heater energy of 2.8%. The interaction of a lower energy Heater was not efficient anymore. Plot (c) pictures the corresponding cut-off energies (black) of the detected ion signal. Although the Heater energy was reduced, the maximum energy was nearly constant at a value of about 150 keV. Plot (b) shows, that He^{++} was identified at a density of $0.228\,n_c$. However, by reducing the Heater energy, the probability to detect the fully ionised Helium decreased. At a Heater energy of 70% the possibility to distinguish either a broadband signal of He^{++} or He^+ or even to detect no signal was nearly equally distributed each at around 30% of 12 laser interactions. By further reducing the Heater energy, the probability of observing He^+ increased measurably to about 75% of 12 interactions with a Heater energy of only 8.7%. The corresponding cut-off energies (plot (c), red) for He^+ were relatively constant at a value of about 100 keV, which is about 1.5 times lower than the ion energies at a lower target density. The trend of the He^{++} cut-off energies decreased probably below the detection limit of the TP by reducing the Heater energy.

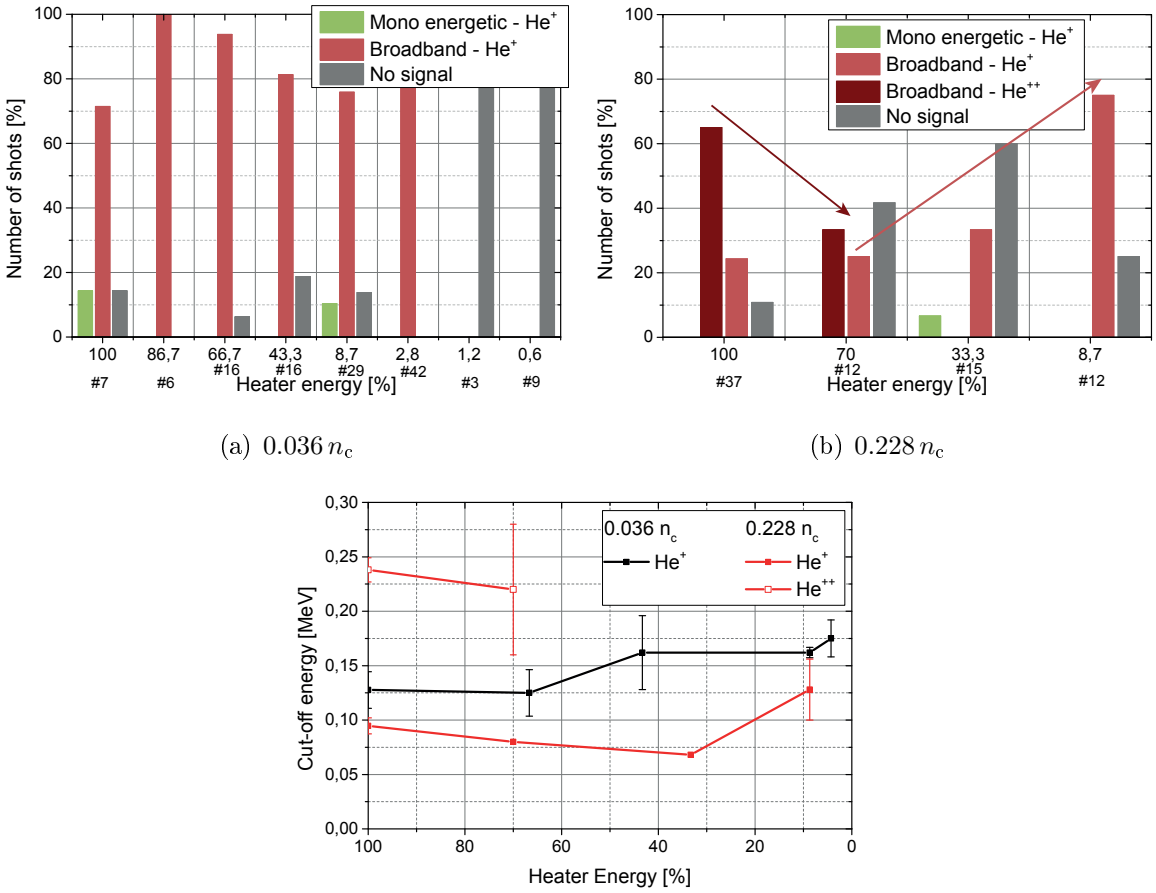

(a) $0.036\,n_c$

(b) $0.228\,n_c$

(c) Cut-off energy vs Heater energy

Figure 7.11: Statistics of the spectral characteristics and species of the Helium ions for a reduction of the Heater energy at two different target densities of $0.036\,n_c$ and $0.228\,n_c$.

7.3 Electron acceleration by the double beam interaction

A magnetic spectrometer was employed as complementary diagnostic in the experimental arrangement, as shown in figure 4.24. First results and specifications were already described in section 6.4. The main purpose of the spectrometer was the detection of ions and electrons at the same time in the transverse direction to the Driver axis. However, no ion signal was observed neither by a single laser interaction, Driver-only or Heater-only, nor by a double beam interaction. Rather, electrons were detected at a Driver-only interaction as presented before or at a double beam interaction. None were accelerated due to a Heater-only interaction.

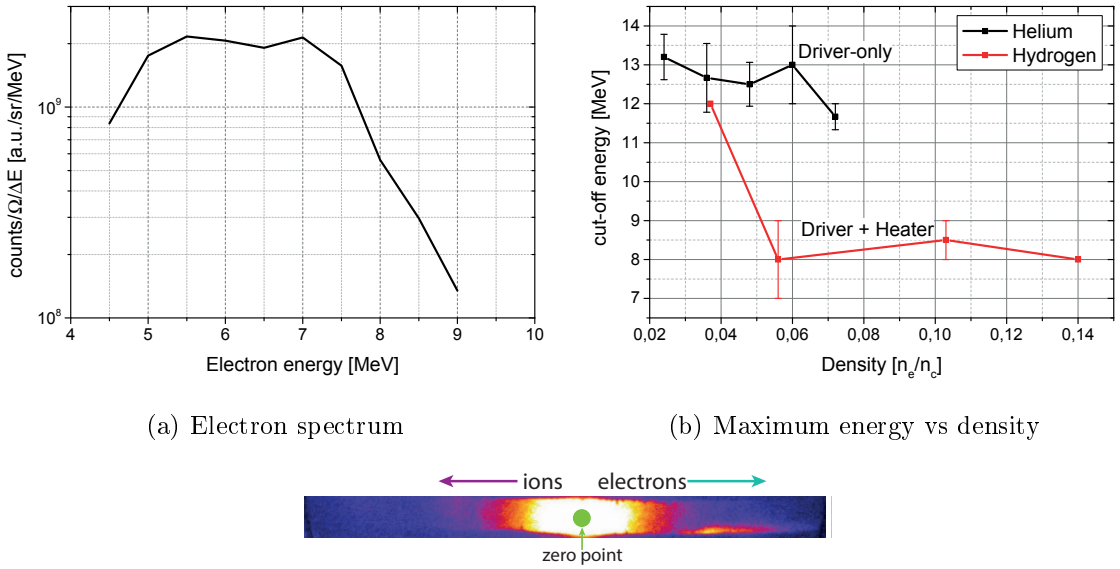

(a) Electron spectrum

(b) Maximum energy vs density

(c) Raw image

Figure 7.12: Electron energy spectrum of a double laser beam interaction with a Hydrogen gas target at a density of $0.103\,n_c$. Image (a) shows the electron energy spectrum, graph (b) the evolution of the maximum energy versus target density and graph (c) illustrates the raw spectrometer image corresponding to graph (a).

Figure 7.12, shows the results of the double beam electron acceleration and a comparison between Driver-only and Driver plus Heater interaction. The electrons in plot (a) and (c) were accelerated by a double beam interaction with a Hydrogen target at a density of $0.103\,n_c$. A maximum electron energy of about 9 MeV was reached. Plot (b) illustrates

a statistics of the maximum cut-off energy versus target density for Helium (black) and Hydrogen (red) targets or rather electrons accelerated by a Driver-only (black) and a double beam (red) interaction. The maximum energy of the Driver-only results decreased very slowly with increasing density. The double beam interaction led to an acceleration up to a density of $0.14\,n_c$ with a constant maximum cut-off energy of about 8 to 9 MeV.

The single Driver was not able to accelerate electrons at densities above $0.072\,n_c$, while electrons could be detected to a density of $0.14\,n_c$ due to the double beam interaction, although the maximum energy was reduced. As already discussed, only by both laser beams interacting with the target, ions were accelerated in the longitudinal direction to the Driver. The preionisation of the very dense targets by the Heater beam, enhanced the conditions for a transverse push of the electrons by the Driver interaction. The energy of the electrons was reduced, because electrons and ions were mainly accelerated in the forward direction. Moreover, the f/25-Heater beam with an intensity of $a_0 < 1$ was not strong enough to accelerate any electrons in the forward direction.

In summary it can be concluded that, by means of the spectrometer in the transverse direction to the Driver, electrons were detected, but no ions in any laser and target configuration.

7.4 Conclusions and discussion about the ion acceleration

Different trends and effects can be summarised following the analysis of the ion acceleration from Hydrogen and Helium gas. The most important fact is, that there was no significant detectable acceleration of ions by a single beam interaction with the gas target. Only both beams interacting together with the gas were able to accelerate ions. In this case, ions were observed by two Thomson parabola spectrometers in 0° and 10° direction related to the Driver laser axis. No ion signal was distinguished in the transverse direction to the Driver laser axis, as described before.

In the following the results of the proton acceleration from Hydrogen gas are summarised:

The evolution of the maximum cut-off energy:

- The maximum energy along 0° was twice as high as along 10°.
- Higher target densities led to higher cut-off energies.
- A relative temporal delay of $< 10\,\mathrm{ps}$ led to a decrease in the maximum energy.
- At a relative temporal delay of 10 ps up to 5 ps the maximum of the cut-off energy was reached.
- A relative temporal delay of $> 5\,\mathrm{ps}$ introduced a very slow decrease.

A density scan leads to:

- At target densities of $< 0.056\,n_\mathrm{c}$ no ions were detected.
- The spectral feature was monoenergetic at target densities of $\leq 0.103\,n_\mathrm{c}$.
- The spectral feature was broadband at target densities of $\leq 0.177\,n_\mathrm{c}$.

In order to further investigate the monoenergetic features, different highlights can be mentioned.

Strong collimation:

- Only along 0°, monoenergetic features were observed.
- The spectral features along 10° were broadband.

Two more dependencies were investigated at the 0° detection angle:

The laser energy affects the acceleration as follows:

- If the Driver energy was decreased and the Heater was kept at its initial energy, monoenergetic features were turned to broadband spectra with a constant maximum cut-off energy.
- If the Heater energy was decreased and the Driver was kept at its initial energy, monoenergetic features with a stable maximum cut-off energy were changed to no detection of ions.

The relative time delay between the laser beams affects the spectral features as follows:

- At negative delays of $-20\,\mathrm{ps}$, the spectral features were broadband.
- At delays between $-10\,\mathrm{ps}$ and $0\,\mathrm{ps}$ monoenergetic features were observed.
- At delays of $> 2.5\,\mathrm{ps}$ the spectra were again broadband.

Summarising the mentioned dependencies: The characteristics of the proton energy spectra were affected by the target density, the laser energy and the relative delay between the laser pulses.

Consecutively, the conclusions of the Helium ion acceleration are summarised:

A change in the target density leads to:

- $0.056\,n_\mathrm{c} \leq n_\mathrm{e} \leq 0.228\,n_\mathrm{c}$: The appearance of He^{+} decreased
- $0.132\,n_\mathrm{c} \leq n_\mathrm{e} \leq 0.228\,n_\mathrm{c}$: The appearance of He^{++} increased
- $0.060\,n_\mathrm{c}$: mostly monoenergetic He^{+} was observed

The maximum cut-off energy per relative delay and target density is related as:

- The maximum energy along 0° was twice as high as along 10° for He^{+} and He^{++}.
- Higher target densities led to higher cut-off energies for He^{+} and He^{++}.
- A relative temporal delay of $< 0\,\mathrm{ps}$ led to a decrease in the maximum energy.
- At a relative temporal delay of $0\,\mathrm{ps}$ up to $20\,\mathrm{ps}$ the maximum of the cut-off energy was reached.
- A relative temporal delay of $> 20\,\mathrm{ps}$ introduced a very slow decrease.

The Heater laser energy affects the acceleration as follows:

- $0.036\,n_c$: If the Heater energy was decreased and the Driver was kept at its initial energy, broadband He^+ spectra were detected with a stable maximum cut-off energy.
- $0.228\,n_c$: If the Heater energy was decreased and the Driver was kept at its initial energy, the appearance of broadband He^{++} spectra and the maximum He^{++} cut-off energy decreased, while the appearance of broadband He^+ spectrum increased with a stable maximum cut-off energy.

Outlining the mentioned dependencies, the characteristics of the Helium ion energy spectra, the type of the accelerated ion species and the maximum cut-off energy were affected by the target density and laser energy.

Analysis of the acceleration mechanisms:

The Heater beam in this experimental setup was too weak to accelerate ions via Coulomb explosion (CE). All necessary parameters for the Coulomb explosion thresholds are listed in table 7.1. Although the plasma frequency was lower than the laser frequency, the focal spot radius was too big ($r_0 = 37.5\,\mu$m) and the normalised vector potential was too low (about $a_0 = 0.3$) to evacuate the channel of electrons by the radial component of the ponderomotive force. Therefore, a transverse ion acceleration via CE by a Heater-only interaction was not possible in this experimental setup, although a plasma channel must have been created (discussion is following).

		target density	min	max
		n_e [cm^{-3}]	$1.6 \cdot 10^{19}$	$3.92 \cdot 10^{20}$
		n_e/n_c	0.009	0.228
ω_0 [Hz]	$2.35 \cdot 10^{15}$	ω_p [Hz]	$2.26 \cdot 10^{14}$	$1.12 \cdot 10^{15}$
τ [fs]	30	$1/\omega_p$ [fs]	4.42	0.9
$c\tau$ [μm]	8.99	r_0 [μm]	37.5	
a_0	0.6	a_{0max}(1D)	398	9767

Table 7.1: Different conditions, which have to be fulfilled in order to accelerate ions due to Coulomb explosion at the minimum and maximum target density in the f/25 Heater setup.

As described in section 6.3, the conditions for a CSA and CE by means of the Driver-only interaction were fulfilled for high target densities, but there were no accelerated ions detected from a Driver-only interaction. Therefore, the new TNSA-like acceleration regime was achieved by the interaction of both laser beams together with the gas target.

The specific kind of pre-formed plasma had to be built inside the target in order to accelerate ions. As discussed in section 6.3, a plasma channel structure is formed already by the pedestal level of the f/10 Heater with an intensity of about $10^{14} - 10^{15}\,\mathrm{W/cm^2}$. Therefore, the f/25 Heater beam with an intensity of about $6.6 \cdot 10^{17}\,\mathrm{W/cm^2}$ creates as well a plasma channel with a larger and more homogenous profile, which depleted slower, because of the increased focal spot size and less intensity. Accordingly, the discussion of the results before and the simulations of the Driver interaction are also valid for this special double beam interaction.

However, as seen in these experimental results, the spectral features depend on the target density, the delay between the beams and the laser energy. All these three parameters affect the plasma channel structure created by the Heater beam. A different target density leads to a different Heater plasma interaction with a different generated plasma channel evolution. The time delay between the two beams leads to a different evolution of the channel structure and channel edge scale lengths, which grow in time. The laser energy provides a different condition for a stronger or weaker interaction and therefore a different channel formation, as analysed in the numerical simulations in section 5.2 and in section 6.2. Only in a specific density regime with a specific plasma structure, the laser plasma interaction was favourable to accelerate monoenergetic ions via a strong spatially homogenous localised and directional electrostatic field acting as sheath field in the TNSA-like mechanism.

A reproducible monoenergetic ion source produced with high repetition rate was not jet investigated in detail. However, there are experimental results about monoenergetic ion sources accelerated via spatially homogenous localised and directional electric sheath fields. By means of special targets, monoenergetic features were achieved, for example *Hegelich et al.* [10] fabricated targets by catalytic processes to create a few monolayers in order to accelerate higher-Z ions by a TNSA process. *Esirkepov et al.* [123] demonstrated via PIC simulations, that double-layer targets can be employed in order to generate a source of monoenergetic protons. A bilayered, microstructured target with a

proton-rich dot at the rear surface was used by *Schwoerer et al.* [124]. *Klimo et al.* [125] investigated a radiation pressure acceleration (RPA) process of ultra thin nm-foils of monoenergetic ions by means of a circular polarized laser. However, monoenergetic ion features from a gas target (overcritical density) were observed by *Palmer et al.* [111] and *Haberberger et al.* [112] by means of a CO_2 laser. *Kahaly et al.* [34] generated a source of quasi-monoenergetic features in the transverse direction to the laser axis at very low target density of about $0.001\,n_c$ by a pinching of the plasma channel in combination with a TNSA sheath field. The monoenergetic features observed in this experimental campaign resulted from the TNSA-like mechanism (discussed in chapter 6). However, due to a reduction of the Heater intensity, a sharp density spike was generated. By the interaction of the Driver with this specially shaped density profile a homogenous electric sheath field was generated, as described in the previous mentioned results in overdense targets, suitable of causing a monoenergetic ion source.

For further investigations of the experimental results, additional simulations have to be performed in order to reproduce the conditions for a monoenergetic ion source. In contrast to the simulation results in section 6.2, a different density profile has to be assumed. A larger channel, less evacuated with smaller density barriers has to be implemented. Small changes lead to an inhomogeneous electric field contributing to a broadband ion energy spectrum. Therefore, the right combination of density and intensity has to be found in favour of a spatially homogenous localised and directional electric sheath field to accelerate monoenergetic ions.

7.5 Summary

The development of an ion source from underdense targets towards a stable, high repetition rate, monoenergetic ion beam is demonstrated in this chapter. The TNSA-like acceleration process, discussed before, led to a narrowband ion source, by the interaction of the Driver beam with a steep density gradient. The results of a modified experimental double beam setup in order to further develop the ion source are presented.

The Heater laser beam was reduced in strength by focusing with an f/25 OAP to an intensity of about $6.6 \cdot 10^{17}\,\mathrm{W/cm^2}$. This Heater beam was not intense enough to accelerate ions via the Coulomb explosion mechanism. However, the interaction was favourable to generate a channel structure, less evacuated of electrons with a slow depletion time of the channel walls, because of the missing strong radial particle acceleration. By the interaction of the Driver with this specially preformed plasma with a sharp density spike, a spatially homogenous localised and directional electric sheath field was generated, suitable for the monoenergetic ion source. Therefore, the ions were accelerated in the longitudinal direction to the Driver laser axis via an adjustment of the TNSA-like mechanism. By changing the relative temporal delay between the beams, the target density or the laser energy, the pre-formed channel structure was varied. Only with specific experimental parameters, the conditions enabled the generation of a spatially homogenous localised and directional electric sheath field by the interaction of the Driver laser with the specific density target profile. From this interaction, monoenergetic ions were accelerated by controlling and manipulating the target profile. Moreover, an increase of the scale length of the density spikes by varying the target, laser delay or laser energy led to a broadband energy spectra.

Additionally, an magnetic spectrometer was employed in the transverse direction to the Driver axis in order to detect ions and electrons at the same time. However, only low energy electrons were identified by a Driver-only or double beam interaction. The conditions for a longitudinal electron acceleration by the low intensity Heater beam were not reached.

Chapter 8

Summary and Outlook

In this thesis experimental investigations on ion acceleration generated by the irradiation of gaseous targets by ultrashort ($\sim 30\,\mathrm{fs}$) Ti:Sapphire laser pulses are presented. The full capacity of the unique capability of the dual beam configuration of the ARCTRUS laser in a 90° geometry with respect to each other was used to interact with a 1 mm diameter Hydrogen or Helium gas target. A Heater laser beam focused to intensities of $\sim 10^{17} - 10^{19}\,\mathrm{W/cm^2}$ and a Driver focused to an ultra-high intensity of $\sim 10^{20}\,\mathrm{W/cm^2}$ were guided into the gas jet. Different ion acceleration regimes were demonstrated and novel ion sources, as well as transitions between the mechanisms were observed. To our best knowledge, these observations are reported for the first time in this thesis.

The thesis is structured in two main topics, distinguishable from each other by the acceleration mechanism: Transverse ion acceleration via Coulomb explosion and longitudinal ion acceleration via a TNSA-like mechanism leading towards the development of a monoenergetic ion source. The key operating diagnostics were two Thomson parabola spectrometers to detect the accelerated ions and to resolve their energy spectra along the Driver beam direction. By means of a magnetic spectrometer ions and electrons could have been detected along the transverse direction. Complementary diagnostics were operated to study the inside of the plasma for a better understanding of the interaction processes. Accelerated electrons were detected by a magnetic spectrometer. The Driver and Heater laser interactions were investigated by optical probing and the Heater-only interaction was further analysed by means of charged particle probing.

In the first part of this thesis, the experimental results of the ion acceleration via CE in underdense targets were investigated. A single laser, the Heater, ($I_{\mathrm{L}} = 2.4 \cdot 10^{19}\,\mathrm{W/cm^2}$, $a_0 = 3.3$, f/10 OAP) interacted with the gas target. Ions were accelerated from the centre of the plasma in the transverse direction to the laser axis by the CE mechanism from a target with densities to about $0.12\,n_{\mathrm{c}}$. A plasma channel was created due to self-focusing and ponderomotive channeling effects along the laser axis, which was experimentally observed by optical and charge particle probing. When the ponderomotive force exceeded the repelling electric field, the accumulated ions were pushed in the transverse direction by their own space-charge field. Numerical simulations reproduced the experimental result and provided the indications of Coulomb explosion. By means of the insights into the laser plasma interaction due to laser, density and field distributions, conclusions about the acceleration mechanism were made. Analytical models confirmed the results via calculations for the self-focusing effects and threshold of the CE. Furthermore, various diagnostics were employed for a thorough understanding of the physical processes taking place inside the interaction region. Electrons accelerated in the longitudinal direction were detected at low target densities. Moreover, the plasma channel evolution in the longitudinal and the transverse directions was investigated via shadowgraphy and interferometry. Additionally, by charged particle probing, soliton structures were distinguished, which can accelerate low energy ions in the radial direction by a CE-like process.

In the second part of the thesis, the experimental results of ion acceleration via a TNSA-like mechanism by a double laser beam interaction with an underdense target were investigated. In addition to the Heater beam, a Driver laser ($I_{\mathrm{L}} = 1.5 \cdot 10^{20}\,\mathrm{W/cm^2}$, $a_0 = 8.2$, f/2 OAP) was included in the experimental setup normal to the Heater laser axis. It is worth mentioning, that no ions were detected by a Driver-only interaction, neither in the longitudinal nor in the transverse direction. Only during the double beam interaction, ions were detected. Here the main highlight was the extension of the acceleration even at very high target densities up to $0.18\,n_{\mathrm{c}}$, where acceleration due to the single beam interaction was diminished. By means of the optical probing and the numerical simulations of the single Heater beam interaction, information about the created plasma channel was extracted. The Driver laser interacted with this pre-formed plasma channel. The density profile with two dense spikes and a density gap in between was implemented in the numerical simulations. The interaction of the Driver with this special shaped target was investigate in order to get information about the

acceleration mechanism. By means of the density distributions and the evolution of the longitudinal electric field, clearly, a TNSA-like process was identified due to the interaction of the Driver with the density spike at the depleted channel wall. Moreover, different acceleration methods were discussed and excluded for this scenario. The results of the TNSA-like mechanism were confirmed by additional analytical calculations. Furthermore, with help of a magnetic spectrometer installed in the transverse direction to the Driver axis, it was confirmed that ions were accelerated preferable only along the Driver beam axis. Only electrons were observed by a Driver-only or a double beam interaction. Moreover, CE by the Driver was not possible, because the created plasma channel blasted in the centre of the target, observed via shadowgraphy of the Driver-only interaction.

In the third part of this thesis, the development of a stable, high repetition rate monoenergetic ion source from underdense targets is presented. A new acceleration scheme was invented. The interaction of the Driver and Heater was adjusted in order to generate a sharp density gradient in favour of a spatially homogenous localised and directional electric sheath field in the TNSA-like process. Therefore, the Heater beam intensity was reduced and the Rayleigh length increased ($I_{\mathrm{L}} = 6.6 \cdot 10^{17}\,\mathrm{W/cm^2}$, $a_0 < 1$, f/25 OAP). A Coulomb explosion initiated by this Heater beam was not possible anymore, whereby a slowly depleting and less evacuated channel was generated. The Driver interaction with this specially shaped target led to a monoenergetic ion acceleration via the TNSA-like mechanism. Different experimental parameters were changed in all configurations in order to get a deeper understanding of the acceleration process. Depending on the target density, the relative time delay between the laser beams and the energy of the individual pulses, a novel source of monoenergetic ions was generated. Small variations in the experimental parameters changed the acceleration regime to a broadband acceleration.

Beyond the scope of this thesis and for further investigation of the acceleration regimes, the ARCTURUS plasma mirror system could be implemented in the experimental setup to enhance the laser contrast by suppressing the ASE pedestal level of the laser beams. In the experiments of this thesis, the creation of the prechannel due to the pedestal level of the f/10 Heater beam assisted the ion acceleration. However, by suppressing the ASE level a change in the acceleration mechanism of the double beam interaction might happen and possible effects on the ion acceleration could be investigated. Moreover, the acceleration referring to the relative time delay between the beams could be analysed

with a precise temporal overlap of the two laser beams. The fundamental question due to the enhanced laser contrast in the f/10 Heater configuration would be, if the ions can still be accelerated due to the Driver interacting with the strong main plasma channel or if the acceleration mechanism cannot occur anymore.

Furthermore, a movable Thomson parabola spectrometer would contribute to an investigation of the spatial location of the source of the ion acceleration. In these experimental campaigns, the spectrometer and the pinhole were aligned to the centre of the target along the Driver axis, which might be almost always the source of the ions. At high target densities, the Heater laser might generate a strong plasma channel evacuated of particles only at the increasing density gradient of the target and not in the target center. A transverse moving spectrometer with a slit pinhole could be employed, in order to observe this possible change in the origin of the ions at high target densities.

Besides these experimental changes, a more powerful laser can be implemented. As discussed by means of the simulation results, the ion energies increase with laser intensity in the transverse direction as well as in the longitudinal direction. An upgrade was implemented in the ARCTURUS laser. Two new high power pump lasers amplify the beams up to 7 J of energy before the compressor, which more than doubles the intensity on the target. This clears the way for higher ion energies.

Apart from these modifications, additional numerical simulations have to be carried out for further investigations of the double beam interaction. Different pre-formed plasma profiles for the Driver beam have to be implemented to study the effect of the particle acceleration and the acting electric and magnetic fields inside the plasma in order to analyse the various acceleration mechanisms. A promising combination of laser intensity and gas profile and density has to be found in order to simulate the monoenergetic ion source.

By means of the experiments presented in this thesis, novel features in the ion acceleration of underdense gas targets were highlighted. Various acceleration mechanisms were reached by a controlled manipulation of the target due to different laser interactions with different gases and gas densities in various laser configurations. These outstanding experiments with various diagnostics were performed exclusively by means of a dual high power laser system. Only a few places presently in the world offer this potential, which can be achieved at the ARCTURS laser facility. In addition, there are several advantages of ion acceleration from gaseous targets compared to solid targets. Solid

targets need a precise alignment for each shot, while gas targets can be used in continuous mode without any setup adjustments. In addition, there is no obligation of a high temporal laser contrast in order not to preheat the target. In these experiments the pedestal level even supported the acceleration mechanism in the double beam configuration. Another advantage of gaseous target is the acceleration of a single atom species, instead of a bunch of different kind of ions. Moreover, monoenergetic ion sources are of great importance for the cancer hadron therapy in order to save the healthy tissues around the tumour. Fast ignition with laser accelerated monoenergetic beams requires an energy, which is much smaller than with a broadband energy ion beam. Hence, these aspects emphasise the benefits of this individual laser and gas target configurations, presented in this thesis, leading to novel acceleration features and regimes with promising investigations for future applications.

Bibliography

[1] H. Daido, M. Nishiuchi, and A. S. Pirozhkov. Review of laser-driven ion sources and their applications. *Rep Prog Phys*, 75(5):056401, 2012.

[2] A. Macchi, M. Borghesi, and M. Passoni. Ion acceleration by superintense laser-plasma interaction. *Reviews of Modern Physics*, 85(2):751–793, 2013.

[3] A. Modena, Z. Najmudin, A. E. Dangor, C. E. Clayton, K. A. Marsh, C. Joshi, V. Malka, C. B. Darrow, C. Danson, D. Neely, and F. N. Walsh. Electron acceleration from the breaking of relativistic plasma-waves. *Nature*, 377(6550):606–608, 1995.

[4] J. Faure, Y. Glinec, A. Pukhov, S. Kiselev, S. Gordienko, E. Lefebvre, J. P. Rousseau, F. Burgy, and V. Malka. A laser-plasma accelerator producing monoenergetic electron beams. *Nature*, 431(7008):541–4, 2004.

[5] G. Sarri, D. J. Corvan, W. Schumaker, J. M. Cole, A. Di Piazza, H. Ahmed, C. Harvey, C. H. Keitel, K. Krushelnick, S. P. Mangles, Z. Najmudin, D. Symes, A. G. Thomas, M. Yeung, Z. Zhao, and M. Zepf. Ultrahigh brilliance multi-mev gamma-ray beams from nonlinear relativistic thomson scattering. *Phys Rev Lett*, 113(22):224801, 2014.

[6] M. Roth, T. E. Cowan, M. H. Key, S. P. Hatchett, C. Brown, W. Fountain, J. Johnson, D. M. Pennington, R. A. Snavely, S. C. Wilks, K. Yasuike, H. Ruhl, F. Pegoraro, S. V. Bulanov, E. M. Campbell, M. D. Perry, and H. Powell. Fast ignition by intense laser-accelerated proton beams. *Phys Rev Lett*, 86(3):436–9, 2001.

[7] S. V. Bulanov, T. Z. Esirkepov, V. S. Khoroshkov, A. V. Kunetsov, and F. Pegoraro. Oncological hadrontherapy with laser ion accelerators. *Physics Letters A*, 299(2-3):240–247, 2002.

[8] B. Dromey, M. Zepf, A. Gopal, K. Lancaster, M. S. Wei, K. Krushelnick, M. Tatarakis, N. Vakakis, S. Moustaizis, R. Kodama, M. Tampo, C. Stoeckl, R. Clarke, H. Habara, D. Neely, S. Karsch, and P. Norreys. High harmonic generation in the relativistic limit. *Nature Physics*, 2(7):456–459, 2006.

[9] S. C. Wilks, A. B. Langdon, T. E. Cowan, M. Roth, M. Singh, S. Hatchett, M. H. Key, D. Pennington, A. MacKinnon, and R. A. Snavely. Energetic proton generation in ultra-intense laser-solid interactions. *Physics of Plasmas*, 8(2):542–549, 2001.

[10] B. M. Hegelich, B. J. Albright, J. Cobble, K. Flippo, S. Letzring, M. Paffett, H. Ruhl, J. Schreiber, R. K. Schulze, and J. C. Fernandez. Laser acceleration of quasi-monoenergetic mev ion beams. *Nature*, 439(7075):441–4, 2006.

[11] K. Krushelnick, E. L. Clark, Z. Najmudin, M. Salvati, M. I. K. Santala, M. Tatarakis, A. E. Dangor, V. Malka, D. Neely, R. Allott, and C. Danson. Multi-mev ion production from high-intensity laser interactions with underdense plasmas. *Physical Review Letters*, 83(4):737–740, 1999.

[12] M. S. Wei, S. P. Mangles, Z. Najmudin, B. Walton, A. Gopal, M. Tatarakis, A. E. Dangor, E. L. Clark, R. G. Evans, S. Fritzler, R. J. Clarke, C. Hernandez-Gomez, D. Neely, W. Mori, M. Tzoufras, and K. Krushelnick. Ion acceleration by collisionless shocks in high-intensity-laser-underdense-plasma interaction. *Phys Rev Lett*, 93(15):155003, 2004.

[13] L. Willingale, S. P. Mangles, P. M. Nilson, R. J. Clarke, A. E. Dangor, M. C. Kaluza, S. Karsch, K. L. Lancaster, W. B. Mori, Z. Najmudin, J. Schreiber, A. G. Thomas, M. S. Wei, and K. Krushelnick. Collimated multi-mev ion beams from high-intensity laser interactions with underdense plasma. *Phys Rev Lett*, 96(24):245002, 2006.

[14] A. Lifschitz, F. Sylla, S. Kahaly, A. Flacco, M. Veltcheva, G. Sanchez-Arriaga, E. Lefebvre, and V. Malka. Ion acceleration in underdense plasmas by ultra-short laser pulses. *New Journal of Physics*, 16, 2014.

[15] A. Macchi. *A superintense laser plasma interaction theory primer*. Springer, Dordrecht, 2013.

[16] F. F. Chen. *Introduction to plasma physics and controlled fusion / Bd. 1 : Plasma physics*. Plenum Press, New York u.a., 2. ed. edition, 2010.

[17] P. Gibbon. *Short pulse laser interactions with matter : an introduction*. Imperial College Press, London, 2005.

[18] W. L. Kruer. *The physics of laser plasma interactions*. Westview Pr., Boulder, Colo., 2003.

[19] G. Mainfray and C. Manus. Multiphoton ionization of atoms. *Reports on Progress in Physics*, 54(10):1333–1372, 1991.

[20] S. S. Bulanov, V. Y. Bychenkov, V. Chvykov, G. Kalinchenko, D. W. Litzenberg, T. Matsuoka, A. G. Thomas, L. Willingale, V. Yanovsky, K. Krushelnick, and A. Maksimchuk. Generation of gev protons from 1 pw laser interaction with near critical density targets. *Phys Plasmas*, 17(4), 2010.

[21] S. S. Bulanov, E. Esarey, C. B. Schroeder, W. P. Leemans, S. V. Bulanov, D. Margarone, G. Korn, and T. Haberer. Helium-3 and helium-4 acceleration by high power laser pulses for hadron therapy. *Physical Review Special Topics-Accelerators and Beams*, 18(6), 2015.

[22] G. Z. Sun, E. Ott, Y. C. Lee, and P. Guzdar. Self-focusing of short intense pulses in plasmas. *Physics of Fluids*, 30(2):526–532, 1987.

[23] P. E. Young, J. H. Hammer, S. C. Wilks, and W. L. Kruer. Laser-beam propagation and channel formation in underdense plasmas. *Physics of Plasmas*, 2(7):2825–2834, 1995.

[24] J. Fuchs, P. Antici, E. D'Humieres, E. Lefebvre, M. Borghesi, E. Brambrink, C. A. Cecchetti, M. Kaluza, V. Malka, M. Manclossi, S. Meyroneinc, P. Mora, J. Schreiber, T. Toncian, H. Pepin, and R. Audebert. Laser-driven proton scaling laws and new paths towards energy increase. *Nature Physics*, 2(1):48–54, 2006.

[25] S. C. Wilks, W. L. Kruer, M. Tabak, and A. B. Langdon. Absorption of ultra-intense laser pulses. *Phys Rev Lett*, 69(9):1383–1386, 1992.

[26] G. S. Sarkisov, V. Y. Bychenkov, V. N. Novikov, V. T. Tikhonchuk, A. Maksimchuk, S. Y. Chen, R. Wagner, G. Mourou, and D. Umstadter. Self-focusing, channel formation, and high-energy ion generation in interaction of an intense short laser pulse with a he jet. *Phys Rev E Stat Phys Plasmas Fluids Relat Interdiscip Topics*, 59(6):7042–54, 1999.

[27] A. Macchi, F. Ceccherini, F. Cornolti, S. Kar, and M. Borghesi. Electric field dynamics and ion acceleration in the self-channeling of a superintense laser pulse. *Plasma Physics and Controlled Fusion*, 51(2):18, 2009.

[28] L. O. Silva, M. Marti, J. R. Davies, R. A. Fonseca, C. Ren, F. S. Tsung, and W. B. Mori. Proton shock acceleration in laser-plasma interactions. *Phys Rev Lett*, 92(1):015002, 2004.

[29] M. Gauthier, A. Levy, E. d'Humieres, M. Glesser, B. Albertazzi, C. Beaucourt, J. Breil, S. N. Chen, V. Dervieux, J. L. Feugeas, P. Nicolai, V. Tikhonchuk, H. Pepin, P. Antici, and J. Fuchs. Investigation of longitudinal proton acceleration in exploded targets irradiated by intense short-pulse laser. *Physics of Plasmas*, 21(1), 2014.

[30] P. Antici, E. Boella, S. N. Chen, D. S. Andrews, M. Barberio, J. Böker, F. Cardelli, J. L. Feugeas, M. Glesser, P. Nicolai, L. Romagnani, M. Sciscio, M. Starodubtsev, O. Willi, J. C. Kieffer, V. Tikhonchuk, H. Pepin, L. O. Silva, E. d'Humieres, and J. Fuchs. Acceleration of collimated 45 mev protons by collisionless shocks driven in low-density, large-scale gradient plasmas by a 10^{20} w/cm^2, 1 μm laser. *Scientific Reports*, 7(1):16463, 2017.

[31] E. d'Humieres, P. Antici, M. Glesser, J. Boeker, F. Cardelli, S. Chen, J. L. Feugeas, F. Filippi, M. Gauthier, A. Levy, P. Nicolai, H. Pepin, L. Romagnani, M. Sciscio, V. T. Tikhonchuk, O. Willi, J. C. Kieffer, and J. Fuchs. Investigation of laser ion acceleration in low-density targets using exploded foils. *Plasma Physics and Controlled Fusion*, 55(12):7, 2013.

[32] S. V. Bulanov and TZh Esirkepov. Comment on "collimated multi-mev ion beams from high-intensity laser interactions with underdense plasma". *Phys Rev Lett*, 98(4):049503; discussion 049504, 2007.

[33] L. Willingale, S. P. D. Mangles, P. M. Nilson, R. J. Clarke, A. E. Dangor, M. C. Kaluza, S. Karsch, K. L. Lancaster, W. B. Mori, Z. Najmudin, J. Schreiber, A. G. R. Thomas, M. S. Wei, and K. Krushelnick. Comment on "collimated multimev ion beams from high-intensity laser interactions with underdense plasma" - willingale et al. reply. *Physical Review Letters*, 98(4), 2007.

[34] S. Kahaly, F. Sylla, A. Lifschitz, A. Flacco, M. Veltcheva, and V. Malka. Detailed experimental study of ion acceleration by interaction of an ultra-short intense laser with an underdense plasma. *Sci Rep*, 6:31647, 2016.

[35] P. Maine, D. Strickland, P. Bado, M. Pessot, and G. Mourou. Generation of ultrahigh peak power pulses by chirped pulse amplification. *Ieee Journal of Quantum Electronics*, 24(2):398–403, 1988.

[36] H. Kiriyama, T. Shimomura, H. Sasao, Y. Nakai, M. Tanoue, S. Kondo, S. Kanazawa, A. S. Pirozhkov, M. Mori, Y. Fukuda, M. Nishiuchi, M. Kando, S. V. Bulanov, K. Nagashima, M. Yamagiwa, K. Kondo, A. Sugiyama, P. R. Bolton, T. Tajima, and N. Miyanaga. Temporal contrast enhancement of petawatt-class laser pulses. *Opt Lett*, 37(16):3363–5, 2012.

[37] A. Ricci, A. Jullien, J. P. Rousseau, Y. Liu, A. Houard, P. Ramirez, D. Papadopoulos, A. Pellegrina, P. Georges, F. Druon, N. Forget, and R. Lopez-Martens. Energy-scalable temporal cleaning device for femtosecond laser pulses based on cross-polarized wave generation. *Review of Scientific Instruments*, 84(4), 2013.

[38] B. Dromey, S. Kar, M. Zepf, and P. Foster. The plasma mirror - a subpicosecond optical switch for ultrahigh power lasers. *Review of Scientific Instruments*, 75(3):645–649, 2004.

[39] C. Thaury, F. Quere, J. P. Geindre, A. Levy, T. Ceccotti, P. Monot, M. Bougeard, F. Reau, P. D'Oliveira, P. Audebert, R. Marjoribanks, and P. H. Martin. Plasma mirrors for ultrahigh-intensity optics. *Nature Physics*, 3(6):424–429, 2007.

[40] A.-L. Giesecke. *Propagation Dynamics and High Harmonic Generation Using High Contrast Ultrashort Laser Pulses*. Phd thesis, Heinrich Heine University Düsseldorf, 2013.

[41] S. Semushin and V. Malka. High density gas jet nozzle design for laser target production. *Review of Scientific Instruments*, 72(7):2961–2965, 2001.

[42] K. Schmid and L. Veisz. Supersonic gas jets for laser-plasma experiments. *Review of Scientific Instruments*, 83(5), 2012.

[43] Mikhail N. Polyanskiy. Refractive index database. https://refractiveindex.info. Accessed on 2017-03-20.

[44] K. Svensson, M. Hansson, F. Wojda, L. Senje, M. Burza, B. Aurand, G. Genoud, A. Persson, C. G. Wahlström, and O. Lundh. Supersonic jets of hydrogen and helium for laser wakefield acceleration. *Physical Review Accelerators and Beams*, 19(5):051301, 2016.

[45] P. Hariharan. *Basics of interferometry.* Academic press of Elsevier, 2 edition, 2007. p. 93 ff.

[46] F. H. Seguin, J. A. Frenje, C. K. Li, D. G. Hicks, S. Kurebayashi, J. R. Rygg, B. E. Schwartz, R. D. Petrasso, S. Roberts, J. M. Soures, D. D. Meyerhofer, T. C. Sangster, J. P. Knauer, C. Sorce, V. Y. Glebov, C. Stoeckl, T. W. Phillips, R. J. Leeper, K. Fletcher, and S. Padalino. Spectrometry of charged particles from inertial-confinement-fusion plasmas. *Review of Scientific Instruments*, 74(2):975–995, 2003.

[47] A. P. Fews. Fully automated image-analysis of etched tracks in cr-39. *Nuclear Instruments and Methods in Physics Research Section B-Beam Interactions with Materials and Atoms*, 71(4):465–478, 1992.

[48] M. Fromm, F. Membrey, A. Chambaudet, and R. Saouli. Proton and alpha track profiles in cr39 during etching and their implications on track etching models. *International Journal of Radiation Applications and Instrumentation. Part D. Nuclear Tracks and Radiation Measurements*, 19(1-4):163–168, 1991.

[49] J. J. Thomson. Bakerian lecture: Rays of positive electricity. *Proceedings of the Royal Society A: Mathematical, Physical and Engineering Sciences*, 89(607):1–20, 1913.

[50] A. Alejo, D. Gwynne, D. Doria, H. Ahmed, D. C. Carroll, R. J. Clarke, D. Neely, G. G. Scott, M. Borghesi, and S. Kar. Recent developments in the thomson parabola spectrometer diagnostic for laser-driven multi-species ion sources. *Journal of Instrumentation*, 11(10):C10005–C10005, 2016.

[51] D. Gwynne, S. Kar, D. Doria, H. Ahmed, M. Cerchez, J. Fernandez, R. J. Gray, J. S. Green, F. Hanton, D. A. MacLellan, P. McKenna, Z. Najmudin, D. Neely, J. A. Ruiz, A. Schiavi, M. Streeter, M. Swantusch, O. Willi, M. Zepf, and M. Borghesi. Modified thomson spectrometer design for high energy, multi-species ion sources. *Review of Scientific Instruments*, 85(3):6, 2014.

[52] D. Jung, R. Horlein, D. Kiefer, S. Letzring, D. C. Gautier, U. Schramm, C. Hubsch, R. Ohm, B. J. Albright, J. C. Fernandez, D. Habs, and B. M. Hegelich. Development of a high resolution and high dispersion thomson parabola. *Rev Sci Instrum*, 82(1):013306, 2011.

[53] J. L. Wiza. Microchannel plate detectors. *Nuclear Instruments and Methods*, 162(1-3):587–601, 1979.

[54] Hamamatsu Photonics. *MCP (Microchannel Plate) and MCP assembly.*

[55] T. W. Jeong, P. K. Singh, C. Scullion, H. Ahmed, K. F. Kakolee, P. Hadjisolomou, A. Alejo, S. Kar, M. Borghesi, and S. Ter-Avetisyan. Experimental evaluation of the response of micro-channel plate detector to ions with 10s of mev energies. *Rev Sci Instrum*, 87(8):083301, 2016.

[56] C. Mauger, L. Mees, M. Michard, A. Azouzi, and S. Valette. Shadowgraph, schlieren and interferometry in a 2d cavitating channel flow. *Experiments in Fluids*, 53(6):1895–1913, 2012.

[57] A. Srivastava, K. Muralidhar, and P. K. Panigrahi. Comparison of interferometry, schlieren and shadowgraph for visualizing convection around a kdp crystal. *Journal of Crystal Growth*, 267(1-2):348–361, 2004.

[58] P. K. Panigrahi and K. Muralidhar. *Schlieren and Shadowgraph Methods in Heat and Mass Transfer.* SpringerBriefs in Thermal Engineering and Applied Science. Springer New York, 2012. p. 23 ff.

[59] I. H. Hutchinson. *Principles of Plasma Diagnostics.* Cambridge University Press, 2 edition, 2002. p. 112 ff.

[60] V. Malka, C. Coulaud, J. P. Geindre, V. Lopez, Z. Najmudin, D. Neely, and F. Amiranoff. Characterization of neutral density profile in a wide range of pressure of cylindrical pulsed gas jets. *Review of Scientific Instruments*, 71(6):2329–2333, 2000.

[61] N.H. Abel. Auflösung einer mechanischen aufgabe. *Journal für die reine und angewandte Mathematik*, 1:153–157, 1826.

[62] R. Benattar, C. Popovics, and R. Sigel. Polarized light interferometer for laser fusion studies. *Rev Sci Instrum*, 50(12):1583, 1979.

[63] L. A. Gizzi, D. Giulietti, A. Giulietti, T. Afshar-Rad, V. Biancalana, P. Chessa, C. Danson, E. Schifano, S. M. Viana, and O. Willi. Characterization of laser plasmas for interaction studies. *Physical Review E*, 49(6):5628–5643, 1994.

[64] M. Takeda, H. Ina, and S. Kobayashi. Fourier-transform method of fringe-pattern analysis for computer-based topography and interferometry. *Journal of the Optical Society of America*, 72(1):156–160, 1982.

[65] M. Borghesi. *The Interaction of Ultra-Intense Laser Pulses with Solid Targets and Preformed Plasmas*. Phd thesis, Imperial College of Science, Technology and Medicine, London, U.K., 1998a.

[66] K. A. Nugent. Interferogram analysis using an accurate fully-automatic algorithm. *Applied Optics*, 24(18):3101–3105, 1985.

[67] W. L. Mclaughlin, A. Miller, S. Fidan, K. Pejtersen, and W. B. Pedersen. Radiochromic plastic films for accurate measurement of radiation absorbed dose and dose distributions. *Radiation Physics and Chemistry*, 10(2):119–127, 1977.

[68] Ashland Gafchromic. *Gafchromic HD-V2 film specification and user guide*.

[69] A. Niroomand-Rad, C. R. Blackwell, B. M. Coursey, K. P. Gall, J. M. Galvin, W. L. McLaughlin, A. S. Meigooni, R. Nath, J. E. Rodgers, and C. G. Soares. Radiochromic film dosimetry: recommendations of aapm radiation therapy committee task group 55. american association of physicists in medicine. *Med Phys*, 25(11):2093–115, 1998.

[70] M. J. Butson, P. K. Yu, and P. E. Metcalfe. Effects of read-out light sources and ambient light on radiochromic film. *Phys Med Biol*, 43(8):2407–12, 1998.

[71] F. Nürnberg, M. Schollmeier, E. Brambrink, A. Blazevic, D. C. Carroll, K. Flippo, D. C. Gautier, M. Geissel, K. Harres, B. M. Hegelich, O. Lundh, K. Markey, P. McKenna, D. Neely, J. Schreiber, and M. Roth. Radiochromic film imaging spectroscopy of laser-accelerated proton beams. *Rev Sci Instrum*, 80(3):033301, 2009.

[72] Ashland Gafchromic. *Gafchromic EBT2 self-developing film for radiotherapy dosimetry.*

[73] Global Gafchromic Sales Manager Minasi Raymond. private communication, 2016.

[74] H. Bethe. Zur theorie des durchgangs schneller korpuskularstrahlen durch materie. *Annalen der Physik*, 397(3):325–400, 1930.

[75] F. Bloch. Zur bremsung rasch bewegter teilchen beim durchgang durch materie. *Annalen der Physik*, 408(3):285–320, 1933.

[76] J. Ziegler. Interactions of ions with matter. http://www.srim.org/, 2010. url-date: 2017-03-30.

[77] J. F. Ziegler, M. D. Ziegler, and J. P. Biersack. Srim - the stopping and range of ions in matter (2010). *Nuclear Instruments and Methods in Physics Research Section B-Beam Interactions with Materials and Atoms*, 268(11-12):1818–1823, 2010.

[78] J. A. Cobble, R. P. Johnson, T. E. Cowan, N. Renard-Le Galloudec, and M. Allen. High resolution laser-driven proton radiography. *Journal of Applied Physics*, 92(4):1775–1779, 2002.

[79] T. E. Cowan, J. Fuchs, H. Ruhl, A. Kemp, P. Audebert, M. Roth, R. Stephens, I. Barton, A. Blazevic, E. Brambrink, J. Cobble, J. Fernandez, J. C. Gauthier, M. Geissel, M. Hegelich, J. Kaae, S. Karsch, G. P. Le Sage, S. Letzring, M. Manclossi, S. Meyroneinc, A. Newkirk, H. Pepin, and N. Renard-LeGalloudec. Ultralow emittance, multi-mev proton beams from a laser virtual-cathode plasma accelerator. *Phys Rev Lett*, 92(20):204801, 2004.

[80] M. Borghesi, A. J. Mackinnon, D. H. Campbell, D. G. Hicks, S. Kar, P. K. Patel, D. Price, L. Romagnani, A. Schiavi, and O. Willi. Multi-mev proton source

investigations in ultraintense laser-foil interactions. *Phys Rev Lett*, 92(5):055003, 2004.

[81] A. Buck, K. Zeil, A. Popp, K. Schmid, A. Jochmann, S. D. Kraft, B. Hidding, T. Kudyakov, C. M. Sears, L. Veisz, S. Karsch, J. Pawelke, R. Sauerbrey, T. Cowan, F. Krausz, and U. Schramm. Absolute charge calibration of scintillating screens for relativistic electron detection. *Rev Sci Instrum*, 81(3):033301, 2010.

[82] M. Borghesi, A. J. MacKinnon, L. Barringer, R. Gaillard, L. A. Gizzi, C. Meyer, O. Willi, A. Pukhov, and J. Meyer-ter Vehn. Relativistic channeling of a picosecond laser pulse in a near-critical preformed plasma. *Physical Review Letters*, 78(5):879–882, 1997.

[83] J. Fuchs, G. Malka, J. C. Adam, F. Amiranoff, S. D. Baton, N. Blanchot, A. Héron, G. Laval, J. L. Miquel, P. Mora, H. Pépin, and C. Rousseaux. Dynamics of subpicosecond relativistic laser pulse self-channeling in an underdense preformed plasma. *Physical Review Letters*, 80(8):1658–1661, 1998.

[84] X. L. Liu, X. Lu, X. Liu, T. T. Xi, F. Liu, J. L. Ma, and J. Zhang. Tightly focused femtosecond laser pulse in air: from filamentation to breakdown. *Opt Express*, 18(25):26007–17, 2010.

[85] S. B. Popruzhenko, V. D. Mur, V. S. Popov, and D. Bauer. Multiphoton ionization of atoms and ions by high-intensity x-ray lasers. *Journal of Experimental and Theoretical Physics*, 108(6):947–962, 2009.

[86] M. W.; Harlow F. H.; Bromberg E. Evans. The particle-in-cell method for hydrodynamic calculations. *LA-2139 Physics and Mathematics*, 13(Los Alamos National Lab NM), 1957.

[87] J. Villasenor and O. Buneman. Rigorous charge conservation for local electromagnetic-field solvers. *Computer Physics Communications*, 69(2-3):306–316, 1992.

[88] T. Z. Esirkepov. Exact charge conservation scheme for particle-in-cell simulation with an arbitrary form-factor. *Computer Physics Communications*, 135(2):144–153, 2001.

[89] Y. Sentoku, T. V. Liseikina, T. Z. Esirkepov, F. Califano, N. M. Naumova, Y. Ueshima, V. A. Vshivkov, Y. Kato, K. Mima, K. Nishihara, F. Pegoraro, and S. V. Bulanov. High density collimated beams of relativistic ions produced by petawatt laser pulses in plasmas. *Phys Rev E Stat Phys Plasmas Fluids Relat Interdiscip Topics*, 62(5 Pt B):7271–81, 2000.

[90] T. V. Liseikina, F. Califano, V. A. Vshivkov, F. Pegoraro, and S. V. Bulanov. Small-scale electron density and magnetic-field structures in the wake of an ultraintense laser pulse. *Phys Rev E Stat Phys Plasmas Fluids Relat Interdiscip Topics*, 60(5 Pt B):5991–7, 1999.

[91] A. Macchi, F. Cattani, T. V. Liseykina, and F. Cornolti. Laser acceleration of ion bunches at the front surface of overdense plasmas. *Phys Rev Lett*, 94(16):165003, 2005.

[92] T. V. Liseykina, S. Pirner, and D. Bauer. Relativistic attosecond electron bunches from laser-illuminated droplets. *Phys Rev Lett*, 104(9):095002, 2010.

[93] A. Macchi, S. Veghini, T. V. Liseykina, and F. Pegoraro. Radiation pressure acceleration of ultrathin foils. *New Journal of Physics*, 12, 2010.

[94] A. V. Kuznetsov, T. Z. Esirkepov, F. F. Kamenets, and S. V. Bulanov. Efficiency of ion acceleration by a relativistically strong laser pulse in an underdense plasma. *Plasma Physics Reports*, 27(3):211–220, 2001.

[95] F. Pegoraro, S. V. Bulanov, F. Califano, T. Z. Esirkepov, T. V. Lisejkina, N. M. Naumova, H. Ruhl, and V. A. Vshivkov. Ion acceleration regimes in underdense plasmas. *Ieee Transactions on Plasma Science*, 28(4):1177–1183, 2000.

[96] E. Esarey, C. B. Schroeder, and W. P. Leemans. Physics of laser-driven plasma-based electron accelerators. *Reviews of Modern Physics*, 81(3):1229–1285, 2009.

[97] A. Maksimchuk, S. Reed, S. S. Bulanov, V. Chvykov, G. Kalintchenko, T. Matsuoka, C. McGuffey, G. Mourou, N. Naumova, J. Nees, P. Rousseau, V. Yanovsky, K. Krushelnick, N. H. Matlis, S. Kalmykov, G. Shvets, M. C. Downer, C. R. Vane, J. R. Beene, D. Stracener, and D. R. Schultz. Studies of laser wakefield structures and electron acceleration in underdense plasmas. *Physics of Plasmas*, 15(5), 2008.

[98] Y. W. Yu, L. Jiang, Q. Cao, X. S. Shi, Q. S. Wang, G. Y. Wang, and Y. F. Lu. Ultrafast imaging the light-speed propagation of a focused femtosecond laser pulse in air and its ionized electron dynamics and plasma-induced pulse reshaping. *Applied Physics a-Materials Science and Processing*, 122(3), 2016.

[99] M. H. Key. Compression and hydrodynamics. In *The Scottish Universities Summer School in Physics*, volume Laser-Plasma Interactions 3, page 29.

[100] M. G. Haines. Thermal instability and magnetic field generated by large heat flow in a plasma, especially under laser-fusion conditions. *Physical Review Letters*, 47(13):917–920, 1981.

[101] M. Borghesi, A. Schiavi, D. H. Campbell, M. G. Haines, O. Willi, A. J. MacKinnon, L. A. Gizzi, M. Galimberti, R. J. Clarke, and H. Ruhl. Proton imaging: a diagnostic for inertial confinement fusion/fast ignitor studies. *Plasma Physics and Controlled Fusion*, 43:A267–A276, 2001.

[102] M. Borghesi, S. Bulanov, D. H. Campbell, R. J. Clarke, TZh Esirkepov, M. Galimberti, L. A. Gizzi, A. J. MacKinnon, N. M. Naumova, F. Pegoraro, H. Ruhl, A. Schiavi, and O. Willi. Macroscopic evidence of soliton formation in multiterawatt laser-plasma interaction. *Phys Rev Lett*, 88(13):135002, 2002.

[103] M. Borghesi, D. H. Campbell, A. Schiavi, M. G. Haines, O. Willi, A. J. MacKinnon, P. Patel, L. A. Gizzi, M. Galimberti, R. J. Clarke, F. Pegoraro, H. Ruhl, and S. Bulanov. Electric field detection in laser-plasma interaction experiments via the proton imaging technique. *Physics of Plasmas*, 9(5):2214–2220, 2002.

[104] S. V. Bulanov, T. Z. Esirkepov, N. M. Naumova, F. Pegoraro, and V. A. Vshivkov. Solitonlike electromagnetic waves behind a superintense laser pulse in a plasma. *Physical Review Letters*, 82(17):3440–3443, 1999.

[105] M. V. Goldman. Strong turbulence of plasma-waves. *Reviews of Modern Physics*, 56(4):709–735, 1984.

[106] F. Pegoraro, S. V. Bulanov, F. Califano, T. Z. Esirkepov, T. V. Liseikina, N. M. Naumova, H. Ruhl, and V. A. Vshivkov. Nonlinear electromagnetic phenomena in the relativistic interaction of ultrahigh intensity laser pulses with plasmas. *Laser and Particle Beams*, 18(3):381–387, 2000.

[107] N. M. Naumova, S. Bulanov, T. Z. Esirkepov, D. Farina, K. Nishihara, F. Pegoraro, H. Ruhl, and A. S. Sakharov. Formation of electromagnetic postsolitons in plasmas. *Physical Review Letters*, 87(18), 2001.

[108] L. Romagnani, A. Bigongiari, S. Kar, S. V. Bulanov, C. A. Cecchetti, TZh Esirkepov, M. Galimberti, R. Jung, T. V. Liseykina, A. Macchi, J. Osterholz, F. Pegoraro, O. Willi, and M. Borghesi. Observation of magnetized soliton remnants in the wake of intense laser pulse propagation through plasmas. *Phys Rev Lett*, 105(17):175002, 2010.

[109] G. Sarri, D. K. Singh, J. R. Davies, F. Fiuza, K. L. Lancaster, E. L. Clark, S. Hassan, J. Jiang, N. Kageiwa, N. Lopes, A. Rehman, C. Russo, R. H. Scott, T. Tanimoto, Z. Najmudin, K. A. Tanaka, M. Tatarakis, M. Borghesi, and P. A. Norreys. Observation of postsoliton expansion following laser propagation through an underdense plasma. *Phys Rev Lett*, 105(17):175007, 2010.

[110] T. Esirkepov, K. Nishihara, S. V. Bulanov, and F. Pegoraro. Three-dimensional relativistic electromagnetic subcycle solitons. *Phys Rev Lett*, 89(27):275002, 2002.

[111] C. A. Palmer, N. P. Dover, I. Pogorelsky, M. Babzien, G. I. Dudnikova, M. Ispiriyan, M. N. Polyanskiy, J. Schreiber, P. Shkolnikov, V. Yakimenko, and Z. Najmudin. Monoenergetic proton beams accelerated by a radiation pressure driven shock. *Phys Rev Lett*, 106(1):014801, 2011.

[112] D. Haberberger, S. Tochitsky, F. Fiuza, C. Gong, R. A. Fonseca, L. O. Silva, W. B. Mori, and C. Joshi. Collisionless shocks in laser-produced plasma generate monoenergetic high-energy proton beams. *Nature Physics*, 8(1):95–99, 2012.

[113] S. N. Chen, M. Vranic, T. Gangolf, E. Boella, P. Antici, M. Bailly-Grandvaux, P. Loiseau, H. Pepin, G. Revet, J. J. Santos, A. M. Schroer, M. Starodubtsev, O. Willi, L. O. Silva, E. d'Humieres, and J. Fuchs. Collimated protons accelerated from an overdense gas jet irradiated by a 1 microm wavelength high-intensity short-pulse laser. *Sci Rep*, 7(1):13505, 2017.

[114] F. Fiuza, A. Stockem, E. Boella, R. A. Fonseca, L. O. Silva, D. Haberberger, S. Tochitsky, W. B. Mori, and C. Joshi. Ion acceleration from laser-driven electrostatic shocks. *Physics of Plasmas*, 20(5), 2013.

[115] T. Z. Esirkepov, Y. Sentoku, K. Mima, K. Nishihara, F. Califano, F. Pegoraro, N. M. Naumova, S. V. Bulanov, Y. Ueshima, T. V. Liseikina, V. A. Vshivkov, and Y. Kato. Ion acceleration by superintense laser pulses in plasmas. *Jetp Letters*, 70(2):82–89, 1999.

[116] S. V. Bulanov, T. Z. Esirkepov, F. Califano, Y. Kato, T. V. Liseikina, K. Mima, N. M. Naumova, K. Nishihara, F. Pegoraro, H. Ruhl, Y. Sentoku, and Y. Ueshima. Generation of collimated beams of relativistic ions in laser-plasma interactions. *Jetp Letters*, 71(10):407–411, 2000.

[117] P. Mora. Plasma expansion into a vacuum. *Phys Rev Lett*, 90(18):185002, 2003.

[118] S. C. Wilks, A. B. Langdon, T. E. Cowan, M. Roth, M. Singh, S. Hatchett, M. H. Key, D. Pennington, A. MacKinnon, and R. A. Snavely. Energetic proton generation in ultra-intense laser-solid interactions. *Physics of Plasmas*, 8(2):542–549, 2001.

[119] M. Kaluza, J. Schreiber, M. I. Santala, G. D. Tsakiris, K. Eidmann, J. Meyer-Ter-Vehn, and K. J. Witte. Influence of the laser prepulse on proton acceleration in thin-foil experiments. *Phys Rev Lett*, 93(4):045003, 2004.

[120] P. K. Patel, A. J. Mackinnon, M. H. Key, T. E. Cowan, M. E. Foord, M. Allen, D. F. Price, H. Ruhl, P. T. Springer, and R. Stephens. Isochoric heating of solid-density matter with an ultrafast proton beam. *Phys Rev Lett*, 91(12):125004, 2003.

[121] K. W. D. Ledingham, P. McKenna, T. McCanny, S. Shimizu, J. M. Yang, L. Robson, J. Zweit, J. M. Gillies, J. Bailey, G. N. Chimon, R. J. Clarke, D. Neely, P. A. Norreys, J. L. Collier, R. P. Singhal, M. S. Wei, S. P. D. Mangles, P. Nilson, K. Krushelnick, and M. Zepf. High power laser production of short-lived isotopes for positron emission tomography. *Journal of Physics D-Applied Physics*, 37(16):2341–2345, 2004.

[122] R. Kodama, P. A. Norreys, K. Mima, A. E. Dangor, R. G. Evans, H. Fujita, Y. Kitagawa, K. Krushelnick, T. Miyakoshi, N. Miyanaga, T. Norimatsu, S. J. Rose, T. Shozaki, K. Shigemori, A. Sunahara, M. Tampo, K. A. Tanaka, Y. Toyama, T. Yamanaka, and M. Zepf. Fast heating of ultrahigh-density plasma as a step towards laser fusion ignition. *Nature*, 412(6849):798–802, 2001.

[123] TZh Esirkepov, S. V. Bulanov, K. Nishihara, T. Tajima, F. Pegoraro, V. S. Khoroshkov, K. Mima, H. Daido, Y. Kato, Y. Kitagawa, K. Nagai, and S. Sakabe. Proposed double-layer target for the generation of high-quality laser-accelerated ion beams. *Phys Rev Lett*, 89(17):175003, 2002.

[124] H. Schwoerer, S. Pfotenhauer, O. Jackel, K. U. Amthor, B. Liesfeld, W. Ziegler, R. Sauerbrey, K. W. Ledingham, and T. Esirkepov. Laser-plasma acceleration of quasi-monoenergetic protons from microstructured targets. *Nature*, 439(7075):445–8, 2006.

[125] O. Klimo, J. Psikal, J. Limpouch, and V. T. Tikhonchuk. Monoenergetic ion beams from ultrathin foils irradiated by ultrahigh-contrast circularly polarized laser pulses. *Physical Review Special Topics-Accelerators and Beams*, 11(3), 2008.

List of Figures

List of Tables

Scientific publications

1. S. N. Chen, M. Vranic, T. Gangolf, E. Boella, P. Antici, M. Bailly-Grandvaux, P. Loiseau, H. Pepin, G. Revet, J. J. Santos, **A. M. Schroer**, M. Starodubtsev, O. Willi, L. O. Silva, E. d'Humieres, and J. Fuchs. Collimated protons accelerated from an overdense gas jet irradiated by a 1 microm wavelength high-intensity short-pulse laser. *Scientific Reports*, 7(1):13505, 2017.

2. S. Kar, H. Ahmed, R. Prasad, M. Cerchez, S. Brauckmann, B. Aurand, G. Cantono, P. Hadjisolomou, C. L. Lewis, A. Macchi, G. Nersisyan, A. P. Robinson, **A. M. Schroer**, M. Swantusch, M. Zepf, O. Willi, and M. Borghesi. Guided post-acceleration of laser-driven ions by a miniature modular structure. *Nature Communication*, 7:10792, 2016.

3. S. Kisyov, F. Negoita, M. M. Gugiu, D. P. Higginson, L. Vassura, M. Borghesi, L. Bernstein, D. L. Bleuel, F. Gobet, B. L. Goldblum, A. Green, F. Hannachi, S. Kar, H. Petrascu, D. Pietreanu, L. Quentin, **A. M. Schroer**, M. Tarisien, M. Versteegen, O. Willi, P. Antici, and J. Fuchs. Time of flight measurements for neutrons produced in reactions driven by laser-target interactions at petawatt level. *Physics Procedia*, 77(Supplement C):29-33, 2015.

4. E. d'Humieres, S. Chen, M. Lobet, M. Sciscio, P. Antici, M. Bailly-Grandvaux, T. Gangolf, G. Revet, J. J. Santos, **A. M. Schroer**, O. Willi, V. T. Tikhonchuk, H. Pepin, and J. Fuchs. Longitudinal laser ion acceleration in low density targets: experimental optimization on the titan laser facility and numerical investigation of the ultra-high intensity limit. *SPIE Optics + Optoelectronics*, volume 9514, page 6. SPIE, 2015.

Danksagung

An dieser Stelle möchte ich einigen Personen danken, die zum Erfolg dieser Arbeit über die letzten Jahre beigetragen haben.

Zunächst spreche ich Herrn Prof. Oswald Willi meinen Dank aus für die hervorragende und intensive Betreuung meiner Arbeit. Er hat mir die Möglichkeit gegeben, mit einem bedeutenden Lasersystem zu forschen und methodisch zu arbeiten, womit die Voraussetzung dieser Doktorarbeit geschaffen wurde. Desweiteren hatte ich durch ihn die Chance, internationale Kontakte knüpfen und an großen Forschungslaboren dieser Welt arbeiten zu können. Herrn Prof. Müller danke ich für die Übernahme des Korefe-rats meiner Arbeit. Zusätzlich war er mein Mentor während meiner Promotion und hat durch seine freundliche und verständnisvolle Art Unterstützung geleistet.

Ohne Rajendra Prasad wäre so manches anders im Institut. Auch wenn es im "Bunker" manchmal schweißtreibend war, so hat er mir sehr als Betreuer meiner Arbeit geholfen. Mit immer guten Ideen haben wir gemeinsam den roten Faden gefunden. Und auch der schiefe Turm von Pisa hat keinen Halt vor uns gemacht. Ohne den Laser wäre die Arbeit nicht zu stande gekommen, daher gilt mein Dank Thomas Wowra, Mirela Cerchez und Bastian Aurand, die so oft von morgens früh um 6, an den heißesten Sommertagen, als auch bis tief in die Nacht den Laserbetrieb aufrecht erhalten haben.

Tatjana Liseykina von der Universität Rostock danke ich für ihre Unterstützung bei der Analyse meiner Daten durch PIC-Simulationen. Durch zahlreiche E-mails - auch über den wissenschaftlichen Austausch hinaus - standen wir im regen Kontakt. Prof. Andrea Macchi von der Universität Pisa richte ich ebenfalls meinen Dank aus, denn auch ihm konnte ich Fragen stellen, er half bei der Interpretation der Simulationen und ebnete den Weg zur Zusammenarbeit mit Tatjana.

Allen weiteren PhD Mitstreitern, wie auch dem Sekreteriat und den Technikern des Instituts für Laser- und Plasmaphysik danke ich für die Unterstützung und die netten Unterhaltungen, in der Küche, beim Mittagessen oder im Labor.

Steffi, ohne Dich wäre ich nicht bis zu diesem Punkt gekommen. Du wusstest immer, was ich fühlte oder welche Worte halfen. Gemeinsam waren wir stark und haben so manche Daten erfolgreich gesammelt. Weit mehr als 44 Wochen haben wir zusammen im "Bunker" verbracht, das schweißt mehr als zusammen. Wir sind ein Team geworden auf vielen verschiedenen Ebenen.

Darüber hinaus, danke ich Meiner Mutter, Brigitte, die mir mit *help and advice* sprachlich zur Seite stand, sowie auch meinem Vater, Burkhard, der mich jederzeit moralisch und voller Tatendrang unterstützt hat! Und auch unser Hund, Felix, war immer ein Ruhepol und eine Quelle nötiger Glückshormone.

Erklärung der Urheberschaft

Ich versichere an Eides Statt, dass die Dissertation von mir selbständig und ohne unzulässige fremde Hilfe unter Beachtung der "Grundsätze zur Sicherung guter wissenschaftlicher Praxis an der Heinrich-Heine-Universität Düsseldorf" erstellt worden ist.

Die Dissertation wurde in der vorgelegten oder in ähnlicher Form noch bei keiner anderen Institution eingereicht. Ich habe bisher keine erfolglosen Promotionsversuche unternommen.

Ort, Datum	Unterschrift